

Nanometer-Scale Placement in Electron-Beam Lithography

by

Juan Ferrera

B.S., Massachusetts Institute of Technology (1994)

S.M., Massachusetts Institute of Technology (1994)

Submitted to the Department of Electrical Engineering and Computer
Science

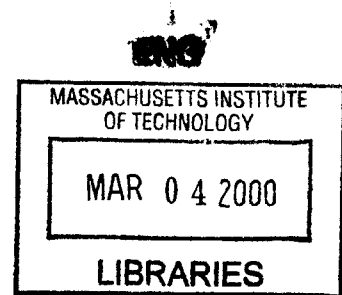
in partial fulfillment of the requirements for the degree of

Doctor of Philosophy

at the

MASSACHUSETTS INSTITUTE OF TECHNOLOGY

February 2000



© Massachusetts Institute of Technology, MM. All rights reserved.

Author

Department of Electrical Engineering and Computer Science

October 12, 1999

Certified by

Henry I. Smith

Keithley Professor of Electrical Engineering

Thesis Supervisor

Accepted by

Arthur C. Smith

Chairman, Department Committee on Graduate Students

Nanometer-Scale Placement in Electron-Beam Lithography

by

Juan Ferrera

Submitted to the Department of Electrical Engineering and Computer Science
on October 12, 1999, in partial fulfillment of the
requirements for the degree of
Doctor of Philosophy

Abstract

Electron-beam lithography is capable of high-resolution lithographic pattern generation (down to 10 nm or below). However, for conventional e-beam lithography, pattern-placement accuracy is inferior to resolution. Despite significant efforts to improve pattern placement, a limit is being approached. The placement capability of conventional e-beam tools is insufficient to fabricate narrow-band optical filters and lasers, which require sub-micrometer-pitch gratings with a high degree of spatial coherence. Moreover, it is widely recognized that placement accuracy will not be sufficient for future semiconductor device generations, with minimum feature sizes below 100 nm. In electron-beam lithography, an electromagnetic deflection system is used in conjunction with a laser-interferometer-controlled stage to generate high-resolution patterns over large areas. Placement errors arise because the laser interferometer monitors the stage position, but the e-beam can independently drift relative to the stage. Moreover, the laser interferometer can itself drift during exposure. To overcome this fundamental limitation, the method of spatial phase-locked electron-beam lithography has been proposed. The beam position is referenced to a high-fidelity grid, exposed by interference lithography, on the substrate surface. In this method, pattern-placement performance depends upon the accuracy of the reference grid and the precision with which patterns can be locked to the grid. The grid must be well characterized to serve as a reliable fiducial. This document describes work done to characterize grids generated by interference lithography. A theoretical model was developed to describe the spatial-phase progression of interferometric gratings and grids. The accuracy of the interference lithography apparatus was found to be limited by substrate mounting errors and uncertainty in setting the geometrical parameters that determine the angle of interference. Experimental measurements were performed, which agreed well with the theoretical predictions. A segmented-grid spatial-phase locking system was implemented on a vector-scan e-beam tool to correct field placement errors, in order to fabricate high-quality Bragg reflectors for optical filters and distributed-feedback lasers. Before this work, Bragg reflectors of adequate fidelity had not been fabricated by e-beam lithography. The phase coherence of the gratings

fabricated with the segmented-grid method was characterized by measuring the displacement between adjacent fields. From these measurements, field-placement errors of ~ 20 nm (mean + 3 sigma) were estimated. The segmented grid method was used to pattern Bragg gratings, which were used in the fabrication of integrated optical filters. The devices demonstrated excellent performance.

Thesis Supervisor: Henry I. Smith

Title: Keithley Professor of Electrical Engineering

Acknowledgments

First of all, I would like to express my gratitude to my advisor, Prof. Henry Smith, for his guidance and encouragement. I have been in his group since 1991, and I haven't stopped learning since. I consider myself extraordinarily privileged to have had the opportunity to work in his laboratory. I would also like to thank Mark Schattenburg for his excellent advice, and for letting me work in his laboratory, where I learned so much about interference lithography. Much of my thesis was related to *e*-beam lithography, so I'm very grateful to Dieter Kern, Steve Rishton, and Phillip Chang for donating VS-2A to our group at MIT. I'd also like to thank Steve and Volker Bögli for teaching me almost all I know about *e*-beam lithography. I'm grateful to the 6-A program, which gave me the opportunity to work at IBM and started a collaboration that has been extremely rewarding to me. The work of Scott Silverman and Mark Mondol was essential in bringing the machine into operation and maintaining it in good working order, work which I really appreciate. I learned very many things from James Goodberlet — his work was quite inspiring and provided much insight. It was a real pleasure to interact with him.

I'd very much like to thank all members of the optics team. It was a wonderful experience to collaborate with such capable, friendly, and highly motivated group of people. Tom Murphy does a fantastic job keeping our efforts coordinated, besides his crucial contributions in design and fabrication. Mike Lim was been a great team-, lab-, office-, and room-mate. His achievements in lithography and etching have been phenomenal, and I have enjoyed spending time with him, in and out of the lab. It is always invigorating to talk to Jalal Khan, who is always very cheerful and does an excellent job designing and modeling devices. The *e*-beam part of the optics work will be in the capable hands of Todd Hastings. I wish him all kinds of success. It was a great pleasure to work with Jay Damask and Vincent Wong, who started the optics work and have since graduated. I very much thank them for their contributions.

I'd like to express my thanks to the staff members of the NSL and SML. I've enjoyed working and interacting with all of them. Special thanks go to Jim Daley, who provided enormous amounts of help, whenever I had trouble with my lab work. He really goes beyond the call of duty to help all students with their problems. Jim Carter and Bob Fleming generously taught me how to do interference lithography, and were always willing to provide advice and help. Ed Murphy's superhuman efforts to make sure x-ray masks were available are appreciated. I also shared many interesting conversations with him. I'd also like to thank Rich Aucoin, Jeanne Porter, Jane Prentiss, Pat Hindle, and Bob Sisson for their help and advice. Thanks are due to Cindy Lewis for her efficient administration and her friendly attitude.

I thank Tim Savas, my office-mate of many years, for his excellent advice, and for keeping the RIE in such good condition. It was always enjoyable to join him and Mike Lim for a few beers after work. I thank Mark Finlayson and Kevin Pipe for their excellent work. I wish them success in their studies. I'm glad to have met Maya

Farhoud and Dave Carter. It was a pleasure to work with Maya. I'm grateful to her for sharing her enthusiasm with me. Dave's good cheer and great advice are very much appreciated. I wish all my other friends and colleagues Alex Bernshteyn, Carl Chen, Dario Gil, Yaowu Hao, Keith Jackson, Paul Konkola, Mitch Meinhold, Rajesh Menon, Euclid Moon, David Pflug, Farhan Rana, Mike Walsh, and Feng Zhang the best of luck with their work.

I'm very grateful to my mother, my aunt Gabi, and my brother Santiago for their unconditional support. Santiago also contributed directly to my thesis work, by teaching me how to use "lex" and "yacc" to parse scripts, and by letting me use some of the code he wrote. I very much appreciate his technical input. I am extremely grateful to Lisa Zeidenberg, not only for her wonderful company and support, but for proofreading every page of this thesis, and enormously improving the quality of the text.

Finally, I would like thank the Organization of American States, DARPA, ARO, AFOSR, and SRC for their financial support, and especially D. Patterson for his early and continuing confidence in our research on SPLEBL.

Contents

1	Introduction	25
1.1	Overview of electron beam lithography	29
1.1.1	History and principles of operation	29
1.1.2	Pattern placement	32
1.1.3	Field stitching	33
1.1.4	Beam scanning strategies	35
1.1.5	Pattern placement performance of modern tools	38
1.2	The global fiducial grid	39
1.3	The segmented grid	43
2	Interference lithography	49
2.1	Description of the MIT apparatus	51
2.2	Laser specifications	55
2.3	Spatial filters	56
2.4	Interference angle	57
2.5	Feedback stabilization	58
2.6	Substrate stage	59

3	Analysis of the spatial filter as a source	61
3.1	Minimum Gaussian beam diameter	61
3.2	Scalar-wave diffraction from a small aperture	63
3.3	The pinhole used in the spatial filter	68
3.4	Measurement of the far-field intensity pattern	70
3.5	Conclusion, further work	75
4	The phase progression of gratings exposed with spherical waves	79
4.1	Interference of two plane waves	79
4.2	Interference of spherical waves	82
4.2.1	Period calculation	82
4.2.2	Phase computation	85
4.3	Substrate-flatness and mounting errors	88
4.3.1	Surface flatness	89
4.3.2	Rotation errors	91
4.3.3	Rotations about the x and y axes	92
4.3.4	Rotation about the z axis	96
4.3.5	Translation errors	97
4.4	Errors in setting a and c	99
4.5	Error budget calculations for IL	100
4.6	Summary	102
5	Measurements of grating phase progression	105
5.1	Background	106

5.2	Moiré pattern exposed in resist	110
5.3	Phase-shifted moiré	115
5.3.1	Reference Grating Fabrication	116
5.3.2	Description of the experiment	120
5.4	Results and discussion	127
5.5	Future work: The IL system as a holographic interferometer	131
5.6	Summary	135
6	Fabrication of Bragg reflectors with segmented-grid spatial-phase locking	137
6.1	Introduction	137
6.2	Distributed Bragg reflectors and resonators	139
6.2.1	Techniques to fabricate DBR gratings	141
6.3	Review of segmented-grid spatial-phase locking	143
6.4	Automatic measurement of interfield errors	147
6.5	Analysis of interfield error requirements	151
6.6	Fabrication of DBR-based transmission reflectors and resonators	156
6.6.1	Bragg-grating pattern generation	157
6.6.2	Alignment issues	161
6.6.3	Measured interfield errors	162
6.6.4	Device fabrication process	167
6.7	Optical transmission results	168
6.8	Summary	172

7	Further development of the segmented-grid method	175
7.1	Implementation on MIT's VS-2A system	175
7.2	Measurement of short-term beam stability	181
7.3	Increasing the resolution of a heterodyne interferometer	189
7.4	Summary	195
8	Bragg grating fabrication for channel-dropping filters	197
8.1	Overview of device characteristics and fabrication process	198
8.2	Description of mask set and lithographic process	202
8.3	Fabrication of the IL-grating mask	206
8.3.1	Period calibration	206
8.3.2	Determination of grating k -vector	211
8.4	Fabrication of fiducial-grating mask	215
8.4.1	Pre-patterning with the fiducial-definition mask	216
8.5	Grating exposure using aligned x-ray lithography	218
8.6	Generation of Bragg-grating data	224
8.7	Bragg grating exposure	228
9	Conclusion	231
A	Substrate preparation for IL exposure	235
B	Substrate preparation for tri-level resist process	237
C	Si sidewall profiles for different etching conditions	239

CONTENTS	11
D Repeatability of alignment with two vector-scan <i>e</i>-beam tools	243
E Bragg-grating definition script	253
References	259

List of Figures

1.1	The planar fabrication process.	26
1.2	Principle of operation of the scanning-electron microscope.	30
1.3	Schematic of an interferometrically controlled x-y stage.	34
1.4	Illustration of raster scan and vector scan methods.	37
1.5	Conceptual depiction of spatial-phase-locked electron-beam lithography (SPLEBL).	42
1.6	Two modes of SPLEBL: global-grid and segmented-grid.	45
2.1	Schematic diagram of the MIT interference lithography setup.	52
2.2	Schematic of the procedure used to adjust the angle of incidence of the secondary beams.	54
2.3	Photograph of the spatial-filter assembly.	58
3.1	An idealized spatial filter: a thin circular aperture of radius $a = \pi w_0/2$ is placed at the beam waist.	63
3.2	Plane wave incident on an ideal aperture.	64
3.3	Fraunhofer diffraction patterns.	67
3.4	Schematic of a spatial filter implemented with a 15.25 μm -thick aperture. The beam is no longer blocked at the minimum-diameter point.	69

3.5	Scanning electron micrographs of a typical pinhole aperture.	70
3.6	Experimental setup to measure the Fraunhofer diffraction pattern produced by one of the IL spatial filters.	71
3.7	Fraunhofer intensity pattern, acquired after adjusting the spatial filter to maximize the intensity at the center.	72
3.8	Intensity pattern, acquired after adjusting the spatial filter to maximize the width of the Gaussian profile.	73
3.9	Field magnitude at the source, calculated from the diffraction pattern shown in Fig. 3.7.	74
3.10	Field magnitude at the source, calculated from the diffraction pattern shown in Fig. 3.8	75
3.11	Calculated Fraunhofer diffraction patterns for a circular aperture illuminated by a uniform plane wave and for the same aperture illuminated by a Gaussian beam.	78
4.1	Two plane waves incident on a surface.	80
4.2	Definition of coordinate system and geometric parameters used in the model.	82
4.3	Geometry that defines the interference angle as a function of position on the substrate.	83
4.4	Comparison of model-predicted values of period with experiments. . .	86
4.5	Plots of the phase discrepancy between gratings exposed by interfering two spherical waves and perfect linear gratings.	88
4.6	Fizeau interferograms showing surface flatness of a 3-inch-diameter silicon wafer.	90

4.7	Grating distortion induced by substrate curvature. The grating's nominal period is 200 nm. The substrate surfaces are assumed to be paraboloids of revolution.	90
4.8	Definition of substrate rotation angles.	92
4.9	Rotation of the substrate about the x -axis.	93
4.10	Grating distortion introduced by substrate rotation about the x -axis.	94
4.11	Grating distortion introduced by substrate rotation about the y -axis.	95
4.12	Grating distortion introduced by substrate rotation about the z -axis.	97
4.13	Grating distortion introduced by substrate shift along the \hat{x} -direction.	98
4.14	Grating distortion introduced by substrate shift along the \hat{y} -direction.	99
4.15	Schematic of the AIL configuration.	104
5.1	Photograph of the IL system's substrate stage. The substrate can be translated along the \hat{x} and \hat{z} directions by means of micrometers . . .	107
5.2	The autocollimator is used to monitor stage-induced rotation about the z axis as the substrate is being translated.	108
5.3	A moiré pattern of "ellipses" results when two hyperbolic gratings are superimposed with a linear shift between them.	109
5.4	Double exposure procedure.	111
5.5	Photograph of moiré pattern obtained by superimposing two grating images, shifted with respect to one another by 1 cm.	112
5.6	Contours of constant phase difference, calculated theoretically for the experimental conditions, overlapped on an enlarged photograph of the moiré pattern.	114

5.7	Errors measured between the theoretical contours and the moiré fringe boundaries.	115
5.8	Fabrication sequence of fluorescent test grating.	119
5.9	Cross sectional scanning-electron micrograph of a finished scintillating grating.	120
5.10	(a) Mechanism by which the fluorescent grating interacts with the standing wave. (b) Photograph of moiré fringes imaged in real time by an integrating CCD camera.	121
5.11	Schematic of the experimental arrangement used to measure the phase difference between the reference grating and the standing wave present at the grating's surface.	122
5.12	A sequence of phase-shifted moiré images.	124
5.13	Data from a piezo calibration run. The solid line is a cosine function fitted to the data.	127
5.14	(a) Contours of constant phase difference, measured at the null position. (b) Cross-sectional plot of the data shown in (a), for $y = 0$	129
5.15	Plots of phase difference as measured using the phase-shifting moiré technique.	130
5.16	Plots of error between the calculated and measured values of phase difference.	130
5.17	The IL system configured as a holographic interferometer.	132
5.18	The IL grating viewed as a reflection hologram. (a) Recording the hologram.	133
5.19	Fringes caused by the interference of the 0 and -1 diffracted orders from a laterally-shifted grating.	135

5.20	Interferogram taken at the null position. The phase was obtained using the phase-shifting technique and the interferometric configuration. . .	136
6.1	Schematic of the integrated resonant channel-dropping filter.	138
6.2	Coupling of forward- and backward-propagating waves by means of constructive interference.	140
6.3	Segmented-grid SPLEBL uses IL-generated reference gratings to accurately place each Bragg-grating segment.	144
6.4	“Outrigger gratings” are used to measure the stitching errors between fields.	148
6.5	Illustration of the procedure used to measure the overlap of two outrigger gratings.	149
6.6	Error statistics of outrigger measurement procedure.	152
6.7	Model of phase errors in a Bragg grating. The grating is composed of distortion-free segments, which are tiled together.	154
6.8	The probability density function (PDF) for the reflection coefficient Γ of a Bragg grating was estimated with a Monte-Carlo simulation. Plot of the results for one case.	155
6.9	Contour plots of the probability of writing an acceptable grating resonator for two representative periods $p = 510$ nm (a) and $p = 240$ nm (b).	156
6.10	Illustration of the strip-loaded rib waveguide geometry used for the silica/silicon nitride grating devices.	157
6.11	Schematic diagram of the optical and x-ray mask levels used in the fabrication of the devices.	158

6.12 Schematic depiction of the process used to generate segmented fiducial gratings on an x-ray mask.	159
6.13 Scanning-electron micrograph of two uniform Bragg grating patterns on a finished mask. Note the outrigger structures, used to measure field-placement errors.	163
6.14 Close-up of the quarter-wave section of a resonator grating on the same mask.	164
6.15 Distribution of a representative subset of interfield errors on the Bragg-grating mask, as measured between the <i>e</i> -beam deflection field and the fiducial reference prior to writing the grating segments.	165
6.16 Distribution interfield errors as measured on the Bragg grating mask.	166
6.17 Effect of grating angular error on the orthogonality of beam-deflection axes.	166
6.18 Scanning-electron micrograph of a self-aligned grating etched onto a waveguide.	168
6.19 Diagram of a finished chip.	170
6.20 Transmission spectra of two uniform Bragg reflector gratings, with lengths of ~ 1 cm, ~ 2 cm.	171
6.21 Transmission spectra of six quarter-wave shifted resonators with the same nominal period and increasing grating length.	172
6.22 Comparison of the measured data for a QWS resonator with the theoretically-calculated spectrum. The performance of the devices agrees very well with the theoretical prediction.	173
6.23 Resonance offset from the stopband center, plotted for twelve resonators.	174
7.1 System diagram of the VS-2A <i>e</i> -beam tool.	176

7.2	Method used to evaluate VS-2A's pattern-placement capability	178
7.3	Field alignment strategy used to accommodate angular error.	181
7.4	Histogram of interfield errors obtained with the newly implemented segmented-grid SPLEBL system	182
7.5	Diagram of the edge-measurement technique.	183
7.6	Transmitted-electron image of a cleaved silicon edge.	184
7.7	Oscilloscope trace of the signal collected as the beam is scanned across the edge.	185
7.8	Measurement of beam-position fluctuations with the interferometer feedback disabled.	186
7.9	Measurement of beam-position fluctuations with the interferometer feedback enabled.	187
7.10	Power spectrum of beam position, which shows the noise floor.	188
7.11	Schematic diagram of a heterodyne interferometer.	190
7.12	Phase-measuring circuit proposed to increase the resolution of the e -beam tool's heterodyne interferometer.	192
7.13	Circuit diagram of prototype phase-measuring circuit.	193
7.14	Test of the interferometer's resolution with the analog phase-measuring circuit.	194
8.1	Waveguide geometry for the InGaAsP/InP-based optical devices.	199
8.2	The dual-layer hardmask process.	200
8.3	A Bragg-grating structure etched into the core layer with the dual-layer hardmask process	203

8.4	Flowchart of the lithographic process used in fabricating the second generation devices.	204
8.5	Histogram demonstrating the precision achieved in measuring the period of the standard wafer	208
8.6	Schematic of the white-light Michelson interferometer used as a front-surface reference.	210
8.7	Processing sequence used in fabricating the IL-grating mask.	212
8.8	Scanning electron micrograph of the <i>e</i> -beam written alignment marks on the IL-grating mask. The plating base has been cleared from the irregularly-shaped area to facilitate alignment under an optical microscope.	214
8.9	Fabrication sequence used to fabricate the fiducial-grating mask.	215
8.10	Method used to pre-pattern the x-ray mask.	217
8.11	Photograph of the x-ray lithography system used to align and expose the IL-grating pattern on a pre-patterned x-ray mask.	219
8.12	Cross-sectional scanning electron micrographs of a grating exposed in PMMA. Poor process latitude was observed, due to excessive penumbra.	220
8.13	Cross-sectional SEM's of a grating exposed after increasing the source-to-mask distance.	221
8.14	Images of alignment marks, as observed through the alignment microscope.	222
8.15	AFM scans of alignment crosses, used to measure overlay errors.	223
8.16	Layout of the CDF mask.	225
8.17	Sample script, which generates a three-field-long quarter-wave shifted grating pattern.	229

8.18 Scanning electron micrographs of <i>e</i> -beam-written Bragg gratings. . .	230
--	-----

List of Tables

- 1.1 Sources of pattern distortion. 36
- 1.2 Performance of the MEBES 4500S. 38
- 1.3 Predicted lithography requirements. 40
- 1.4 Research areas 43

- 2.1 Effect of interference-angle errors on grating period. 59

- 4.1 Tolerances calculated for a 200-nm period grating with a maximum phase error corresponding to 3 nm. 101

- 6.1 Optical and geometrical parameters of silica/silicon nitride devices. . . 169

- 7.1 Alignment repeatability as a function of beam current. 179
- 7.2 Beam diameter vs. beam current. 184

- 8.1 Optical and geometrical parameters of InGaAsP/InP devices. 201

Chapter 1

Introduction

Since its invention in 1960 [1], the integrated circuit (IC) has grown both in complexity and in processing power at a vertiginous pace. Today, ICs are inexpensive enough to be found in children's toys, and they are so reliable that they are used to control the safety devices in automobiles, to which people entrust their lives. The memory capacity, speed and complexity of digital computers has been increasing exponentially: The number of components in microprocessor circuits doubles every 18 months; likewise, their clock speed doubles every 18 to 24 months.

Arguably, this rate of growth is enabled by a “virtuous cycle”. Computers are used to implement increasingly sophisticated mathematical models of semiconductor devices, which allow engineers to design improved devices for subsequent generations, as well as the complex tools to fabricate them. Computers also allow for the design and layout of complex circuits.

The process used in the manufacture of integrated circuits is known as the planar fabrication process (see Fig. 1.1). A substrate is coated with a radiation-sensitive polymer. Then, a pattern is created in the polymer by selective exposure to radiation and subsequent development. This step is known as lithography. In most industrial processes the exposure is done with ultraviolet (UV) radiation. The pattern is encoded in a mask, which blocks the radiation in some areas and lets it reach the substrate in

others. During development, either the exposed or the unexposed areas of the resist are removed (positive and negative process, respectively). The uncovered areas of the substrate are modified by etching, doping with impurities, or material deposition. The remaining polymer is used to locally protect the underlying material; for this reason the polymer is referred to as a *resist*. Devices are built by adding layers of different materials and repeating the process described (in slightly different forms) several times, each time with a different pattern. To obtain the desired end result, all patterns must be aligned to one other.

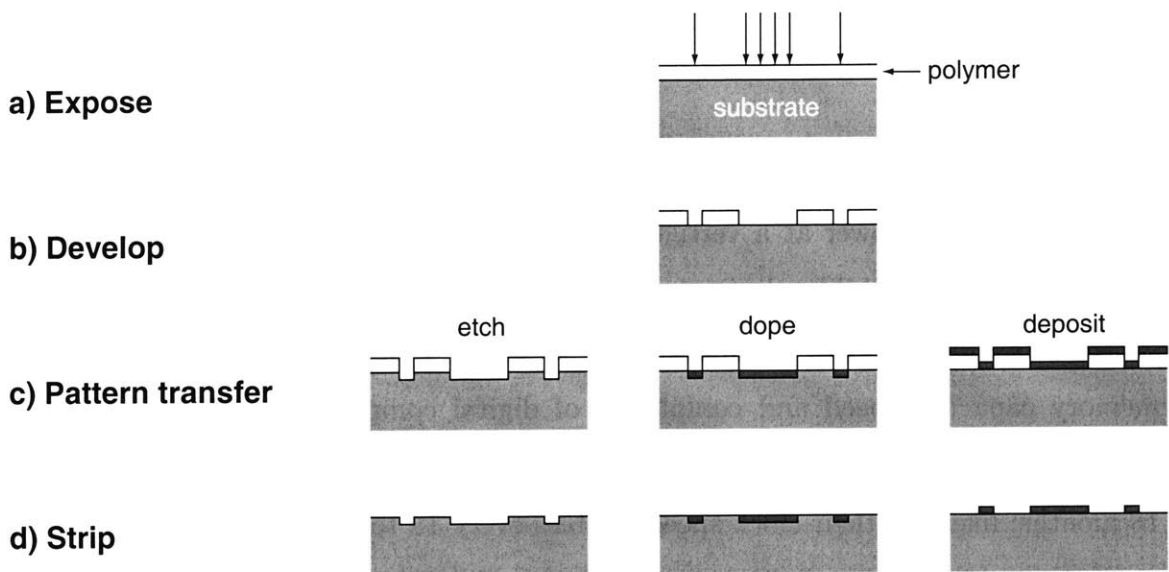


Figure 1.1: The planar fabrication process (after [2]).

This planar process allows several devices to be fabricated in parallel, and in the final steps of the process, to be interconnected to each other, forming a circuit. Not only can several devices be fabricated in parallel, but the principle can be applied to the batch fabrication of several circuits on one substrate.

The rapid development of semiconductor technology can be attributed to three factors:

1. The inherent parallelism of the planar fabrication process.
2. The decrease of the linear dimensions of individual components.

3. The fact that the area covered by a component scales as the square of its linear dimensions.

It follows that more complex circuits can be manufactured economically only by decreasing the size of their components. Consequently there has been a constant drive to shrink device dimensions to the absolute minimum. Since device dimensions are, to a large extent, limited by the smallest feature that can be defined lithographically, the development of lithography to improve its resolution has been of crucial importance.

For years, the semiconductor industry has relied on the same basic fabrication processes: optical lithography has been used to define patterns on semiconductor wafers. Throughout this time, it has been speculated that the wavelength of light would impose a limit to the resolution of optical lithography. A different lithographic technique would be needed to fabricate features smaller than this limit.

The field of nanostructure fabrication has been evolving since the 1960's. In order to circumvent the limited resolution of optical lithography, different techniques to pattern features with dimensions of 100 nm or below were developed. These techniques used various kinds of radiation to perform the exposure, such as electron-beam lithography, x-ray lithography [3], and ion-beam lithography [4, 5], but for a variety of reasons they were impractical for manufacturing integrated circuits. At the time of writing of this document, the minimum feature size of ICs is approaching 100 nm. Tools developed for the fabrication and characterization of nanometer-scale structures, such as the atomic force microscope, are now being applied in the mass-production of commercial electronics.

Electron-beam lithography, the subject of this thesis, is a technique initially developed for nanostructure fabrication, in a regime inaccessible to industrial micro-fabrication technology. E-beam lithography was championed by some as destined to replace optical printing when optical technology reached its resolution limit, but this has not happened yet.

As the techniques used to print patterns using UV light are refined, the resolution

limit has been pushed back more and more, to the extent that features smaller than one wavelength are printed on circuits currently in the market. Recently, the Taiwan Semiconductor Manufacturing Company announced a production process with 180 nm minimum feature size [6].

In today's semiconductor industry, virtually all lithography is done by optical projection of a mask onto the substrate, since this proven technology has advanced enough to meet the resolution requirements and has high throughput. Although *e*-beam lithography does not meet the throughput requirements to be used directly in production, it is nonetheless of crucial importance in mask making. No other mask patterning technique can match the resolution of electron beams, and all masks for the most advanced device generations are patterned in this way.

When used in a fabrication process, the mask patterns must overlay with each other to a specified tolerance (for integrated circuits, the tolerance is $1/3 - 1/5$ of the minimum feature size or critical dimension). Consequently, as feature sizes shrink, better pattern placement accuracy is required of *e*-beam mask makers. Historically, the pattern placement of electron beam machines has not been as good as their resolution, and will likely be inadequate for the manufacture of future IC generations.

E-beam lithography is also used in the fabrication of Bragg-grating integrated optical devices [7]. For this class of devices, pattern placement requirements are quite strict. Each one of the features that comprise a grating must be placed within a small fraction of one wavelength, which current *e*-beam tools are either unable or hard-pressed to achieve. Higher-performance grating based devices will depend on nanometer-scale feature placement.

The next section presents an overview of the development of electron beam technology, in order to more clearly illustrate the origin of the problem.

1.1 Overview of electron beam lithography

1.1.1 History and principles of operation

In an electron microscope, high-energy electrons, with de Broglie wavelengths on the order of 0.1 nm, are used, enabling the resolution to surpass that of the light microscope. As optical systems, the light microscope and optical projection lithography tools are closely related. Extending this analogy to the electron microscope, a logical step is to use systems based on the electron microscope to perform lithographic patterning.

The first demonstration of patterning with an electron beam dates back to 1958. Buck and Shoulders used electron-beam-induced deposition and etching to create sub-micron patterns on substrate surfaces [8]. Möllenstedt and Speidel [9] used the optics from a transmission electron microscope (TEM) to project the demagnified image of an aperture onto a collodion membrane. The pattern was created by local evaporation of the collodion material in the locations irradiated with electrons. They mechanically moved the aperture to scan the fine probe on the sample. Möllenstedt and Speidel obtained patterns with a resolution of 10-20 nm, but due to the method they used to scan the beam, only simple, very small patterns were made. This experiment does not really qualify as lithography, since the generated pattern could not be transferred to a substrate for fabrication purposes.

The most successful implementation of *e*-beam patterning is scanning-electron-beam-lithography (SEBL). It is based on the scanning-electron microscope (SEM), first implemented by von Ardenne in 1938 [10]¹.

The principle of operation of the SEM is depicted in Fig. 1.2. Briefly, electrons are extracted from a source (usually a heated sharp tip). The electrons are accelerated to

¹Other systems, based on the TEM, project a demagnified image of a mask or a shaped aperture onto the substrate. Mask-based systems promise high throughput through parallel exposure. For these tools, the masks are made using thin membranes because they must be transparent to electrons. These membranes tend to deform when subjected to high electron flux.

energies ranging from 10 keV to 100 keV by biasing the tip to the appropriate voltage with respect to an extraction electrode, which is grounded.

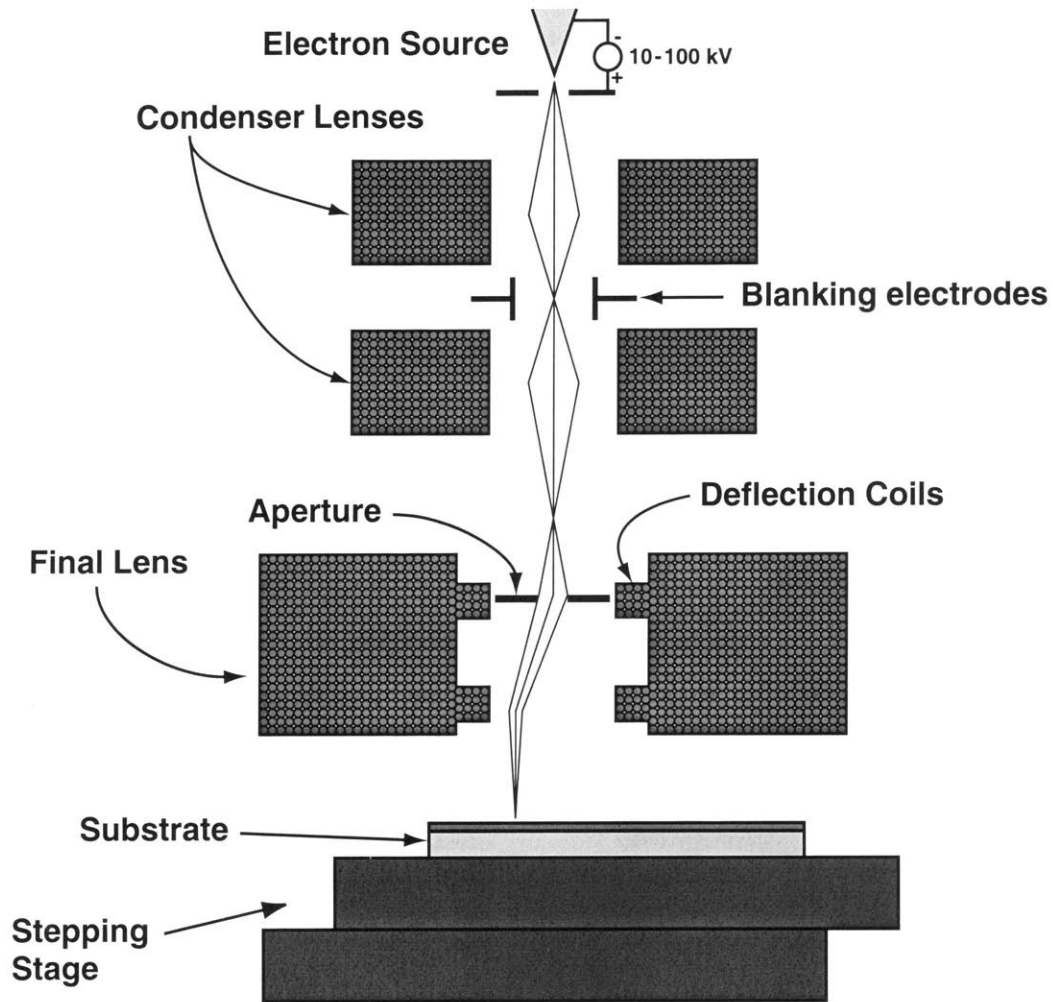


Figure 1.2: Principle of operation of the scanning-electron microscope: Electrons emitted from a heated tip are focused by a set of magnetic lenses to form a probe on the workpiece. The probe is scanned by transverse electric or magnetic fields. For lithography, the beam is turned off by a set of blanking electrodes.

A set of magnetic lenses forms a probe by projecting a demagnified image of the source on the surface of the sample. The amount of demagnification depends on the effective diameter of the source and the probe diameter desired. The probe is scanned across the surface by means of electric or magnetic fields, transverse to the trajectory of the electron beam.

For lithography, a means to turn the beam on and off is necessary. This is imple-

mented by adding a set of blanking electrodes, which produce an electric field that deflects the beam away from the axis of the column. An aperture stops the off-axis electrons.

During the late 1950's and early 1960's, the SEM was further developed at Cambridge University [11, 12]. Application of these instruments to lithography was also investigated: Research programs were initiated at Westinghouse, IBM Research, Cambridge University, Texas Instruments, and Hughes Research [13, 14].

To automate the patterning process, the beam deflection was controlled by programmable digital computers. Registration between different lithographic levels was achieved by using the instrument in microscope mode, imaging registration marks present on the substrate, and aligning the pattern to them.

The electron beam was used to modify polymer resist films, as is done in photolithography. Irradiation of the polymer modifies its dissolution in the appropriate developer solution. The first exposures were carried out using the photoresist compounds used by the industry at the time, but the resolution obtained was relatively poor. The use of poly(methyl methacrylate) (PMMA) as an electron resist, reported in 1968 [15], greatly improved the resolution.

Substrates were also successfully patterned by "contamination", which denotes the *e*-beam-induced polymerization of residual organic contaminants in the vacuum chamber [16]. This technique was able to achieve very high resolution, but the process was extremely slow and unreliable.

The initial objective of the various research efforts was to develop *e*-beam tools to replace photolithographic printers on the manufacturing floor, when the resolution limit of photolithography was reached [17]. One very significant shortcoming of SEBL is its serial nature: the picture elements (pixels) that form the pattern are exposed one after the other. Increasing the exposure rate of *e*-beam lithography has been one of the major priorities in the development of the technology. Even so, the low throughput of *e*-beam lithography is one of the reasons that its application in industrial

production is limited to mask making.

1.1.2 Pattern placement

Although resolution is an important element of a lithographic technology, pattern placement is just as important. As mentioned above, in IC's patterns must be placed within a fraction of the minimum resolvable feature. Electron-beam lithography has demonstrated resolution down to 10 nm, but the pattern placement accuracy of this technique does not match its resolution.

In very general terms, the electron microscope's lenses are inhomogeneous electric or magnetic fields, which cause electron trajectories to converge towards a focal point. The fields have cylindrical symmetry around the axis of the lens. In order to scan the beam it must be deflected away from the axis. Off-axis, electron lenses show aberrations, such as astigmatism, coma, and chromatic aberration. Because of these aberrations, as the beam is scanned across the surface, the shape of the probe can vary from the minimum circular spot obtained on-axis. If the spot is not allowed to vary in shape by more than a fraction of the nominal beam diameter, there is a limit on the maximum deflection possible [18, 19, 20].

Initially, most efforts in SEBL were put into designing lenses with low aberration, which would allow for maximum possible deflection. At that time (in the 1960's and 70's), the area covered by one integrated circuit was $\sim 1 \text{ mm} \times 1 \text{ mm}$, which could be covered by one field. A device wafer could be put on a mechanical stage, which would position the substrate so that one chip was exposed at a time (see Fig. 1.2). Overlay could be ensured by imaging registration marks. The electromagnetic deflection of an e -beam is much faster than mechanical stage movements, so in order to maximize the speed of writing, stage movement must be minimized. This implies that the field should be made as large as possible.

With careful engineering of electron optics and dynamic correction of the focus, astigmatism, and beam deflection, fields as large as $5 \text{ mm} \times 5 \text{ mm}$ were exposed [21,

22, 23] with a resolution of $0.5 \mu\text{m}$ and placement accuracy of $0.12 \mu\text{m}$.

Modern IC technology is evolving in the direction of sub-100 nm features over fields of $25 \text{ mm} \times 25 \text{ mm}$ and larger. To write a linewidth of 100 nm, the beam diameter and pixel spacing should be about 25 nm. (In order to have control over the exposed linewidth, the minimum dimension is usually required to consist of at least 4 resolvable elements [13].) Hence the full field consists of $10^6 \times 10^6$ pixels. There are at least two reasons why such a large field containing such a number of pixels cannot be exposed by *e*-beam lithography: limitations of electron optics; and limitations of beam-deflection electronics.

In practice the field of view of an electron lens never exceeds about 5 mm. This is because in electron optics only simple converging lenses exist [24]. In contrast, in light optics both diverging as well as converging lenses exist. In this case spherical aberration can be eliminated by arranging the design so that the positive spherical aberration coefficient of the converging lens cancels the negative coefficient of the diverging lens. This has allowed the field of view of light-optical systems to be increased without sacrificing their resolution.

To expose a field with $10^6 \times 10^6$ addressable elements would require 20-bit digital-to-analog converters (with linearity better than 20 bits) operating at pixel rates of 160 MHz or more, in order to satisfy throughput requirements. The electronic amplifiers that drive the deflection system would require similar bandwidths and dynamic range. To the author's knowledge, electronics that meet these requirements are not currently available.

For the reasons stated above, increasing the field size of *e*-beam systems to cover the area of an entire IC was considered impractical and was abandoned.

1.1.3 Field stitching

An alternative approach was first developed in 1970 at Thomson CSF [25, 26]. The pattern was exposed as a mosaic of small fields ($\sim 100\text{-}300 \mu\text{m}$). To ensure that the

fields were properly placed (so-called field stitching), the stage position was measured with two laser interferometers, one for each axis of motion, as depicted in Fig. 1.3. The beams of the interferometers were reflected off two orthogonal mirrors. The resolution of the interferometers was $\lambda/16$, or ~ 40 nm (HeNe laser), and a pattern-placement accuracy of 100 nm was achieved over a 5 cm x 5 cm area. This method has been almost universally adopted for high-accuracy lithography machines (including photolithography tools) [27]-[35] and position metrology instruments [36]-[39].

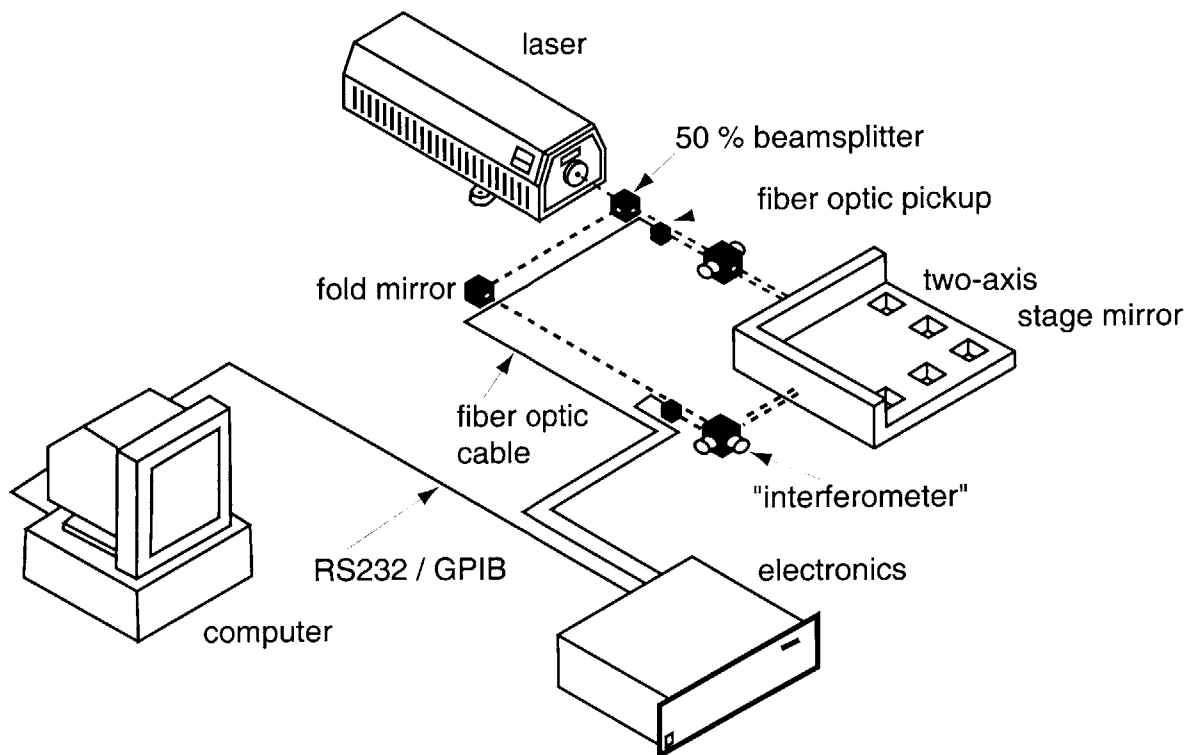


Figure 1.3: An interferometrically controlled x-y stage uses two orthogonal plane mirrors as the references. Two Michelson interferometers measure the displacement along each axis. Sub-wavelength precision is achieved by interpolating between fringes.

The invention of the heterodyne interferometer [40], made position measurement with a resolution of $\lambda/128 \approx 5$ nm possible. Today, instruments with $\lambda/2048$ resolution are available commercially²

²from the Hewlett-Packard Company and Zygo Corp.

When a lithography tool relies on field stitching, beam deflection and stage motion must be exactly matched to prevent errors in feature placement. This can be accomplished by calibrating the deflection to stage motion. However, the exposure of a pattern covering an area of several square centimeters can take several hours; both subsystems have to stay matched throughout this period. In practice, despite strict control of the environment, the beam will drift with respect to the stage.

From the discussion above, the contributions to pattern placement errors can be divided in two classes:

1. Intrafield distortion: the distortion in beam positioning within one field.
2. Interfield distortion, the mismatch between two adjacent fields.

Using this classification, the contributions to pattern placement can be more readily identified. Table 1.1 lists several contributors to pattern placement errors. Both classes of errors have static and dynamic sources. In principle, static sources of error can be eliminated by implementing proper calibration procedures, but dynamic sources of error require the machine to be periodically recalibrated. The duration of calibration procedures can add prohibitive amounts of overhead to exposure times. Further, fast contributions, such as vibrations and stray electromagnetic fields, cannot be eliminated.

1.1.4 Beam scanning strategies

Each field can be thought of as a square array of pixels. In a serial exposure technique, such as SEBL, the individual pixels within one field have to be exposed according to a predetermined sequence. The choice of exposure sequence can influence throughput and pattern placement. Two main strategies have been implemented [41]:

1. Vector scan: For each shape the beam is deflected to the location of the first pixel and unblanked. The pattern generator then deflects the beam to fill in

Table 1.1: Sources of pattern distortion.

Intrafield errors	
Static	Lens aberrations Deflection non-linearity
Dynamic	Electrical charging of sample and <i>e</i> -beam system parts Stray magnetic fields, both static and dynamic Differential motions of the electron optics (vibrations, thermal)
Interfield errors	
Static	Mismatch of interferometer and beam-deflection length scales Rotation of deflection axes relative to stage motion axes Non-flatness of stage mirrors Non-orthogonality of stage mirrors Non-rectilinear stage motion Non-flatness of sample
Dynamic	Electrical charging of sample and <i>e</i> -beam system parts Stray magnetic fields Temperature changes Mechanical vibrations

the rest of the pixels contained within the shape. The beam is then blanked and deflected to the next shape. In this way, only the pixels to be exposed are addressed.

2. Raster scan: In this mode of operation, the beam addresses all pixel locations within the array and is unblanked to expose a pixel. The pixels are addressed sequentially, starting, for example, with the top row and deflecting the beam left-to-right (see Fig. 1.4). Once all the pixels in the first row have been addressed, the beam is deflected downwards, to the second row, and all pixels in the row are addressed right-to-left. The process continues until all the pixels within the field have been addressed ³.

Vector scanning is generally considered desirable if the area to be exposed is less than half the total area, since only exposed pixels have to be addressed. However,

³This mode of scanning is known as boustrophedonic, from the Greek *boustrophedon*, “following the ox furrow”. A more common type of raster scan, used in cathode-ray-tube displays, is performed the same way as European writing, from left to right and from top to bottom [42].

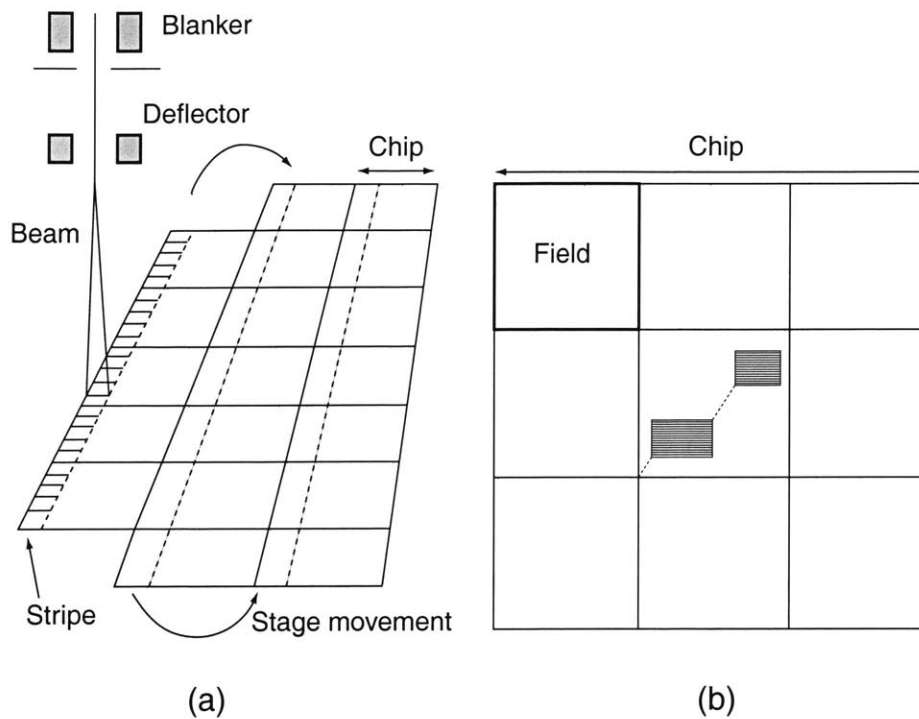


Figure 1.4: Illustration of raster scan (a) and vector scan (b) methods.

the beam settling time must be taken into account; it can add significant overhead if the pixel addressing rate of the machine is high (> 20 MHz).

On the other hand, the regularity of the raster technique allows for a simpler implementation. The EBES machine, initially developed at Bell Laboratories [43], is a raster-scan tool. The fast, horizontal scanning is done by electrostatic beam deflection on a $140\ \mu\text{m}$ field, while the slow vertical scan is implemented by moving the sample stage under the beam at a constant rate. Small amounts of vertical deflection are necessary to compensate for the continuous motion of the stage. In this way, field boundaries are eliminated in the vertical direction: the pattern across the substrate is subdivided in vertical stripes. At the end of each stripe the stage reverses direction vertically, horizontally steps to the next stripe, and the beam commences writing again. The stage position is monitored with laser interferometers, and correction signals are applied to the beam deflection to compensate for stage errors. Since the beam is scanned in a very regular manner, and essentially along only one axis,

Table 1.2: Performance of the MEBES 4500S.

lithographic performance	
write time (64 Mb DRAM)	140 min
write scan linearity	20 nm
pattern position accuracy	40 nm
resolution	0.2 μm
linewidth control	35 nm
linewidth uniformity	35 nm
environment stability requirements	
column temperature	20-23 \pm 0.1 $^{\circ}\text{C}$
electronics temperature	20-23 \pm 0.5 $^{\circ}\text{C}$

deflection distortion correction can be implemented more effectively. The horizontal deflection signal is simply a sawtooth, and deviations from linearity can be calibrated out. Blanking timing determines which pixels are exposed. High pixel exposure rates can be achieved by implementing a fast blanker.⁴

1.1.5 Pattern placement performance of modern tools

The performance specifications of a MEBES 4500 electron-beam mask maker are listed in table 1.2.

Compared with the first *e*-beam machines, implemented in the 1970's, the specifications for this machine show very significant improvements in both the throughput and the data handling capacity of the control computer, which make possible the exposure of complex patterns in a few hours. However, there is only moderate improvement in resolution and pattern placement errors.

In today's semiconductor industry, virtually all lithography is done by optical projection of a mask onto the substrate, since this proven technology has advanced enough to meet the resolution and manufacturing requirements. Although *e*-beam

⁴The MEBES tools, successors of the EBES, have pixel exposure rates of up to 160 MHz [44, 45, 46, 47, 48, 49].

lithography does not meet the throughput requirements, it is nonetheless of crucial importance in mask making [44]. No other mask patterning technique can match the resolution of electron beams, and all masks for the most advanced device generations are patterned in this way. Patterns cannot be directly registered to substrate marks when performing lithography on masks, since all patterning is done on a blank substrate. Instead, placement errors are decreased by imaging a fiducial mark on the stage, away from the writing area. This operation is time consuming and is therefore performed infrequently. The system must run open-loop between registration operations.

The Semiconductor Industry Association, in its 1997 Technology Roadmap for Semiconductors, lists estimates for lithographic pattern placement accuracy and metrology requirements for future integrated circuit generations, characterized by the minimum feature size (critical dimension). (See table 1.3.) It is estimated that conventional technology will not yield the pattern overlay required for the 70 nm generation (in the year 2009). This document states that [50]:

Overlay and CD [critical dimension] improvements have not kept pace with resolution improvements. The estimates for overlay appear to plateau around 30 nm. This will be inadequate for ground rules less than 100 nm. Overlay and CD control over large field sizes continue to be a major concern from sub-130 nm lithography.




Lithographic tools may have to rely on a different method to correct feature placement errors. Indirect referencing has worked well for 30 years, but may have to be replaced with a direct reference scheme.

1.2 The global fiducial grid

The interference of two mutually coherent laser beams has been used for several years to produce high-quality diffraction gratings. To provide adequate performance in

Table 1.3: Predicted lithography requirements. (From [51])

<i>Year of First Product Shipment Technology Generation</i>	<i>1997 250 nm</i>	<i>1999 180 nm</i>	<i>2001 150 nm</i>	<i>2003 130 nm</i>	<i>2006 100 nm</i>	<i>2009 70 nm</i>	<i>2012 50 nm</i>
Gate CD control (nm)	20	14	12	10	7	5	4
Final CD output metrology precision (nm, 3 sigma)*	4	3	2	2	1.4	1	0.8
Overlay control (nm)	85	65	55	45	35	25	20
Overlay output metrology precision (nm, 3 sigma)*	9	7	6	5	4	3	2

Solutions Exist  Solutions Being Pursued  No Known Solution 

* Measurement tool performance needs to be independent of line shape, line materials, and density of lines

spectroscopy apparatus, the lines that comprise the gratings must be spaced with great regularity (a very small fraction of the grating period).

The application of gratings produced with interference lithography as metrological standards follows from their regularity, or to use a different expression, from their spatial-phase coherence.

Smith *et al.* [52] recognized that structures fabricated by interference lithography could, due to their coherence, be used as metrological standards. They addressed the problem of intra-field distortion. They used a grid (made by patterning two gratings at a right angle to one another) to measure the deflection field of a vector-scan electron-beam tool. Anderson *et al.* [53] performed similar measurements. As a result of these measurements, they found that most of the distortion was caused by non-linearities of the digital-to-analog (D/A) converters used to generate beam deflection signals. They also found that increasing the field size beyond 100 μm caused distortion induced by electron-optical aberrations. Having quantified the magnitude of the distortion, they corrected it by calibrating the D/A converters. Electron-optical distortion was not corrected because it is negligible if field sizes $\leq 100 \mu\text{m}$ are used. If larger field sizes are desired, it is relatively straightforward to implement calibration tables to remove non-linearities in the deflection field. Using this approach, it is possible to eliminate intra-field distortion, but inter-field distortion, due to drift, still remains.

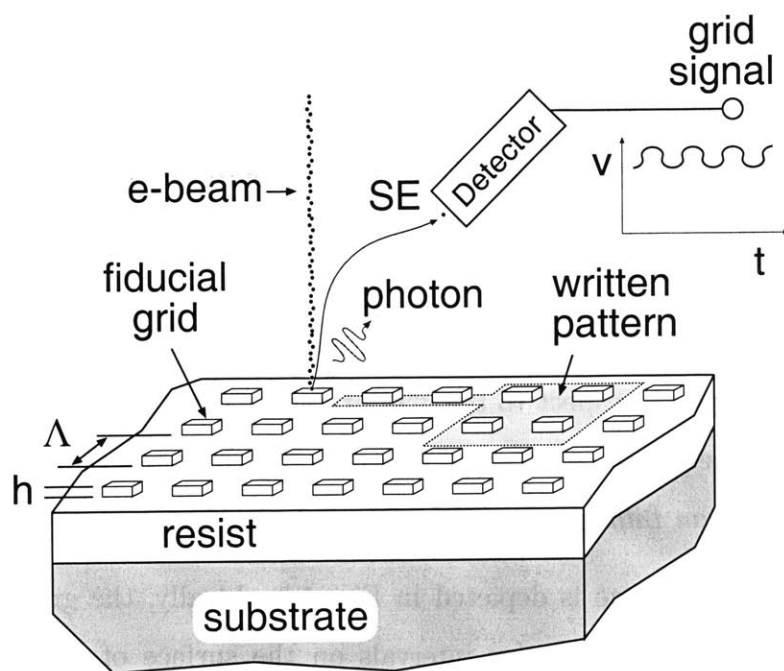
Smith *et al.* [54] applied the use of IL-generated grids to the correction of interfield

distortion. They proposed to reference the beam position directly to a global fiducial grid placed on the substrate. This scheme makes it possible to measure beam position on the sample, without relying on intermediate variables, such as the position of the sample stage. In other words, the global fiducial grid on the sample becomes the metrological standard of the lithography tool, replacing the interferometer-controlled stage. The grid is a periodic structure, so that a spatial phase can be assigned to it. This will be described in more detail in a later section. Since in this scheme the patterns are placed with respect to the grid, it can be said that they are “locked” to its spatial phase. Hence, the method proposed by Smith *et al.* is called *Spatial-Phase-Locked Electron-Beam Lithography* (SPLEBL).

A version of the scheme is depicted in Fig. 1.5. Ideally, the grid consists of an array of features placed at regular intervals on the surface of the workpiece. As the electron beam is scanned, a time-varying signal is collected, such as secondary electrons, photons, etc. The collected signal changes when the beam is placed on one of the features. Thus, the signal is modulated by the position of the beam on the substrate. If the position of the nodes is known one can infer the beam position from the collected signal, and any deviations in the beam’s position can be corrected concurrently with exposure.

The fiducial grid, like the interferometer stage, relies on the interference of coherent light waves for distance metrology. There is an important difference, however: the physical grid is part of the workpiece and is therefore a time-invariant reference, while the virtual grid of the interferometer stage is not directly linked to the sample, and is subject to drift. Moreover, sample distortion caused by clamping in the SEBL tool or temperature effects, will affect the grid in the same way. Since SPLEBL references pattern placement to the grid, sample distortion should not affect pattern placement.

The use of a periodic fiducial implies that position measurement is ambiguous to one half of the period, so the lithography machine must be accurate enough to remove this ambiguity. If the period of the fiducial grid is 200 nm, then the pattern placement accuracy of the stage by itself must be better than 100 nm. For this, it is



$$\Lambda < 2 \mu\text{m}$$

$$h < 50 \text{ nm}$$

Figure 1.5: Conceptual depiction of a direct referencing scheme for SEBL machines, denominated spatial-phase-locked electron-beam lithography (SPLEBL). A fiducial grid is placed directly on the substrate surface. It is intended to interact with the electron beam and produce a signal, which is collected by a detector. The position of the beam relative to the grid is encoded in this signal.

simplest to rely on an interferometer stage, but this is not required.

When the sample stage steps to a new field, the residual error of the beam position on the sample is unknown, and can only be corrected once the beam has started scanning the sample. To pre-align the field, the grid must be sampled at very low dose, causing no resist exposure. After the pre-alignment step, exposure can commence and continuous feedback is then possible.

The concept of the global fiducial grid opened a vast area of investigation. Subsequent work demonstrated the feasibility of the technique, but many issues need to

be resolved before applications outside of the research laboratory can be considered. The open areas of research are summarized in Table 1.4.

Table 1.4: Research areas

-
1. Measurement of grid fidelity
 2. Optimization of signal type
 - (a) Choice of electron-beam generated signal
 - (b) Grid material
 - Must provide adequate signal
 - Must not introduce artifacts into the patterns being written (such as line broadening due to beam scattering)
 - Must be easily stripped before development, without affecting resist
 - (c) Grid fabrication process must be simple and reliable
 3. Optimization of signal-detector parameters: collection angle, frequency response, gain, etc.
 4. Signal processing to extract beam position information from detected signal, and remove noise
 5. Optimization of beam scanning strategy, to ensure that position information for both directions is effectively acquired
 6. Applications of SPLEBL
-

1.3 The segmented grid

One fundamental constraint in the implementation of a SPLEBL tool is that acquisition of the signal must not interfere with the patterning of features. However, to obtain a signal from the fiducial grid, it is necessary to irradiate it, which will expose the resist if the dose is high enough. The SPLEBL process must be designed so that an adequate signal can be obtained without unwanted exposure of the resist.

A second constraint relates to the implementation of the feedback loop. It is neces-

sary to know the time constants and magnitudes of the different sources of interference within the e -beam tool. From Table 1.1, these include drift terms (with long time constants), such as charging in the column; thermally induced expansion/contraction of the different mechanical components; and thermal drift of the electronics that focus and deflect the beam.

Fast (short time constant) interference includes vibrations in the mechanical components, as well as 60 Hz and RF electromagnetic interference. (RF interference can be eliminated by proper use of shielding and electrical filtering.) Once the sources of interference are known, a feedback loop can be designed to lock the beam to the substrate below a specified tolerance.

Figure 1.6 (a) depicts the most general implementation of SPLEBL. The fiducial grid is present throughout the surface of the substrate, and patterns may be exposed anywhere on the surface. This implies that the grid may not disturb the lithographic exposure — the signal must either be collected while patterns are being exposed, or collected prior to exposure, but at such a low dose that the resist is not exposed.

Dynamically, interference must be eliminated up to frequencies of several hundred Hertz, so that real-time signal processing is required. These requirements make the implementation of the feedback loop quite challenging.

In applications where patterns need not be exposed at all locations on the substrate, areas for the fiducial can be allocated which are separate from areas where the lithography is to be performed. It is then possible to relax some of the requirements outlined in the previous section, thus significantly simplifying the implementation of a SPLEBL system, which is nonetheless quite useful for some applications. Ferrera *et al.* [55, 56] proposed and implemented such a scheme, the *segmented fiducial grid* (illustrated in Fig. 1.6 (b)).

The areas containing the fiducial grid can be small (e.g. 0.1% of the total sample area). If such a compromise is made, the fiducial can be sampled for long periods of time to obtain an adequate signal, and locking to the grid can be done with high

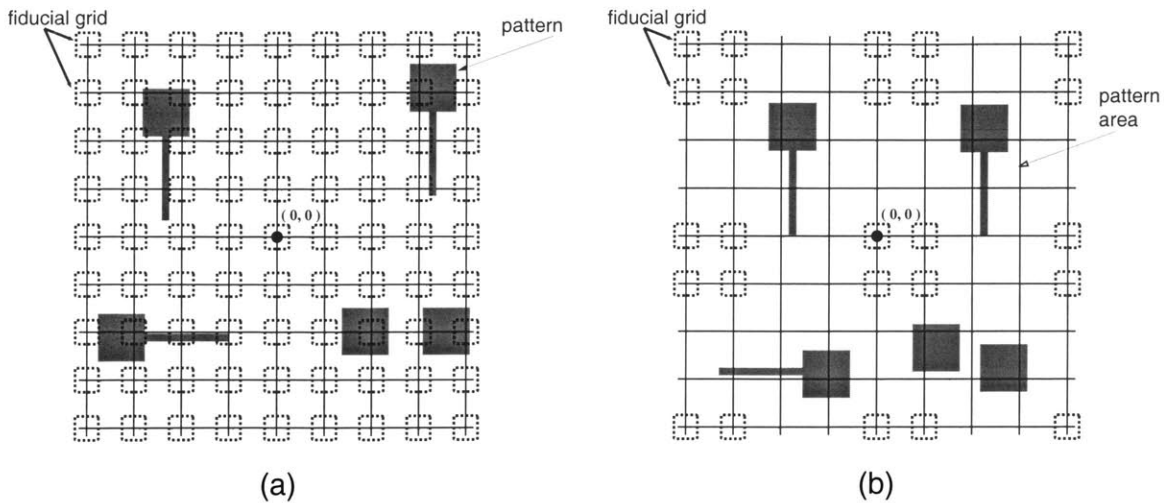


Figure 1.6: (a) The global grid: reference nodes are present everywhere on the substrate surface. Patterns may be written at any location on the sample. (b) The segmented grid, a simplification of the global grid concept: reference nodes are present within small areas allocated for them. Patterns may be written at any location, except the reference areas.

precision.

The segmented-grid approach assumes that the SEBL system is stable for short time scales (< 1 s — the typical writing time for a single field), so that sampling of the grid does not have to occur concurrently with writing. This eliminates the need for real-time signal processing.

In addition, the deflection of the beam within one field must meet the pattern placement requirements.

The implementation of a segmented-grid scheme was motivated by the need to fabricate Bragg gratings for a variety of integrated optical devices. In such devices, a grating with feature sizes on the order of 100 nm is patterned on an optical waveguide. The grating is up to several millimeters long, and each one of the lines that comprise it must be positioned within 5 nm. Such fabrication is beyond the capabilities of a conventional lithography system, but was carried out successfully using a 1-D segmented fiducial-grid scheme.

The work reported in this document is not intended to address all of the issues listed in Table 1.4. It is restricted to two main avenues of research:

1. The characterization of grids exposed by interference lithography
2. The application of the segmented-grid scheme to the fabrication of integrated optical devices

Chapter 2 describes the interference lithography apparatus used to fabricate fiducial grids. This apparatus uses the interference of two diverging optical waves, which emanate from two spatial filters, to produce high-fidelity gratings. The use of diverging waves implies that the spacing between the grating lines is not uniform throughout the substrate, i.e., the grating is non-linear. Chapters 3 and 4 develop a model to predict the feature locations of a grid recorded by interference lithography. Grids are made by exposing two gratings at right angles to one another, so that the analysis of gratings can also be applied to grids. A model is proposed, which assumes that spherical wavefronts interfere at the substrate plane to form the grating image. Chapter 3 presents an argument to support this assumption, based on scalar diffraction theory and the Fraunhofer far-field approximation. Measurements of far-field intensity patterns are reported, which indicate that the proposed model is valid in describing the operation of the interference lithography apparatus. The spherical-wave model is used in Chapter 4 to develop a model, which predicts the feature locations of a grating recorded by interference lithography. The model is used to estimate grating distortion induced by substrate non-flatness, mounting errors, and the uncertainty in determining the distance and angle between the point sources and the substrate surface. Chapter 5 describes several methods to measure the characteristics of interferometric gratings and reports the experimental results. The experimental results are found to agree well with the model of Chapter 4.

Subsequent chapters report the implementation of a segmented-grid scheme on an SEBL system, and its application in the fabrication of Bragg-grating based optical devices. Chapter 6 briefly describes the principle of operation of a Bragg-grating based

device: the integrated channel-dropping filter. A stochastic model is used to evaluate the impact of pattern-placement errors on device performance. The implementation of the segmented grid algorithm, which is covered in detail in the author's M.S. thesis, is briefly reviewed. The use of SPLEBL in generating Bragg-grating patterns is reported, and the quality of these gratings is evaluated. This chapter also describes the process used to fabricate $\lambda/4$ -shifted resonators on waveguides and reports the measured device performance. Chapter 7 describes further refinements made to the segmented grid scheme. Chapter 8 reports the development of a process to fabricate a second generation of optical devices. Several problems found during the fabrication of the first device generation are addressed. Chapter 9 concludes with a brief summary.

Chapter 2

Interference lithography

Thomas Young's famous experiment was the first demonstration of the interference of light [57]. The experiment is set-up as follows: light from a monochromatic point source illuminates two pinholes located very close together on a screen. The pinholes act as secondary point sources. The light beams that emanate from them are projected onto a screen, placed at a distance significantly larger than the separation between the pinholes. In the region where the two beams overlap a pattern of bright and dark bands appears. These bands are called *interference fringes*. As the angle of interference of the two beams is increased, the fringes quickly become microscopic. Albert Michelson suggested recording the interference fringes produced by such an arrangement on Lippmann photographic plates [58], to improve on the quality of ruled gratings for spectroscopy.

Today, interference lithography (IL) is widely used to produce periodic structures. The modern apparatus used for interference lithography is in principle no different from Young's interference experiment, although significant technological advances have been made, which enable the repeatable fabrication of well-characterized periodic structures over large areas. Until the invention of the laser it was not possible to perform interferometric exposures over large areas. Rudolph and Schmahl used light from a high-power laser to expose photoresist films, and were able to fabricate high-

quality gratings for high resolution spectroscopy [59, 60].

Interference lithography has been under development at MIT for over 25 years, at the Nanostructures Laboratory and the Space Microstructures Laboratory [52]-[70]. Patterns produced by this technique have been successfully used in a variety of applications, such as x-ray spectroscopy [71]-[73], epitaxial growth [74], atom-beam diffraction [75]-[77] and filtering [78], x-ray mask distortion measurements [79, 80], and fabrication of optoelectronic devices [81]-[84]. These applications require gratings of high fidelity, i. e., the gratings' lines must not deviate from their ideal position by more than a small fraction of their period.

The MIT IL system, now located in the Space Microstructures Laboratory, is specifically designed to produce gratings with minimum amounts of distortion. The current system is the product of numerous contributions by a large number of people over several years [52]-[66]. For the work reported in this document, the system was used in its current configuration — no modifications were made to the apparatus, except to implement phase-shifting measurements, as described in Chapter 4. The apparatus is described in this chapter, with emphasis on the various factors that affect the repeatability and accuracy of the gratings. Although it is known that gratings with very small distortions have been fabricated with this apparatus, the amount of distortion has not been quantified to the nanometer level.

Subsequent chapters present a study of the fidelity of gratings fabricated by interference lithography, with reference to their application as metrological standards in spatial-phase-locked electron-beam lithography (SPLEBL). The aim of SPLEBL is to improve the pattern placement accuracy of *e*-beam tools beyond the limits found in today's equipment, i.e., an accuracy better than 30 nm (mean + 3σ) over ~ 10 cm diameter substrates. As described in the previous chapter, a global fiducial grid is patterned on the substrate surface by interference lithography. The position of the beam is measured with respect to this grid, and any errors are corrected. Thus, in SPLEBL, the grid is the main metrological reference for the whole system.

In an error-budget analysis for SPLEBL, residual pattern-placement errors are

assumed to be caused by two factors: distortions of the fiducial grid, and errors made by the SPLEBL system in locking the beam position to the grid. The grid's fidelity must be guaranteed to be significantly better than the maximum error allowed. Although the fiducial grid's accuracy requirements cannot be explicitly stated until an exhaustive analysis of the e -beam tool's pattern placement specifications and sources of error has been carried out, it is a reasonable estimate that the tool's metrology standard must be accurate to 1/10 of the pattern placement specification. That is, for a total error specification of 30 nm (mean + 3σ), grid distortion, when the substrate is unstrained,¹ must be guaranteed to be less than 3 nm over its entire area.

2.1 Description of the MIT apparatus

Figure 2.1 is a schematic diagram of the MIT interference lithography (IL) apparatus. The light source is an argon-ion laser. It emits a beam of linearly polarized light with wavelength $\lambda = 351.1$ nm. The primary beam is divided by a dielectric beamsplitter into two secondary beams or arms, each carrying 50% of the total power. The two beams separate and are directed by mirrors towards two spatial filters.

The spatial filters eliminate any unwanted scattered light and coherent radiation other than the fundamental Gaussian mode of the laser cavity, to produce two "pure" diverging wavefronts, which impinge on the substrate at an angle and produce interference fringes. To ensure the fidelity of the grating, it is necessary to ensure that only the wavefronts emanating from the spatial filters are contributing to the standing wave at the substrate. Due to the long coherence length of the radiation used, any light scattered by the optic components or the table will coherently interfere, resulting in grating distortion. The additional information in the hologram is encoded as phase modulation of the interference fringes. For this reason, the space between the

¹Once the grid has been exposed on the substrate surface, any mechanical changes introduced by temperature changes, clamping, etc. do not contribute to pattern distortion, since the grid is rigidly attached to the substrate. Conversely, it must be ensured that the substrate is unstrained when the fiducial grid is exposed.

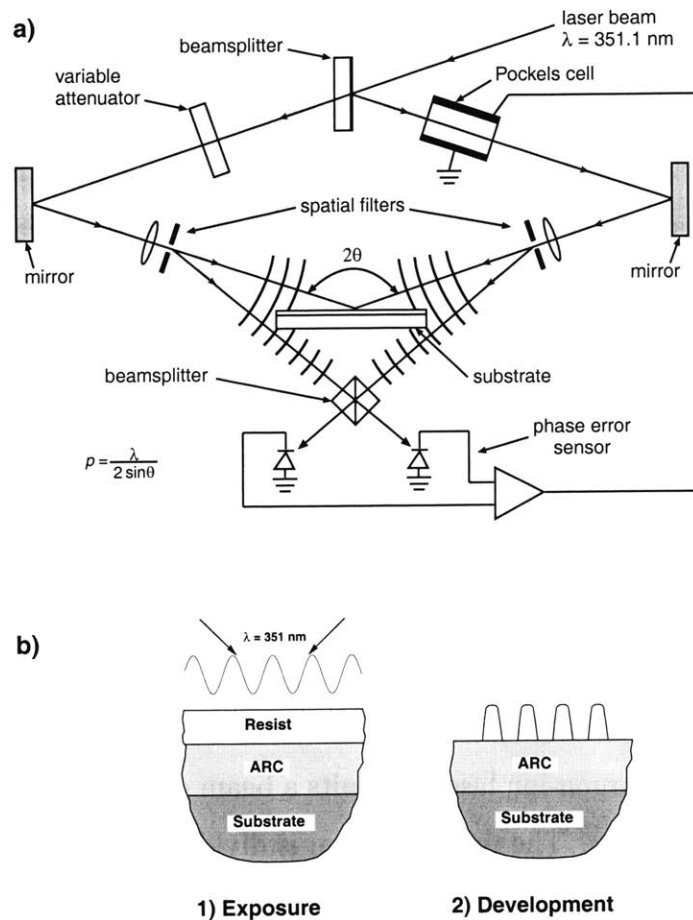


Figure 2.1: (a) Schematic diagram of the MIT interference lithography setup. (b) Detail of the interference-lithographic process.

spatial filters and the substrate is enclosed by non-reflecting barriers to prevent any scattered light from reaching the substrate.

When interfering two optical waves to record gratings, one would ideally use plane waves in order to produce a grating with a linear phase progression — a grating of straight, parallel and equidistant lines. However, it is questionable whether truly plane waves, free of unpredictable errors at the nanometer level, can be produced with conventional apparatus. In order to have plane waves incident on the substrate, one would use collimating lenses between the spatial filters and the substrate. However, figure errors in the lenses cause deviations from plane waves. The required lenses, with diameters of several centimeters and phase errors of only a few nanometers are

either currently unavailable, or prohibitively expensive. Moreover, defects in the lens material, or dust particles on the lens surface will scatter light, creating spurious wavefronts. As a consequence of research being performed on extreme ultra-violet (EUV) lithography, reflectors with figure specifications in the nanometer range and surfaces free of defects might be available in the future. It might then become feasible to fabricate linear-phase gratings with deviations from perfect linearity in the 1 nm range. The system would have to be engineered to prevent particles from settling on the reflecting surfaces, a problem which is avoided in the MIT system by using diverging waves and having no optics between the spatial filter and the substrate.

The interference pattern is recorded in a photoresist film that covers the substrate. The substrate is typically reflective, so that the additional unwanted wavefronts arise from reflection at the resist-substrate boundary. To attenuate these reflections an absorbing anti-reflection coating (ARC) is applied to the substrate surface before the resist layer. The refractive index and thickness of the ARC designed to minimize substrate reflection [85, 86].

The periodicity of the fringes is determined by the wavelength and the angle of interference. The spatial filters are positioned so that straight lines connecting them to the center of the substrate enclose an angle 2θ . The period p of the fringes at the center of the substrate is then given by

$$p = \frac{\lambda}{2 \sin \theta} . \quad (2.1)$$

The system can be set up to expose gratings ranging in period from 200 nm to approximately $4 \mu\text{m}$. The period of the exposure is selected as follows: the spatial filters are removed from the setup, and the steering mirrors that direct the secondary beams towards the substrate are adjusted so that the beams impinge on the substrate at a desired angle θ with respect to the substrate surface normal. The angle is measured by means of a special assembly, which consists of a mirror mounted on a goniometer. The mirror is rotated by $\pm\theta$ (see Fig. 2.2). The steering mirrors are

adjusted until the beam retroreflects off the goniometer mirror. This procedure is carried out for both beams. Then, the spatial filters are aligned to both beams.

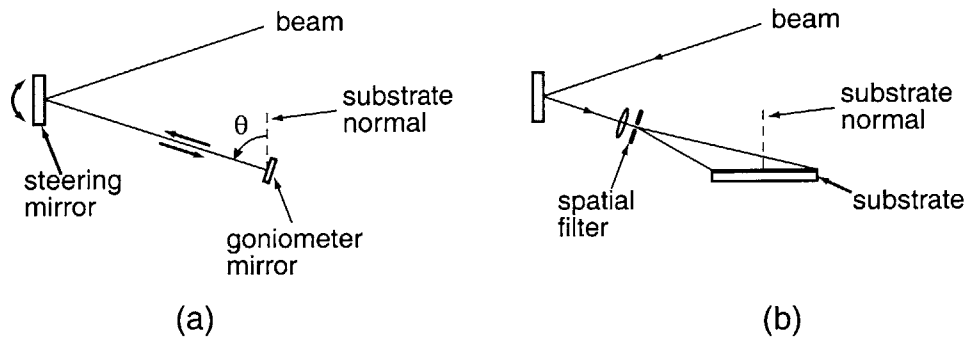


Figure 2.2: Schematic of the procedure used to adjust the angle of incidence of the secondary beams. (a) The steering mirror is adjusted until the beam retroreflects on a mirror, which has been turned by θ . (b) The spatial filter is aligned to the beam.

The use of diverging waves implies that the angle of interference varies as a function of position on the substrate. As a result, the period of the grating changes as a function of position on the substrate surface as well. Equation 2.1 will be extended in a later section to include this effect.

The two interfering wavefronts must be equal in intensity to achieve maximum contrast in the interference pattern (perfect destructive interference at the nulls). To this end, a variable attenuator (see Fig. 2.1) is placed in one of the secondary beams, so that the power in that beam can be fine-tuned to match the power in the other.

To minimize particle defects during grating exposure, the IL system is located in a cleanroom environment. In this environment the air is constantly being passed through filters to remove particulates. The consequences are turbulent air flow and acoustic vibrations, which disturb the optical components and cause dynamic optical path variations. After splitting the primary beam, the secondary beams traverse paths of approximately 3 meters before being recombined, and the effective length of each arm may change by several wavelengths in a fraction of a second. Optical path variations directly influence the position of the interference pattern. If the interference pattern is not stationary over the $\sim 10 - 30$ seconds necessary for resist exposure,

the result is an exposure with very poor contrast. A feedback system, depicted in Fig. 2.1, measures the optical path difference between the two arms of the system and modulates the phase of one of the arms to keep the interference pattern static in space.

The following factors are important for grating fidelity and repeatability: laser wavelength, quality of the wavefront, and interference-fringe stability. The relevant IL-setup components are discussed in more detail in the sections below.

2.2 Laser specifications

The light source used in the IL apparatus is a Coherent INNOVA Sabre argon-ion laser. The gain medium, an argon plasma, supports emission at several wavelengths, ranging from 528.7 nm to 275.4 nm. The corresponding modes will all “lase” simultaneously if they are allowed to resonate within the laser cavity. If emission at a single wavelength is required, as is the case in IL, a prism is inserted into the cavity, to select the desired wavelength. This configuration is referred-to as “single-line”. The wavelength used for IL is $\lambda = 351.1$ nm. At this wavelength the laser provides 1 W of continuous-wave (CW) power.

Within one emission line, the gain of the medium as a function of wavelength has a finite width, which is 10 GHz for the 351.1 nm line [87]. For TEM₀₀ operation, the longitudinal resonant modes of the 2 m-long cavity, are spaced by 75 MHz. The gain bandwidth thus corresponds to roughly 130 resonant cavity modes. Emission occurs for several of these modes, restricting the coherence length to ~ 3 cm. Interference fringes are formed only if the difference between the optical paths transversed by the two waves, from the beamsplitter to a given point on the substrate, is less than the coherence length. For a 3 cm coherence length, gratings with a 200 nm period would only cover a vertical stripe 3.4 cm wide in the middle of the substrate.

It is possible to obtain oscillation from only one single longitudinal mode of the

cavity by inserting an etalon into the resonator. The longitudinal mode closest to the transmission peak of the etalon will not experience as much loss as the other modes and will preferentially oscillate, suppressing the other modes. This is known as “single-frequency operation”. When operated in single-frequency mode, the laser will have a bandwidth of 10-15 MHz, which translates to a coherence length of 20-30 m.

Variations in the laser’s power output are significant in setting the exposure dose. The magnitude of short-term (10 Hz - 2 MHz) variations is specified to be 2% of the total output power, which does not present a problem in exposing resist. Long-term power drift is, however, significant. The proper dose is set by regularly monitoring the power density at the substrate plane and setting the exposure time to obtain the proper dose.

Two other important characteristics of the laser are wavelength repeatability and stability. The laser’s frequency of oscillation is repeatable to within 10 MHz upon power-up, and will not vary by more than 5 MHz if the room and cooling water temperature are kept controlled to within 1°C [87]. From these data, the conclusion can be drawn, that the wavelength accuracy and repeatability of the laser is ~ 2 parts in 10^8 .

2.3 Spatial filters

The wavefronts that interfere at the substrate plane emanate from the spatial filters. Therefore, their performance directly impacts the fidelity of the gratings produced.

Each spatial filter consists of a converging lens, with focal length $f = 10$ mm, which focuses the beam into a 5- μ m diameter pinhole aperture. The pinhole acts as a low-pass filter. At the focal plane of the lens, the Fourier transform of the incident amplitude distribution is obtained [88, 89]. The incident amplitude consists of the laser beam plus spurious reflections and scattered light, which, due to the long co-

herence length of the laser, can contribute to the exposure if allowed to propagate to the substrate. The Gaussian laser beam transforms into a Gaussian spot of diameter $2.6 \mu\text{m}$ at the center of the Fourier transform plane, while the scattered light, assumed to impinge on the lens in random directions, is distributed throughout the transform plane. The pinhole is an aperture stop that passes those spatial frequencies corresponding to the Gaussian beam, and stops all others.

Figure 2.3 is a photograph of the spatial filter assembly, designed by M. Schattenburg and R. Fleming, which includes several micrometer-driven actuators. The lens distance from the plane of the aperture can be changed, as well as its pitch and yaw with respect to the incoming beam's axis. The aperture can be moved in the plane transverse to the beam's axis. To achieve optimal alignment of the aperture to the beam's minimum diameter ("waist"), motions of less than $1 \mu\text{m}$ are needed. This makes the alignment of the aperture quite challenging, since merely touching the micrometers disturbs the whole assembly. To circumvent this difficulty, the pinhole fine adjustments are done with piezoelectric actuators. Finally, the whole assembly can be moved along the plane transverse to the beam to align the center of the lens to the beam. Many independent parameters must be adjusted to obtain optimum alignment of lens and aperture to the beam's direction of propagation.

2.4 Interference angle

The smallest angular increment the goniometer (Fig. 2.2) is 5 arc-min. In practice, it has been found that after the beams have been set to retroreflect off the goniometer mirror and the spatial filters have been aligned to the beam, the error in setting the interference angle is 0.1 degrees (see Chapters 6 and 8). Table 2.1 illustrates the impact of the limited precision of the interference angle for several nominal grating periods.

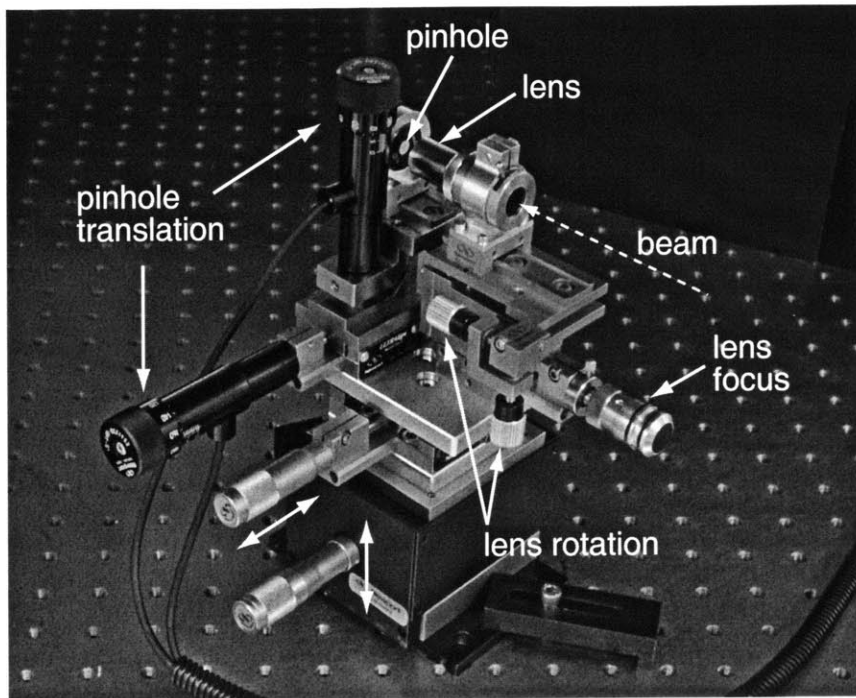


Figure 2.3: Photograph of the spatial-filter assembly. The beam passes through the lens, and is focused to a diffraction-limited spot. The assembly sits on a pair of translation stages that enable alignment of the lens to the beam. The lens rotation is adjusted with a pair of angular stages. A translation stage is used to place the lens exactly one focal length away from the pinhole. The pinhole is mounted on a translation stage to locate it at the focal spot of the lens. Pinhole translation is effected by means of micrometer/piezoelectric actuators.

2.5 Feedback stabilization

To improve the yield of the IL process, a feedback system has been implemented to stabilize the fringe pattern on the substrate [90, 91]. A 50% beamsplitter is attached to the top part of substrate mount, so that light coming from the spatial filters illuminates it. This beamsplitter recombines the two wavefronts, forming a Mach-Zehnder interferometer. The outputs of both ports of the interferometer impinge on two photodiodes, as illustrated in Fig. 2.1. Any change in path length of either arm of the interferometer will cause the photodiode signal to change. Thus, by keeping the photodiode signal constant, a feedback system can stabilize the fringe pattern on the substrate by modulating the phase of one of the arms. This is accomplished by feeding

Table 2.1: Effect of interference-angle errors on grating period.

p_0 (nm)	θ_0 (deg.)	$\Delta p(\Delta\theta = + 0.1 \text{ deg.})$ (nm)	$\Delta p(\Delta\theta = - 0.1 \text{ deg.})$ (nm)
200	61.37	- 0.19	0.19
300	35.81	- 0.72	0.73
400	26.03	- 1.42	1.44
500	20.55	- 2.32	2.34
1000	10.11	- 9.69	9.89
2000	5.04	- 38.84	40.42
3000	3.36	- 86.74	92.07
4000	2.52	- 152.84	165.50

the photodiode signals into a differential amplifier. The output of the differential amplifier is used to drive an electrooptic modulator (Pockels' cell). Within the cell, the beam propagates through a potassium dihydrogen phosphate (KDP) crystal. An electric field applied to the crystal induces a change in its refractive index. The phase of the beam is thus modulated.

2.6 Substrate stage

To fabricate a good fiducial grid, the two grating exposures must be orthogonal to each other to a tolerance of less than 1 microradian. To this end, the substrate is placed on a rotation stage and rotated 90° between the two grating exposures. The right-angle rotation is measured by comparing it to a standard with an autocollimator. The resolution of this instrument is $0.05 \mu\text{rad}$. and it is specified to be accurate to 1% of the magnitude of the indicated angular displacement.

A new substrate holder has been designed and built by K.P. Pipe, to allow the substrate rotation to be accurately measured [92]. The design for the holder is based on previous designs by R.C. Fleming, M.L. Schattenburg and E.H. Anderson. The standard is a prism, two faces of which are polished to form a right angle. The error in the right angle has been measured interferometrically, and determined to be 6 arc-

seconds. If the error in the right-angle standard is known, and it is possible to measure small angular increments with the autocollimator, the error can be eliminated (to the accuracy of the autocollimator). With this instrumentation, it should be possible to obtain grids that are orthogonal to $0.3 \mu\text{rad}$.

Chapter 3

Analysis of the spatial filter as a source

This chapter presents an argument to support the proposed spherical-wave model for deriving the phase progression of IL gratings. The argument is based on standard scalar-wave diffraction theory and the Fraunhofer far-field approximation. Measurements of far-field intensity patterns produced by the spatial filters suggest that the proposed model does indeed apply.

3.1 Minimum Gaussian beam diameter

When a Gaussian beam is passed through a converging lens, the minimum beam diameter at the focal spot is limited by diffraction effects. The paraxial Gaussian beam model [88, 93] accurately describes these effects. A beam of radius w_L , which is focused by a lens of focal length f , propagates along the \hat{z} direction according to the following equation:

$$w(z) = w_0 \sqrt{1 + \left(\frac{z}{b}\right)^2} \quad , \quad (3.1)$$

where w_0 , the minimum beam radius, is given by

$$w_0 = \frac{\lambda f}{\pi w_L} \quad , \quad (3.2)$$

and b , known as the confocal parameter, is given by

$$b = \frac{\pi w_0^2}{\lambda} \quad . \quad (3.3)$$

The radius of curvature of the constant-phase fronts is given by

$$\frac{1}{R(z)} = \frac{z}{z^2 + b^2} \quad . \quad (3.4)$$

At the minimum diameter point (the “waist”), $R = \infty$, i. e. the field is a plane wave with a Gaussian amplitude distribution $E(r) \sim e^{-\frac{r^2}{w_0^2}}$, where r is the distance from the beam axis.

The IL system spatial filters use the following parameters:

- The intensity profile of the beam has a diameter (at the $1/e^2$) points) of 1.7 mm [94], so that $w_L = 0.85$ mm.
- The focal length of the lens is $f = 10$ mm.

The minimum beam radius is thus computed to be $w_0 = 1.31 \mu\text{m}$.

Unwanted transverse amplitude variations in the propagating beam can be removed by spatial filtering. To perform the spatial filtering function, the focused beam is passed through an aperture. The aperture diameter must be large enough to transmit most of the beam’s power, but small enough to suppress unwanted scattered radiation. When the aperture diameter is large compared to its depth (see Fig. 3.1), the fractional power transfer through an aperture of radius a is given by:

$$T = \frac{2}{\pi w^2} \int_0^a 2\pi e^{-\frac{2r^2}{w^2}} r dr = 1 - e^{-\frac{2a^2}{w^2}} \quad (3.5)$$

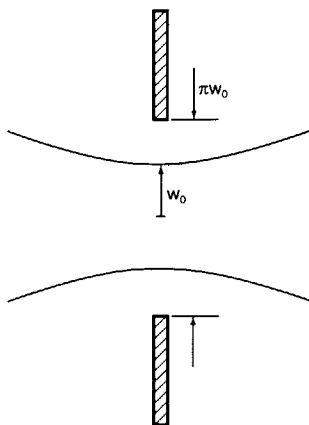


Figure 3.1: An idealized spatial filter: a thin circular aperture of radius $a = \pi w_0/2$ is placed at the beam waist. This aperture passes slightly more than 99% of the incident beam power.

A common design criterion is to set $a = \pi w_0/2$. The aperture then transmits $\sim 99\%$ of the incident beam power, and eliminates variations in the original beam profile with spatial periods smaller than $2w_L$.

The presence of the aperture disturbs the field as it propagates through it. Diffraction of electromagnetic waves emanating from an aperture is discussed in the next section.

3.2 Scalar-wave diffraction from a small aperture

The diffracted field from a small aperture is commonly described using scalar diffraction theory. The problem is set-up as follows: assume a plane wave is incident on a perfectly conducting screen, on which an aperture has been cut (see Fig. 3.2). The wave passes through the aperture, but is blocked by the screen.

Assuming time harmonic fields, and factoring out the time dependence, the field at the aperture has the form

$$\vec{E} \sim \hat{t} \psi_0(\vec{r}') e^{-jkz} , \quad (3.6)$$

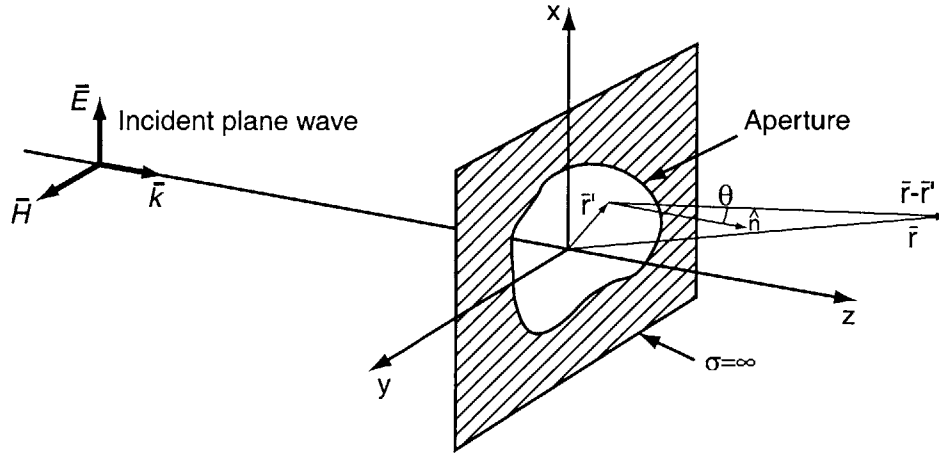


Figure 3.2: Plane wave incident on an ideal aperture.

where \hat{t} is a unit vector in a direction along the plane of the aperture (i.e. its polarization), ψ_0 is the scalar wave amplitude, and \bar{r}' denotes the coordinates of a point on the aperture plane.

Using scalar diffraction theory and Kirchhoff boundary conditions, the field amplitude at a point with coordinates \bar{r} is given by the Fresnel-Kirchhoff diffraction integral [95, 96]:

$$\psi(\bar{r}) = -\frac{j}{2\lambda} \int_S (1 + \cos \theta) \psi_0(\bar{r}') \frac{e^{-jk|\bar{r}-\bar{r}'|}}{|\bar{r}-\bar{r}'|} da' \quad (3.7)$$

where S denotes a surface that spans the aperture, and θ is the angle of inclination between \bar{r} and the z -axis.

If \bar{r} is sufficiently far from the aperture, the Fraunhofer approximation can be made by expanding the distance $|\bar{r} - \bar{r}'|$ as a Taylor series [97]:

$$\begin{aligned} |\bar{r} - \bar{r}'| &= \sqrt{(\bar{r} - \bar{r}') \cdot (\bar{r} - \bar{r}')} = \sqrt{r^2 - 2\bar{r} \cdot \bar{r}' + |\bar{r}'|^2} \\ &= r \sqrt{1 - \frac{2\bar{r} \cdot \bar{r}'}{r^2} + \frac{|\bar{r}'|^2}{r^2}} \\ &\approx r - \frac{\bar{r} \cdot \bar{r}'}{r} + \frac{|\bar{r}'|^2}{2r} + \dots \end{aligned} \quad (3.8)$$

The third term in the equation can be ignored in the far field. One can estimate how good the approximation is by looking at the magnitude of this term. For a 5- μm -diameter aperture, if the observation point \bar{r} is one meter away, $k|\bar{r}'|^2/2r \sim 10^{-5} \times 2\pi$, a negligible phase contribution, so that for these dimensions the approximation is excellent. The integral of eq. (3.7) becomes:

$$\begin{aligned} \psi(\bar{r}) &\approx -\frac{j}{2\lambda} \frac{e^{-jk_r}}{r} \int_S (1 + \cos \theta) \psi_0(\bar{r}') e^{-j\bar{k} \cdot \bar{r}'} da' \\ &\approx -\frac{j}{2\lambda} \frac{e^{-jk_r}}{r} (1 + \cos \theta) \int_S \psi_0(x', y') e^{-jk_x x'} e^{-jk_y y'} dx' dy' \\ &\approx -\frac{j}{2\lambda} \frac{e^{-jk_r}}{r} (1 + \cos \theta) \int_{-\infty}^{+\infty} \int_{-\infty}^{+\infty} [\psi_0(x', y') \cdot s(x', y')] e^{-jk_x x'} e^{-jk_y y'} dx' dy' \end{aligned} \quad (3.9)$$

where $\bar{k} = \hat{r}k$, i. e., the wavefront is propagating radially. The factor $\cos \theta$ has been approximated as a constant and taken out of the integral. On the last line of eq. (3.9), the integral is brought to the form of a Fourier transform, by defining an aperture function $s(x', y')$, which is 1 within the aperture, 0 otherwise, so that, within the Fraunhofer approximation:

$$\psi(\bar{r}) = -\frac{j}{2\lambda} \frac{e^{-jk_r}}{r} (1 + \cos \theta) [\Psi_0(k_x, k_y) * \mathcal{S}(k_x, k_y)] \quad , \quad (3.10)$$

where $\Psi_0(k_x, k_y)$, $\mathcal{S}(k_x, k_y)$ are the Fourier transforms of $\psi_0(x', y')$, $s(x', y')$ respectively, and the symbol $*$ denotes convolution.

In the far field, the surfaces of constant phase (the wavefronts) are spheres, described by the term e^{-jk_r}/r , whose origin is at the center of the aperture. Additional phase is contributed by the term $\Psi_0(k_x, k_y) * \mathcal{S}(k_x, k_y)$. However, from the properties of the Fourier transform, if the field at the source is real and spatially symmetric about the origin, the Fourier transform pattern at the far field must be also be real and symmetric. Therefore, the Fourier-transform term does not contribute any additional phase. This implies that the far-field wavefronts are spherical.

The Fourier-transform relationship between source and Fraunhofer diffraction pat-

terns enable one to analyze them quite simply using image processing techniques.

The functions that describe the operation of the spatial filter are now presented. The incoming wave is a Gaussian beam

$$\psi(x', y') = \sqrt{P} \frac{1}{w_0} \sqrt{\frac{2}{\pi}} e^{-\frac{1}{w_0^2}(x'^2 + y'^2)} \quad (3.11)$$

with transform

$$\Psi(k_x, k_y) = \sqrt{P} \sqrt{2\pi} w_0 e^{-\left(\frac{w_0}{2}\right)^2 (k_x^2 + k_y^2)} . \quad (3.12)$$

The Gaussian beam wavefunction has been normalized to contain the total power in the beam P :

$$\int_{-\infty}^{\infty} \int_{-\infty}^{\infty} |\psi|^2(x', y') dx' dy' = P . \quad (3.13)$$

Figure 3.3 (a) is a cross-sectional plot of $\Psi(k_x, k_y = 0)$ for the parameters appropriate for the spatial filter: $\lambda = 351.1$ nm, $w_0 = 1.314$ μ m and $P = 0.5$ W.

For the spatial filter the aperture function is circular:

$$s(r') = \begin{cases} 1 & \text{for } r' < a \\ 0 & \text{otherwise} \end{cases} . \quad (3.14)$$

whose transform is given by [96]

$$\mathcal{S}(k_x, k_y) = 2\pi a^2 \frac{J_1(\sqrt{k_x^2 + k_y^2} a)}{\sqrt{k_x^2 + k_y^2} a} . \quad (3.15)$$

where $J_1(x)$ represents the Bessel function of the first kind and first order. The diffraction pattern described by 3.15 is generally known as the Airy pattern. Figure 3.3 (b) is a plot of $\mathcal{S}(k_x, k_y = 0)$ for $a = \pi w_0/2$.

Finally, the far-field pattern for a Gaussian beam transmitted through the circular

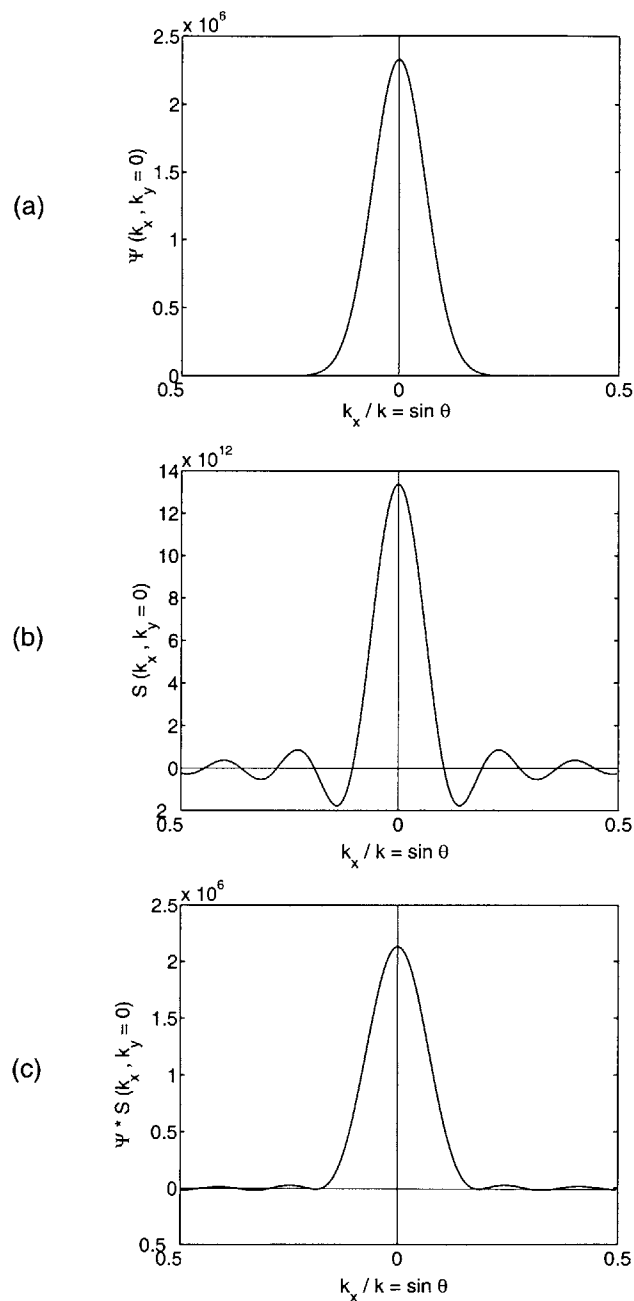


Figure 3.3: Fraunhofer diffraction patterns. (a) Cross-section of Gaussian-beam far-field pattern with parameters $\lambda = 351.1$ nm, $w_0 = 1.314$ μm and $P = 0.5$ W. (b) Far-field pattern (i.e. Fourier transform) of aperture function $s(x', y')$ for $a = \pi w_0/2 = 2.06$ μm . (c) Far-field pattern for a Gaussian beam passed through a circular aperture: convolution of beam wavefunction (a) with aperture far-field pattern (b). All functions are real and symmetric around the origin.

aperture is plotted in Fig. 3.3 (c). No closed form solutions have been found for this convolution integral. Approximate solutions are given in the form of an infinite series expansion with successively higher-order Bessel functions [93]. For this example, the convolution was computed numerically in the frequency domain, using the following procedure: two arrays of 512 x 512 elements were filled with values of $\Psi(k_x, k_y)$ and $\mathcal{S}(k_x, k_y)$ for discrete values of k_x and k_y , ranging from $-k/2$ to $k/2$, where $k = 2\pi/\lambda$. The convolution was then calculated by taking the 2-dimensional fast Fourier transform (FFT) of both arrays, multiplying the two transform arrays, element by element, and taking the inverse 2D-FFT of the result. This algorithm implements circular convolution [98], which is an aliased version of the linear convolution result. To obtain a linear convolution, the arrays were “zero-padded” to 1024 x 1024 points. In other words, 1024 x 1024 arrays were used, and only the first 512 x 512 elements were filled with the correct values; the rest of the elements were set to zero. After the convolution was performed, the appropriate elements were selected to form a 512 x 512 array.

As a result of the convolution, the side lobes of the Airy pattern due to the circular aperture have been greatly diminished. The aperture has been in effect *apodised* by the incoming Gaussian wavefront [99]. It is well known that the approximate Kirchhoff boundary conditions, which require ψ and $\partial\psi/\partial z$ to be discontinuous, make this approximation mathematically inconsistent. However, the use of the Kirchhoff approximation can be somewhat justified if the aperture is illuminated with a Gaussian distribution, because in this case the field amplitude at the aperture boundary is significantly smaller than for a uniformly illuminated aperture. Errors contributing to the diffraction integral can then be neglected.

3.3 The pinhole used in the spatial filter

In practice, the apertures used are not thin, infinitely conducting sheets. They consist of a circular hole $5 \pm 0.5 \mu\text{m}$ in diameter, drilled on a $15.25 \mu\text{m}$ -thick molybdenum

foil.¹ Figure 3.4 illustrates the beam passing through the aperture. As the beam goes through the aperture the beam radius changes substantially. At $z = \pm 7.62 \mu\text{m}$, the beam radius has increased to $1.63 \mu\text{m}$, roughly a 25% increase from the minimum beam radius $w_0 = 1.63 \mu\text{m}$.

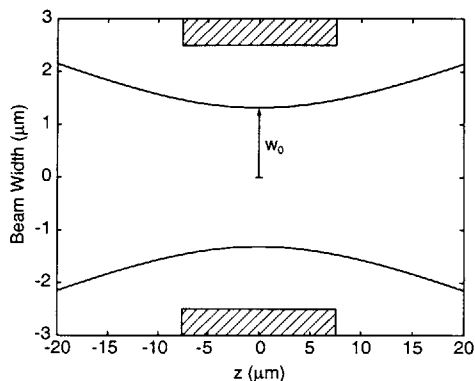


Figure 3.4: Schematic of a spatial filter implemented with a $15.25 \mu\text{m}$ -thick aperture. The beam is no longer blocked at the minimum-diameter point.

The beam is now blocked at $z = -7.62 \mu\text{m}$, where the radius of curvature of the wavefronts is finite: $R(z = 7.62 \mu\text{m}) = 39.0 \mu\text{m}$. To rigorously model the propagation of the electromagnetic field after this point, the field would have to be calculated numerically as it propagates through the finite depth of the aperture. Once the near-field diffraction pattern had been calculated, it would be possible to propagate it to the far field using the Fraunhofer approximation. Tools for performing the numerical simulation exist (see for example ref. [100]), but are not available to the author. Therefore, a further simplification will be made: the aperture will be replaced by an “effective” thin aperture placed at the beam waist that transmits as much power as a $5 \mu\text{m}$ -diameter aperture placed at $z = -7.62 \mu\text{m}$. The diameter of this aperture is $d_{\text{eff}} = 4.48 \mu\text{m}$, which is quite close to πw_0 .

In addition to having finite thickness the apertures used have an irregular shape, because of the method used in drilling the holes, ablation with a high-power laser pulse. A scanning electron micrograph of a typical aperture is shown in Fig. 3.5,

¹Available from Newport Inc., part no. 910-PH5

which clearly illustrates its non-ideal shape. The aperture is not perfectly round, and large protrusions can be seen on the sidewall. These defects will scatter the beam as it propagates through the aperture.

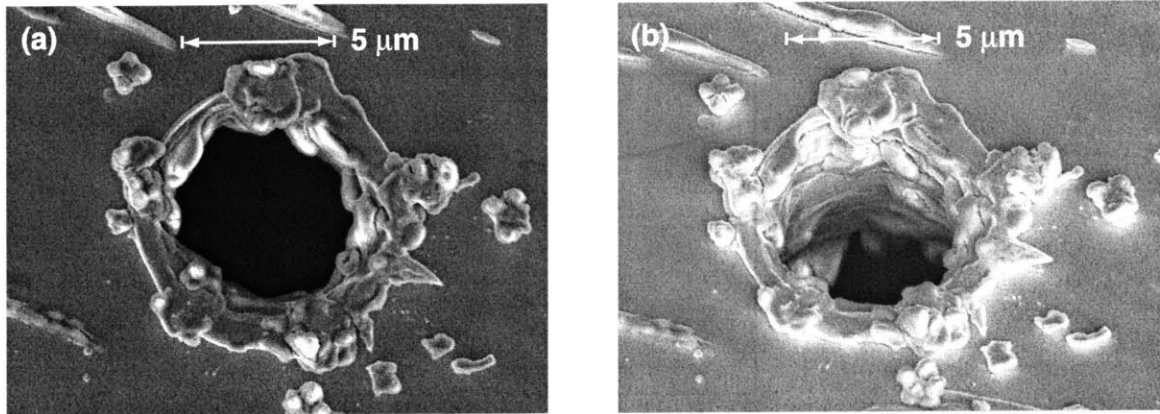


Figure 3.5: Scanning electron micrographs of a typical pinhole aperture. (a) Top view. (b) 30° inclination.

Numerical simulation of such an irregular structure would be a very challenging task, and would not likely provide meaningful data. First, all features present on the pinhole sidewall would have to be measured. They would then have to be coded into the program. A very fine mesh would have to be used in the simulation to get accurate results, which would probably result in prohibitive simulation-run times.

It is unclear how much the far-field wavefronts will deviate from perfect spheres as a consequence of the apertures' non-ideal characteristics. However, if the pinholes are introducing distortion, it should manifest itself in the far-field intensity pattern.

3.4 Measurement of the far-field intensity pattern

To verify whether the spatial filters are indeed producing expanding Gaussian beams, the intensity profile of the far-field diffraction pattern was measured using a simple experimental arrangement, shown in Fig. 3.6.

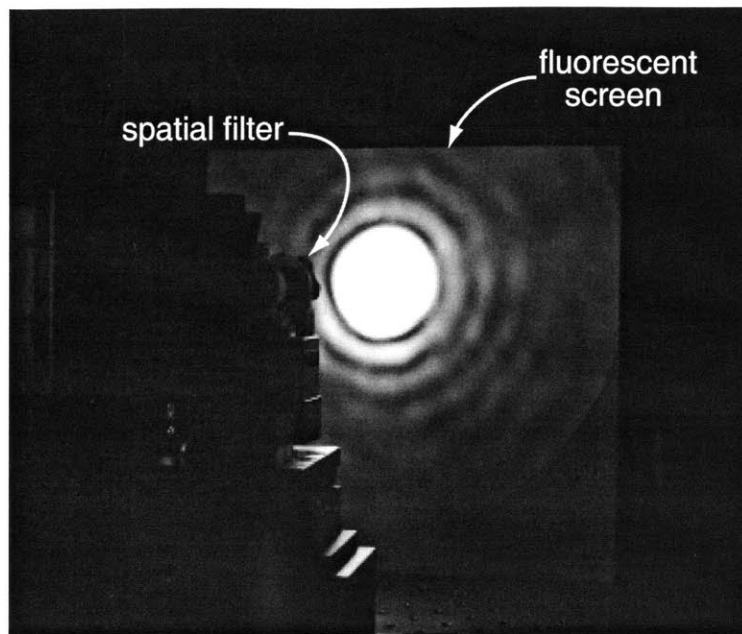


Figure 3.6: Experimental setup to measure the Fraunhofer diffraction pattern produced by one of the IL spatial filters. The UV radiation excites a fluorescent screen placed in front of the spatial filter. The emitted visible light is proportional to the excitation intensity. The image is captured with a CCD camera and a frame-grabber.

A fluorescent screen² was placed in front of the spatial filter, at a distance of $z = 30$ cm. The emitted visible light, centered around $\lambda = 520$ nm (green) was imaged with a CCD camera. The camera was mounted beside the spatial filter, and viewed the screen at an angle approximately 5° from the perpendicular to the screen. The 640×480 pixel images were digitized by means of an 8-bit frame grabber and stored in a computer for further analysis. The gain and zero-offset of the camera were adjusted so that the brightest pixel was assigned the highest level (255) and the darkest pixel was assigned 0.

The pinhole location and lens focus were optimized to maximize the intensity at the center of the diffraction pattern, and the image shown in Fig. 3.7 (a) was acquired. A cross-section of the data at $y = 0$ is plotted as a function of the x position in Fig. 3.7 (b). As expected, the image profile has a Gaussian-like shape.

²Labsphere Inc., North Sutton, NH, part no. SFS-210

The high-frequency noise is most likely due to imperfections on the fluorescent-screen surface and camera noise.

The circular fringes visible around the central bright area in Fig. 3.6 are not visible in Figs. 3.7 and 3.8 since the ordinate scale in these figures is linear and such fringes are almost below detection. The photograph in Fig. 3.6 was obtained with a long exposure time, so that the central pattern is, in fact, saturated.

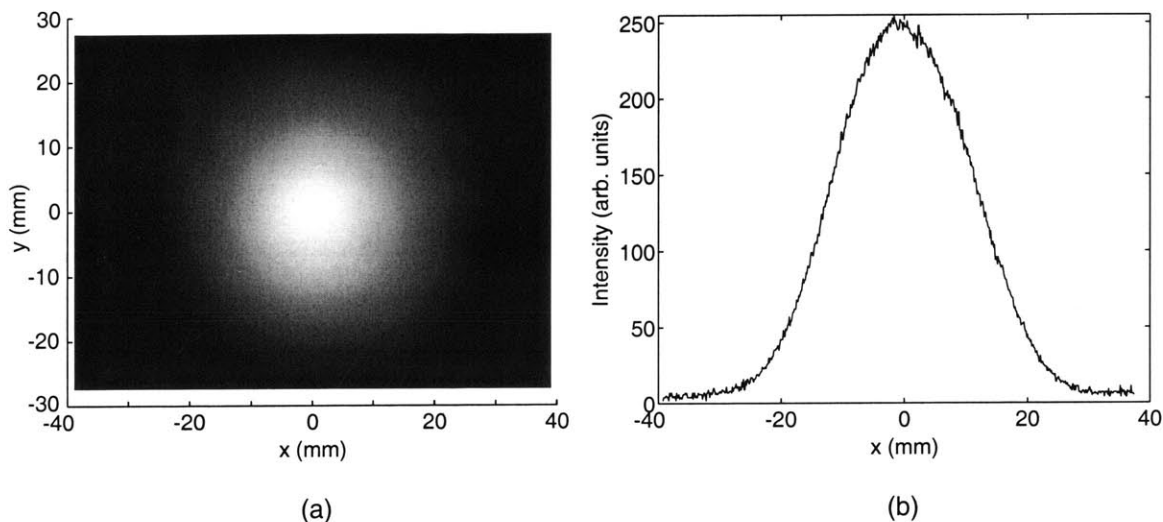


Figure 3.7: (a) Fraunhofer intensity pattern, acquired after adjusting the spatial filter to maximize the intensity at the center. (b) Cross section through the data for $y = 0$.

The sampling rate (the spacing between pixels) was determined by imaging a sheet of graph paper attached to the surface of the fluorescent screen, and counting the number of pixels per unit distance. The sampling rate was determined to be 8.45 pixels/mm for both \hat{x} and \hat{y} directions.

One could not simultaneously achieve maximum intensity and maximum width in the intensity profile. Maximum width was obtained by moving the lens 4.2 μm towards the pinhole, as measured by the lens-focus micrometer, a Newport DS-4 actuator with a specified resolution of 0.15 μm . The image shown in Fig. 3.8 was taken at this point.

Very prominent artifacts (fringes) appeared in the center region of the diffraction

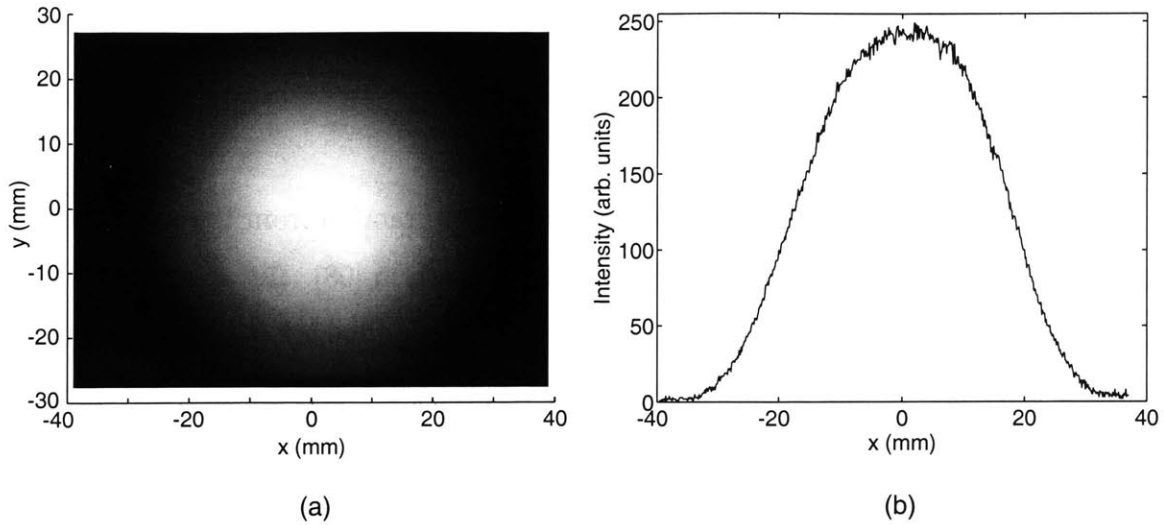


Figure 3.8: (a) Intensity pattern, acquired after adjusting the spatial filter to maximize the width of the Gaussian profile. (b) Cross section through the data for $y = 0$.

pattern as a result of slight axial misadjustment of the lens focus relative to the aperture. The Gaussian character of the diffraction pattern was then lost. Since the diffraction pattern is very sensitive to small changes in focus, the spatial filter must be carefully adjusted to prevent unwanted fringes from appearing.

The measured intensity patterns are in effect discrete samples of $|\Psi|^2(k_x, k_y)$. These can be used to estimate the field amplitude present at the aperture plane. Values for k_x and k_y were assigned to each pixel according to its spatial location using

$$k_x = k \frac{x}{\sqrt{x^2 + z^2}} \approx k \frac{x}{z}, \quad k_y = k \frac{y}{\sqrt{y^2 + z^2}} \approx k \frac{y}{z}. \quad (3.16)$$

The calculated source field amplitude was trivially obtained by taking the square root of the array values and taking the 2-D inverse FFT of the result. (For better frequency-domain resolution, the array was zero padded to 2048×2048 pixels before taking the transform.) To obtain the estimated source size, the sampling rate at the

source was calculated from the relationships

$$\Delta x' = \frac{z\lambda}{N_1\Delta x} \quad , \quad \Delta y' = \frac{z\lambda}{N_2\Delta y} \quad . \quad (3.17)$$

These relationships are derived for Fraunhofer diffraction from the sampling theorem and the definition of the discrete Fourier transform [98]. $\Delta x', \Delta y'$ are the sampling rates at the source plane; N_1, N_2 denote the number of points in the transformed sequence in the x and y directions respectively; $\Delta x, \Delta y$ are the sampling rates at the screen (the “transform domain”). In this case $N_1 = N_2 = 2048$ and $\Delta x = \Delta y = 118.3 \mu\text{m}$. Using these numbers, $\Delta x' = 0.435 \mu\text{m}$.

The calculated field profiles are shown in Figs. 3.9 and 3.10.

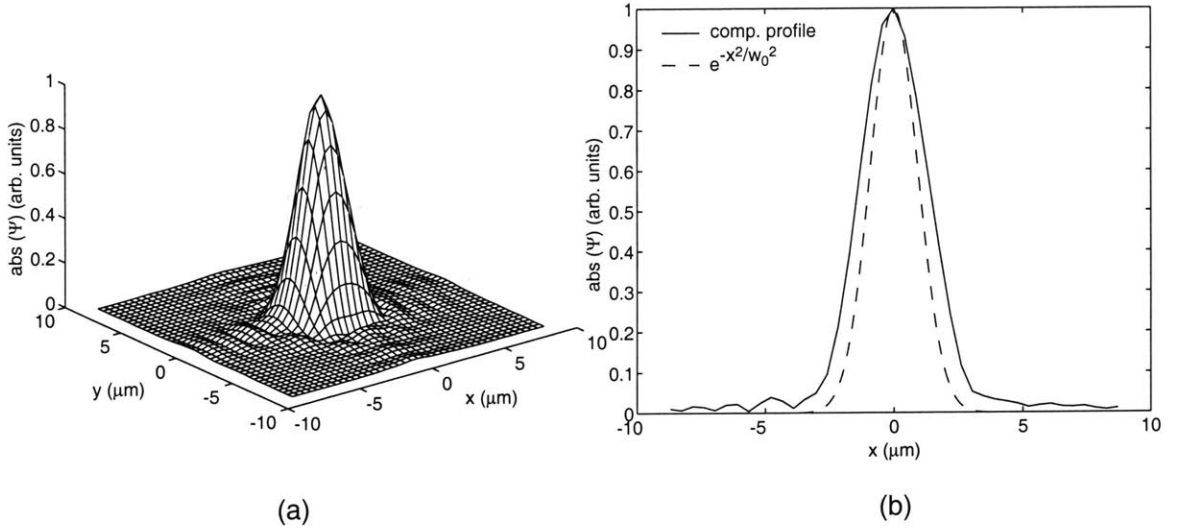


Figure 3.9: Field magnitude at the source, calculated from the diffraction pattern shown in Fig. 3.7: (a) 2-D profile (b) Cut through $y = 0$. The solid line is the calculated field magnitude. The dashed line represents a Gaussian beam profile with width $w_0 = 1.31 \mu\text{m}$, as calculated from the spatial-filter parameters.

The sidelobes along the x and y axes are due to noise in the image. (Any feature that is not circularly symmetric, or nearly so, is most likely an image processing artifact.) Cross-sectional plots show the calculated beam profile (solid line) together with an ideal Gaussian beam profile with width w_0 calculated in section 3.1. While the

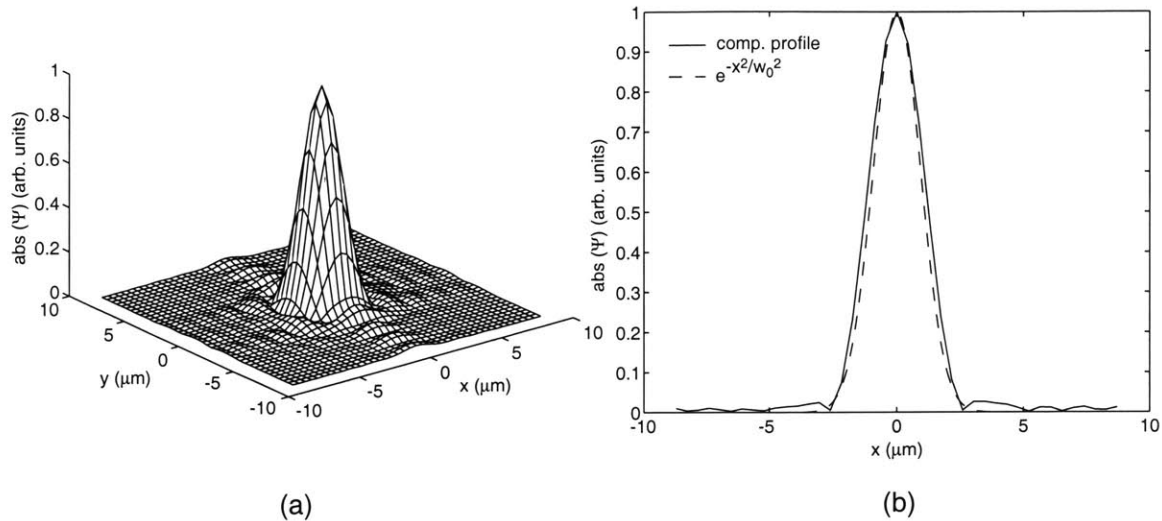


Figure 3.10: Field magnitude at the source, calculated from the diffraction pattern shown in Fig. 3.8: (a) 2-D profile (b) Cut through $y = 0$. The solid line is the calculated field magnitude. The dashed line represents a Gaussian beam profile with width $w_0 = 1.31 \mu\text{m}$, as calculated from the spatial-filter parameters.

beam profile corresponding to the maximum intensity at the center of the Fraunhofer pattern is slightly wider, the profile corresponding to the maximally wide diffraction pattern is remarkably close to the ideal Gaussian beam (although a small circular fringe can be seen around the main Gaussian lobe).

3.5 Conclusion, further work

The measurements presented above have some shortcomings. First, the phase information is lost, since only intensity was recorded. Therefore, the phase information of the transformed image has to be discarded, and the field at the source must be assumed to be a plane wave. Second, the dynamic range of the frame grabber and image noise limit prevent the faithful measurement of the sidelobe intensity, which were quantized to values of $\sim 3 - 7$ (out of 255).

Nevertheless, these measurements seem to indicate that the Fraunhofer model adequately describes waves emanating from the spatial filter apertures. Specifically,

the evidence supports the assumption that spherical wavefronts are being interfered at the substrate.

In the next chapter, the phase progression of IL gratings will be calculated, assuming that the spatial filters behave like point sources, i.e., using geometrical optics.

Further work in modeling the performance of the spatial filter might include the numerical calculation of near-field diffraction through a 15- μm deep hole, taking into account the vectorial nature of the electromagnetic field and the boundary conditions imposed by the metal surface. As suggested in section 3.2, the result of the numerical simulation can be propagated to the far field to compute the magnitude and phase. Deviations from spherical waves could then be quantified more adequately.

Using an exact solution to the problem of scalar, plane-wave diffraction from a uniformly illuminated circular aperture, Cerjan [101] computed the magnitude and phase of diffracted waves in the far field. He compared the exact solution with the Kirchhoff approximation and found that the Kirchhoff approximation is close to the exact solution in magnitude, but there are significant phase deviations from spherical wavefronts. A brief and qualitative description of these results follows. In the Kirchhoff approximation, as derived in section 3.2, the diffracted wavefunctions take a form of a dipole field multiplied by the Fourier transform of the aperture source amplitude (Fig. 3.3). As mentioned above, the Fourier transform of a real, symmetric function is also real and symmetric, but not restricted to be positive or negative. If the Kirchhoff approximation were valid, there would be an abrupt phase transition from 0 to π at the point where the sign of the transform changes (see Fig. 3.11). This is clearly unphysical, and a consequence of the boundary conditions.

Cerjan found that the phase of the exact solution does not change abruptly at the zero-crossings, but changes continuously, the rate of change increasing near the zero-crossings. Consequently the wavefronts of the diffracted field are no longer completely spherical over the entire transverse extent of the beam.

From these results, one might make the conjecture that zero crossings in ψ induce

phase distortion, and eliminating them from the far field diffraction pattern would result in perfectly spherical waves. In this sense, “apodisation” of the aperture (illuminating the aperture with a Gaussian beam, rather than a uniform beam) has beneficial effects. Figure 3.11 shows the magnitude and phase of two Fraunhofer diffraction patterns. One is due to a uniformly illuminated aperture of radius a and the other is a Gaussian beam of width $w_0 = 2a/\pi$ transmitted through the same aperture. The phase transitions for the apodised aperture are further away from the center than for the uniformly illuminated one, so one might expect less phase distortion at the center. For a diffraction pattern with no zero-crossings, there should be no phase discrepancies. Phase distortion at the center could then be minimized by optimization of the aperture size with respect to the Gaussian beam radius. Numerical simulation of the appropriate diffraction problems will prove or disprove these conjectures.

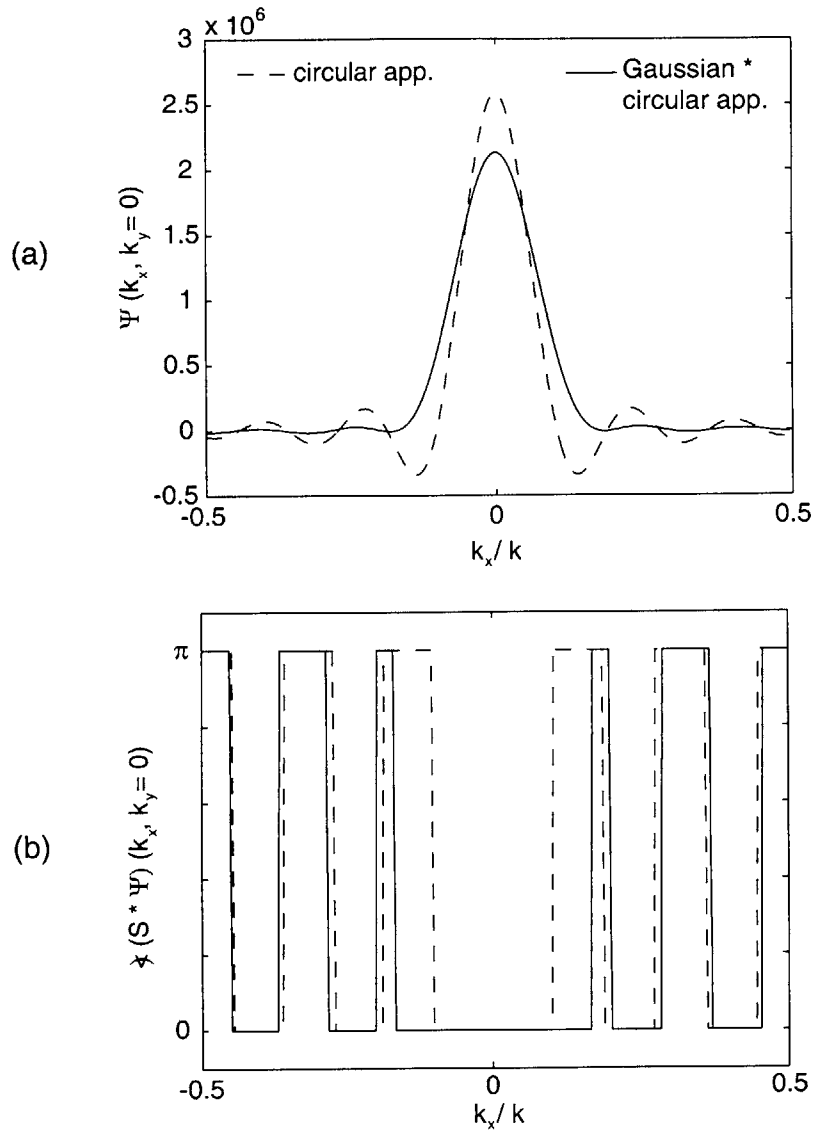


Figure 3.11: Calculated Fraunhofer diffraction patterns for a circular aperture illuminated by a uniform plane wave (dashed line) and for the same aperture illuminated by a Gaussian beam. (a) Wave function. (b) Phase of (a). If the aperture size is slightly increased (or the beam more tightly focused), the first and second nodes will disappear altogether.

Chapter 4

The phase progression of gratings exposed with spherical waves

Using geometrical optics, it is a simple matter to predict the phase progression of a grating exposed with spherical waves, originating from point sources placed at specified locations. The derivation begins by analyzing the intensity pattern produced by two mutually coherent waves incident on a substrate.

4.1 Interference of two plane waves

Let there be two monochromatic plane waves incident on a surface, such as those depicted in Fig. 4.1. The electric field for both waves is oriented along the \hat{y} direction, and has magnitude E_0 . The phase offset of each wavefront (π_1, π_2) is specified with respect to the origin. The total field is given by the superposition of the incoming fields:

$$\bar{E} = E_0 \hat{y} [e^{-jk_{x1}x} e^{-jk_{y1}y} e^{jk_{z1}z} e^{j\pi_1} + e^{+jk_{x2}x} e^{-jk_{y2}y} e^{+jk_{z2}z} e^{j\pi_2}] \quad (4.1)$$

$$\begin{aligned} &= E_0 \hat{y} e^{-j\frac{1}{2}(k_{x1}x+k_{y1}y-k_{z1}z-\pi_1-k_{x2}x+k_{y2}y-k_{z2}z-\pi_2)} \\ &\quad \cdot 2 \cos \left[\frac{1}{2}(k_{x1}x + k_{y1}y - k_{z1}z + k_{x2}x - k_{y2}y + k_{z2}z + \pi_1 - \pi_2) \right] \quad (4.2) \end{aligned}$$

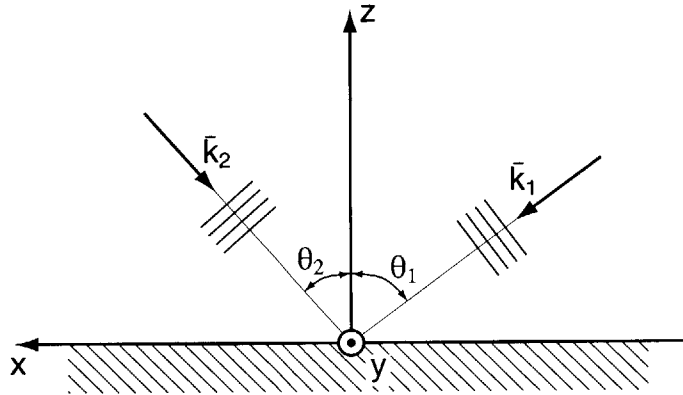


Figure 4.1: Two plane waves incident on a surface.

The intensity of the aerial image, which determines the image recorded in the resist, is proportional to $|\bar{E}|^2$.

$$|\bar{E}|^2 = 2E_0^2 [1 + \cos((k_{x1} + k_{x2})x + (k_{y1} - k_{y2})y + (k_{z2} - k_{z1})z - \pi_1 + \pi_2)] \quad (4.3)$$

In this case, the magnitude of the intensity is not important, since the amount of energy deposited in the resist can be varied by changing the exposure time. Of interest here are the locations of the loci of maximum and minimum intensity, which determine the locations of the grating's lines and spaces. Since the grating is a periodic structure, the position of grating lines can be specified in terms of phase angle: the intensity maxima occur where the argument of the cosine in eq. (4.3) is equal to an even multiple of π . Conversely, intensity minima occur at the loci where the argument is an odd multiple of π . In a positive-tone lithographic process, resist lines will be obtained in the areas of low intensity, while for a negative-tone process the reverse is true¹. Hence, to obtain the positions of the grating lines, it is only necessary to compute the argument of the cosine. One can therefore speak of the "phase" of the grating.

Since the fringe pattern is a periodic structure, it can be described in terms of

¹The dose, the total amount of energy absorbed in the resist, only determines whether the resist will fully develop out (positive tone), or will remain on the substrate surface (negative tone).

wave vectors. Using this notation, eq. (4.3) is rewritten as

$$\begin{aligned} |\bar{E}|^2 &= 2E_0^2 [1 + \cos(\kappa_x x + \kappa_y y + \kappa_z z - \phi)] \\ &= 2E_0^2 [1 + \cos(\bar{\kappa} \cdot \bar{r} - \phi)] \quad , \end{aligned} \quad (4.4)$$

where $\phi = \pi_1 - \pi_2$, $\kappa_x = k_{x1} + k_{x2}$, $\kappa_y = k_{y1} - k_{y2}$, and $\kappa_z = k_{z2} - k_{z1}$.

The grating period is defined as the spacing between two adjacent intensity maxima, in the direction perpendicular to the fringes. Put in terms of phase, the period is the distance it takes for the argument to change by 2π in the direction of maximum phase change:

$$p = \frac{2\pi}{|\kappa|} \quad . \quad (4.5)$$

Consider the following simplified example, depicted in Fig. 4.1. Both incident waves propagate on the x - z plane, i.e., $k_{y1} = k_{y2} = 0$. Both π_1 and π_2 are set to zero. The periodicity of the grating is determined by the geometry of the problem. Referring to the figure, $k_{x1} = k \sin \theta_1$ and $k_{x2} = k \sin \theta_2$, where $k = 2\pi/\lambda$. At the plane $z = 0$, the aerial image is described by

$$|\bar{E}|^2 = 2E_0^2 [1 + \cos(k(\sin \theta_1 + \sin \theta_2)x)] \quad . \quad (4.6)$$

Therefore, the period of the grating is:

$$p = \frac{2\pi}{k(\sin \theta_1 + \sin \theta_2)} = \frac{\lambda}{\sin \theta_1 + \sin \theta_2} \quad . \quad (4.7)$$

If $\theta_1 = \theta_2 = \theta$, eq. (4.7) reduces to eq. (2.1). In addition, if a phase shift is introduced into either wavefront, the period of the grating will remain the same, but the fringes will shift according to eq. (4.3).

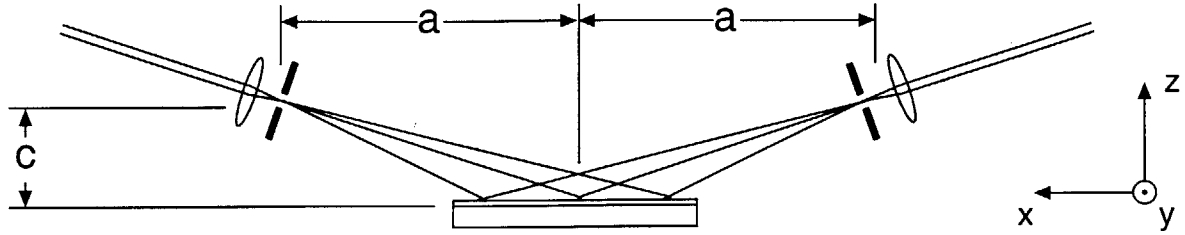


Figure 4.2: Definition of coordinate system and geometric parameters used in the model.

4.2 Interference of spherical waves

4.2.1 Period calculation

Figure 4.2 illustrates in simplified form the interference lithography (IL) configuration described in Chapter 2 and gives the dimensions used in the model. Initially, the substrate is assumed to be perfectly flat; its surface coincides with the $\hat{x} - \hat{y}$ plane. The substrate center is at position $(x, y, z) = (0, 0, 0)$. Two point sources are placed at $\bar{r}_1 = (-a, 0, +c)$ and $\bar{r}_2 = (+a, 0, +c)$.

The radius of curvature of the wavefronts is quite large (~ 1 m) compared to one grating period. To calculate the periodicity of the grating, the spherical waves are approximated as plane waves over small distances. The local period is computed as a function of the local interference angle, and is assumed to vary continuously as a function of position. The periodicity of the fringe pattern was derived in previous work [102], restricted to the condition $z = 0$. The derivation is extended here to all points where interference occurs, to allow for the inclusion of effects such as substrate rotation and non-flatness.

The Cartesian components of wavevectors \bar{k}_1 and \bar{k}_2 in eq. (4.3) are calculated as a function of position on the substrate surface \bar{r} from the geometry shown in Fig. 4.3,

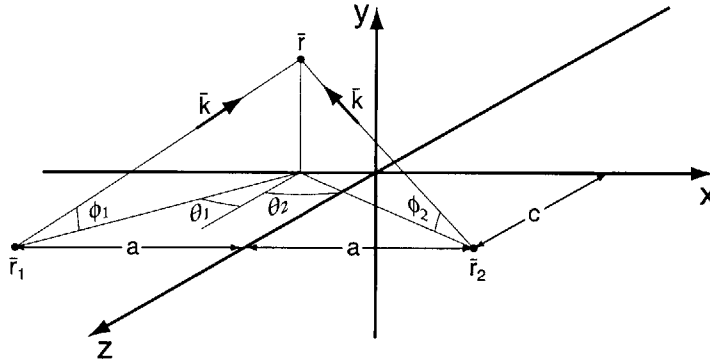


Figure 4.3: Geometry that defines the interference angle as a function of position on the substrate. The two sources are placed at \bar{r}_1 and \bar{r}_2 . \bar{r} is a point on the substrate surface.

and according to

$$\bar{k}_1 = k \frac{\bar{r} - \bar{r}_1}{|\bar{r} - \bar{r}_1|} \quad , \quad \bar{k}_2 = k \frac{\bar{r} - \bar{r}_2}{|\bar{r} - \bar{r}_2|} \quad (4.8)$$

With the aid of the figure, the vector components are determined to be

$$\begin{aligned} k_{x1} &= k \cos \phi_1 \sin \theta_1 \\ k_{y1} &= k \sin \phi_1 \\ k_{z1} &= k \cos \phi_1 \cos \theta_1 \\ k_{x2} &= k \cos \phi_2 \sin \theta_2 \\ k_{y2} &= k \sin \phi_2 \\ k_{z2} &= k \cos \phi_2 \cos \theta_2 \end{aligned} \quad (4.9)$$

Furthermore, from trigonometry,

$$\begin{aligned}
\cos \phi_1 &= \frac{\sqrt{(a+x)^2+(c-z)^2}}{\sqrt{(a+x)^2+y^2+(c-z)^2}} \\
\cos \phi_2 &= \frac{\sqrt{(a-x)^2+(c-z)^2}}{\sqrt{(a-x)^2+y^2+(c-z)^2}} \\
\sin \phi_1 &= \frac{y}{\sqrt{(a+x)^2+y^2+(c-z)^2}} \\
\sin \phi_2 &= \frac{y}{\sqrt{(a-x)^2+y^2+(c-z)^2}} \\
\cos \theta_1 &= \frac{c-z}{\sqrt{(a+x)^2+(c-z)^2}} \\
\cos \theta_2 &= \frac{c-z}{\sqrt{(a-x)^2+(c-z)^2}} \\
\sin \theta_1 &= \frac{a+x}{\sqrt{(a+x)^2+(c-z)^2}} \\
\sin \theta_2 &= \frac{a-x}{\sqrt{(a-x)^2+(c-z)^2}}
\end{aligned} \tag{4.10}$$

Making use of eqs. (4.9) and (4.10) in (4.4), the spatial frequencies of the fringe pattern are obtained.

$$\begin{aligned}
\kappa_x &= k_{x1} + k_{x2} = k \left(\frac{a+x}{\sqrt{(a+x)^2+y^2+(c-z)^2}} + \frac{a-x}{\sqrt{(a-x)^2+y^2+(c-z)^2}} \right) \\
\kappa_y &= k_{y1} - k_{y2} = k \left(\frac{y}{\sqrt{(a+x)^2+y^2+(c-z)^2}} - \frac{y}{\sqrt{(a-x)^2+y^2+(c-z)^2}} \right) \\
\kappa_z &= k_{z2} - k_{z1} = k \left(\frac{c-z}{\sqrt{(a-x)^2+y^2+(c-z)^2}} - \frac{c-z}{\sqrt{(a+x)^2+y^2+(c-z)^2}} \right)
\end{aligned} \tag{4.11}$$

To obtain the period, the approximation $|\bar{\kappa}| \approx \kappa_x$ is made, since $\kappa_x \gg \kappa_y, \kappa_z$. Eq. (4.5) becomes

$$\boxed{p = \frac{\lambda}{\frac{a+x}{\sqrt{(a+x)^2+y^2+(c-z)^2}} + \frac{a-x}{\sqrt{(a-x)^2+y^2+(c-z)^2}}} } \tag{4.12}$$

Figure 4.4 shows contour plots of the period predicted by eq. (4.12) as a function of position on the substrate. The period is plotted for two cases: (a) 200 nm nominal period and (c) 400 nm nominal period. The parameters a and c used in the calculations are stated in the insets of each plot. Included for comparison are experimentally-measured period maps for gratings with 200 nm (b) and 400 nm (c)

nominal periods. The experimental results, taken from the literature [103], were obtained by another research group, by measuring the diffraction angle of a laser beam. The characteristics of the measured data agree with the theoretical predictions within the quoted error for the measurements, which is 40 ppm.

4.2.2 Phase computation

The phase offset (ϕ in eq. (4.4)) can be calculated by integrating the local spatial frequency as a function of position along a path. The phase of the intensity pattern should change self-consistently with the period. If a distance is traversed from the origin to any point \bar{r} , the accumulated phase $\phi(\bar{r})$ is given by the path integral

$$\phi(\bar{r}) = \int_0^{\bar{r}} \bar{\kappa} \cdot d\bar{s} \quad . \quad (4.13)$$

This integral is found quite easily, since its value is the same along any of the Cartesian directions:

$$\begin{aligned} \int \kappa_x dx &= \int \kappa_y dy = \int \kappa_z dz \\ &= k \left(\sqrt{(a+x)^2 + y^2 + (c-z)^2} - \sqrt{(a-x)^2 + y^2 + (c-z)^2} \right) + C \end{aligned} \quad (4.14)$$

where C is an arbitrary constant.

Any path integral can be constructed by selecting appropriate paths along \hat{x} , \hat{y} and \hat{z} . Therefore, the phase is found to be:

$$\phi(x, y, z) = \frac{2\pi}{\lambda} \left(\sqrt{(a+x)^2 + y^2 + (c-z)^2} - \sqrt{(a-x)^2 + y^2 + (c-z)^2} \right)$$

(4.15)

As a check, the same result can be derived by much simpler means from eq. (4.3). The phase shifts π_1, π_2 for each of the interfering wavefronts are computed, using the fact that in propagating from its source to the point (x, y, z) , each one of the

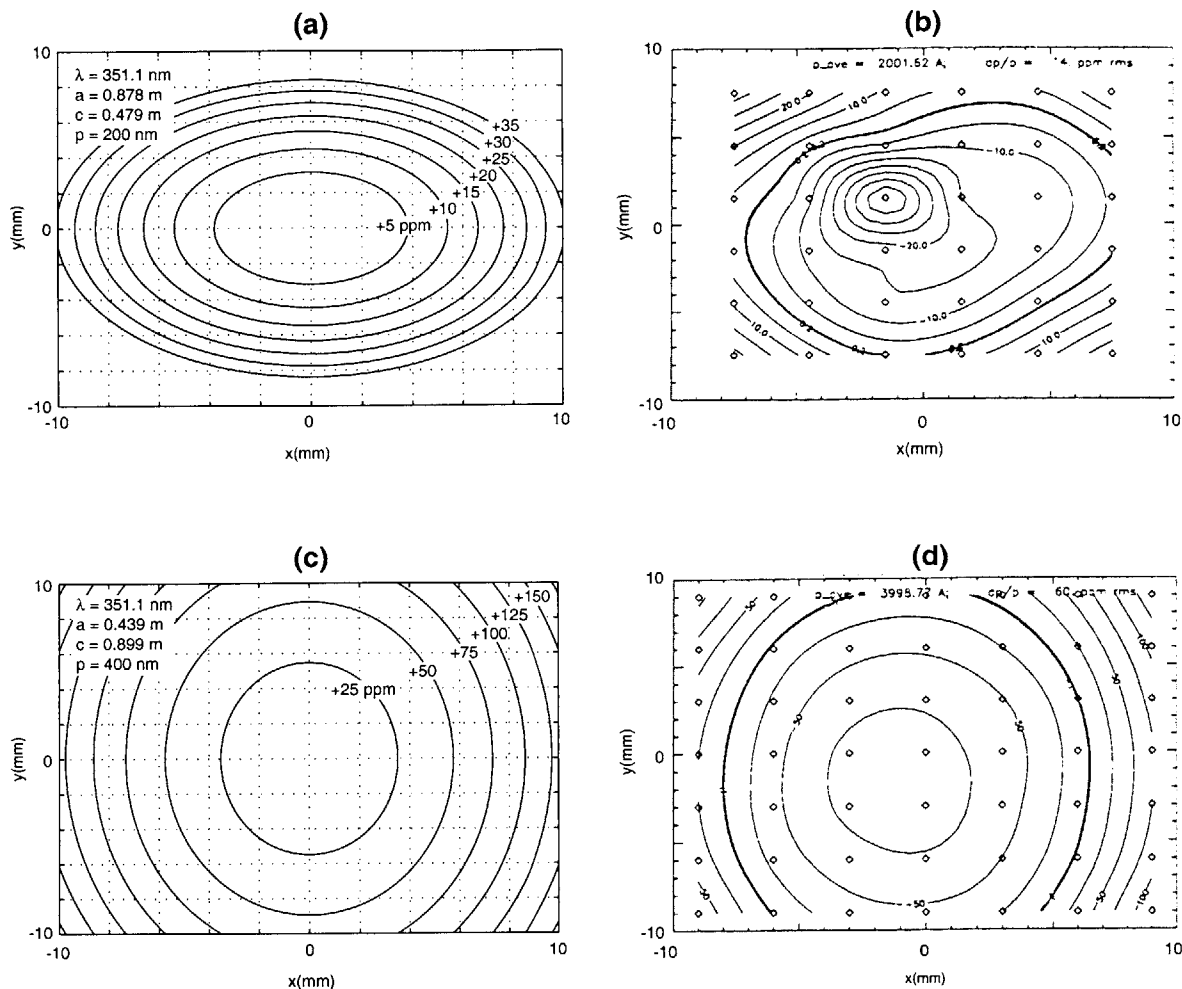


Figure 4.4: Comparison of model-predicted values of period with experiments. (a) Calculated period map of a grating with 200-nm nominal period. (b) Experimentally measured period variation of an IL-fabricated grating. The grating was exposed on a silicon wafer and electroplated with gold. (c) Calculated period variation of a 400 nm grating. (d) Measured period of a 400-nm gold-plated IL grating. The experimental results are taken from ref. [103] The error in the experimental measurements is specified as 40 ppm. The experiments agree with the theory within the quoted error bounds.

wavefronts accumulates a phase shift $\pi = kr$, where r is the distance between the source and the point (x, y, z) . Therefore, from Fig. 4.3,

$$\pi_1 = k \sqrt{(a+x)^2 + y^2 + (c-z)^2} \quad (4.16)$$

$$\pi_2 = k \sqrt{(a-x)^2 + y^2 + (c-z)^2} \quad . \quad (4.17)$$

Inserting these values into equation (4.3) gives equation (4.15).

The loci of the interference maxima are determined for the condition $\phi = n 2\pi$, where n is an integer. Setting $z = 0$, and using this condition, eq. (4.15) can be manipulated to obtain

$$x^2 = \frac{n^2 \lambda^2}{4} \left(1 + \frac{c^2 + y^2}{a^2 - \frac{1}{4} n^2 \lambda^2} \right) \quad , \quad (4.18)$$

which describes a series of hyperbolas. This equation is the same as that derived by Schmahl and Rudolph [60]. The shorthand notation ‘‘hyperbolic phase’’ will henceforth be used to describe the phase progression of gratings produced with spherical waves.

The curvature of the grating lines is typically very slight, i.e., the phase deviation from perfect linearity is very small compared to the absolute phase. Setting ($z = 0$), the non-linear component of the phase progression is given by

$$\phi_{\text{non-linear}} = \frac{2\pi}{\lambda} \left(\sqrt{(a+x)^2 + y^2 + c^2} - \sqrt{(a-x)^2 + y^2 + c^2} - \frac{2ax}{\sqrt{a^2 + c^2}} \right) \quad . \quad (4.19)$$

The last term is the linear phase progression of a grating with constant period $p(x, y, z = 0) = (\lambda\sqrt{a^2 + c^2})/2a$, which would result if both beams were plane waves. Contour plots of the non-linear component for hyperbolic gratings of nominal periods 200 nm and 400 nm are shown in Fig. 4.5. As can be seen from the figure, the maximum deviation from perfect linearity is approximately 3 periods in a 2 cm \times 2 cm area for a 200 nm-period grating, and slightly more than 2 periods for a 400

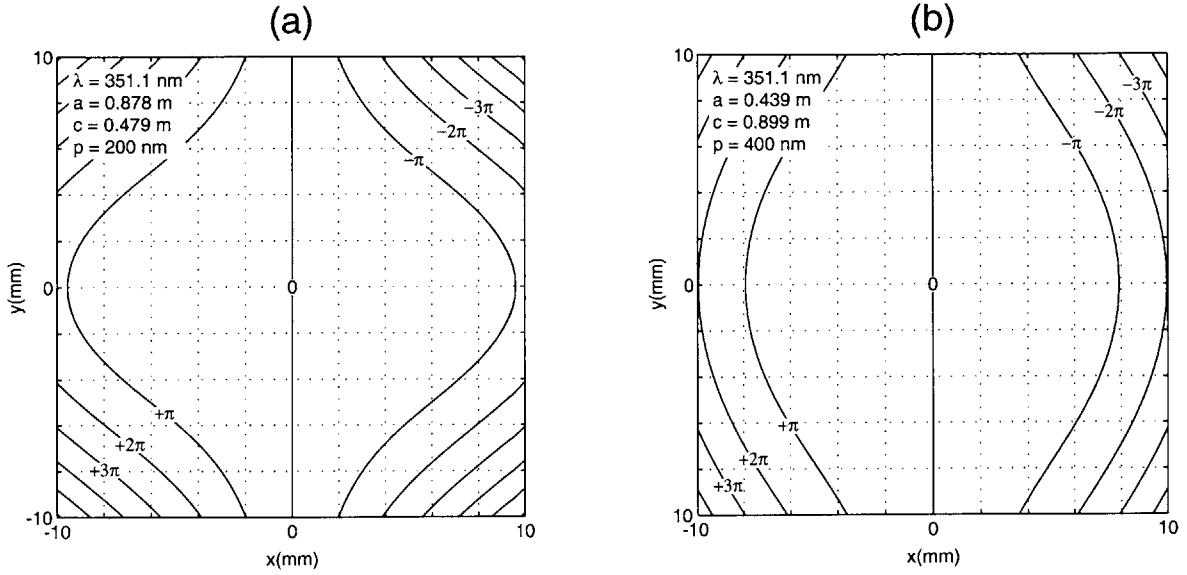


Figure 4.5: Plots of the phase discrepancy between gratings exposed by interfering two spherical waves and perfect linear gratings. The parameters used in the calculations are the same as those used in Fig. 4.4. Contours represent loci of equal phase discrepancy. (a) 200 nm period (b) 400 nm period.

nm-period one. At $(x = 1 \text{ cm}, y = 1 \text{ cm})$ the non-linearity amounts to -614.8 nm for the 200 nm grating, and -903.6 nm for the 400 nm one. Although these numbers amount to a distortion of several periods, they represent small fractions of the total accumulated phase; 6 parts in 10^5 and 9 parts in 10^5 respectively. The accurate measurement of these comparatively small amounts of non-linearity is a challenging problem. Procedures to measure the phase progression of IL-exposed gratings will be presented in the next chapter.

4.3 Substrate-flatness and mounting errors

The expressions given in eqs. (4.12) and (4.15) have been applied to examples where the surface of the substrate is assumed to be perfectly flat and positioned on the $\hat{x} - \hat{y}$ plane. In a practical situation, however, these assumptions no longer hold. Surface deviations from the $z = 0$ plane can be specified in terms of the following parameters:

1. Surface flatness
2. Substrate mounting errors:
 - (a) Substrate shift: the center of the substrate does not coincide with the origin.
 - (b) Substrate rotation about the y -axis
 - (c) Substrate rotation about the x -axis
 - (d) Substrate rotation about the z -axis

The effect of errors in each parameter is analyzed separately in the following sections.

4.3.1 Surface flatness

Substrate surfaces are in general not flat. Figure 4.6 shows two Fizeau interferograms of 3-inch-diameter silicon wafer. The first one (a) shows the wafer in its relaxed state. The out-of-plane distortion of the wafer front surface is in excess of $20\ \mu\text{m}$. Most of the wafer surface distortion is typically due to warpage, although the two surfaces of a wafer tend to be parallel. The second interferogram (b) shows the wafer after its back surface has been made to conform — using vacuum — to an optically-flat “pin chuck” [104]. In this case, the peak-to-valley distortion is $3.4\ \mu\text{m}$.

If the substrate non-flatness is known, its effect on the grating’s phase progression can be readily calculated using eq. (4.15), by making $z = f(x, y)$, where the function f reflects the topography of the surface.

The deviation from perfect hyperbolic phase, calculated for two examples that loosely reflect the surface topography of Fig. 4.6, is shown in Fig. 4.7. The grating’s nominal period is $200\ \text{nm}$ ($a=0.878\ \text{m}$, $b=0.479\ \text{m}$). The contours display phase deviation in nm (i.e. $\Delta\phi \cdot (200\ \text{nm}/2\pi)$). The substrate surfaces are taken to be paraboloids of revolution ($z = A(x^2 + y^2)$), where the constant A sets the amount of distortion. The constant A has been chosen so that the maximum out-of-plane distortion, is $20\ \mu\text{m}$ (a) and $3\ \mu\text{m}$ (b). If the surface deviates from perfect flatness

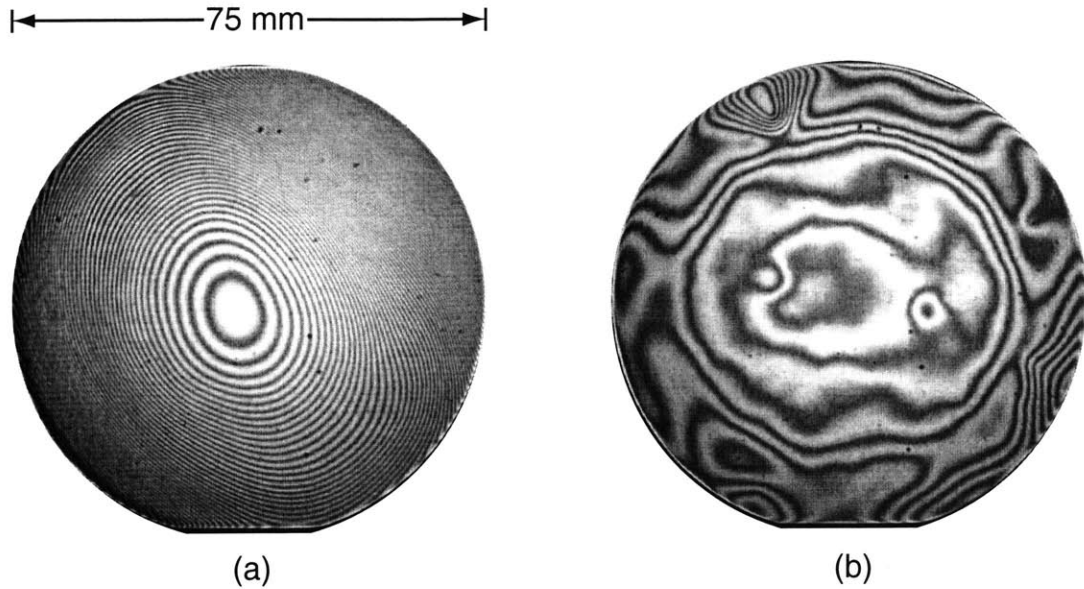


Figure 4.6: Fizeau interferograms showing surface flatness of a 3-inch-diameter silicon wafer. (a) Wafer in its relaxed state. (b) The same wafer, after the surface has been made to conform to an optically-flat “pin chuck”. The height difference between adjacent fringes is ~ 316 nm.

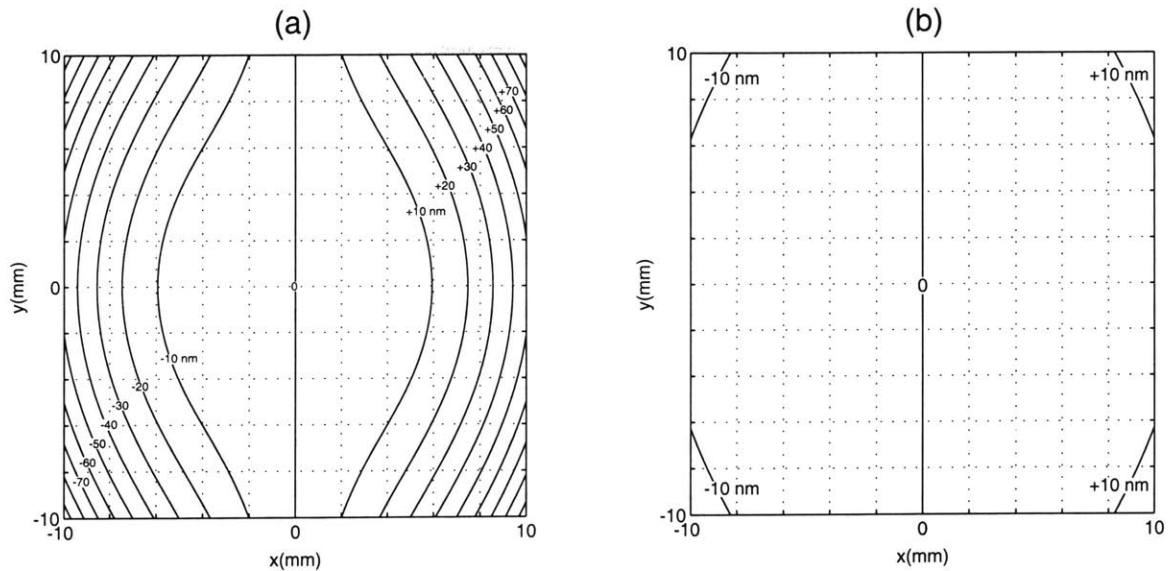


Figure 4.7: Grating distortion induced by substrate curvature. The grating’s nominal period is 200 nm. The substrate surfaces are assumed to be paraboloids of revolution. The maximum deviation in z occurs at $x, y = \pm 10$ mm. (a) 20 μm maximum deviation. (b) 3 μm max. dev. Phase distortion is expressed in nanometers.

by 20 μm , the phase progression of the grating is distorted by as much as 90 nm at the corners. However, when the surface is flat to 3 μm the phase distortion is only slightly more than 10 nm.

For small changes in z , the change in phase can be estimated using

$$\Delta\phi_z = \left. \frac{\partial\phi}{\partial z} \right|_{z=0} \Delta z \quad . \quad (4.20)$$

From eqs. (4.13) and (4.14), $\partial\phi/\partial z = \kappa_z$. Given a maximum phase error tolerance, the surface-flatness requirement can be estimated using eq. 4.20.

4.3.2 Rotation errors

Angular errors are to be expected when a substrate is mounted in the IL system. The effect of substrate rotations on the grating's phase progression can be modeled by performing a coordinate transformation. Assume the substrate surface is perfectly flat, but has been rotated about the x and y axes as shown in Fig. 4.8. Let x', y' denote the coordinates of a point on the substrate surface. The coordinates of the point in the coordinate system of the IL apparatus are computed by means of the Euler angle transformations [105]. The substrate is assumed to start perfectly aligned to the original coordinate system, and to undergo a sequence of rotations. The xyz convention is used here, where the first rotation occurs about the z axis, by an angle γ , the second rotation about an intermediary y' axis with angle β and the third rotation about the final x' axis with angle α . The transformation from the $x'y'z'$ coordinates to the original coordinates xyz is expressed as a matrix multiplication:

$$\begin{bmatrix} x \\ y \\ z \end{bmatrix} = A \begin{bmatrix} x' \\ y' \\ z' \end{bmatrix} \quad (4.21)$$

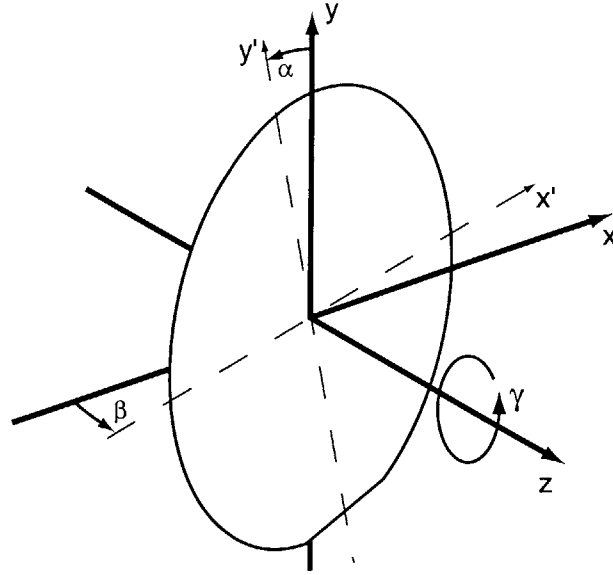


Figure 4.8: Definition of substrate rotation angles. (In this diagram $\alpha < 0$.)

$$A = \begin{bmatrix} \cos \beta \cos \gamma & \sin \alpha \sin \beta \cos \gamma - \cos \alpha \sin \gamma & \cos \alpha \sin \beta \cos \gamma + \sin \alpha \sin \gamma \\ \cos \beta \sin \gamma & \sin \alpha \sin \beta \sin \gamma + \cos \alpha \cos \gamma & \cos \alpha \sin \beta \sin \gamma - \sin \alpha \cos \gamma \\ -\sin \beta & \cos \beta \sin \alpha & \cos \beta \cos \alpha \end{bmatrix} \quad (4.22)$$

Substrate rotations about the x - and y -axes will be examined first, where there is no coupling between the x and y variables.

4.3.3 Rotations about the x and y axes

In this case there is no rotation about the z axis ($\gamma = 0$). Assuming a flat substrate surface, $z' = 0$. The transformation simplifies to

$$\begin{bmatrix} x \\ y \\ z \end{bmatrix} = \begin{bmatrix} \cos \beta & \sin \alpha \sin \beta \\ 0 & \cos \alpha \\ -\sin \beta & \cos \beta \sin \alpha \end{bmatrix} \begin{bmatrix} x' \\ y' \end{bmatrix} . \quad (4.23)$$

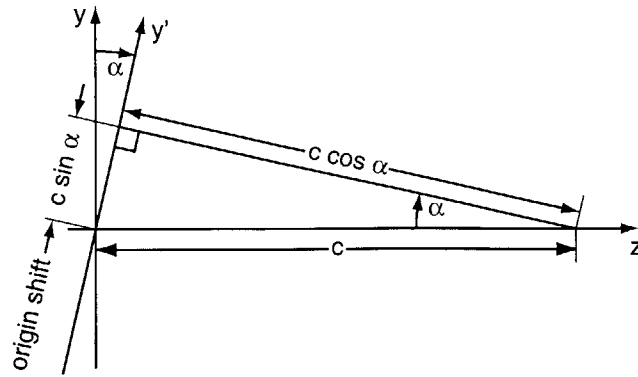


Figure 4.9: Rotation of the substrate about the x -axis.

To obtain the phase progression of the grating as a function of x' and y' , the coordinates are transformed using eq. (4.23) and inserted into eq. (4.15). The resulting equation becomes quite complex. To make the analysis more tractable, special cases, where rotations occur about one axis exclusively, are analyzed below.

If the substrate is rotated only about the x axis, the coordinate transformation is

$$\begin{aligned} x &= x' \\ y &= y' \cos \alpha \\ z &= y' \sin \alpha \end{aligned} \quad (4.24)$$

Eq. (4.15) then becomes

$$\phi(x', y', \alpha) = \frac{2\pi}{\lambda} \left(\sqrt{(a + x')^2 + (y' - c \sin \alpha)^2 + c^2 \cos^2 \alpha} - \sqrt{(a - x')^2 + (y' - c \sin \alpha)^2 + c^2 \cos^2 \alpha} \right) \quad (4.25)$$

From the equation above, a rotation about the x -axis is equivalent to a vertical shift of the origin by $c \sin \alpha$, and a foreshortening of the dimension c . Eq. (4.25) could have been derived by inspection from the diagram in Fig. 4.9.

Figure 4.10 is a plot of the grating-line position errors (i.e, deviation from hyperbolic phase) induced in a 200 nm period grating by rotating the substrate by 100

μrad . Specifically, the function $\phi_\alpha(x', y', \alpha = 100 \mu\text{rad.}) - \phi_\alpha(x', y', \alpha = 0)$ is plotted. The phase errors have been translated into errors in grating-line position, in nm. As the figure illustrates, position errors of several nm result from a relatively small rotation about the x -axis.

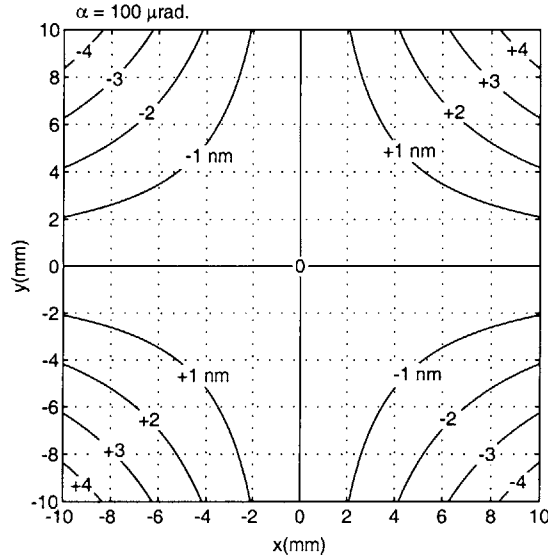


Figure 4.10: Grating distortion introduced by substrate rotation about the x -axis. The period of the grating is 200 nm. The rotation angle is $\alpha = 100 \mu\text{rad}$.

For small angles, i.e., $c \sin \alpha \ll x'_{\max}, y'_{\max}$ (in Fig. 4.10 $x'_{\max}, y'_{\max} = \pm 1 \text{ cm}$), the incremental phase error can be calculated using the approximation

$$\Delta\phi_\alpha(x', y') \approx \kappa_z|_{z=0} \cdot \Delta z = \kappa_z|_{z=0} \cdot y' \sin \alpha \quad . \quad (4.26)$$

For the example of Fig. 4.10, the maximum error between the approximation given by eq. (4.26) and the exact solution is equivalent to $4 \cdot 10^{-6} \text{ nm}$.

For a rotation around the y axis, the following transformation applies:

$$\begin{aligned} x &= x' \cos \beta \\ y &= y' \\ z &= -x' \sin \beta \end{aligned} \quad (4.27)$$

Inserting in eq. (4.15) and regrouping terms gives

$$\phi(x', y', \beta) = \frac{2\pi}{\lambda} \left(\sqrt{((a \cos \beta + c \sin \beta) + x')^2 + y'^2 + (c \cos \beta - a \sin \beta)^2} - \sqrt{((a \cos \beta - c \sin \beta) - x')^2 + y'^2 + (c \cos \beta + a \sin \beta)^2} \right) \quad (4.28)$$

In the above equation, the lengths a and c are projected into the substrate's rotated coordinate system, but unlike eq. (4.25), the transformation is not equivalent to a shift in x . This is because the phase described by eq. (4.15) is an even function of y , but an odd function of x .

Figure 4.10 is a plot of the grating errors (i.e., deviation from hyperbolic phase) induced in a 200 nm period grating by rotating the substrate about the y -axis by 100 μrad .

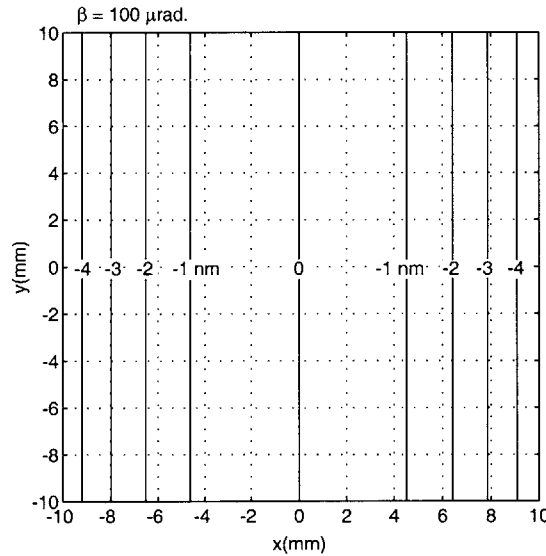


Figure 4.11: Grating distortion introduced by substrate rotation about the y -axis. The period of the grating is 200 nm. The rotation angle is $\beta = 100 \mu\text{rad}$.

For small angles (compare eq. (4.26)), κ_z can be used to calculate the phase error:

$$\Delta\phi_\beta(x', y') \approx \kappa_z|_{z=0} \cdot \Delta z = -\kappa_z|_{z=0} \cdot x' \sin \beta \quad (4.29)$$

For the data displayed in Fig. 4.11, the maximum error between the approximation given by eq. (4.29) and the exact solution is 0.04 nm.

4.3.4 Rotation about the z axis

Again, it is assumed that the substrate surface is flat, so that $z = 0$. With $\alpha = \beta = 0$, the matrix A simplifies to

$$\begin{bmatrix} x \\ y \\ z \end{bmatrix} = \begin{bmatrix} \cos \gamma & -\sin \gamma \\ \sin \gamma & \cos \gamma \\ 0 & 0 \end{bmatrix} \begin{bmatrix} x' \\ y' \end{bmatrix} . \quad (4.30)$$

Inserting in eq. (4.15) and rearranging terms, one obtains

$$\phi(x', y', \gamma) = \frac{2\pi}{\lambda} \left(\sqrt{(a \cos \gamma + x')^2 + (y' - a \sin \gamma)^2 + c^2} - \sqrt{(a \cos \gamma - x')^2 + (y' - a \sin \gamma)^2 + c^2} \right) \quad (4.31)$$

Therefore, a rotation about the z -axis is equivalent to a vertical shift of the substrate origin $y = y' - a \sin \gamma$, and a change of the dimension a to $a \cos \gamma$.

The effect on the grating's phase progression for a rotation of $\gamma = 100 \mu\text{rad}$. is shown in Fig. 4.12. For this relatively small angle, the phase varies linearly with y , as one would expect. The effect is quite pronounced: the maximum phase errors, at $y = \pm 1$ cm, amount to 5 periods. However, eliminating this phase distortion amounts to finding the angle between the grating lines and the substrate's coordinate system. This can be accomplished after the grating has been fabricated, as will be reported in later chapter.

For small angles the phase error can be estimated using

$$\Delta\phi_\gamma(x', y') \approx -\kappa_x|_{z=0}y' \sin \gamma + \kappa_y|_{z=0}x' \sin \gamma = -a \sin \gamma(k_{y1} + k_{y2}) \quad , \quad (4.32)$$

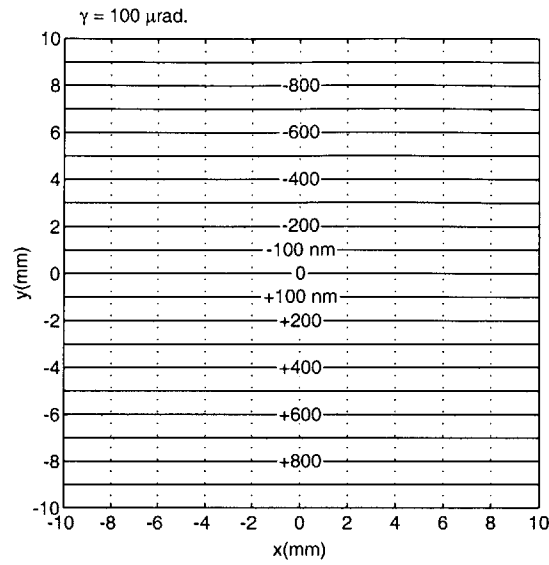


Figure 4.12: Grating distortion introduced by substrate rotation about the z -axis. The period of the grating is 200 nm. The rotation angle is $\gamma = 100 \mu\text{rad}$.

where k_{y1} and k_{y2} are defined in eq. (4.11). For the data displayed in Fig. 4.12, the maximum error between the approximation given by eq. (4.32) and the exact values is 0.05 nm.

4.3.5 Translation errors

Translation errors occur when the origin of the substrate coordinate system (x', y') does not coincide with the origin of the interference-fringe system (x', y', z') . Assuming that the substrate surface is perfectly flat and no rotation errors exist, substrate shifts are straightforwardly modeled with eq. (4.15) using

$$\begin{aligned} x &= x' + \Delta x \\ y &= y' + \Delta y \end{aligned} \quad (4.33)$$

where $\Delta x, \Delta y$ denote the amount of translation.

When the translation occurs along the \hat{x} direction, the accumulated phase error contains a constant term, due to the linear component of the grating's phase pro-

gression. Grating distortion is only due to the non-linear component, since shift of a perfectly periodic structure implies a constant phase offset. Therefore, the grating distortion due to x -translation is computed using eq. (4.19) instead of eq. (4.15):

$$\phi_{\text{non-linear}}(x', y', \Delta x) = \frac{2\pi}{\lambda} \left(\sqrt{(a + x' + \Delta x)^2 + y'^2 + c^2} - \sqrt{(a - x' - \Delta x)^2 + y'^2 + c^2} - \frac{2a(x + \Delta_x)}{\sqrt{a^2 + c^2}} \right) \quad (4.34)$$

Again, for small Δx , the phase change can be approximated as a linear function:

$$\Delta\phi_x(x', y') \approx [\kappa_x(x', y', 0) - \kappa_x(0, 0, 0)] \cdot \Delta x \quad (4.35)$$

The grating errors caused by a substrate shift of $\Delta x = 100 \mu\text{m}$ are plotted in Fig. 4.13. For these data, the values calculate using eq. (4.35) differ by no more than 0.04 nm from the exact calculation.

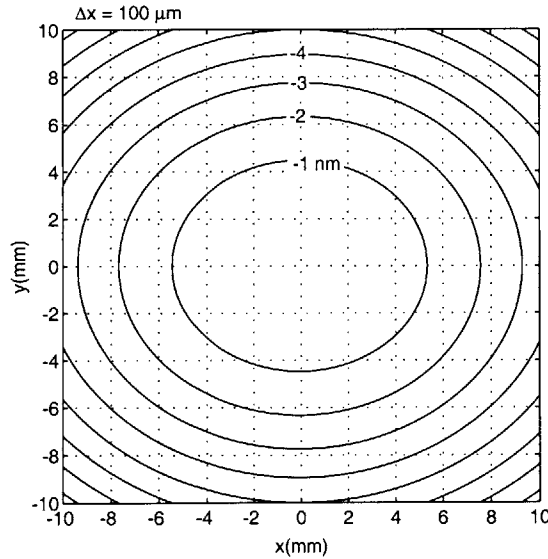


Figure 4.13: Grating distortion introduced by substrate shift along the \hat{x} -direction of $\Delta x = 100 \mu\text{m}$. The nominal period of the grating is 200 nm.

Finally, the grating distortion induced by a shift along the \hat{y} direction is calculated

from eqs. (4.15) and (4.33). For small Δy :

$$\Delta\phi_y(x', y') \approx \kappa_y(x', y', 0) \cdot \Delta y \quad (4.36)$$

Figure 4.14 is a plot of the grating errors caused by a substrate shift of $\Delta y = 100 \mu\text{m}$. The maximum error incurred by using the incremental approximation of eq. (4.36) is 0.05 nm. It is interesting to note the similarity between the contours of this figure and those plotted in Fig. 4.10.

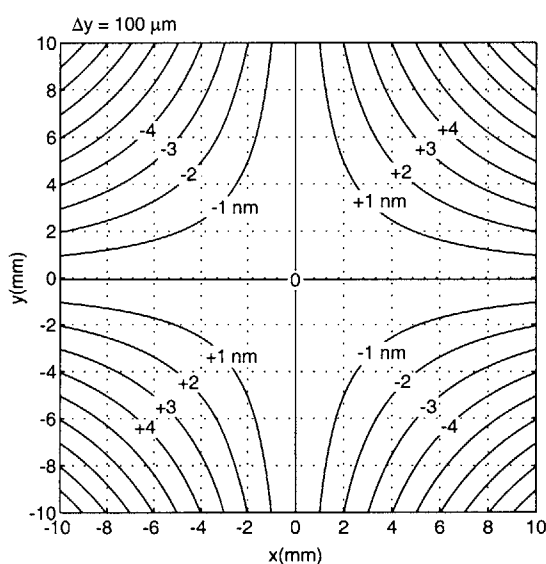


Figure 4.14: Grating distortion introduced by substrate shift along the \hat{y} -direction of $\Delta y = 100 \mu\text{m}$. The nominal period of the grating is 200 nm. Note the similarity of the contours to those in Fig. 4.11.

4.4 Errors in setting a and c

In addition to the errors incurred in locating the substrate surface on the $z = 0$ plane, the accuracy with which the geometric parameters a and c can be set also introduces phase errors into the grating. These distortions can be modeled within the framework

already developed. As before, incremental phase errors are estimated using

$$\begin{aligned}\Delta\phi_a(x', y') &\approx \left. \frac{\partial\phi}{\partial a} \right|_{z=0} \cdot \Delta a \\ \Delta\phi_c(x', y') &\approx \left. \frac{\partial\phi}{\partial c} \right|_{z=0} \cdot \Delta c\end{aligned}\quad (4.37)$$

From eq. (4.15), it is easily shown that

$$\begin{aligned}\frac{\partial\phi}{\partial a} &= \frac{2\pi}{\lambda} \left(\frac{a+x}{\sqrt{(a+x)^2 + y^2 + (c-z)^2}} - \frac{a-x}{\sqrt{(a-x)^2 + y^2 + (c-z)^2}} \right) \\ \frac{\partial\phi}{\partial c} = -\kappa_z &= \frac{2\pi}{\lambda} \left(\frac{c-z}{\sqrt{(a+x)^2 + y^2 + (c-z)^2}} - \frac{c-z}{\sqrt{(a-x)^2 + y^2 + (c-z)^2}} \right).\end{aligned}\quad (4.38)$$

4.5 Error budget calculations for IL

It is a simple matter to estimate the tolerances for each one of the parameters that contribute phase errors to a hyperbolic grating using the expressions derived above. Calculations for two representative cases are carried out below.

Assume that 200-nm period gratings are to be used as metrological references for a SPLEBL system, to generate mask patterns with a pattern-placement accuracy better than 30 nm. The distortion of the grating with respect to a perfect hyperbolic grating is required to be less than 3 nm over the entire useful area of the mask, which will be referred to as one field. Two cases are examined here:

1. A 2.5 cm x 2.5 cm square field, which would correspond to a 1:1 mask (e.g. a mask for proximity x-ray lithography) of a single microprocessor die.
2. A 10 cm x 10 cm square field — a mask to be used in a 4:1 reduction lithographic tool, such as an optical stepper.

The maximum error is specified as $\Delta\phi_{\text{tot}} = 3 \cdot \pi/100$, or 3 nm. The error tolerance is divided equally among the different contributors to grating phase errors. To obtain

the worst case estimate, the magnitudes of individual error contributions are added:

$$\Delta\phi_{\text{tot}} = |\Delta\phi_z| + |\Delta\phi_x| + |\Delta\phi_y| + |\Delta\phi_\alpha| + |\Delta\phi_\beta| + |\Delta\phi_a| + |\Delta\phi_c| \quad (4.39)$$

The error $\Delta\phi_\gamma$ has been ignored, because its linear phase can be eliminated, as will be shown in a later chapter. Each term may not contribute an error larger than $3 \text{ nm}/7 = 0.43 \text{ nm}$. The field is assumed to be centered on the origin, so that for a field size d the maximum distortion occurs at $x', y' = \pm d/2$.

The maximum allowable errors were calculated using eqs. (4.20), (4.26), (4.29), (4.35), (4.36), and (4.37). The results are shown in table 4.1.

Table 4.1: Tolerances calculated for a 200-nm period grating with a maximum phase error corresponding to 3 nm.

Parameter		Field size	
		2.5 cm	10 cm
Surface flatness	$ \Delta z $	$0.072 \mu\text{m}$	$0.018 \mu\text{m}$
x -shift	$ \Delta x $	$3.24 \mu\text{m}$	$0.202 \mu\text{m}$
y -shift	$ \Delta y $	$2.74 \mu\text{m}$	$0.171 \mu\text{m}$
Rotation about x -axis	$ \alpha $	$5.73 \mu\text{rad.}$	$0.359 \mu\text{rad.}$
Rotation about y -axis	$ \beta $	$5.73 \mu\text{rad.}$	$0.359 \mu\text{rad.}$
Source-substrate distance	$ \Delta a $	$0.131 \mu\text{m}$	$0.032 \mu\text{m}$
Source-substrate distance	$ \Delta c $	$0.072 \mu\text{m}$	$0.018 \mu\text{m}$

These tolerances are extremely tight. Only the surface flatness requirement can likely be met. Most discouraging is the fact that the distances a and c must be set within error bounds measured in nanometers, i.e. less than one part in 10^7 . At these length scales, factors such as thermal expansion of the IL apparatus, variations in thickness between different substrates, the way they are mounted, etc. play a significant role. To set up the IL system to meet these requirements would indeed be a heroic feat.

4.6 Summary

Based on the assumption that the spatial filters act as point sources, from which spherical waves emanate, a simple model has been developed to describe the gratings' hyperbolic phase progression. The model has been used to estimate phase errors induced by substrate non-flatness, mounting errors, and the uncertainty in determining the distance and angle between the point sources and the substrate surface.

From the calculations presented in the last section, the author draws the conclusion that it is next to impossible to determine *a priori* the phase progression of a hyperbolic grating. Moreover, it appears unlikely that gratings and grids with phase distortions in the nanometer range can be fabricated accurately and repeatably by means of exposure with the IL apparatus.

However, interferometrically generated gratings do have the property of spatial phase coherence. In other words, the phase progression of such gratings is slowly-varying monotonic function of position. A more feasible alternative to direct IL exposure would be to fabricate a master grid using IL. The area of the grid would be several times larger than the usable area of the grid. The phase progression of the grating could then be measured by means of a high-performance coordinate-measuring tool, such as the Leica LMS 2020, which can measure feature positions on a substrate 6 inch \times 6 inch with an accuracy of < 25 nm (3σ). Since the phase progression of the grid would be measured on an area larger than the intended usable area, the errors of the coordinate-measuring tool could be reduced by interpolation, using the spatial-phase coherence of the interferometric grid.

Once characterized, the master grid image would be replicated onto substrates. For this purpose, the technique of near-field holography could be used [106, 107, 63, 108, 7, 109]. This method has been successfully used to replicate highly-accurate grating patterns for distributed Bragg reflectors.

Another promising technique to accomplish grid replication is the method of Achromatic Interferometric Lithography (AIL) [110, 111], depicted in schematic form

in Fig. 4.15. The technique uses three parent gratings with nominally identical hyperbolic phase progression. The parent gratings are fabricated by means of IL. The first grating is illuminated with radiation from a ArF laser ($\lambda = 193$ nm). The grating splits the beam into zero- and ± 1 -order beams. The zero-order is stopped, and the ± 1 diffracted orders illuminate the other two gratings, which recombine the two diffracted orders via 2nd-order diffraction, to create an interference fringe pattern at the substrate surface. The periodicity of the fringe pattern is one-half the periodicity of the parent gratings. In principle, if all three parent gratings have identical phase progressions and are aligned perfectly, the phase progression of the fringe pattern is identical to that of the parent gratings, scaled down by a factor of two. Of course, errors in exposing and aligning the parent gratings are to be expected, but once assembled into the AIL apparatus and aligned, the gratings need not be moved again, so that good repeatability should be achievable with this method. The estimation of grating fidelity for AIL is beyond the scope of this document, but detailed analysis is given in ref. [111].

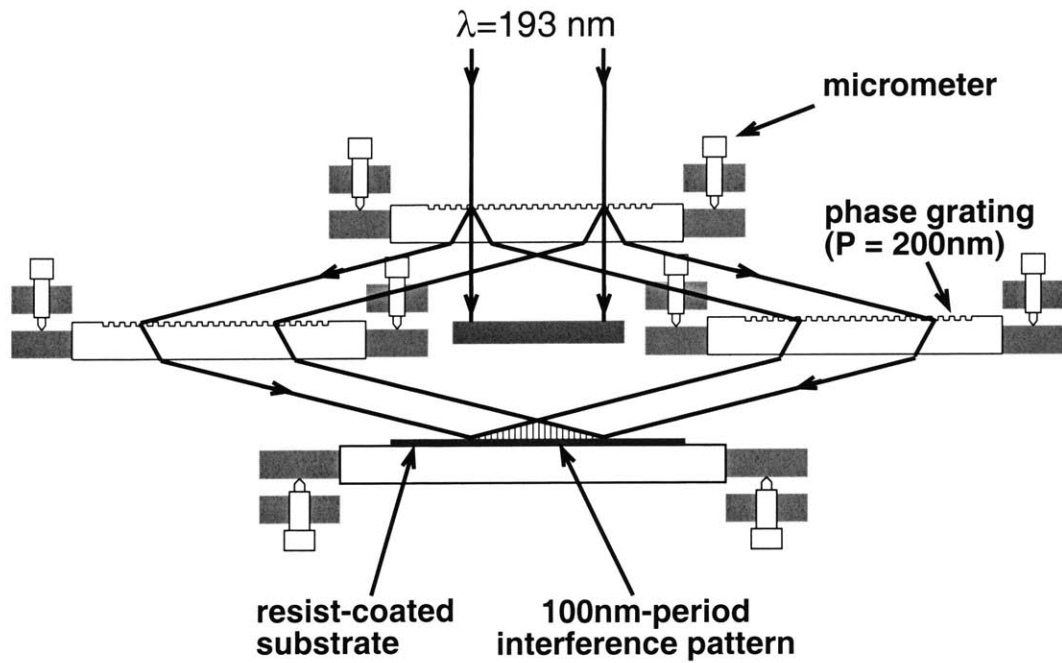


Figure 4.15: Schematic of the AIL configuration.

Chapter 5

Measurements of grating phase progression

This chapter describes the execution and results of an initial set of experiments to directly measure the phase progression of gratings produced by interference lithography. The objective was to determine the magnitude of distortions, i.e., deviations from the idealized model presented in the previous chapter, and to identify the origin of any distortion.

Although the results reported in chapter 3 seem to indicate that spherical waves are being interfered at the substrate plane, these results are based only on intensity measurements, and no phase information was obtained. Phase errors may be present in the gratings, due to spurious reflection from optical components on the table top. These can contribute scattered light, resulting in coherent phase noise, or “ghost” images, although every effort has been made to eliminate this effect. Additionally, air currents and, in general, a non-uniform refractive index in the air space between the pinholes and the substrate will distort the phase fronts.

The experiments reported below represented a significant challenge, since they were aimed at measuring nanometer-scale errors over areas measured in centimeters. In other words, detectivity on the order of one part in 10^7 was required. The method

chosen to measure the phase progression of IL gratings was self-comparison (see, for example, ref. [112]), which has been used to calibrate high-precision 2D metrology stages. The gratings were in effect compared to translated versions of themselves.

5.1 Background

In the experiments reported in this chapter, two grating images recorded with the IL system were compared to each other. As was shown theoretically in the previous chapter, any spatial displacement or rotation of the substrate will induce changes in the phase progression of the grating as a function of x' and y' , the substrate coordinates. Substrate translation in the \hat{x} and \hat{z} directions can be achieved straightforwardly with the IL substrate stage, which is depicted in Fig. 5.1. Translation along the \hat{x} direction was introduced between the two grating images. This direction was chosen for the following reasons:

1. A perfectly linear grating is invariant under translation along the direction perpendicular to the grating's lines. Since the IL-exposed gratings have a non-linear phase progression, the non-linearities manifest themselves upon introducing a linear shift between the two grating images.
2. In order for the collected data to be meaningful, it is necessary to change only one of the substrate parameters. If other parameters change in an unpredictable way, their effects will make the analysis of the collected data unnecessarily complicated, and in the worst case intractable. As the analysis of the previous chapter showed, the grating phase progression is very sensitive to any changes in position and orientation of the substrate. In practice, it is impossible to change the substrate's position without altering any of the other parameters to some extent. Translation stages do not merely translate in one direction; the orientation of the object being translated tends to change as well (this is known as "stage wobble"). As was shown in the previous chapter, the grating phase

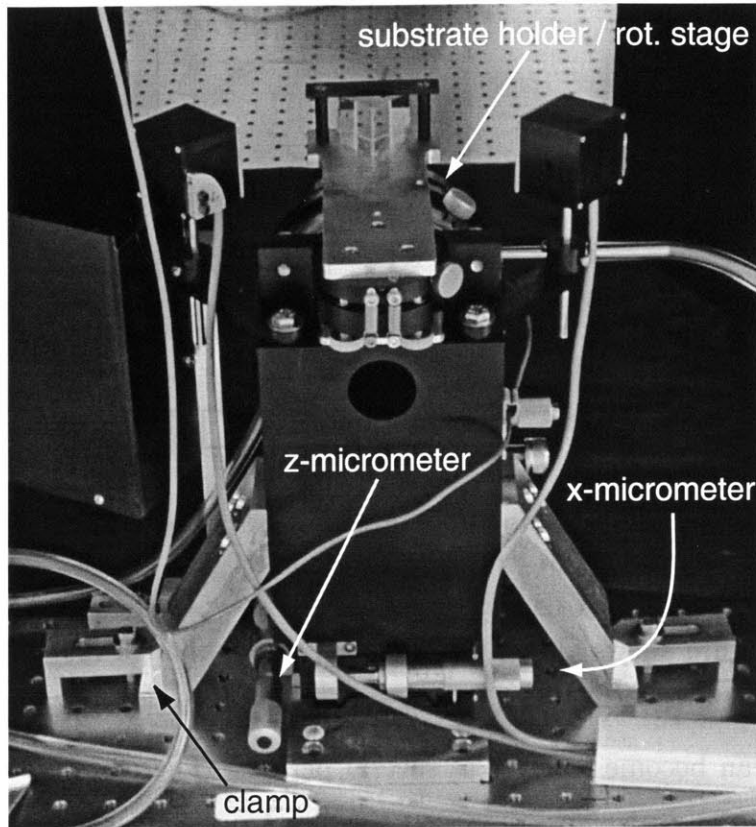


Figure 5.1: Photograph of the IL system's substrate stage. The substrate can be translated along the \hat{x} and \hat{z} directions by means of micrometers. The stage is clamped to the optical table to eliminate vibrations. The substrate can also be rotated about the z axis, by means of the rotation stage incorporated into the substrate holder.

progression is most sensitive to rotations about the z axis. Translation along the \hat{x} direction was chosen, because the angle γ could be measured by means of the autocollimator, as shown in Fig. 5.2 (recall that the autocollimator is used to set the right angle between grating exposures, when grids are being fabricated). As the stage was translated, any variations in γ could be monitored with the autocollimator, to a resolution of 1 arc-sec ($\sim 5 \mu\text{rad.}$), and corrected by means of the rotation stage shown in Fig. 5.1.

Referring to the analysis of the previous chapter, if the substrate is translated along the \hat{x} direction, the phase progression of the grating will change according to eq. 4.34. As shown in Fig. 4.13, the contours of constant phase change resemble

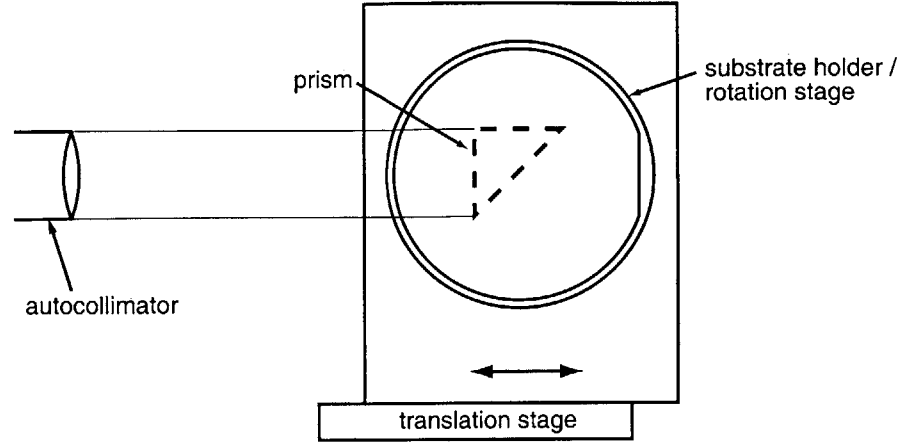


Figure 5.2: The autocollimator is used to monitor stage-induced rotation about the z axis as the substrate is being translated.

ellipses. The figure shows that the maximum phase change for a shift of Δx is a small fraction of a period. However, if Δx is made larger, the magnitude of the phase change can become as large as several periods. Therefore, if two gratings are overlapped, shifted with respect to one another by a sufficiently large distance, a moiré pattern will be observed, as the two gratings “beat” in and out of phase. An example is shown in Fig. 5.3. Here, two identical hyperbolic gratings, whose lines have pronounced curvature, have been shifted along the \hat{x} direction. The lines in the moiré pattern are similar to the contours of Fig. 4.13.

It can be shown that these contours are ellipses to second order in x, y by expanding eq. 4.15 (repeated here for convenience) as a Taylor series:

$$\phi_{\text{non-linear}} = \frac{2\pi}{\lambda} \left(\sqrt{(a+x)^2 + y^2 + c^2} - \sqrt{(a-x)^2 + y^2 + c^2} - \frac{2ax}{\sqrt{a^2 + c^2}} \right) \quad (5.1)$$

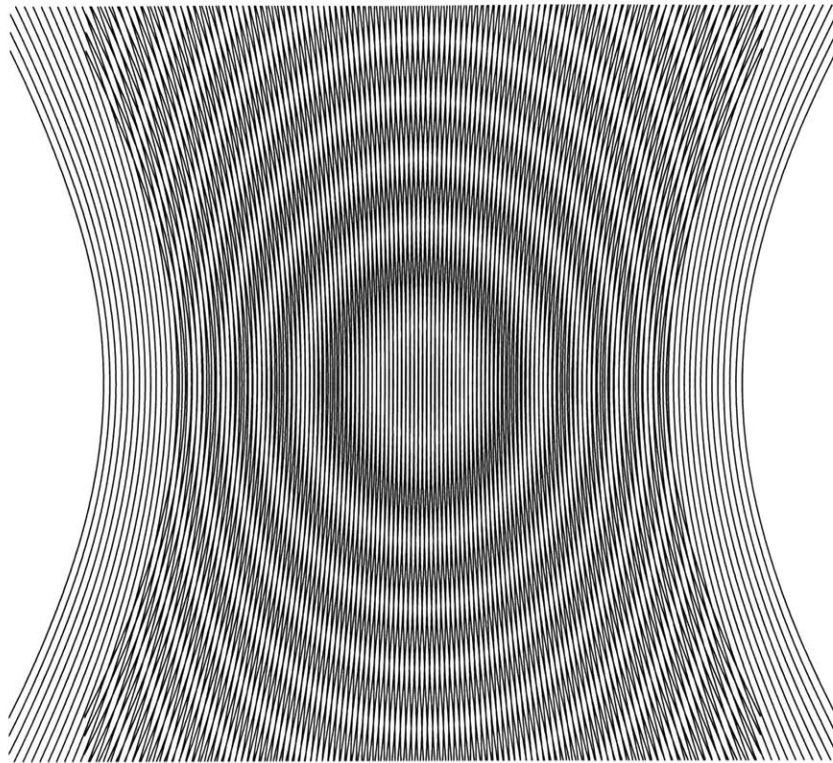


Figure 5.3: A moiré pattern of “ellipses” results when two hyperbolic gratings are superimposed with a linear shift between them.

Using $r^2 = x^2 + y^2$, the first and second terms in the right-hand side are:

$$\begin{aligned}
 \sqrt{(a+x)^2 + y^2 + c^2} &= \sqrt{r^2 + (a^2 + c^2) + 2ax} \\
 &= \sqrt{(a^2 + c^2) \left(1 + \frac{r^2 + 2ax}{a^2 + c^2}\right)} \\
 &\approx \sqrt{a^2 + c^2} \left(1 + \frac{r^2 + 2ax}{2(a^2 + c^2)} - \frac{(r^2 + 2ax)^2}{8(a^2 + c^2)^2} + \dots\right)
 \end{aligned} \tag{5.2}$$

$$\begin{aligned}
 \sqrt{(a-x)^2 + y^2 + c^2} &= \sqrt{r^2 + (a^2 + c^2) - 2ax} \\
 &\approx \sqrt{a^2 + c^2} \left(1 + \frac{r^2 - 2ax}{2(a^2 + c^2)} - \frac{(r^2 - 2ax)^2}{8(a^2 + c^2)^2} + \dots\right)
 \end{aligned} \tag{5.3}$$

Ignoring higher-order terms, eq. 5.1 becomes

$$\phi_{\text{non-linear}} \approx \frac{2\pi}{\lambda} \left(-\frac{axr^2}{(a^2 + c^2)^{3/2}} \right) . \quad (5.4)$$

The equation that describes the contours of constant phase difference for two gratings, with one of them displaced by Δx is, within this approximation,

$$\begin{aligned} \Delta\phi_x(x, y) &= \phi_{\text{non-linear}}(x + \Delta x, y) - \phi_{\text{non-linear}}(x, y) \\ &= -\frac{2\pi}{\lambda} \frac{a}{(a^2 + c^2)^{3/2}} \Delta x \left[3\left(x + \frac{\Delta x}{2}\right)^2 + y^2 + \frac{1}{4}\Delta x^2 \right] , \end{aligned} \quad (5.5)$$

which describes ellipses centered at $(x = \Delta x/2, y = 0)$. Note that for a positive x shift, $\Delta\phi$ is negative. Of course, the constant-phase-difference contours are not ellipses, since the higher-order terms in the Taylor series expansion cannot be ignored, except for infinitesimal shifts.

5.2 Moiré pattern exposed in resist

The experiment simulated in Fig. 5.3 was carried out with the IL apparatus. The optics were aligned to set the nominal period to 200 nm ($a = 439$ mm, $c = 899$ mm). The substrates used were 3-inch-diameter silicon wafers. They were prepared for exposure according to the procedure described in Appendix A

The exposure procedure is shown schematically in Fig. 5.4. A wafer was mounted on the substrate holder and an exposure was performed. One half of the clearing dose was used (4 mJ/cm²). A 6-second exposure was typically required. The substrate stage was then unclamped from the optical table and translated along the \hat{x} direction by a specified distance. The distance was set by the micrometer actuator, which has a resolution of 10 μ m. The stage was clamped to the table, and the autocollimator used to measure how much the substrate had been rotated upon translation. γ -rotations of ~ 10 arc-sec were typically seen. They were corrected by means of the rotation

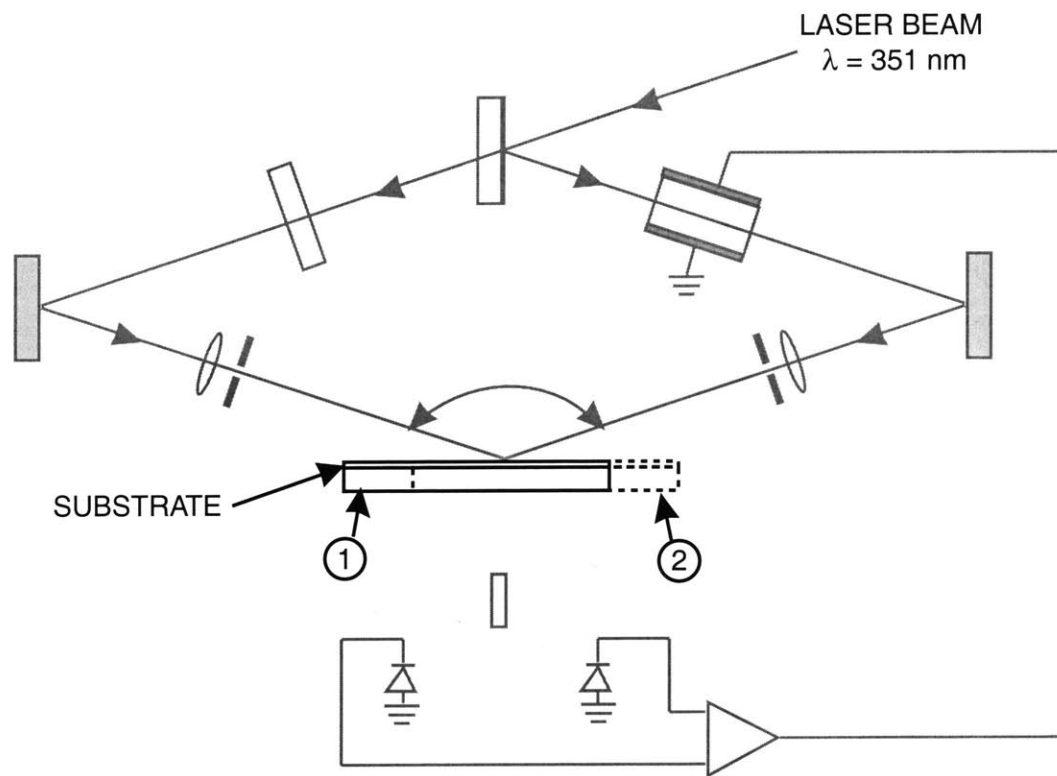


Figure 5.4: Double exposure procedure: a grating was recorded with the stage in position 1. The stage was then moved to position 2, and a second grating exposed.

stage. The autocollimator also detected significant rotations about the y axis (β). These were corrected by the somewhat primitive method of pushing against the stage with one's finger while clamping it down. The stage usually had to be clamped and unclamped several times, until β was measured to be under 1 arc-sec. Once the wafer had been translated and the angles β and γ had been minimized, another half-dose exposure was carried out. Typically no more than a few minutes elapsed between exposures, so it is unlikely that the positions of the spatial filters drifted by any appreciable amount. After the second exposure, the wafer was removed from the system and immediately spray-developed with a 5:1 water:Shipley-351 developer solution, for 45 seconds. The developer was kept at a constant temperature (21°C) by immersing the bottle in a temperature-controlled bath. After development, the wafer was rinsed with DI water and dried.

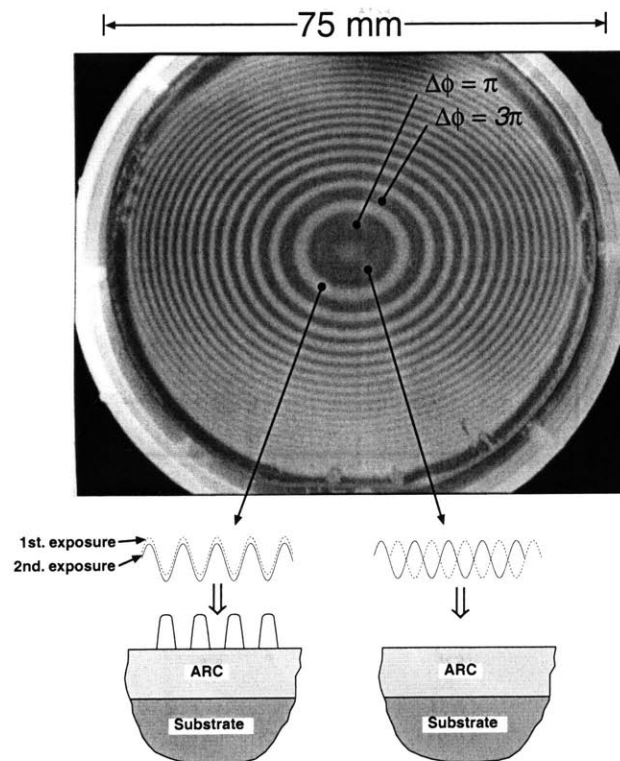


Figure 5.5: Photograph of moiré pattern obtained by superimposing two grating images, shifted with respect to one another by 1 cm. The nominal period of each grating is 200 nm. Each fringe corresponds to a differential phase increment of 2π .

At that point, a macroscopic moiré pattern could be clearly seen. An example is shown in Fig. 5.5. This moiré was obtained by introducing a 1-cm shift between exposures; the wafer center was located at $x_1 = -5$ mm and $x_2 = 5$ mm respectively for each exposure (recall that the principal axes of the “ellipses” are centered at $x = (x_2 - x_1)/2$). This moiré, like the one shown in Fig. 5.3, can be explained as the “beat” between the two superimposed grating exposures. In the areas where the two gratings were in phase, a resist grating remained after development. Conversely, in the areas where the two gratings were opposite in phase, no grating was recorded. Thus, the moiré fringes delineate contours of constant phase difference between the two gratings. The fringes are not sharp. The points at which the phase difference between the two gratings was an even multiple of π are in the middle of the bright fringes (grating), while odd multiples of π occur in the middle of the dark fringes (no grating).

To compare the result of this experiment to the theory, contours of constant phase difference were calculated numerically for the experimental conditions. Since the stage movement had limited precision ($10 \mu\text{m}$), it was not possible to translate the wafer by an exact number of periods. A constant was added to the calculated phase difference, so that the theoretically derived contours would match the transitions between fringes, which are the sharpest features of the pattern. These transitions occur where $\Delta\phi_x = n\pi/2$, where n is an odd integer number. Figure 5.6 shows the modeled constant-phase contours, overlapped on an enlarged photograph of the wafer shown in Fig. 5.5. Qualitatively, the agreement between the model and the experiment is quite good. The shape of the moiré fringes indicates that the gratings’ phase progression is hyperbolic, or very close to it. The absence of abrupt transitions and ghost images in the fringes indicate that stray light is not measurably contributing to the grating exposure. Upon closer inspection, the figure reveals that while the contours coincide with fringe transitions for those fringes away from the center, they do not coincide with the central fringes. The contours fall “out of step” with the fringes in a progressive fashion. This is attributed to the uncertainty in setting the geometrical parameters a and c .

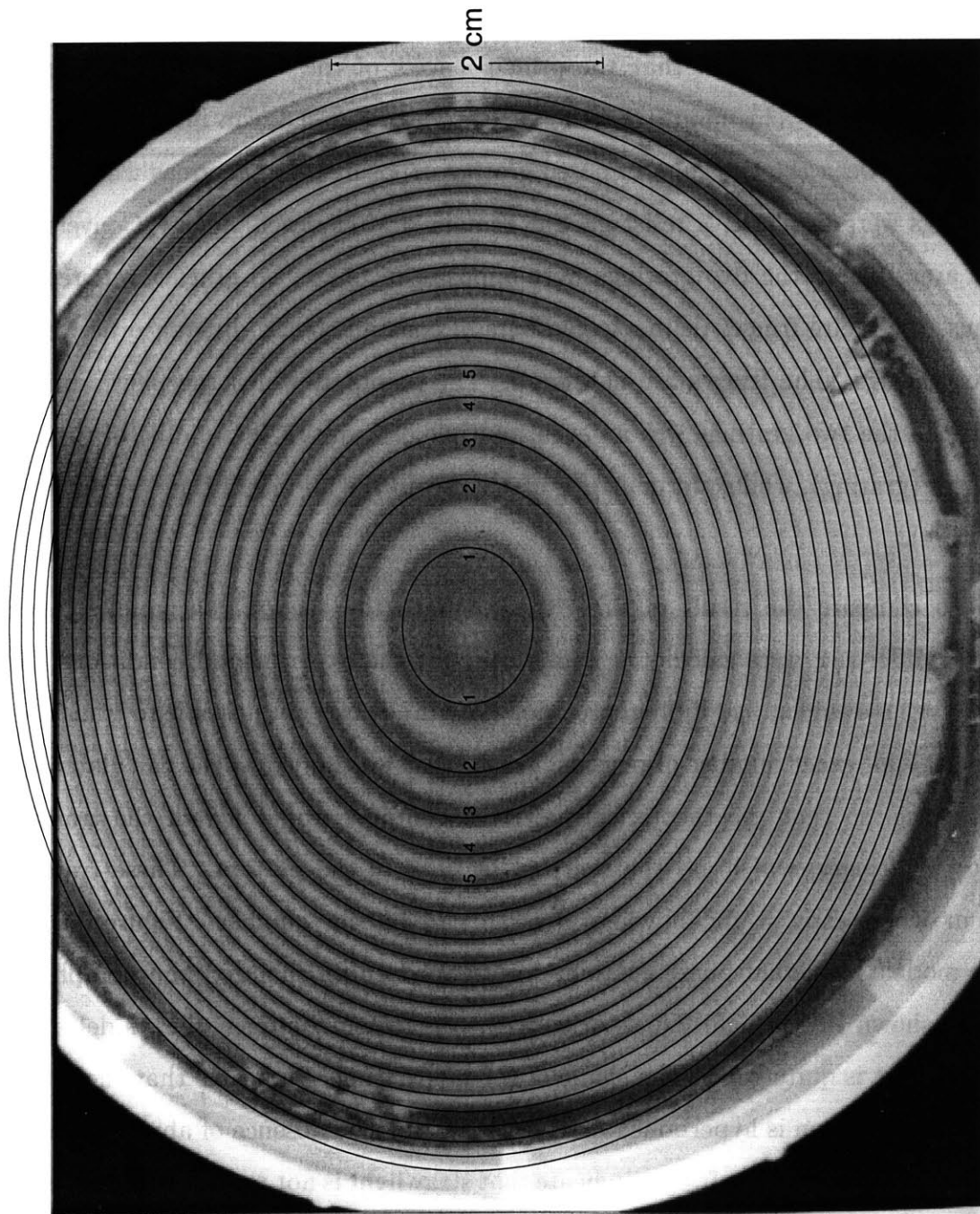


Figure 5.6: Contours of constant phase difference, calculated theoretically for the experimental conditions, overlapped on an enlarged photograph of the moiré pattern. For clarity, only contours for which $\Delta\phi = (n + \frac{1}{2})\pi$; n odd, are shown.

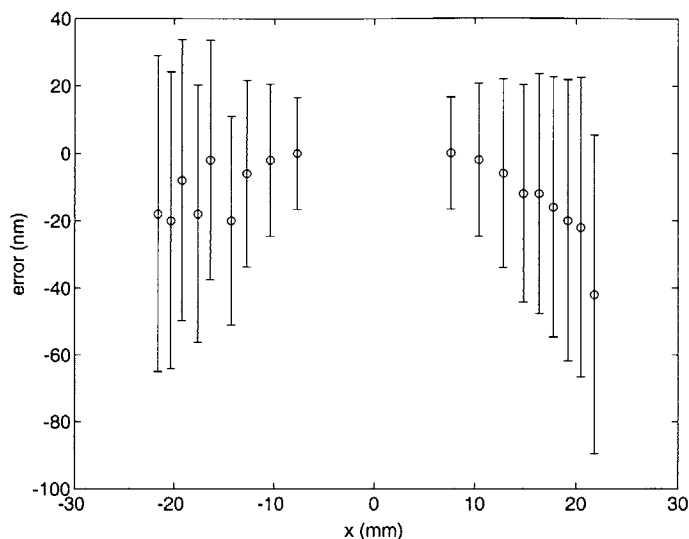


Figure 5.7: Errors measured between the theoretical contours and the moiré fringe boundaries. The error bars reflect an uncertainty in setting a and c of $\pm 20 \mu\text{m}$.

More quantitative data were obtained by measuring the distance between each one of the contours and the corresponding fringe boundary. That distance was translated into phase error by normalizing it with respect to the width of one fringe. The data are plotted in figure 5.7.

Despite its obvious limitations, the results of this experiment were very encouraging. The phase difference between the gratings was observed to be a smooth function, and no significant distortion was observable. The experimental results agree with the model, but the lack of sharpness of the moiré fringes makes a precise, quantitative measurement difficult. Moreover, phase information can only be obtained at the fringe boundaries. Ideally, one would like to obtain a map of the phase difference for all points on the wafer surface.

5.3 Phase-shifted moiré

To achieve higher precision, a measurement was implemented based on the method of phase-shifting interferometry [113]. In interferometry, the phase of a wavefront is

measured by comparing it to a reference wavefront. In phase-shifting interferometry, a time-varying phase shift is introduced between the reference and the test wavefronts. Consequently, the intensity at each point of the interferogram also varies in time. The phase difference between the reference and the test wavefronts thereby manifests itself in the time domain. Similarly, a phase-shifted moiré experiment involves the comparison of a reference grating and a test grating, but in real-time as opposed to exposure/development of resist.

To obtain a moiré pattern that could be modulated in real time, the test grating used was the standing wave pattern, whose phase progression is nominally identical to that of the recorded grating, since the standing wave was used to record the grating pattern. The phase of the fringe pattern can be scanned quite straightforwardly by applying a voltage offset to the phase modulator (Pockels' cell). The reference grating was designed to interact with the standing wave, to produce a signal proportional to the phase difference between the reference and test gratings. Fluorescence was considered to be an adequate signal, so a grating with fluorescent "lines" and dark "spaces" was fabricated.

5.3.1 Reference Grating Fabrication

The test grating used to sample the standing wave was fabricated by etching grooves into the surface of a silicon wafer and filling them with a fluorescent polymer. A commercially available polymer¹ emits light centered at $\lambda = 425$ nm when irradiated with ultra-violet light. The polymer is sold as a plastic sheet, and was dissolved in toluene in order to be able to spin-coat substrates with it.

To record the IL grating, a tri-layer resist process similar to that described in ref. [86] was used. In this process, a thin SiO_x interlayer was deposited between the ARC and resist films. The substrate preparation sequence is described in Appendix B.

¹Available from Bicon Corp., Newbury, Ohio. This material is intended to be used as a scintillator, but it also emits radiation via fluorescence.

The IL system was set up to expose gratings with 400 nm period. The parameters $a = 533.5 \pm 0.5$ mm and $c = 1092.7 \pm 0.5$ mm were carefully measured, to obtain a good match between the experimental results and the theoretical predictions. The larger period was chosen to simplify the fabrication process. When recording a grating, the dose used for exposure was 28 mJ/cm^2 . The resist was developed immediately after exposure. The developer was a 0.242 *N* solution of tetramethyl ammonium hydroxide (TMAH) in water. The developer temperature was kept at 21.0°C using a temperature-controlled bath.

The grating pattern was transferred to the wafer surface by reactive-ion etching (RIE) through the oxide and ARC layers. All RIE was done with a PlasmaTherm 790 tool. The oxide interlayer was etched with CF_4 (15 sccm flow rate, 10 mTorr, 300 V DC bias; 3 min. duration), using the resist pattern as a mask. The interlayer then served as the mask to etch through the ARC film (etch conditions: O_2 :He 5 sccm:10 sccm; 7 mTorr; 280 W incident RF power; 4 min. 40 s). The resist grating was removed during the oxygen etch step.

The rest of the fabrication sequence is shown schematically in Fig. 5.8. Once the silicon surface was exposed in the areas corresponding to the grating spaces, a 40-nm-thick layer of chromium was evaporated at normal incidence and lifted off. Lift-off is usually accomplished by dissolving the organic mask in a strong solvent. However, the dry-etching process tends to cross-link the ARC polymer, so that it cannot be removed using organic solvents. It was found, however, that the RCA organic-clean solution (5:1:1 water:ammonium hydroxide:hydrogen peroxide, at 80°C) was effective in removing the ARC. After lift-off, a grating of chromium lines was present at the wafer surface. The metal lines served as a hard mask to transfer the grating into the silicon substrate. Prior to etching into the silicon, the surface was cleared of any organic contaminants by oxygen-plasma ashing for 2 min. The grating was etched into the substrate by RIE, to a depth of 600 nm. The etch conditions were: CF_4 : O_2 13.5 sccm:1.5 sccm; 20 mTorr; 400 V DC bias for 25 min. The silicon dry-etch process was optimized to obtain sufficiently straight sidewalls. The effect of different etch

conditions on sidewall profile is shown in Appendix C. After the grating grooves had been etched into the substrate, the chromium hard mask was stripped, using a wet etchant².

The fluorescent-polymer solution was then spun on the wafer and baked at 90°C for 30 min. It was observed that fluorescence no longer occurred if the polymer was baked at a higher temperature. After baking, the polymer layer was 800 nm thick and fully planarized. The extra 200 nm of polymer were then etched back by RIE (30 sccm O₂; 50 mTorr; 50 V DC bias for 4 min.). Very low power was used in this step to prevent damage to the polymer. Alternatively, oxygen plasma ashing could be used. A cross sectional scanning-electron micrograph of a finished grating is shown in Fig. 5.9

When the grating was illuminated by a standing wave in the IL system, moiré fringes appeared (see Fig. 5.10). These fringes occur because the intensity of the light emitted at the wafer surface is proportional to the overlap between the standing wave and the scintillating grooves of the sample. A 3-CCD RGB camera³ was used to collect the images of the moiré fringes. As is the case with most experiments involving scintillation or fluorescence, light emission was weak; therefore, it was collected by the CCD for intervals of 0.5-2 s to form an image. Background light in the laboratory, which does not have any components in the blue part of the visible spectrum, was filtered out by using the blue signal from the RGB camera.

After a few hours of use, the grating's fluorescence became weak and hard to detect, so that the fluorescent material had to be stripped from the wafer and re-applied. The fluorescent polymer was easily removed by immersion in a caustic solution of 3:1 sulfuric acid:hydrogen peroxide ("piranha" solution). A new polymer coating was then applied, baked, and etched back with oxygen plasma.

²CR-7 photomask etchant, Cyantek Corp., Fremont, CA

³Sony model no. XC-003

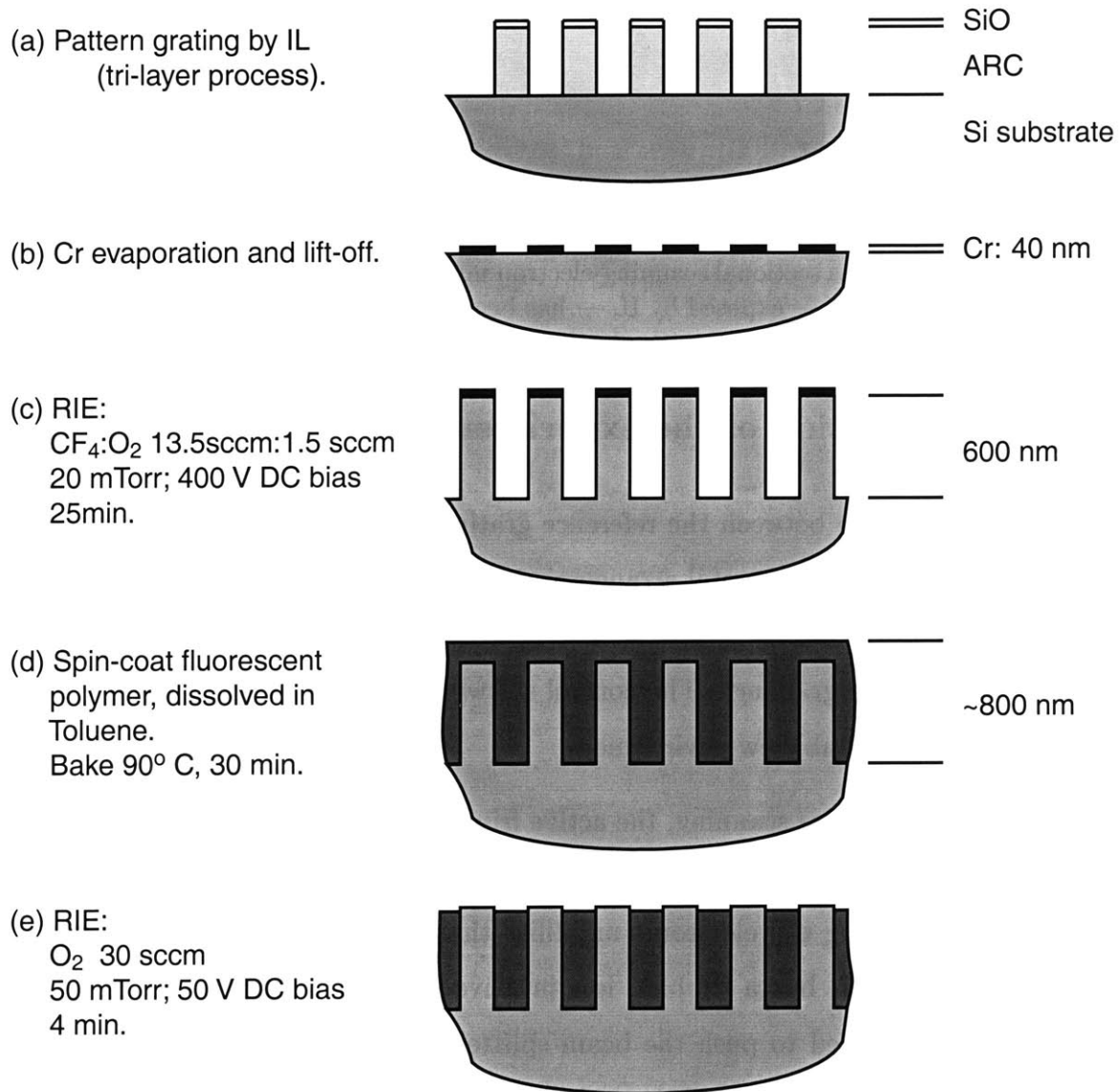


Figure 5.8: Fabrication sequence of fluorescent test grating.

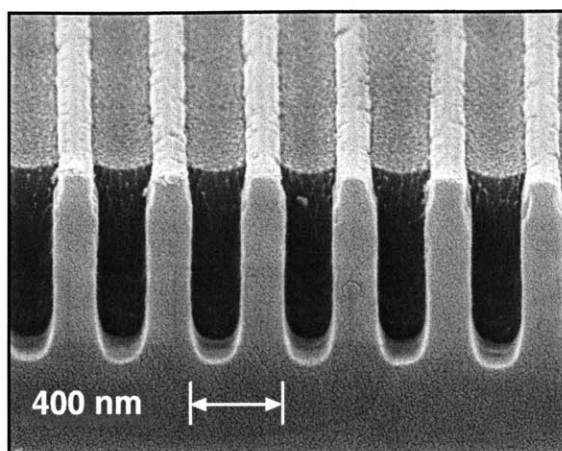


Figure 5.9: Cross sectional scanning-electron micrograph of a finished scintillating grating. A grating — exposed by IL — has been etched into a silicon substrate to a depth of 600 nm and filled with plastic fluorescent material.

5.3.2 Description of the experiment

The phase difference between the reference grating and the interference pattern was measured with the experimental arrangement shown in Fig. 5.11. The apparatus was controlled by a Macintosh computer, equipped with a digital/analog input/output board⁴ and a frame grabber⁵. The control software was implemented using the National Instruments LabView environment.

To implement phase scanning, the active fringe-stabilization system was modified to introduce voltage offsets to the phase modulator. This could have been accomplished by modifying the electronic amplifier that produces the feedback signal to drive the modulator, but a simpler, less invasive strategy was found. A piezoelectric actuator was used to push the beam splitter sideways (in the \hat{x} direction) (see Fig. 5.11). If the beam splitter is pushed in the $-\hat{x}$ direction, the left arm of the Mach-Zehnder interferometer is lengthened, while the right arm becomes shorter. Accordingly, the feedback system drives the electro-optic modulator to introduce a phase shift in the left arm, such that the difference in optical path between the two arms

⁴National Instruments LabNB

⁵Perceptics Corp.

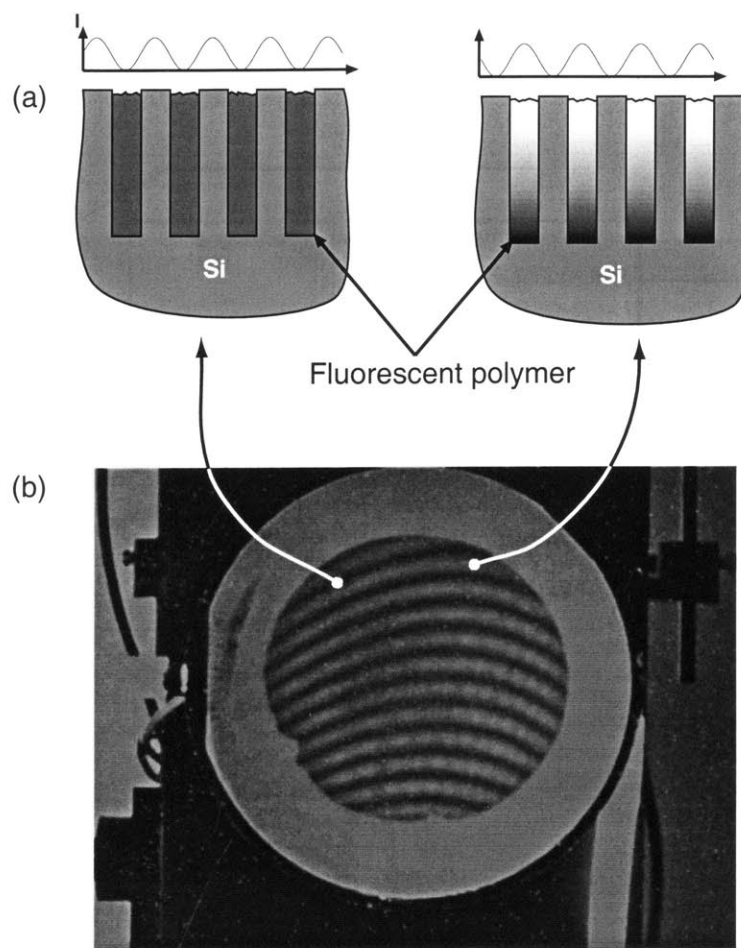


Figure 5.10: (a) Mechanism by which the fluorescent grating interacts with the standing wave. (b) Photograph of moiré fringes imaged in real time by an integrating CCD camera. The fringes are due to the beating between the fluorescent grooves and the standing wave present at the wafer surface. The substrate has been rotated to show many fringes.

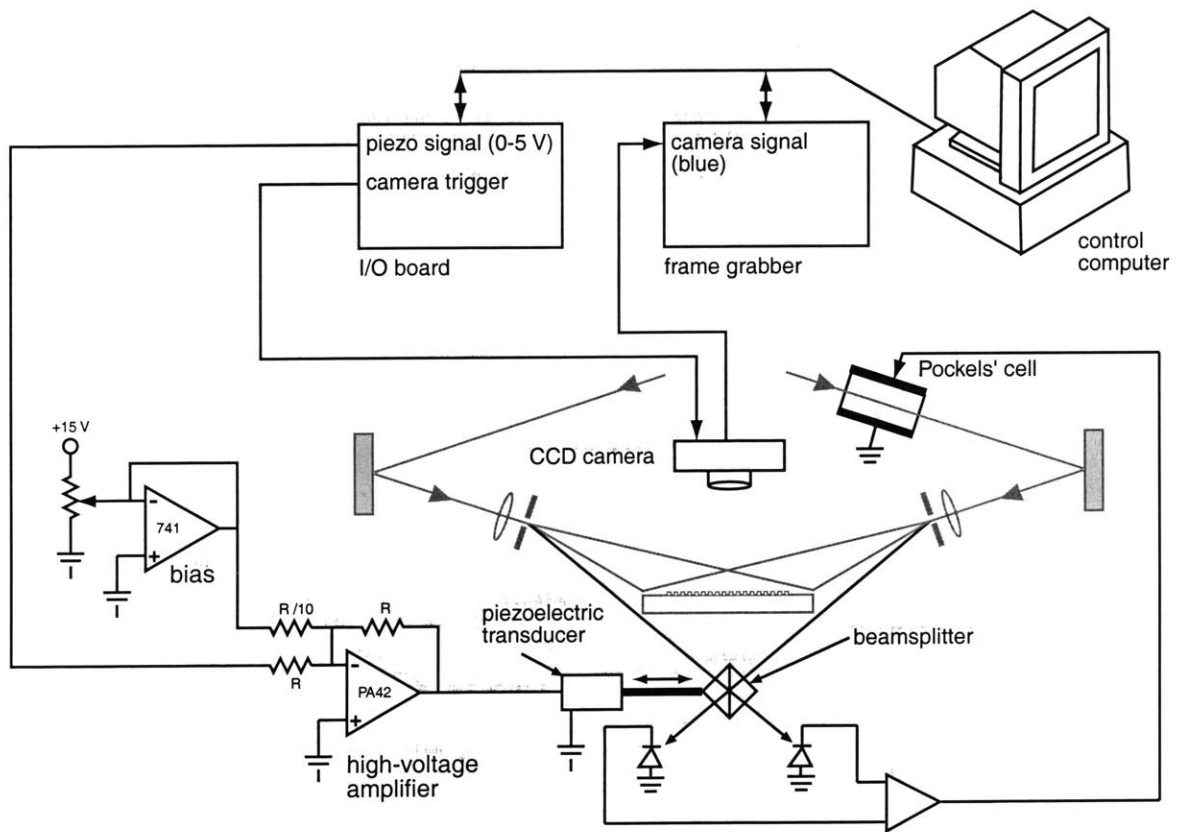


Figure 5.11: Schematic of the experimental arrangement used to measure the phase difference between the reference grating and the standing wave present at the grating's surface.

remains constant. Thus, the phase of the standing wave pattern can be modulated by applying a voltage to the piezo. The actuator used to displace the beam splitter⁶ will produce up to 30 μm of motion when a voltage between 20 and 160 V is applied to its terminals. These actuators have been optimized by the manufacturer for low hysteresis and drift. According to the manufacturer's specifications, the linearity of displacement is best when the input voltage is above 60 V. A circuit was built to drive the piezoelectric actuator, using a high-voltage operational amplifier⁷. This circuit allows one to set the operating point for the piezo voltage using a potentiometer (see Fig. 5.11). One of the analog outputs of the I/O board was then used to generate an incremental signal to scan the phase of the standing wave under computer control.

To measure the phase difference between the reference grating and the interference pattern, the phase of the latter was set to values δ_i , spaced evenly over one period and thus given by

$$\delta_i = \frac{i2\pi}{N}, \quad 0 \leq i < N. \quad (5.6)$$

An image $I_i(x, y)$ was acquired for each step. Sixteen images (440×440 pixels) were taken for each measurement ($N = 16$). The sampling rate — the spacing between pixels — was determined by imaging a sheet of graph paper attached to the surface of a 4-inch-diameter wafer, which was mounted on the IL substrate holder, and counting the number of pixels per unit distance. The position of the camera was adjusted so that the center of the wafer coincided with the center of the acquired images.

Each one of the images $I_i(x, y)$ was acquired according to the following sequence: the control computer set the piezo signal to the appropriate value and waited 0.1 s for any mechanical vibrations to settle. It then sent a trigger pulse to the CCD camera, to start collecting the image. After the proper integration time, the frame grabber

⁶Newport Corp., part no. ESA1330-OPT-01

⁷Apex Microtechnology Corp., Tucson, AZ, part no. PA-42A

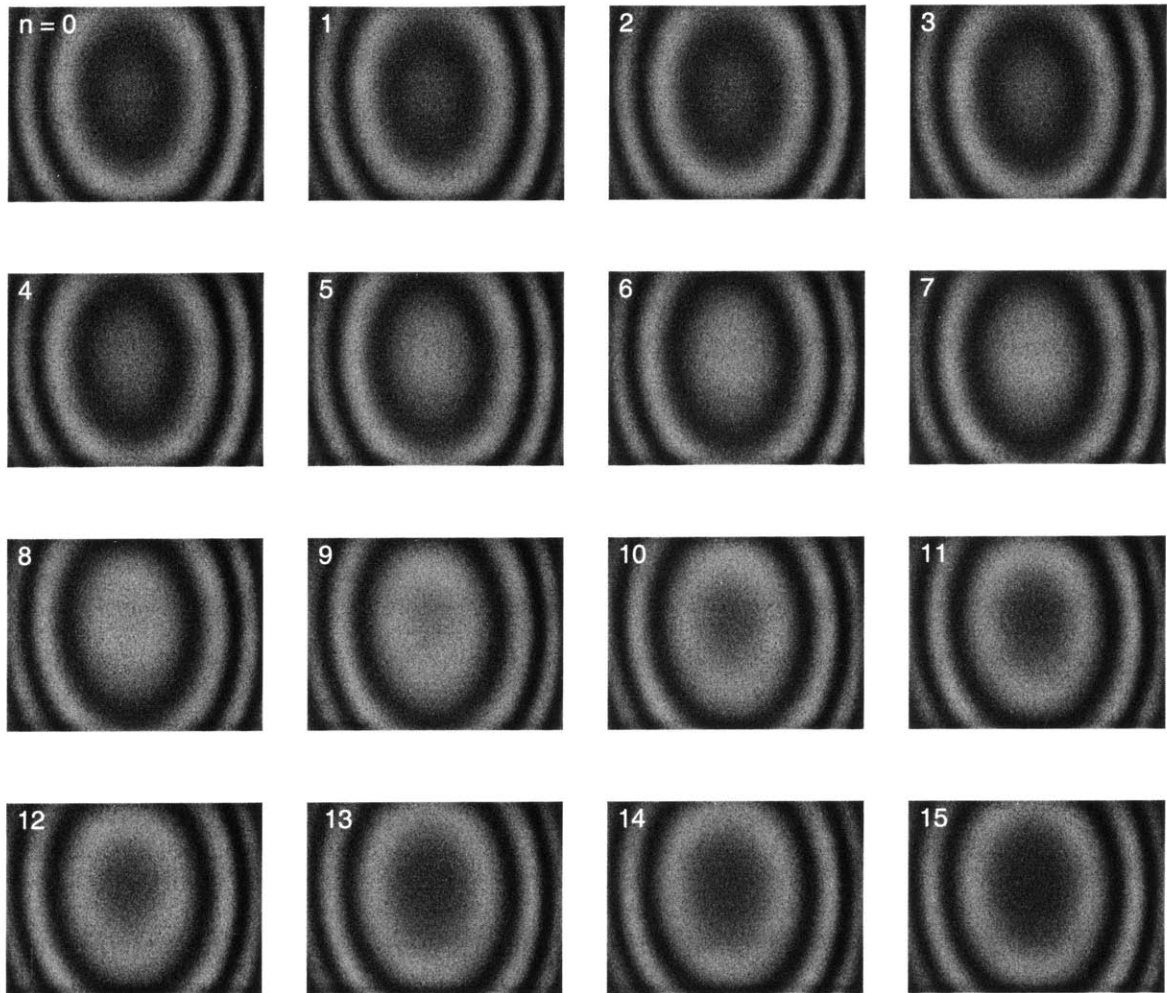


Figure 5.12: A sequence of phase-shifted moiré images. The phase of the standing wave was set to $\delta_n = \frac{n2\pi}{16}$ for each image.

was instructed to acquire the next frame, and a second trigger pulse was sent to the camera, to stop the integration. The camera immediately transferred the image to the frame grabber. Due to memory constraints, all 16 images could not be stored in memory. Each image was saved to disk, and further processing was done off-line, using a UNIX workstation. A sequence of acquired images is shown in Fig. 5.12.

The phase and the amplitude modulation were then estimated for each picture element by least-squares fitting to a cosine function. The phase ϕ that minimizes the squared error between a function of the form $I_i(x, y) = I'(x, y) + I''(x, y) \cos[\phi(x, y) +$

$\delta_i]$ and the data is given by [113]

$$\phi(x, y) = \arctan \left(\frac{-\sum_i I_i(x, y) \sin \delta_i}{\sum_i I_i(x, y) \cos \delta_i} \right). \quad (5.7)$$

The estimated phase ϕ , computed from the equation above is restricted to $0 < \phi \leq 2\pi$. If the phase of the moiré varies by more than 2π , discontinuities will occur. These discontinuities must be removed by a procedure called “phase unwrapping” [114], which is straightforward to do in one dimension [98], but can be rather challenging for two-dimensional phase maps. Fortunately, it was found that a one-dimensional phase-unwrapping algorithm could be applied to the collected data. The 1-D algorithm was applied to each row of the image separately, and then to each column. The correct results were obtained using this procedure.

The data modulation $\gamma(x, y)$, which is the ratio between the modulation amplitude I'' and the DC term I' , is used to identify bad pixels in the CCD or areas with no grating. Data from those pixels were ignored. The estimate for $\gamma(x, y)$ is given by

$$\gamma(x, y) = \frac{2 \sqrt{(\sum_i I_i(x, y) \sin \delta_i)^2 + (\sum_i I_i(x, y) \cos \delta_i)^2}}{\sum_i I_i(x, y)}. \quad (5.8)$$

In this procedure, it is critical to scan the phase over one period exactly, because it is not a variable in the least-squares fit. Therefore, small errors in the period can lead to large deviations in the estimated parameters. The phase shift of the moiré pattern was therefore calibrated against the piezo signal generated by the control computer. This was accomplished as follows: once the piezoelectric actuator had been brought into contact with the beam-splitter mount (by means of a micrometer), the DC operating point was set to ~ 60 V with the biasing circuit. The piezo incremental signal was then ramped up and down between 0 and 5 V several times, in order to remove residual hysteresis as much as possible. The piezo signal was then scanned between values V_{\min} and V_{\max} in 128 steps. For each step, one image of the moiré pattern was acquired by the frame grabber, and the intensity variation

of one pixel was recorded. Once the scan was complete, the intensity variation of that pixel was known as a function of the piezo signal. A function of the form $I = I' + I'' \cos[\xi V_{\text{piezo}} + \phi]$ was fitted to these data using a non-linear least-squares method. V_{min} and V_{max} were chosen so that the condition $\xi(V_{\text{max}} - V_{\text{min}}) = 2\pi$ was satisfied.

The collected data for one calibration run, as well as the best-fit cosine function, are shown in Fig. 5.13. For the data shown in the figure, V_{min} and V_{max} had already been calibrated to give a total phase shift of 2π . Large variations between the data and the ideal cosine function can be seen. These deviations are attributed to air turbulence. One data point was acquired every 2 seconds (the CCD integration time), so that the scan lasted slightly more than 4 minutes. These data show that the phase of the interference pattern varied significantly over time intervals of ~ 20 s, even though the active fringe-stabilization system was engaged. This effect was confirmed visually: the moiré fringes could be seen to distort as thermal air currents drifted in front of the sample. Thermal currents could be induced by simply putting a heat source (one's hand, for example) directly below the substrate. The effects were similar in nature, but much more pronounced. The magnitude of the phase errors can be estimated graphically by comparing the data to the fitted cosine function, according to the construction shown in Fig. 5.13. The magnitude of the largest deviation was thus estimated to be approximately $\frac{1}{10}$ of a period, i.e. 40 nm. To minimize the effect of air currents on the phase measurements, the clean-room air handlers were shut off, and the laboratory temperature was allowed to stabilize for two hours before any measurements were taken. Even so, a small amount of residual air turbulence was observed, presumably caused by the heat generated by the CCD camera, which by necessity had to be mounted inside the IL apparatus. A large number of images was collected, in order to remove the effects of random phase fluctuations (as well as noise in the individual images) as much as possible.

Once calibrated, the repeatability of phase scanning was measured by performing the calibration procedure 5 times with fixed values of V_{min} and V_{max} . The average

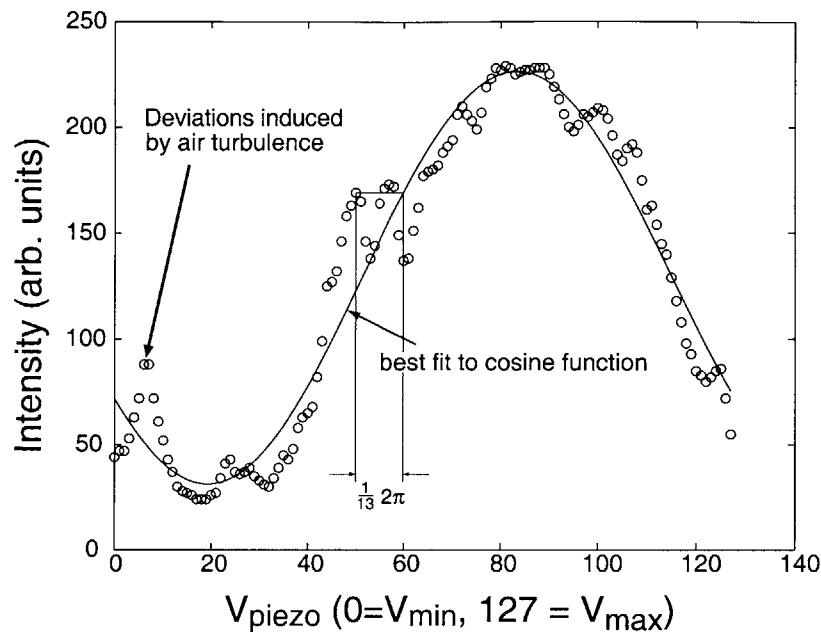


Figure 5.13: Data from a piezo calibration run. The solid line is a cosine function fitted to the data.

value of $\xi(V_{\max} - V_{\min})$ was $1.02 \cdot 2\pi$ and the standard deviation was $0.0244 \cdot 2\pi$.

5.4 Results and discussion

The reference grating must be removed from the IL apparatus to fabricate the fluorescent grooves, as opposed to the exposure of two gratings in resist, where the two grating exposures are performed without unmounting the substrate. Therefore, considerable care must be taken when remounting the reference grating, in order to avoid errors in the measurement. After remounting the reference grating, the wafer's rotation and shift were adjusted to match the conditions of exposure as closely as possible. The first measurement was taken at this null position. Ideally, if the reference grating and the standing wave were exactly matched, no phase errors should be detectable. However, the match was imperfect, as can be seen from the phase error measured, shown in Fig. 5.14(a). The wafer's position along the \hat{y} direction and its rotation were the least repeatable parameters, and introduced the largest errors. The

systematic errors incurred by imperfectly mounting the wafer limited the accuracy of the measurements. The detectivity of the phase-shifting measurement can be estimated from the amplitude of random noise in the phase-error map (see Fig. 5.14(b)). The detectivity was estimated to be $\sim \frac{1}{15}$ of a period, and is most likely limited by the signal-to-noise ratio (SNR) of the images. Brighter fringe patterns should improve the SNR and result in finer detectivity.

After the null measurement, the sample was displaced along the \hat{x} direction by a specified distance, which was set with the sample stage micrometer, and the phase difference was again measured. Figure 5.15 shows two measurements, for lateral displacements of 2.5 mm (a) and 5.0 mm (b). Note the similarity between the contours of constant phase in the plots and the moiré fringes obtained by exposing two gratings in resist (Fig. 5.5).

The effects of systematic errors can be seen clearly in both plots. The principal axes of the “ellipses” are rotated with respect to the coordinate axes of the plots. This effect is consistent with an error in the wafer’s position along \hat{y} . Also, the symmetry points of the contours show an extraneous shift from their expected positions ($x' = \frac{\Delta x}{2}, y' = 0$) on the wafer, which is the combined effect of the mounting error Δy and small rotations $\Delta\gamma$.

To compare the experimental data to the theoretical predictions, a constant was added to the measured phase-difference values, and the coordinate system for the theoretical calculation was shifted so that the points of symmetry for calculation and experiment coincided. The error (the difference between the calculated and measured values) is plotted in Fig. 5.16. Most significant in this measurement are the systematic errors introduced by errors in sample position. Even if these systematic errors are included, the upper bound in phase deviation as obtained from this measurement is one eighth of a period (50 nm) in 30×30 mm.

To reiterate, the variable measured in these experiments is the phase difference between the measurement and test gratings. Their individual phase progression is not uniquely specified. The phase errors of the individual gratings are probably

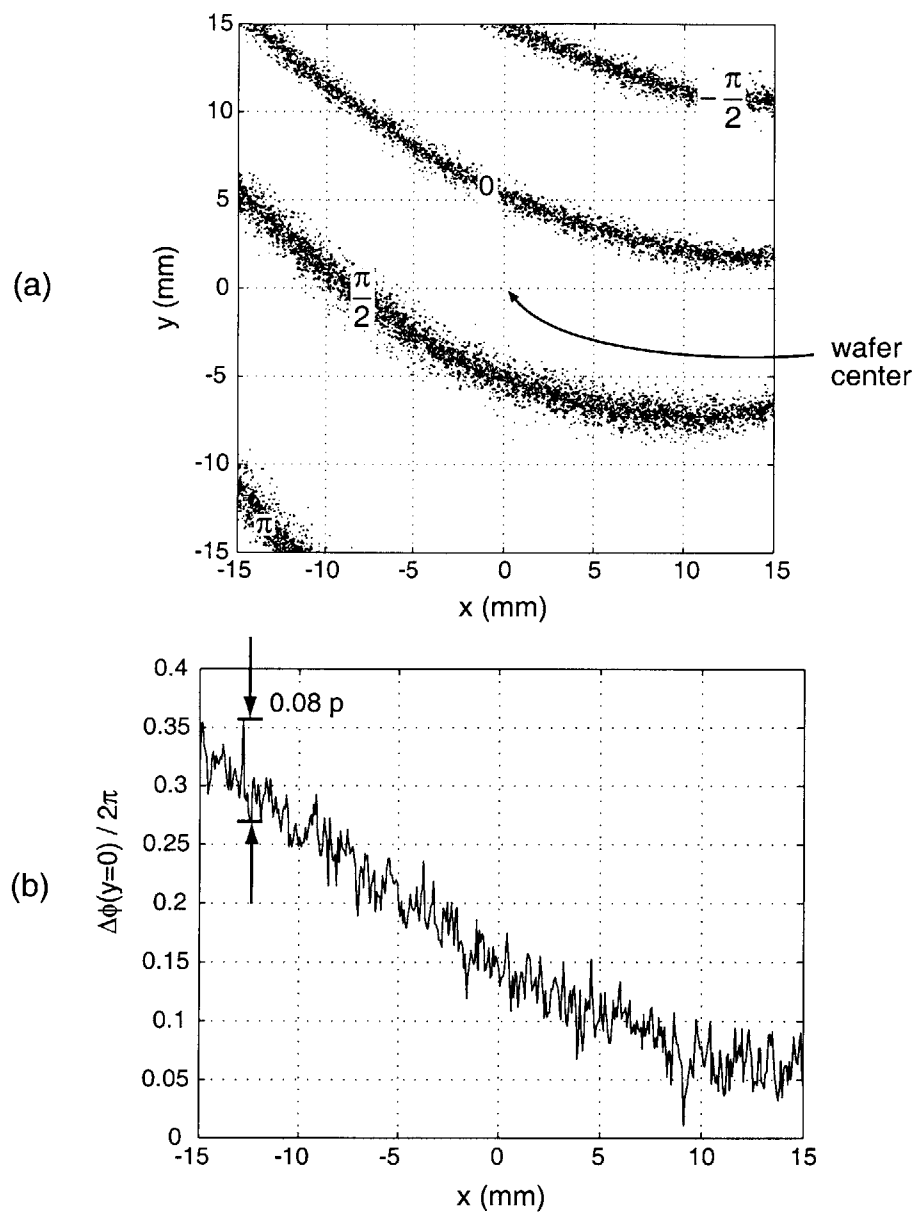


Figure 5.14: (a) Contours of constant phase difference, measured at the null position. (b) Cross-sectional plot of the data shown in (a), for $y = 0$. The detectivity of the measurement is estimated to be ~ 0.08 periods, or 32 nm.

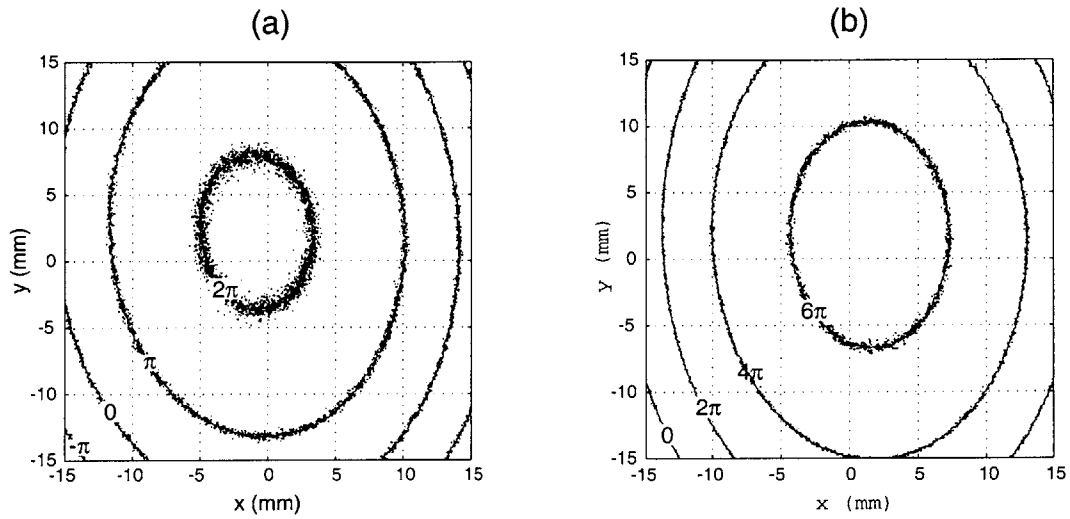


Figure 5.15: Plots of phase difference as measured using the phase-shifting moiré technique. Contours of constant phase are plotted for \hat{x} -direction wafer displacements of 2.5 mm (a) and 5.0 mm (b).

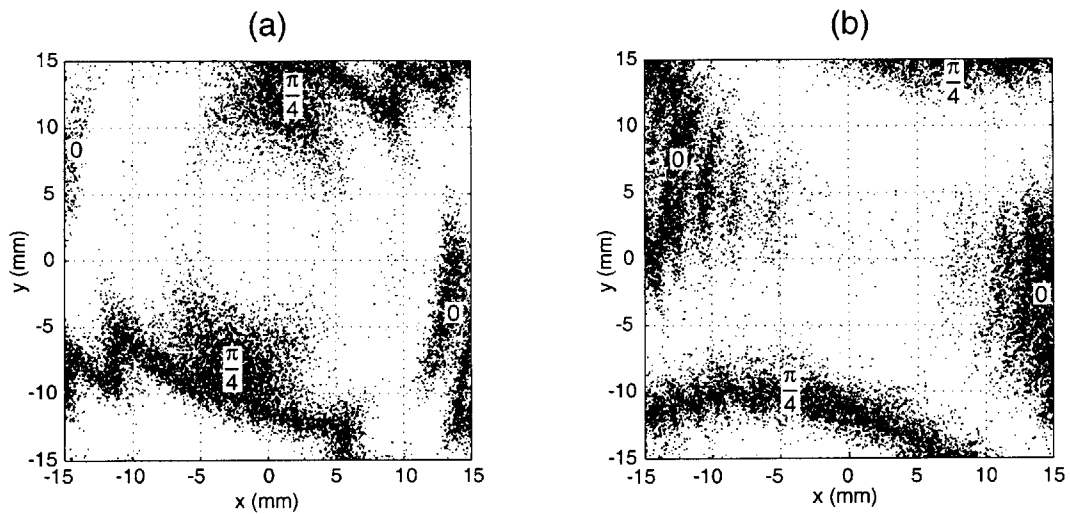


Figure 5.16: Plots of error between the calculated and measured values of phase difference. As measured, the largest deviation in phase is one eighth of a period, or 50 nm, in 30×30 mm. Systematic errors are present in this measurement; therefore, the real distortion of the grating is expected to be lower.

smaller than the worst-case estimate given above. However, based on the analysis of the previous chapter, it is unlikely that the parameters of the IL system could be set accurately enough to eliminate systematic errors. Therefore, phase-difference measurements accurate to less than 10 nm do not seem feasible with this setup.

5.5 Future work: The IL system as a holographic interferometer

The IL apparatus can be configured as a holographic interferometer by simply placing a fluorescent screen in front of the spatial filters, as shown in Fig. 5.17. The screen has a hole cut in the center, so that it does not block light coming from the spatial filter. When a grating is mounted on the substrate holder, fringes can be seen on the screen, whose shape and number match the moiré pattern observed on the surface of the fluorescent grating. The fringes are due to the interference of two wavefronts: one wavefront is the specular reflection of light emanating from the spatial filter opposite to the screen. The second is a diffracted wavefront, which emanates from the spatial filter behind the screen and is diffracted into the -1 order by the grating (i.e., back-diffraction).

When the grating is mounted in the exact location where it was exposed, i.e. when the spatial phase of the grating and the standing wave are exactly matched, the reflected and back-diffracted wavefronts co-propagate, and no fringes appear at the screen. This can be shown by treating the grating as a reflection hologram. When the hologram is recorded (see Fig. 5.18 (a)), wavefront 1 can be thought of as the object wavefront, and wavefront 2 as the reference. When the hologram is “read”, by illuminating it with the reference wavefront (see Fig. 5.18 (b)), the object wavefront is obtained. For spherical reference and object waves, this effect can be shown quantitatively by tracing the rays of the specularly reflected beam and the back-diffracted beam.

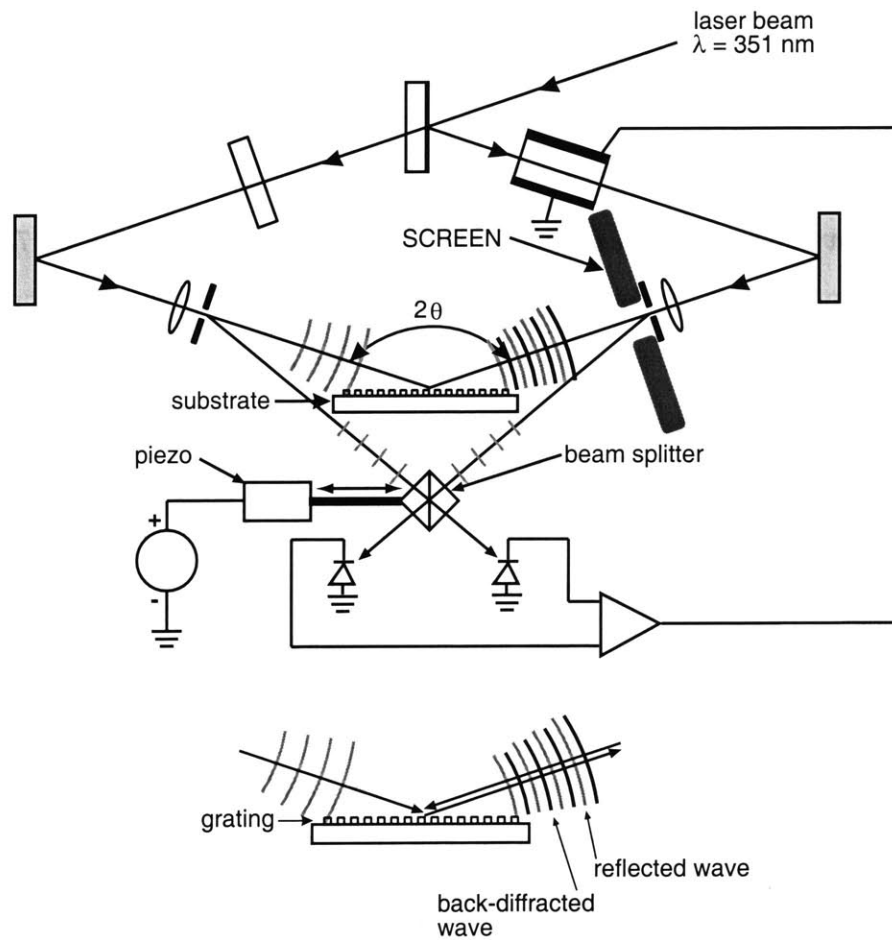


Figure 5.17: The IL system configured as a holographic interferometer.

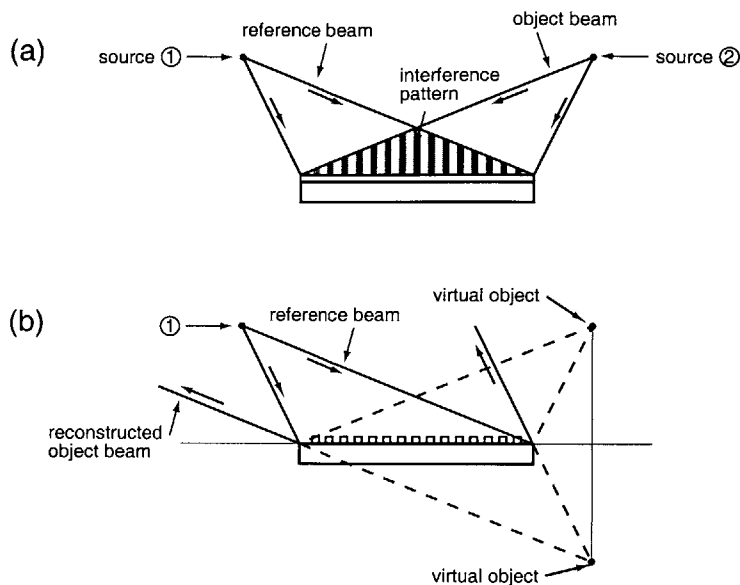


Figure 5.18: The IL grating viewed as a reflection hologram. (a) Recording the hologram. (b) Wavefront reconstruction by the grating.

The angle of diffraction of an incoming ray by a grating of period p is given by the grating equation [96]

$$\sin \theta_d - \sin \theta_o = \frac{m\lambda}{p} \quad , \quad (5.9)$$

where θ_o is the angle of the incoming ray (with respect to the surface normal), θ_d is the angle of the diffracted ray, and m is the order of diffraction. Diffraction of the incoming beam along the \hat{x} and \hat{y} directions is treated separately.

In the \hat{x} direction, the grating equation is rewritten as

$$k(\sin \theta_d - \sin \theta_o) = \frac{2\pi m}{p_x} \quad . \quad (5.10)$$

Since the grating is in the same position as when it was recorded, and the illuminating wavefront is one of the spherical waves used in recording it, one may set, according

to eqs. (4.10) and (4.11), $k \sin \theta_o = k_{x1}$ and $p_x = \frac{2\pi}{\kappa_x} = \frac{2\pi}{k_{x1} + k_{x2}}$. For the $m = -1$ order:

$$k_{xd} = k \sin \theta_d = -\kappa_x + k_{x1} = -k_{x2} \quad , \quad (5.11)$$

i.e. the angle of the back-diffracted ray from source **1** and the specularly-reflected ray from source **2** are equal for all points on the grating.

Similarly, in the \hat{y} direction, for $m = -1$,

$$k_{yd} = -\kappa_y + k_{y1} = k_{y2} \quad . \quad (5.12)$$

Again, the angles are identical.

This straightforward analysis shows that the specularly-reflected and back-diffracted waves co-propagate exactly. Furthermore, if the phase of the grating is advanced or retarded, the phase of the back-diffracted wave will be similarly affected. Therefore, the interferogram seen at the screen, which reflects the difference in phase between reflected and back-diffracted beams, is equivalent to the moiré pattern that arises from a phase difference between the gratings and the standing wave pattern (see Fig. 5.19). The analogy between moiré patterns and holographic interferograms has been shown more rigorously (and is widely used) in the literature [115]-[118].

This analysis assumes a perfectly flat substrate. As shown in the previous chapter, surface topography introduces distortions in the grating's phase progression (deviations from hyperbolic phase), which will result in measurement errors. In order to minimize errors, optically-flat substrates should be used to perform measurements of grating phase progression. It may be possible to remove the deleterious effects of substrate non-flatness by measuring surface topography, and incorporating it into the theoretical model of the apparatus.

The phase-shifting technique is equally applicable to the operation of the IL system as a holographic interferometer. Since the fringes are much brighter, the SNR of the acquired images is significantly improved. As shown by the plot of Fig. 5.20, the

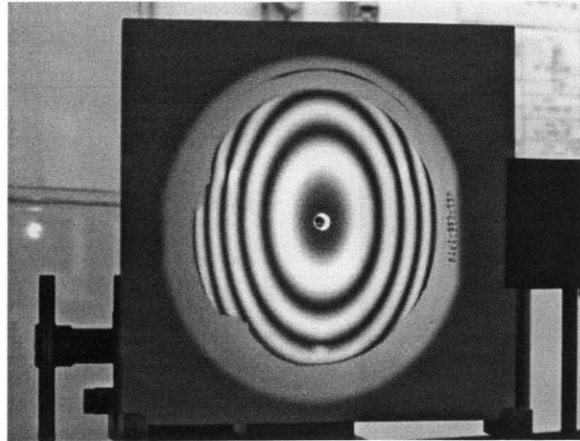


Figure 5.19: Fringes caused by the interference of the 0 and -1 diffracted orders from a laterally-shifted grating.

detectivity of this technique is much superior than that achieved using a fluorescent grating. However, no measurements of grating phase difference were made with this technique, because there were no means to determine the sampling rate, i.e. to determine the coordinates (x', y') of the point on the wafer imaged by each pixel.

The interferometric configuration of the IL system may find many uses in the measurement of in-plane distortion of surfaces. The apparatus has been used recently to measure process-induced distortion in x-ray mask membranes [80, 92].

5.6 Summary

Three techniques to measure the phase progression of hyperbolic gratings by self-comparison have been proposed and implemented. The detectivity of the first technique, the superposition of two grating exposures in resist, has poor resolution, due to lack of sharpness in the moiré fringes. The fringe sharpness could be increased by using a higher dose in the exposures. Even so, quantitative results are difficult to obtain with this technique, since the location of the contours must be measured graphically.

By using a moiré that can be modulated in real time, together with a phase-shifting

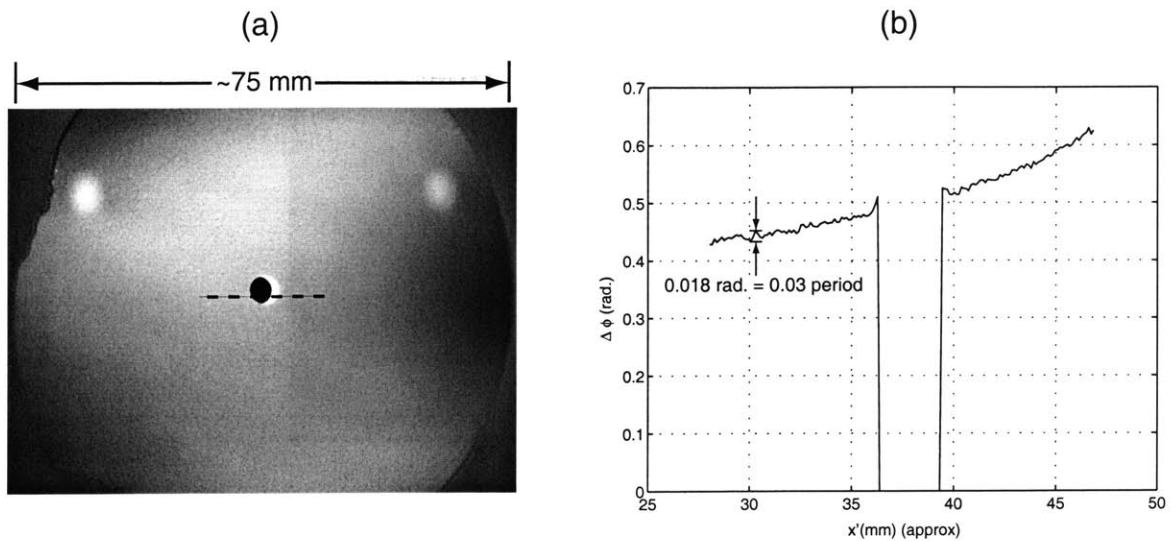


Figure 5.20: (a) Interferogram taken at the null position (b) Plot of phase difference, calculated for the points on the dotted line in (a). The phase was obtained using the phase-shifting technique and the interferometric configuration. The random phase noise amplitude is equivalent to 0.03 periods, or 12 nm. The phase was arbitrarily set to zero at those locations where the fringe modulation was poor, such as the hole on the screen. Note the grating distortion at the points of contact between the wafer and the substrate holder (two bright spots).

implementation, a map of phase difference between a reference grating and the interference fringe pattern can be obtained. Measurements made using this method were in reasonable agreement with theoretically calculated values, but showed large systematic errors, induced by imperfect wafer mounting. (As shown in Chapter 4, the system is very susceptible to wafer mounting errors). The sensitivity of the phase shifting technique can be increased by configuring the IL system as a holographic interferometer, which merely requires the addition of a fluorescent screen to the apparatus. This produces a map of the phase difference between the standing wave and the grating which has reduced phase noise.

Chapter 6

Fabrication of Bragg reflectors with segmented-grid spatial-phase locking

6.1 Introduction

Since 1991, there has been a continuous effort at MIT to develop the technology necessary to fabricate the integrated resonant channel-dropping filter (CDF), as proposed by Haus and Lai [119]. The device, shown in schematic form in Fig. 6.1, is intended to be one of the building blocks in an optical wavelength-division multiplexed (WDM) network [120]-[123].

The principle of operation is described as follows: several independent data streams, which modulate carrier wavelengths $\lambda_1 \dots \lambda_n$, are multiplexed onto a single-mode “bus” waveguide. Quarter-wave shifted (QWS) Bragg resonators are placed on either side of the waveguide. Each one of the resonators consists of a waveguide segment onto which two Bragg gratings have been etched, separated at the center by a 180° phase-shift [124]. The resonators are weakly coupled to the bus by the evanescent fields that extend laterally beyond the bus waveguide (side-coupling).

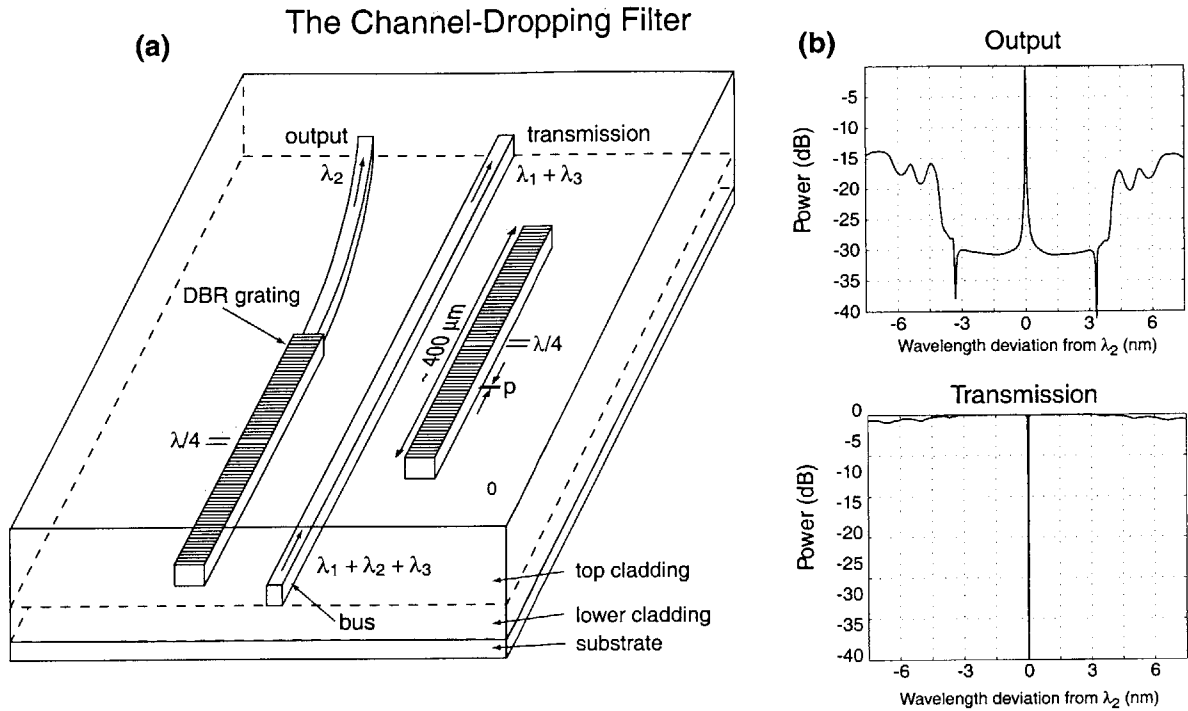


Figure 6.1: (a) Schematic of the integrated resonant channel-dropping filter. (b) Calculated spectral responses at the “output” and “transmission” ports.

The natural frequency of oscillation of both resonators corresponds to one of the wavelengths in the data stream (λ_2 in Fig. 6.1). For this particular wavelength, the optical power is efficiently transferred from the bus into the resonators, and can be tapped off into an output waveguide. Two resonators are needed for full power transfer from the bus to the output port [119]. The other wavelengths do not excite the resonators, and propagate undisturbed within the bus. Thus, one of the channels is selectively “dropped” from the bus. Included in Fig. 6.1 are the calculated spectral responses for the “output” and “transmission” ports, which further clarify the operation of the filter. The device can be operated in reverse to add a channel in to the data stream, although the device’s geometry must be mirrored, so that the added signal will propagate in the correct direction.

The implementation of this class of devices is an ambitious project, which has required significant developments in theory and design methodologies, lithography, etching, and materials growth. The multidisciplinary nature of the project encouraged

the collaboration of three research groups at MIT: the Nanostructures Laboratory (Prof. H.I. Smith), the Quantum Electronics and Femtosecond Optics Group (Prof. H.A. Haus), and the Chemical Beam Epitaxy Group (Prof. L.A. Kolodziejcki). Several people have contributed to the project, in design and modeling (Dr. J.N. Damask, M.J. Khan, T.E. Murphy); fabrication (Dr. V.V. Wong, Dr. J.N. Damask, M.H. Lim, T.E. Murphy, and the author); materials research (E. Koontz, M.H. Lim); device testing and measurement (Dr. J.N. Damask, T.E. Murphy, M.J. Khan).

The work reported here, which is but a small fraction of the total effort, was carried out in order to provide lithographically-defined distributed Bragg reflector (DBR) and QWS gratings that met the specifications required by the device design. Specifically, to prevent cross-talk between channels, one must ensure that the resonators are excited by the intended wavelength only. This implies that the width of their resonant peaks — as a function of wavelength — must be a fraction of the wavelength separation (errors in the channel center wavelength, due to various causes, must be allowed in the design of the system). Also, the location of the filter's resonance must be adequately controlled. These requirements translate into concrete specifications for the lithographically-defined gratings, as described in the following sections.

6.2 Distributed Bragg reflectors and resonators

In the context of integrated optics technology, a Bragg grating is a periodic corrugation, etched into a single-mode waveguide (or in close proximity to it) so that the light within the waveguide interacts with the grating. The grating couples a forward-propagating wave to one propagating in the opposite direction, when the condition

$$p = \frac{\lambda}{2} \tag{6.1}$$

is satisfied. (p is the grating period and λ is the wavelength of the radiation within the waveguide: $\lambda = \frac{2\pi}{\beta}$, where β is the propagation constant.) This condition can

be derived from the grating equation (5.9). Only the $m = \pm 1$ diffraction orders are allowed to propagate¹, while all other orders are cut-off. Thus, the grating acts as a reflector. In an alternative explanation the grating acts as a dielectric-stack mirror: each of the grating corrugations scatters a small fraction of the forward wave (see Fig. 6.2). When $p = \lambda/2$, the scattered waves interfere constructively in the direction opposite to the propagation of the incident wave. If the grating corrugations deviate from perfect periodicity, full constructive interference is no longer achieved, and the magnitude and phase of the backward propagating wave are adversely affected, resulting in sub-optimal grating performance.

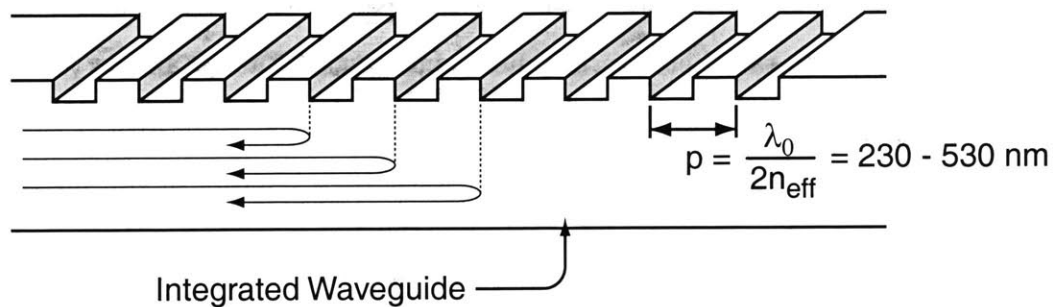


Figure 6.2: Coupling of forward- and backward-propagating waves by means of constructive interference.

The gratings used in the CDF may be thought of as a small periodic perturbation of an otherwise normal waveguide. Therefore to achieve large reflectivities (i.e. to couple most of the forward wave to the backward wave) a large number of corrugations is needed. The coupling between forward and backward waves is expressed in terms of the parameter $\kappa[\text{m}^{-1}]$ [88], referred to as the coupling strength of the grating. The reflection coefficient Γ of a grating of length l operating at the Bragg wavelength is given by [88]

$$\Gamma = \tanh(|\kappa|l) \quad . \quad (6.2)$$

In the regime used in the design of CDF gratings, κ values range from 20 cm^{-1} to

¹Third-order gratings are sometimes used, but higher diffraction efficiency is typically achieved with first-order gratings.

230 cm⁻¹ [125]. To obtain grating reflectivities (given by $|\Gamma|^2$) greater than 99%, $|\kappa|l > 3$. To satisfy this condition, the grating sections must be longer than 1.5 mm ($\kappa = 20$ cm⁻¹), 130 μm ($\kappa = 230$ cm⁻¹). The value of κ depends upon the choice of materials, as well as waveguide and grating geometry, which determine the extent to which the optical mode overlaps with the grating.

If the wavelength is detuned from the Bragg condition, the grating may still couple forward and backward waves, as long as the backward wave is allowed to propagate within the waveguide. Thus, the grating acts as a reflector for a range of wavelengths around the Bragg wavelength, which constitute the *stopband*, if the grating is used as a transmission filter.

A resonant cavity can be constructed by placing two uniform gratings on the waveguide, separated by an odd number of quarter wavelengths. This spacing between the gratings is equivalent to a phase-shift of 180° (recall that the Bragg wavelength is one half of the grating period). The transmission characteristic of this structure has a narrow resonance at the Bragg wavelength. The width of the resonance depends on the reflectivities of the grating reflectors, so that [88]

$$\omega_{1/2} = 4 v_g |\kappa| e^{-2|\kappa|l} \quad (6.3)$$

where $\omega_{1/2}$ is the resonance's full width at half-maximum (as a function of frequency) and v_g is the group velocity $\frac{d\omega}{d\beta}$. Hence, the bandwidth of the resonator depends exponentially on the $|\kappa|l$ product. As a result, very narrow resonances can be achieved with this type of structure.

6.2.1 Techniques to fabricate DBR gratings

Since the grating coupling strength is relatively small, the scattered contributions from a large number of corrugations must interfere in phase. Therefore, the grating must be spatially coherent over its entire length, which can be on the order of millimeters. Bragg gratings for free-space wavelengths of $\lambda \approx 1.55$ μm have periods ranging

from ~ 200 nm to ~ 500 nm, depending on the refractive indices of the media used to construct the device, and on waveguide geometry [125]. The resolution of conventional optical lithography techniques may be adequate for patterning grating pitches on the upper range of this scale, but feature sizes of ~ 100 nm are definitely not possible with current optical lithography. Moreover, the pattern-placement accuracy of conventional lithographic technology, while adequate for integrated circuit fabrication, does not satisfy the long-range coherence requirements of DBR structures.

Interference lithography (IL) is ideally suited to pattern gratings with deep sub- μm pitch and excellent spatial-phase coherence. IL has been used extensively to fabricate narrow-band distributed-feedback (DFB) semiconductor lasers, which rely on uniform gratings patterned on the resonator cavity [82, 83], [126]-[129]. However, fabrication of QWS gratings with this technique is problematic. Such structures have been fabricated by means of IL exposure, by covering part of the substrate with a dielectric layer, to shift the phase of the fringe pattern by 180° [130]; by using a combination of positive and negative resists, the positive resist covering half of the device and the negative covering the other half [131, 132]; by a double-exposure [133]. These techniques have been used successfully in the fabrication of devices, but they offer limited patterning flexibility. Abrupt phase shifts are difficult to obtain, as are multiple quarter-wave shifts. Moreover, alignment of IL exposure to a pre-existing pattern on the substrate is not possible.

High-resolution scanning e -beam lithography (SEBL) has also been used to fabricate QWS gratings [134]-[137]. This technique offers great flexibility — any pattern can be generated on the substrate, so it is possible to implement designs that involve multiple quarter-wave shifts [138, 139], windowed gratings with apodised responses [140, 141], etc. The drawback of the technique, as discussed in the introductory material of Chapter 1, is the relatively poor pattern-placement accuracy, which results in gratings that lack the required spatial-phase coherence.

By combining the spatial-phase coherence of IL with the versatility and resolution of SEBL, the shortcomings of both technologies can be eliminated. The result is

a general-purpose patterning technology for the fabrication of phase-coherent structures. That is the approach followed in the work reported here: a segmented-grid spatial-phase-locked e -beam lithography system was separately implemented on two vector-scan SEBL tools, and utilized to fabricate DBR gratings. The design and implementation of the system are covered in detail in the author's M. S. thesis [56], but will be summarized in the next section. The experiments, fabrication procedures, and device results presented in subsequent sections build upon the segmented-grid method.

6.3 Review of segmented-grid spatial-phase locking

The segmented-grid SPLEBL system was specifically designed to pattern DBR gratings with adequate phase coherence. To accomplish this, it was necessary to reduce the random placement errors of an SEBL tool to a few nanometers. (The pattern placement requirements for DBR gratings were determined using a stochastic model of pattern placement in a segmented-grid system, which is presented in detail in the next section.)

The segmented-grid technique was initially implemented on IBM's VS-6 vector-scan tool [142, 143, 144]. The technique consists of two major elements: a spatially coherent reference grid, fabricated by IL, and the alignment algorithm necessary to align the e -beam writing to the reference (i.e., parallel to the grating's k -vector). For this particular application, pattern-placement accuracy is critical only along the direction perpendicular to the grating's lines, so that the use of a grating reference was sufficient. Pattern-placement errors in the other direction were left uncorrected. The non-linearity of the IL gratings is negligible in this case, because the lengths of the gratings are at most 1 mm.

Waveguide-based devices are long in one dimension (several millimeters), but

quite narrow in the other (on the order of tens of micrometers). Furthermore, they are sparsely laid out: the distance between individual waveguides is usually $50\ \mu\text{m}$ or greater. These characteristics made the implementation of the segmented-grid method quite straightforward; the unused areas between waveguides were allocated to fiducial gratings, which were patterned by IL only in these areas. The process for selectively patterning gratings in the desired areas is described in ref. [56]. Figure 6.3 illustrates the *e*-beam patterning sequence. The sample stage is positioned to expose the first field in the pattern. The distance between fiducial areas is designed so that the deflection field encloses two reference gratings on either side of the area to be patterned. On the other hand, the fiducial gratings must be sufficiently far away from the device waveguide, so that they will not perturb the mode propagating within the waveguide. The center-to-center distance between fiducial gratings was chosen to be $50\ \mu\text{m}$.

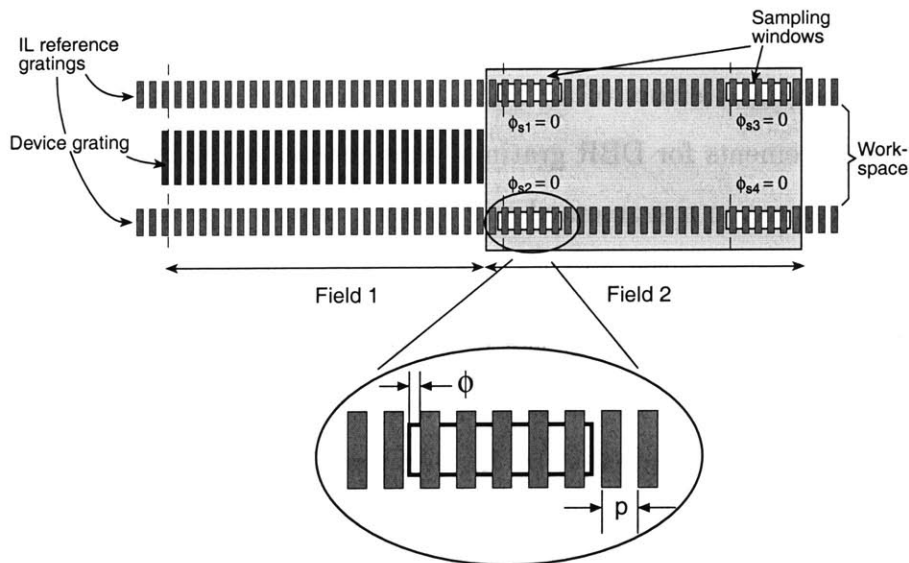


Figure 6.3: Segmented-grid SPLEBL uses IL-generated reference gratings to accurately place each Bragg-grating segment. The reference gratings are imaged within four sampling windows. The relative spatial phase of the grating images is extracted using image-processing techniques. The position of the field with respect to the grating is determined from these data, and fine electronic adjustments are made to “lock” the field to the reference grating.

The alignment procedure was based on the system implemented by Bögli and

Kern [145], where each field is aligned to four registration marks present in the substrate. Images of the marks are acquired by operating the tool as a scanning-electron microscope (i.e., by raster-scanning the beam over the marks), while collecting a signal. The offsets of the marks from their desired locations are computed by performing a cross-correlation between the mark images and a set of templates. The mark offsets are used to compute the field position with respect to the substrate, and electronic correction signals are fed into the beam-deflection subsystem to align the field to the marks. Residual errors in the field's position are usually observed after one alignment iteration, so the procedure is repeated until the field is aligned to the marks. Three or four iterations are sufficient.

The spatial-phase-locking procedure is carried out in a similar fashion [55]. With the stage stationary, the reference gratings are sampled in four areas, called *alignment windows*, to form images. Since the fiducial gratings are separate from the areas to be patterned, they can be sampled at high dose, in order to obtain the highest SNR possible. The resist is exposed in the sampled areas, but the device patterns are not affected. The four fiducial grating images $x_i(n_1, n_2)$ (where $i = 1, 2, 3, 4$ is the image index and $0 \leq n_1, n_2 < 256$ are the column and row indices, respectively — see, for example, Fig. 6.5 (a)) are loaded into image processing hardware to compute the field position of the alignment windows with respect to the spatial phase of the gratings. The computation is done in the frequency domain in order to take advantage of the gratings' periodicity. The two-dimensional DFT, $X_i(\omega_1, \omega_2)$, of each image is computed, and the spatial frequencies with the largest magnitude, corresponding to the fundamental component of the grating, are located in the Fourier plane. Finding the magnitude maxima in the DFT arrays can be computationally intensive if the search space is not restricted. The assumption is made that the gratings are closely aligned to the principal axes of beam deflection, so that the fundamental peaks appear at points $X(\omega_1 = \pm\omega_f, \omega_2 = 0)$ for a grating with vertical lines, or $X(\omega_1 = 0, \omega_2 = \pm\omega_f)$ for a horizontally-oriented grating. To minimize the computation time, the search for the fundamental peaks was restricted to the subspace $X(\omega_1 = 0, \omega_2) + X(\omega_1, \omega_2 = 0)$.

The relative shift of the grating, with respect to reference planes located at $n_1 = 0$ (vertical grating) or $n_2 = 0$ (horizontal grating), is estimated from the phase angle of the two fundamental peaks, according to the delay theorem [98]

$$x[n_1 - m_1, n_2 - m_2] \xleftrightarrow{\mathcal{F}} X(\omega_1, \omega_2) e^{-j\omega_1 m_1} e^{-j\omega_2 m_2} \quad (6.4)$$

where \mathcal{F} denotes Fourier transformation.

The shift of a grating can be accurately estimated in the presence of noise, assuming that noise spectral power is distributed across the frequency domain (as is the case here) because information from a narrow band of frequencies is used in the estimate. Therefore, most of the noise is rejected². The estimated grating shift is used to correct the field position in the same manner as in the mark-based registration procedure. Several iterations (typically four or five) are necessary to obtain optimum alignment. After the field position is locked to the grating, the pattern is exposed. When one field has been aligned and exposed, the stage moves the sample to the next field, and the alignment/exposure procedure is repeated.

During exposure, the beam position is no longer directly referenced to the grating, so the e -beam tool must be stable during the exposure in that field. If the beam's position is disturbed between the time the fiducial gratings are sampled and the time the last feature in the field is exposed, the pattern will no longer be locked to the grating's spatial phase. This is a practical problem with the approach: the e -beam tool must have excellent short-term stability. However, it can be argued that stability on a short time-scale (affected primarily by mechanical vibrations of the sample with respect to the column and electromagnetic interference), is more readily achievable than the elimination of drift due to charging, temperature changes, etc.

To measure the performance of the phase-locking algorithm, the uncertainty in determining the position of the field with respect to the fiducial grating was estimated; the phase of a stationary grating was measured repeatedly to obtain alignment statis-

²A useful analogy is the principle of operation of the lock-in amplifier [146]

tics. The collected statistics showed that the position of the field with respect to the fiducial grating could be measured with an uncertainty $\sigma = 0.3$ nm, when a 200-nm-thick gold grating and a beam current of 100 pA were used [56].

6.4 Automatic measurement of interfield errors

In order to evaluate the quality of *e*-beam-written gratings after fabrication, a method to measure interfield errors was developed. A common way to measure field-to-field alignment is to write vernier marks close to the field boundaries [145]. The alignment of two adjacent fields can then be measured by imaging the vernier marks at high magnification, using a scanning-electron microscope. Alignment of the two fields along the direction parallel to the field boundary can be measured using this method. However, this method cannot be used to measure alignment in the direction perpendicular to the field boundary. In the fabrication of Bragg gratings, the most important parameter is the phase discontinuity across the field boundary, i.e., alignment in the direction perpendicular to the field boundary. The vernier technique was adapted in order to make this measurement possible. The *e*-beam fields were made to overlap, and small grating segments were written on either side of the Bragg grating, as shown in Fig 6.4. These structures, called *outrigger gratings*, are written in such a way that the grating lines which are part of one field are co-linear with the lines corresponding to the other field, if the two fields are tiled together perfectly. An interfield error causes misalignment between the two outrigger gratings.

Gratings of the same period were chosen as measurement structures (instead of the more common vernier structure, where there exists a slight difference in period), because alignment of the two gratings can be very accurately measured by determining their spatial phase.

The measurement is done according to the following procedure: once the *e*-beam pattern has been developed and transferred to the substrate, each pair of outrigger gratings is imaged at high magnification. This can be done with an SEM, but beam

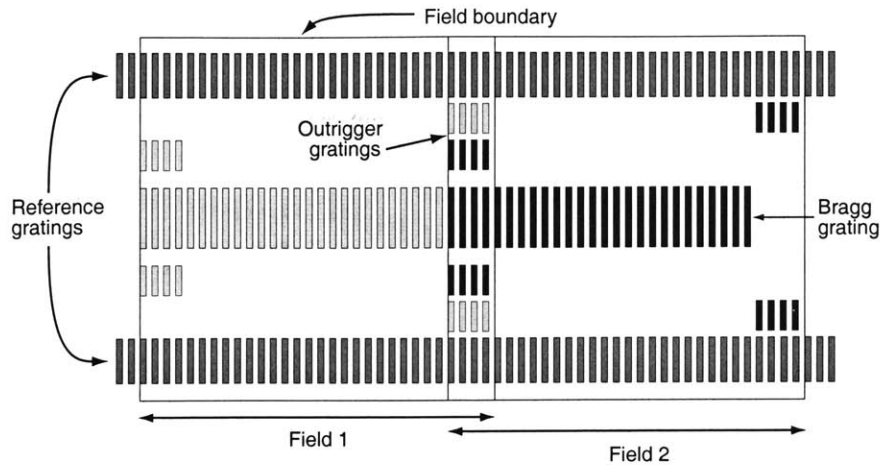


Figure 6.4: “Outrigger gratings” are used to measure the stitching errors between fields. The fields are made to overlap, and outrigger grating patterns are exposed within each field, so that the two gratings are colinear if there is no misalignment between adjacent fields. In this illustration, the light patterns were exposed within the field on the left, while the darker ones belong to the field on the right.

deflection in such an instrument is not as well calibrated as in an SEBL system. For this reason, the measurements were performed with the SEBL tool. An image of the outrigger structure was collected into an array of 512×512 pixels. Figure 6.5 (a) shows an example. The image processing hardware used for mark registration was configured with an algorithm specifically designed to perform the measurement. The spatial phase of the grating’s fundamental component was calculated for each row of the array, by computing the (1-D) DFT (see Fig. 6.5 (b)). If the calculated spatial phase is plotted as a function of row number, one obtains two nearly straight lines, with added measurement noise, corresponding to the two gratings in the outrigger. The phase in the gap between the lines is undefined, since no grating exists there. If the grating lines are rotated with respect to the axis of the raster scan used to acquire the image, the phase will change linearly as a function of vertical position (row number). Misalignment of the two outrigger gratings will result in a phase step.

In previous work [55, 56], the phase step had been estimated graphically, by plotting the phase as a function of row number on a piece of paper, and drawing two straight lines through the data. The phase step was estimated by measuring the

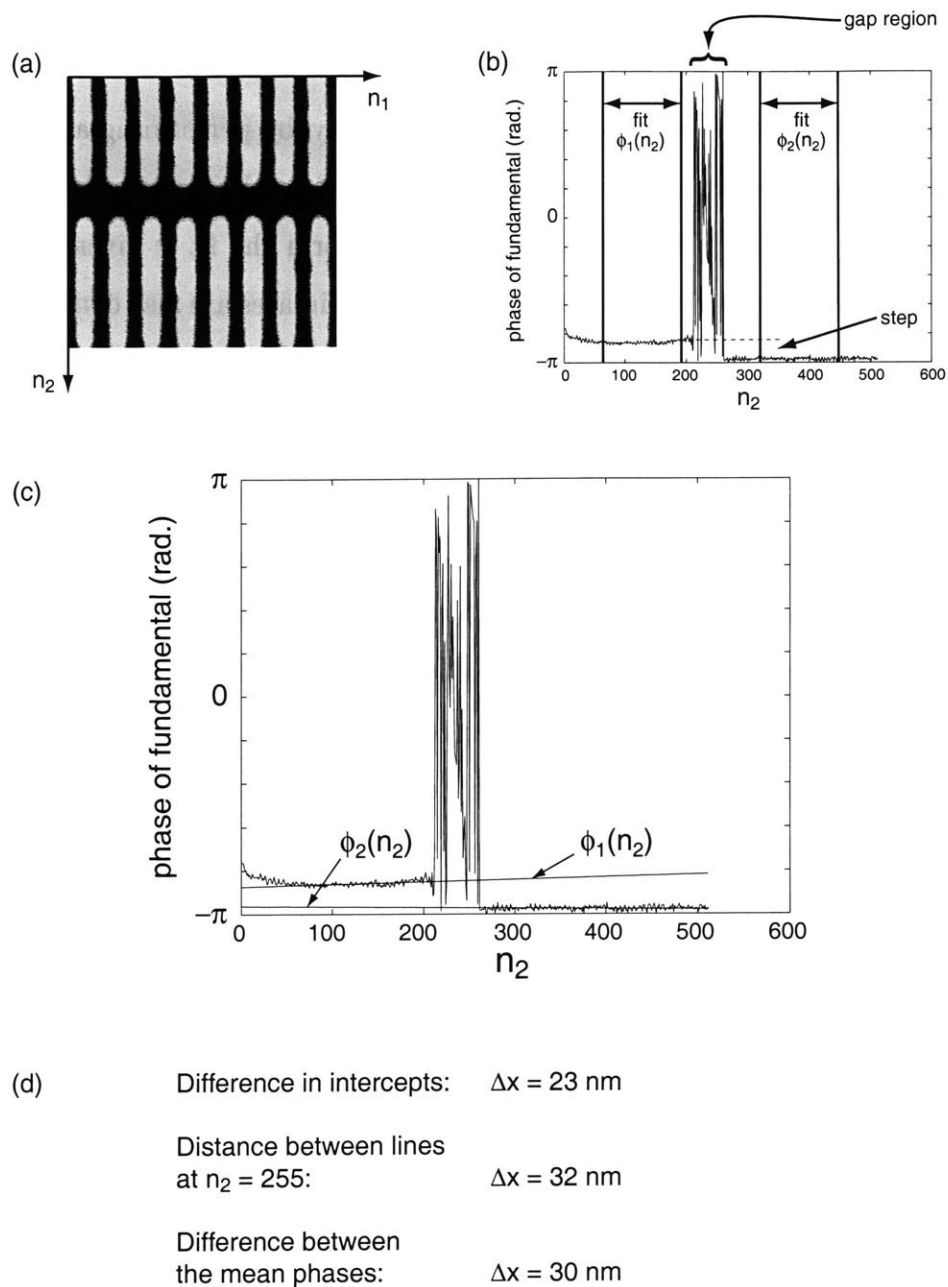


Figure 6.5: (a) High-magnification image of an outrigger-grating structure, obtained with the SEBL system. (b) Spatial phase of the fundamental, computed for each row. Two straight lines $\phi_1(n_2) = m_1 n_2 + b_1$, $\phi_2(n_2) = m_2 n_2 + b_2$ were least-squares fitted to the data in the regions indicated. (c) Overlay of the fitted straight lines on the data. Note the different slopes. (d) Different estimates of the alignment error.

distance between the lines with a ruler. In this form, the procedure is unreliable and time consuming, so that it is not feasible to accurately measure all interfield errors in a large pattern.

The same procedure was implemented numerically, by performing a least-squares fit of each grating's phase data to a straight line, to obtain the slope and zero intercept of the best-fitting line. The algorithm used to perform the fit is given in ref. [147]. The standard deviations of the slope and intercept estimates are also computed, which allow one to evaluate the quality and statistical significance of the fit.

If the slopes of the two lines are identical, the phase step (and hence the misalignment of the two gratings) is given by the difference between the line intercepts. If the two slopes are different, it is somewhat unclear how to specify the degree of misalignment between the two gratings. The example of Fig. 6.5 was chosen, because the slopes of the two fitted lines are different, due to a defective top outrigger grating. In this case, there are several possibilities; one can estimate misalignment from the difference in intercepts, from the distance between the lines at the image midpoint ($n_2 = 255$), or from difference between the average phases. These three estimates are given in Fig. 6.5 (d).

However, if the slopes of the two lines are equal to four significant figures, the ambiguity is negligible, and the intercept difference is a good estimate of misalignment. This was found to be the case when interfield measurements of Bragg grating patterns were performed.

Let $\Delta\phi$ be the difference in intercepts. Misalignment of the two outrigger gratings is then given simply by

$$\Delta x = -\frac{\Delta\phi}{2\pi} \cdot p \quad (6.5)$$

where p is the grating period.

The example of Fig. 6.5 shows another potential problem. The spatial phases of the two gratings are close to $-\pi$. If the phase data cross the $\pm\pi$ boundaries, the

ambiguity of the phase function will render the data meaningless. It is possible to unwrap the phase (see the previous chapter), but since the expected phase steps are significantly less than one period, it is only necessary to ensure that all phase data are close to zero. This was accomplished by positioning the raster scan so that the phase data would be centered within the $\pm\pi$ boundaries.

The phase measurement was implemented as an automatic procedure. The control computer reads the outrigger grating positions from a file. For each measurement, it directs the stage to move to the appropriate location on the substrate; the raster scan is prealigned to the gratings by acquiring an image, computing the average grating phase, and shifting the *e*-beam field to center the phase data around $\phi = 0$; an image is acquired and two straight lines are fitted to the phase data. The slopes and intercepts of the best-fit lines are then written to an output file, to be processed off-line.

To evaluate the performance of the phase-measuring algorithm, a sample with a known phase discontinuity, namely an IL-fabricated grating with $\Delta\phi = 0$, was measured [148]. In order to collect statistics, the procedure was repeated several times on the same area of the sample. The measurement was found to have an uncertainty $\sigma_{\text{meas}} = 3.8$ nm (see Fig. 6.6). This number agreed well with the confidence intervals returned by the least-squares fitting algorithm, which predicted uncertainties between 3 and 5 nm.

6.5 Analysis of interfield error requirements

Although the requirement that a Bragg grating be coherent over its whole length is immediately apparent, quantitative error tolerances should be determined when fabrication of an actual device is contemplated. In a practical situation, pattern placement errors cannot be altogether avoided, and it would be unreasonable to request that they be eliminated completely. In order to make the fabrication process as straightforward and reliable as possible, error tolerances should be forgiving, while

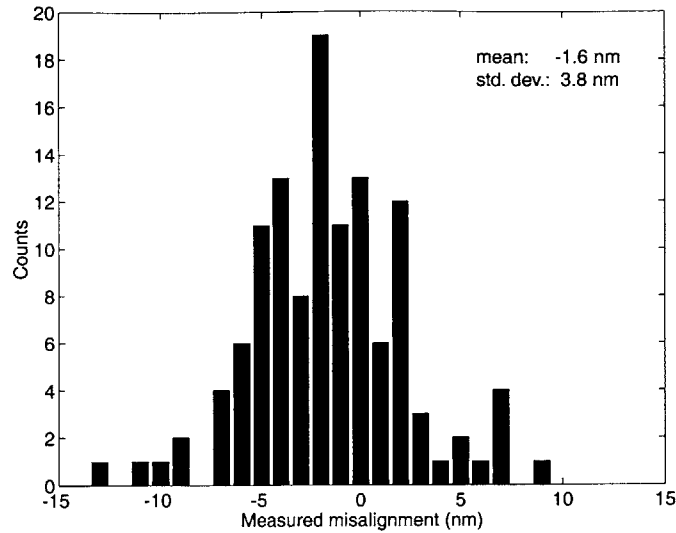


Figure 6.6: Error statistics of outrigger measurement procedure. The calibration sample used was a 400-nm-period gold grating. The actual misalignment between the lines was, by definition, zero.

at the same time ensuring that a working device will result.

A model was developed in order to evaluate the effect of grating phase errors on the performance of QWS resonators [125, 149, 150]. It was necessary to ascertain how fabrication-induced phase errors would affect device performance, i.e., what parameters would be significantly affected. Desirable device operation could then be specified in terms of these parameters, and fabrication tolerances could be determined. To develop the model, several assumptions were made:

1. Segmented-grid spatial-phase locking would be used to generate grating patterns.
2. Intrafield distortion (see Chapter 1) is deterministic, and can be eliminated for all practical purposes by calibrating beam deflection against an IL-generated reference grid. It was determined that by keeping the field size smaller than 200 μm , electron-optical distortion did not introduce significant errors. Therefore, only the deflection electronics need to be calibrated to eliminate the intrafield distortion.

3. The DBR gratings span several e -beam fields, which have to be tiled together.
4. Interfield distortion (stitching errors) is the most significant contribution to pattern-placement errors.

These assumptions led to the model shown schematically in Fig. 6.7 (a). The grating was taken to be composed of distortion-free segments (corresponding to the tiled fields). Interfield errors introduce random offsets to the position of each field. The resonator parameters most affected by grating phase errors were found to be the location of the resonance within the stopband, and its width, as shown in Fig. 6.7 (b). The resonator response can be calculated by computing the reflection coefficient Γ of each grating, at a reference plane located in the middle of the quarter-wave section. Since Γ is a complex number, it can be written as

$$\Gamma = |\Gamma| \exp(j\angle\Gamma) \quad (6.6)$$

Given a known set of values x_i , the displacements of grating segments from their intended locations, a method was developed by J.N. Damask to calculate the magnitude and phase of the reflection coefficient [151].

The displacements x_i were then treated as random variables. They were assigned Gaussian probability density functions, with zero mean and a given standard deviation. A Monte-Carlo simulator was then implemented to evaluate the sensitivity of the magnitude and phase of Γ to random field-placement errors. Many gratings were constructed with randomly-placed grating segments, and the reflection coefficient was computed for each grating. The parameters used to construct gratings were the κl product, the grating period p and the standard deviation of field-placement errors σ_x . Fig. 6.8 shows the resulting Γ -distribution for a simulation of 2000 gratings consisting of 3 grating segments, with $\kappa l = 1.2$, $p = 240$ nm and $\sigma_x = 20$ nm. This figure is for illustrative purposes only. A small value has been chosen for κl , in order to show the effects of phase errors on the magnitude and phase of the reflection coefficient more clearly. The effects are less pronounced for higher values of κl .

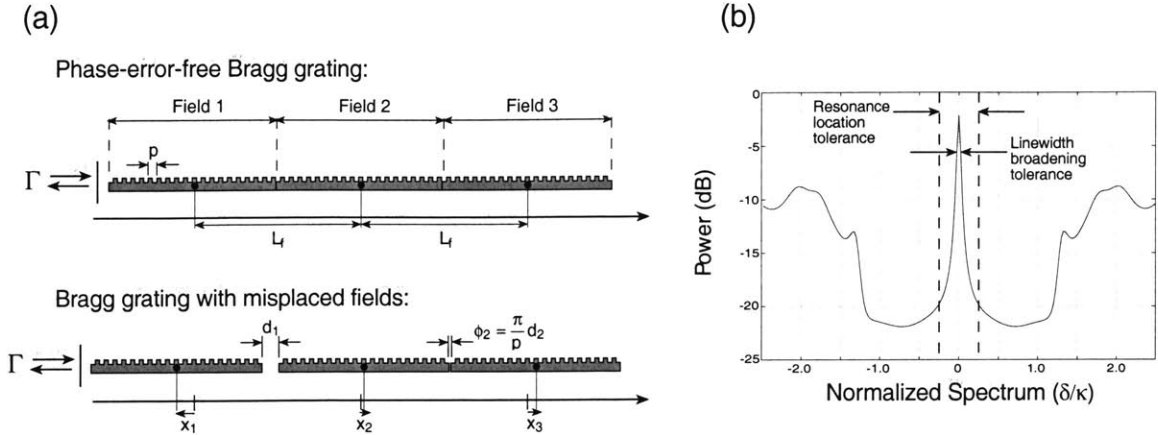


Figure 6.7: (a) Model of phase errors in a Bragg grating. The grating is composed of distortion-free segments, which are tiled together. The top grating has no stitching errors, while the grating segments of the bottom grating have unwanted placement errors, x_i . (b) Resonator-response parameters affected by grating phase errors: resonance location and linewidth. Acceptable resonator performance was specified in terms of these parameters.

In the absence of interfield errors, the reflection coefficient would be given by $\Gamma_0 = \tanh(\kappa l)$, which is a real number. Random segment positions result in a random distribution of the magnitude and phase of Γ . The phase distribution $\angle\Gamma$ was Gaussian-like, with zero-mean. The distribution of $|\Gamma|$ shows a small deviation from Γ_0 , the deterministic value.

When a resonator is constructed with two gratings having reflection coefficients Γ_1 and Γ_2 , which are now considered to be random variables, the frequency response is affected in two fundamental ways: first, the non-zero phase of Γ causes an offset in the resonance location, according to [125]

$$\frac{\delta}{\kappa} = \sin\left(\frac{\angle\Gamma_1 + \angle\Gamma_2}{2}\right) \quad (6.7)$$

where δ is a normalized frequency offset: $\delta = \frac{\omega - \omega_0}{v_g}$ and ω_0 is the angular frequency corresponding to the Bragg wavelength. Second, the reduced magnitudes of the re-

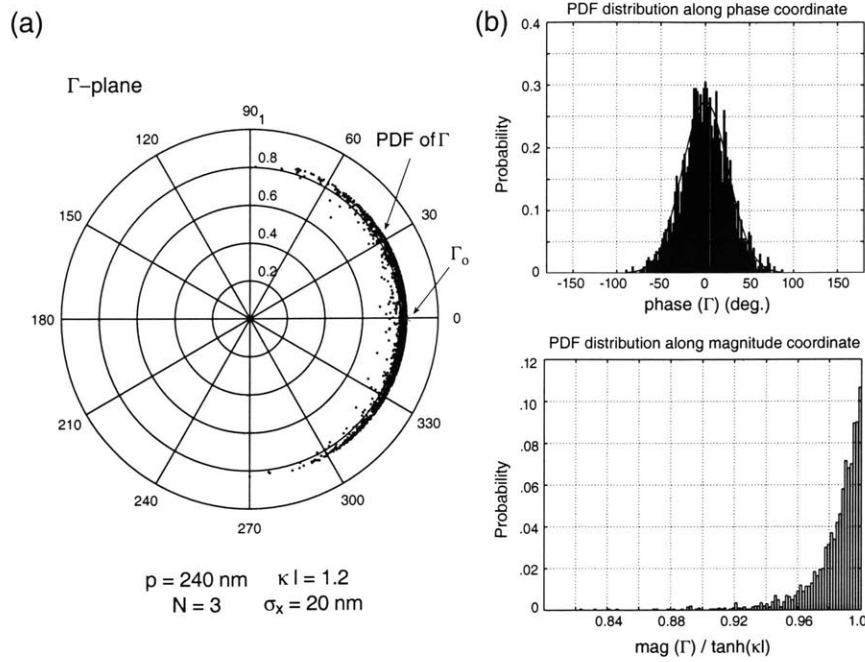


Figure 6.8: The probability density function (PDF) for the reflection coefficient Γ of a Bragg grating was estimated with a Monte-Carlo simulation. (a) Results plotted in the Γ -plane. (b) Projections onto the phase and magnitude coordinates. From ref. [125].

reflection coefficient affect the finesse (Q) of the cavity, according to [125]

$$\frac{1}{Q} = \frac{\kappa \lambda_0}{\pi n_g} [\exp(-2 \tanh^{-1} |\Gamma_1|) + \exp(-2 \tanh^{-1} |\Gamma_2|)] \quad (6.8)$$

where n_g is the group refractive index and λ_0 is the resonant wavelength.

Thus, resonator performance was specified in terms of maximum allowable resonance offset and linewidth broadening. The model described above was used to estimate the fabrication yield (the probability of fabricating an acceptable resonator) given bounds for linewidth broadening and resonance offset. Figure 6.9 shows two contour plots of the probability of writing an acceptable resonator for two typical grating periods $p = 240, 510$ nm, given the specifications

$$\frac{\omega_{1/2\text{-actual}}}{\omega_{1/2\text{-design}}} < 1.1 \quad \text{and} \quad \frac{|\omega_0\text{-actual} - \omega_0\text{-design}|}{\kappa v_g} < 0.25 \quad .$$

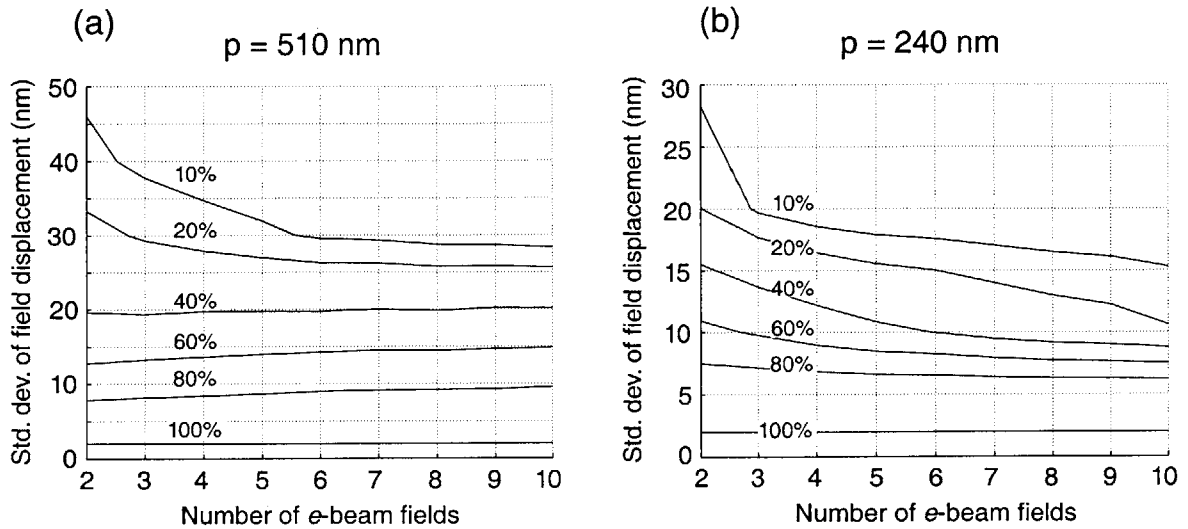


Figure 6.9: Contour plots of the probability of writing an acceptable grating resonator for two representative periods $p = 510$ nm (a) and $p = 240$ nm (b). In both plots, the value of κ is decreased at the grating length is increased, to keep the $\kappa l = 2.4$ product constant. The plots were obtained for a maximum linewidth broadening of 10% and an offset in the resonance location no larger than $\pm 25\%$ of the stopband width. From ref. [125].

The contours are plotted as functions of the grating length (abscissa) and the standard deviation of field-displacement errors (ordinate). The length of the gratings was varied, while the κl product was kept constant (grating length is expressed as the number of fields required to write it).

Under these conditions, the standard deviation of e-beam field displacement is required to be under 10 nm to obtain acceptable yields. As will be shown in subsequent sections, this requirement was met by using segmented-grid SPLEBL.

6.6 Fabrication of DBR-based transmission reflectors and resonators

As a first step in developing and evaluating fabrication methods appropriate for grating-based integrated optics, a set of uniform Bragg-grating reflectors and QWS resonators were fabricated by V.V. Wong, J.N. Damask and the author [125, 139, 152].

The waveguides were fabricated in a $\text{SiO}_2/\text{Si}_3\text{N}_4$ materials system, using a strip-loaded waveguide geometry, shown in Fig. 6.10.

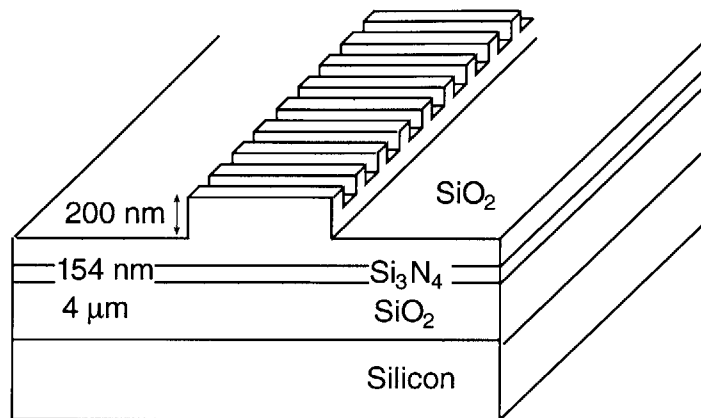


Figure 6.10: Illustration of the strip-loaded rib waveguide geometry used for the silica/silicon nitride grating devices.

Two lithographic steps were used to fabricate these devices (see Fig. 6.11). The first to define the waveguide ribs and the second to pattern the Bragg gratings on the waveguides. A “mix-and-match” strategy was adopted — two types of lithography were used to accomplish the goal. The ribs were $2\mu\text{m}$ wide and $\sim 3\text{mm}$ long; they were straightforwardly printed using optical lithography. The Bragg gratings, with feature sizes of $\sim 0.25\mu\text{m}$, required a higher-resolution patterning technique; x-ray lithography was chosen for this step.

The optical mask was made by an outside vendor. It was used in an optical stepper at MIT’s Integrated Circuits Laboratory to print the rib patterns. The x-ray mask was considerably more difficult to make. The process used in fabricating it will now be described.

6.6.1 Bragg-grating pattern generation

The grating patterns were generated on the x-ray mask using segmented-grid SPL-EBL. The first step in fabricating the mask was to pattern the fiducial gratings. An x-ray mask blank was coated with a plating base, consisting of a 5-nm-thick

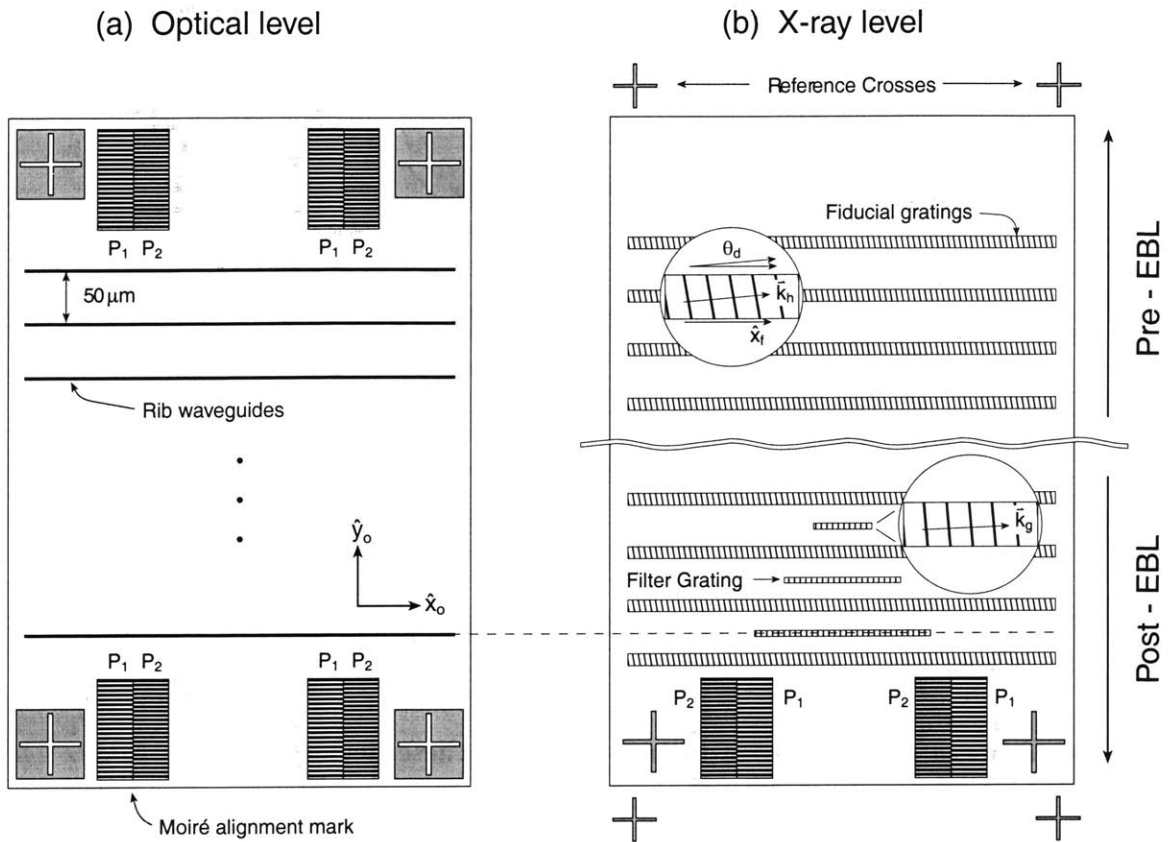


Figure 6.11: Schematic diagram of the optical and x-ray mask levels used in the fabrication of the devices. The upper part of the x-ray mask shows its aspect before the EBL is performed. Only the fiducial marks (reference crosses) and the IL gratings are present. The lower part of the same mask includes the *e*-beam-written Bragg gratings and alignment marks, which are the complement of the marks present on the optical mask.

layer of NiCr and a 20-nm-thick layer of Au, which were deposited by evaporation. An ARC/photoresist film stack (see Appendix A) was then applied. The IL optics were aligned in order to obtain a nominal period $p = 511$ nm, which is the same as the period specified for the Bragg gratings. The fiducial gratings were assigned the same period to simplify the implementation of the SPLEBL system. The segmented gratings were created on the mask by the process shown in Fig. 6.12 [76, 56, 139].

A grating pattern was exposed in the resist with the IL system. Before developing the resist, the fiducial grating segments were defined with a second exposure under a UV ($\lambda = 440$ nm) lamp, using an optical mask. In the areas where the second

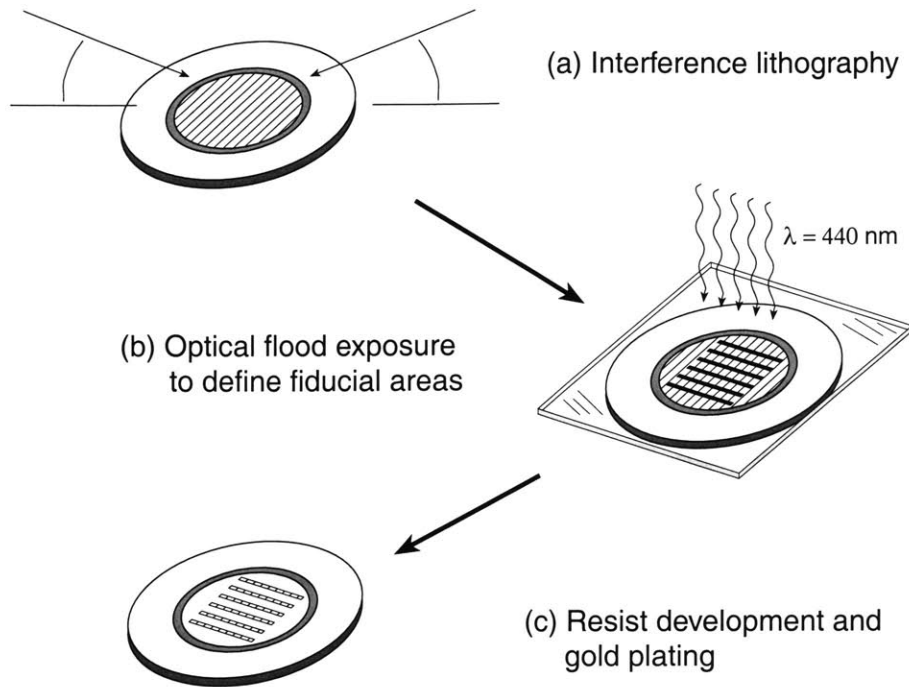


Figure 6.12: Schematic depiction of the process used to generate segmented fiducial gratings on an x-ray mask.

exposure was blocked by the mask absorbers, a grating remained after development. The areas that were “flooded” by the second exposure developed out completely. These areas remained unpatterned and available for *e*-beam lithography. The fiducial gratings were electroplated with gold [153], the resist and ARC were stripped, and the mask was coated with a layer of PMMA. The device grating patterns were *e*-beam exposed, with the holographic gratings acting as a SPLEBL reference. The gratings were exposed in 128-period segments (there were 128 periods in each *e*-beam field). As mentioned above, the period of the *e*-beam-written gratings was chosen to match the period of the IL fiducial gratings — 511 nm. The vector-scan machine has a bit-addressable deflection field of 16384×16384 pixels ($2^{14} \times 2^{14}$). The pixel size can be adjusted by dilating or contracting the field size. The field size can be calibrated to within 1 part in 10^4 of the desired value by using the interferometer-controlled stage as the reference in fine-tuning the beam deflection [56]. To accurately obtain the desired period, the field size must be set so that one period is equivalent to an integer number of pixels.

The field size was set so that each field contained 256 grating periods. Equivalently, a grating period consisted of a line and a space, each being 64 pixels wide. Of the 256 available periods, only 128 were exposed, because to write the outrigger gratings the fields were required to overlap (see Fig. 6.4). To match the period of the *e*-beam grating to the IL fiducials, the sampling windows were set apart by 8192 pixels (128 periods). If the field size is exactly matched to the fiducial's period, 8192 pixels should encompass an integer number of periods, and the phases of the four grating samples should be equal. The field size was initially calibrated to $511 \text{ nm/period} \cdot 256 \text{ periods} = 130.816 \pm 0.005 \text{ } \mu\text{m}$. Upon sampling the fiducial gratings, it immediately became apparent that the actual period of the gratings on the mask was larger than the requested 511 nm. The phases measured at the sampling windows indicated that the period of the grating was $513.3 \pm 0.1 \text{ nm}$. This was confirmed by recalibrating the field size to $131.41 \text{ } \mu\text{m}$; the measured phases at the sampling windows were then very nearly equal. The period error is due to the uncertainty in setting the interference angle (see section 2.4). The error was deemed to be small enough that it would not adversely affect the performance of the Bragg gratings (the only effect would be to change the resonance location). The device gratings were reassigned a nominal period of 513.3 nm. Two additional periods, differing slightly from 513.3 nm, were also exposed, taking advantage of the 2π phase ambiguity of the reference grating. Without modifying the spatial-phase locking software, the field size was adjusted to $130.38 \text{ } \mu\text{m}$ and $132.44 \text{ } \mu\text{m}$, so that there were 127 and 129 fiducial-grating periods between the sampling windows, yielding periods of 509.3 nm and 517.3 nm, respectively.

After writing the gratings, alignment marks, designed to overlay with those on the optical mask, were patterned. Figure 6.11 (b) shows the appearance of the x-ray mask before and after the *e*-beam step. After exposure, the resist was developed, and the patterns were gold plated.

6.6.2 Alignment issues

Optical projection lithography was used to expose the rib waveguides on the substrate. The fiducial gratings were patterned by a combination of IL and proximity optical lithography. The locations of the e -beam generated gratings on the x-ray mask were determined by the e -beam tool's interferometrically-controlled stage. When substrates are mounted on a sample holder and loaded into the e -beam machine, the angle between the substrate's coordinate system — established by pre-existing patterns, with which the e -beam exposure must overlay — and the e -beam coordinate system must be determined. This is accomplished by measuring the positions of fiducial marks (referred to as reference crosses in Fig. 6.11) on the substrate, and transforming the coordinates of the interferometric stage to the sample, by means of a rotation matrix. To ensure that the segmented grid would be sampled in the appropriate locations, i.e, where there are fiducial gratings, the fiducial marks were patterned with the same mask used to define the fiducial grating areas. The Bragg gratings were exposed in the coordinate system defined by these fiducial marks.

Rotational alignment between the Bragg grating and the waveguide lithographic levels is necessary to avoid having the grating walk off from the rib waveguide. Moreover, referring to Fig. 6.11, it is necessary that the \bar{k} -vector of the Bragg grating \bar{k}_g be parallel to the axis of the waveguide \hat{x}_0 . An angular error θ_r between the two axes changes the Bragg wavelength from λ_0 to $\lambda_0/\cos\theta_r$, thus detuning the wavelength from its spectral location [154]. Severe angular misalignment ($> 2^\circ$) causes deguidance of the bound optical mode, resulting in waveguide loss [155]. In order to minimize θ_r , it is first necessary to minimize the angular error θ_d between the \bar{k} -vector of the holographic grating and the axis of the optical mask used to define the fiducial areas, \hat{x}_f . A “flat” on the edge of the x-ray mask frame was used as the angular alignment reference between the IL gratings and the fiducial-area definition mask. Using this indirect reference, θ_d could be reduced to less than 1° , which was sufficient to prevent significant changes in the Bragg wavelength due to cosine errors, but it is speculated that the remaining rotational error affected the accuracy of the

spatial-phase locking step, as will be described below.

Upon transferring the Bragg-grating patterns onto the substrate via x-ray lithography, it was found that the two lithographic levels did not overlay correctly, so that some of the gratings were not aligned to their corresponding rib waveguides. The overlay errors were patently due to a scale mismatch between the optical waveguide mask and the x-ray grating mask (overlay problems are common in “mix-and-match” lithography schemes [156, 157]). In this case, the most likely factor was lack of calibration between the optical stepper used to pattern the ribs and the EBL machine used to make the x-ray mask. An aggravating factor may have been x-ray mask distortion induced by absorber stress [158, 159]. Since stress in the gold absorbers was not controlled during the two electroplating steps used in producing the finished x-ray mask, additional distortion may have been caused.

During the first design phase, the grating patterns were specified to be $0.2\ \mu\text{m}$ wider than the waveguides (which were $2\ \mu\text{m}$ wide). They were to be directly aligned to the waveguide level, using highly sensitive moiré alignment marks [160]. When overlay problems were encountered, a self-alignment method was incorporated into the fabrication process, and the grating mask was redesigned, making the Bragg-grating patterns $5\ \mu\text{m}$ wide [152, 161].

Micrographs of one finished x-ray mask (with $2\text{-}\mu\text{m}$ -wide gratings) are shown in Figs. 6.13 and 6.14

6.6.3 Measured interfield errors

Figure 6.15 displays statistics for field alignment during SPLEBL. In this plot, each datum is the misalignment perceived by the phase-locking routine after the last alignment iteration (recall that 5 iterations of the alignment procedure were performed before exposing each field). The mean misalignment is 0.9 nm and the standard deviation is 0.3 nm. After the grating patterns had been Au-electroplated, the actual interfield errors were obtained by measuring the mismatch in the outrigger gratings,

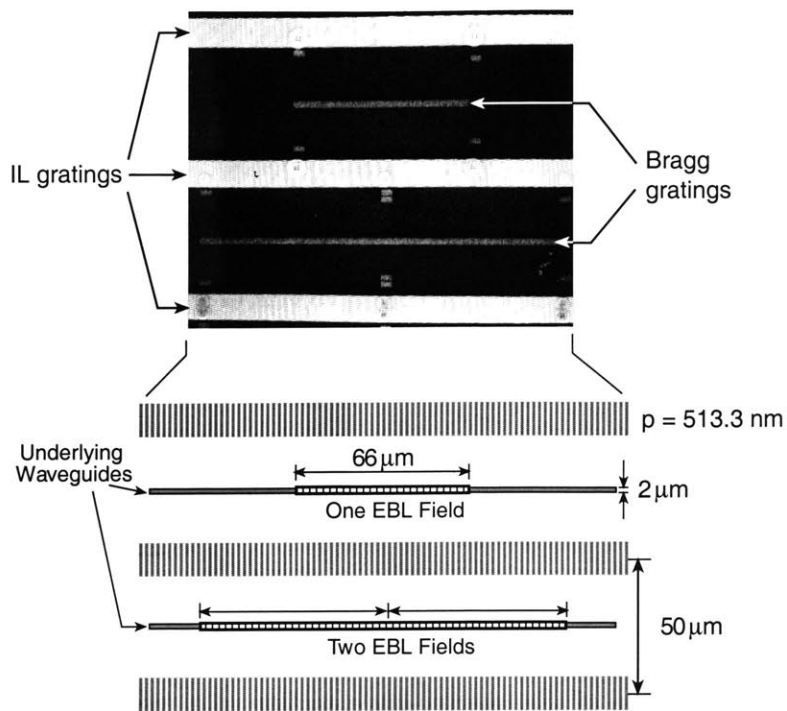


Figure 6.13: Scanning-electron micrograph of two uniform Bragg grating patterns on a finished mask. Note the outrigger structures, used to measure field-placement errors.

according to the method described in Section 6.4. The results are plotted in Fig. 6.16. The interfield errors have a mean of 32 nm and a standard deviation of 13 nm. The origin of the additional pattern-placement errors has not been unequivocally identified, but several potential contributors were identified. These are:

1. Precise alignment, via phase-locking, was performed in one direction (\hat{x}) only. Errors along the perpendicular direction (\hat{y}) were left uncorrected. Ideally, alignment in \hat{x} should be independent of alignment in \hat{y} , since the two directions are orthogonal. Unfortunately, this condition could not be satisfied, due to small angular errors between the grating lines and the waveguide axes. It was necessary to ensure that the Bragg-grating patterns would overlay with the waveguides. At the same time, the phase-locking routine aligned the y -axis of beam deflection with the grating lines. Consequently, the two deflection axes deviated from orthogonality by the degree to which the waveguide axis was

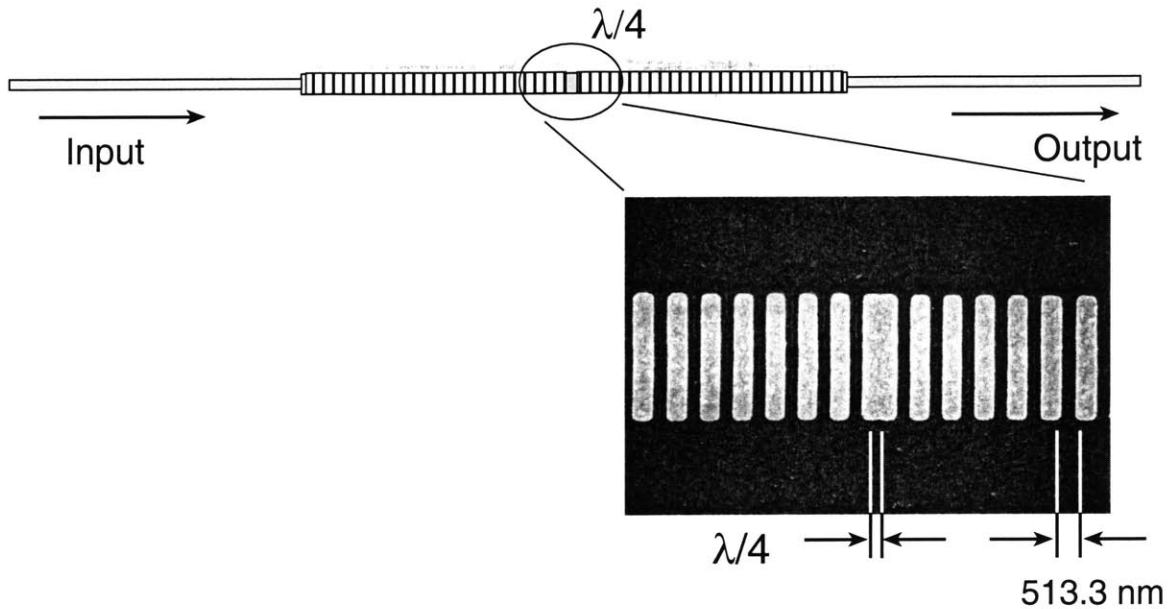


Figure 6.14: Close-up of the quarter-wave section of a resonator grating on the same mask.

originally misaligned to the direction perpendicular to the grating lines, in this case a 0.9 mrad. error (see Fig. 6.17).

2. The stage of the VS-6 tool introduced random rotations to each field. The stage is designed to minimize sample movement with respect to the electron optics while each field is being written [144, 143]. To this end, the sample holder is clamped to the final lens, so that the two elements are held together rigidly and no relative movement occurs. This is accomplished by elevating the sample holder with piezoelectric actuators until four struts touch the plate onto which the lens is attached. Once a field has been written, the sample holder is lowered, and the stage can move to the next field. Up/down motion of the piezos causes the sample holder to rotate slightly, in a random fashion. It is probable that these random rotations adversely affected field placement.

No further experiments to determine the causes of alignment errors on the VS-6 system were performed. At that time, IBM donated a vector scan tool (VS-2A) to MIT's Nanostructures Laboratory. All efforts were directed towards installing the tool

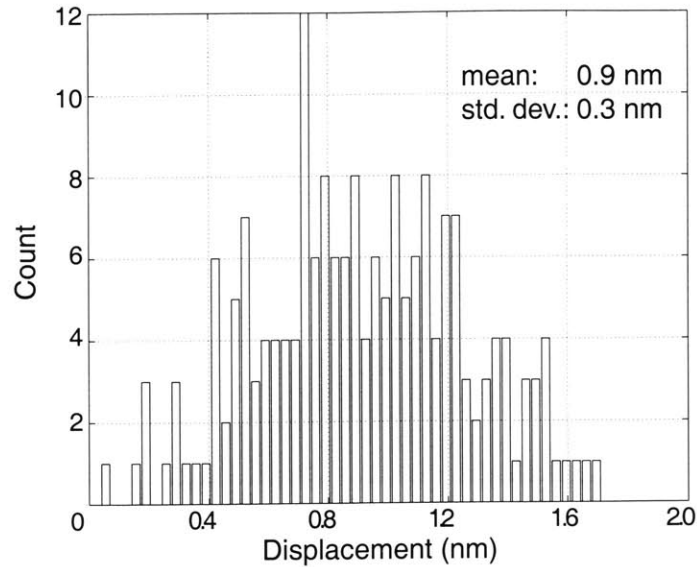


Figure 6.15: Distribution of a representative subset of interfield errors on the Bragg-grating mask, as measured between the e -beam deflection field and the fiducial reference prior to writing the grating segments.

and bringing it into operation. As a result of this work (done by S. Silverman, M. K. Mondol, and the author), e -beam lithography is now available in-house. Segmented-grid SPLEBL was also implemented on VS-2A, as will be reported in the next chapter.

The statistics shown in Fig. 6.16 represent a somewhat pessimistic estimate of field placement, which is the relevant parameter used in the model summarized in Section 6.5. The data in Fig. 6.16 are measurements of interfield errors, which are in effect the difference between the position of two adjacent fields. Furthermore, the uncertainty of the outrigger measurement is also included. Assuming that the random errors introduced by the outrigger measurement are uncorrelated to the interfield data, the uncertainty of the measurement can be deconvolved from the data (making use of the fact that the variance of the addition of two random variables is equal to the sum of the individual variances, if the two random variables are uncorrelated). Removing the measurement uncertainty $\sigma_m = 3.9$ nm, one obtains $\bar{d}_{\text{interfield}} = 32$ nm, $\sigma_d = 12.4$ nm. Assuming that the position of each field is uncorrelated to the others, and all field positions are described by the same probability density function, the field-placement

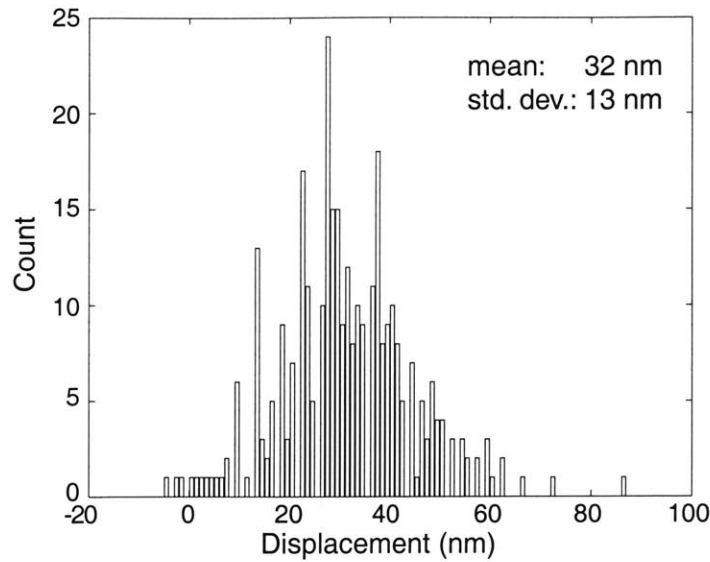


Figure 6.16: Distribution interfield errors as measured on the Bragg grating mask.

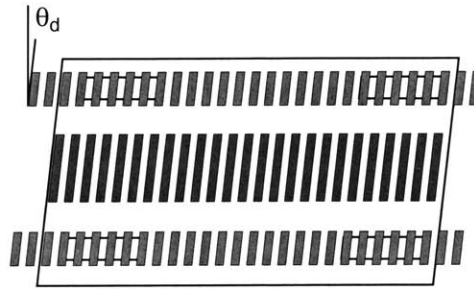


Figure 6.17: Effect of grating angular error on the orthogonality of beam-deflection axes. θ_d is defined in Fig. 6.11.

uncertainty σ_x is found to be

$$\sigma_x = \frac{\sigma_d}{\sqrt{2}} = 8.7 \text{ nm}$$

The mean \bar{x} cannot be derived from statistics for d . The assumption that field positions are uncorrelated may or may not be justified. Justification for this argument can only be supplied experimentally, so the estimate $\sigma_x = 8.7 \text{ nm}$ may be overly optimistic. However, the Monte-Carlo simulation in Section 6.5 *does* assume uncorrelated field placement. Contours of acceptable resonator performance are plotted as a

function of field placement uncertainty σ_x . To read the contour plots in Fig. 6.9 as a function of interfield-error standard deviation σ_d , it is valid to multiply the ordinate axis by $\sqrt{2}$. The performance of the fabricated devices, which is reported in the next section, provided some evidence that the field-placement errors were smaller than the data of Fig. 6.16 would lead one to believe.

6.6.4 Device fabrication process

Fabrication with the self-aligned process proceeded as follows: the rib waveguides were patterned in photoresist with the optical projection stepper. Next, the SiO₂ top cladding layer was reactive-ion etched with CHF₃ to the target etch depth of 220 nm, using the photoresist to mask the etch. A 50-nm-thick layer of chromium was evaporated at normal incidence, without having removed the photoresist. The chromium was then lifted off by dissolving the resist, so that the whole substrate was protected by the chromium layer, with the exception of the top faces of the waveguides (this constituted the self-alignment step). The substrate surface was primed with hexamethyl disilazane, an adhesion promoter (see Appendix B), and spin-coated with a layer of ESCAP³, which was the resist used for x-ray exposure (ESCAP is significantly more sensitive to x-ray exposure than PMMA, although its resolution is limited to $\sim 0.2 \mu\text{m}$). After exposing the Bragg-grating patterns and developing the resist, the gratings were etched into the waveguides (the only unprotected areas) by RIE in CHF₃ (target depth: 118 nm). Finally, the resist and Cr layers were removed. Figure 6.18 shows a grating etched onto a waveguide by the self-aligned process.

³Manufactured by IBM.

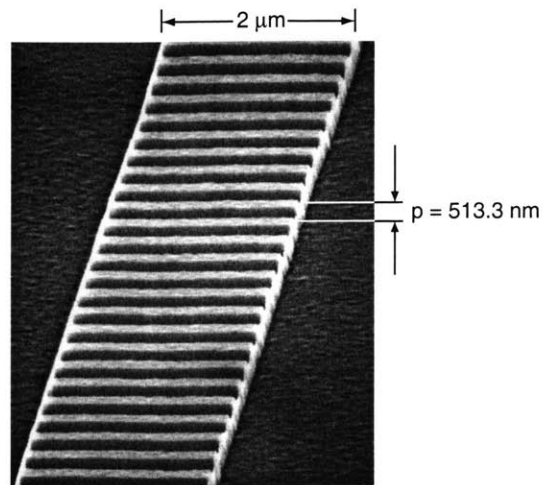


Figure 6.18: Scanning-electron micrograph of a self-aligned grating etched onto a waveguide.

Table 6.1 lists some of the optical and geometrical parameters of the finished devices.

6.7 Optical transmission results

Once fabrication was complete, the 4-inch-diameter silicon wafer was divided into chips using a die saw. The facets of each chip (faces perpendicular to the waveguides) were cut at a 6° angle to reduce facet reflection to 2%, and polished. The layout of one chip is shown schematically in Fig. 6.19

The optical response of the devices was measured by J.N. Damask. Optical transmission measurements of each chip were carried out by coupling the amplified spontaneous emission of an erbium-doped fiber amplifier — which served as a broadband illumination source — into the waveguides, through a micromachined fiber lens. The transmitted light at the output facet was coupled into an optical spectrum analyzer by means of a $40\times$ microscope objective. The spectrum analyzer has a wavelength resolution of 0.1 nm.

Figure 6.20 shows the transmission spectra of two uniform Bragg reflectors with

Table 6.1: Optical and geometrical parameters of silica/silicon nitride devices.

Film parameters and feature dimensions	
Bottom oxide thickness	3.9 μm
Silicon nitride thickness	1540 \AA
Top oxide thickness	3150 \AA
Bottom oxide index	1.45
Silicon nitride index	1.97
Top oxide index	1.45
Rib width	2.0 μm
Rib etch depth	2000 \pm 100 \AA
Grating depth	1180 \pm 100 \AA
Duty cycle	0.54 \pm 0.02
Waveguide parameters	
Effective index (n_{eff})	1.496
Group index (n_g)	1.72
Facet reflectivity (0 $^\circ$ Cut)	7.0%
Facet reflectivity (6 $^\circ$ Cut)	2.5%
Blank waveguide loss (α_{wg})	0.53 \pm 0.05 dB/cm
Grating parameters	
Grating strength (κ)	73 cm^{-1}
Grating period	509, 513, 517 nm
Grating loss (α_{grt})	\sim 0.5 dB/cm
Periods per field	128

$\kappa l = 6.6$ (a) and $\kappa l = 15.2$ (b). The stopband width is 5.3 nm, centered at $\lambda_0 = 1546$ nm. The grating period was $p = 517.3$ nm. The rapidly-varying fringes visible on either side of the stopband are the resonances of parasitic Fabry-Perot cavities (labeled cavity 1,2,3 in Fig. 6.19), due to the non-zero reflectivity of the waveguide facets. On the short-wavelength side of the stopband, the transmission of the device exhibits some loss, due to radiation (scattering of the guided mode into radiation modes, which do not reach the output port of the waveguide) [125].

The transmission spectra of six QWS resonators are shown in Fig. 6.21. All gratings were fabricated with the same nominal period (513.3 nm), but the lengths of the Bragg gratings on either side of the quarter-wave shift were varied. The characteris-

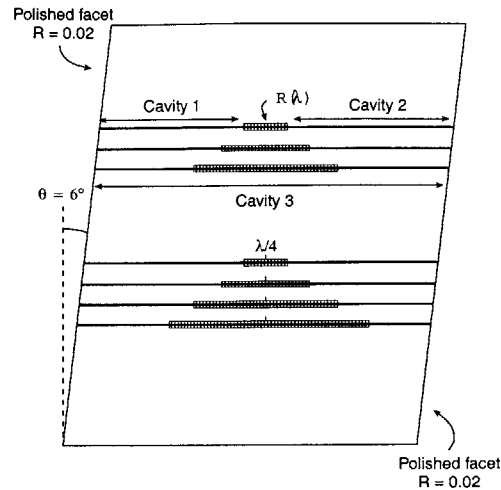


Figure 6.19: Diagram of a finished chip.

tic κl product is stated above each of the transmission responses in the figure, as is the number of fields the device spanned. The expected response was obtained — a stopband with a single resonance in the middle. As the κl product is increased, the width of the resonance decreases, indicating higher Q -factors.

For very narrow resonance linewidth (device length larger than 11 e -beam fields), the transmission response was not accurately measured by the spectrum analyzer, due to its limited wavelength resolution⁴. The resonances of all devices are well centered within the stopband, indicating that the coherence of the SPLEBL-generated gratings was adequate.

The extinction level within the resonator stopband was limited to ~ -45 dB; these devices show slightly better extinction than the uniform Bragg gratings, but the discrepancy is probably due to slight differences in the measurement conditions.

The resonator response characteristics, including the parasitic Fabry-Perot cavities, were also theoretically calculated [125], and a comparison of the results with the measured data is shown in Fig. 6.22. Again, the correspondence is remarkable.

⁴An improved measurement setup, with significantly better wavelength resolution has been implemented to measure future device generations.

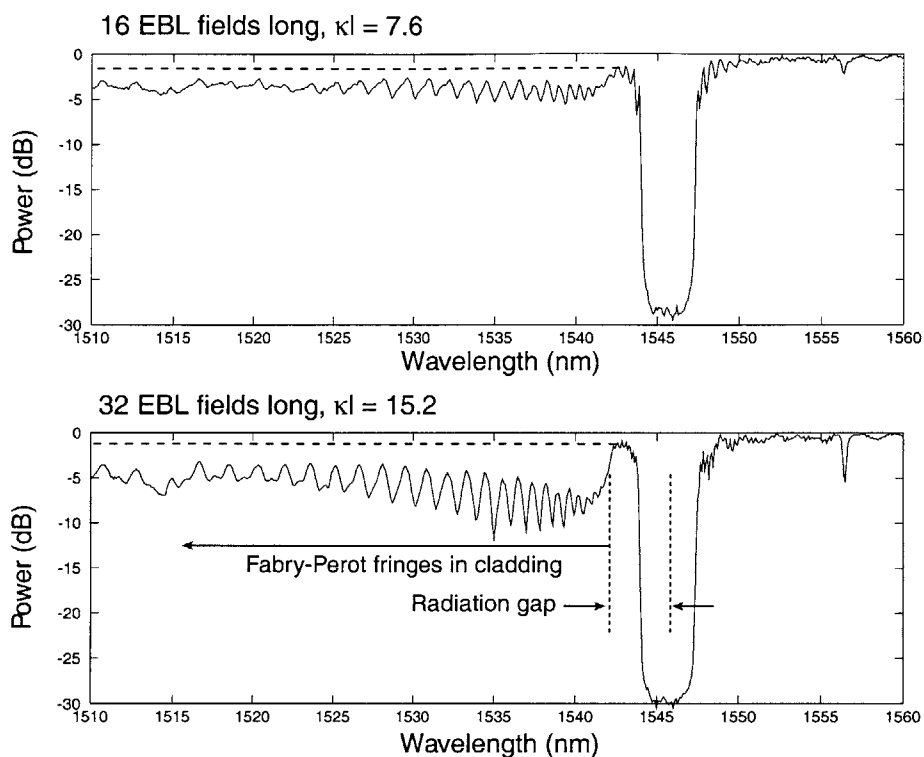


Figure 6.20: Transmission spectra of two uniform Bragg reflector gratings, with lengths of ~ 1 cm, ~ 2 cm. The stopband is 5.3 nm wide, and centered at $\lambda_0 = 1546$ nm. Note the artifacts due to spurious Fabry-Perot resonances and radiation loss.

In order to assess the coherence of the gratings across e -beam field boundaries, the offset from the stopband center was determined for 12 resonators of different Q -factors and periods. The small number of data points available implies that the measurements lack statistical significance, but they do provide an indication of grating quality. The resonance offset with respect to the stopband center is plotted in Fig. 6.23. A deviation of 1 Å corresponds to 1.5% of the stopband width. The largest deviation is less than 1 Å, and there are no clear systematic effects associated with grating length. From these data, the standard deviation of e -beam-written field displacement was inferred to be ~ 5 nm, similar to the value of $\sigma_x \sim 8.7$ nm estimated from the outrigger data.

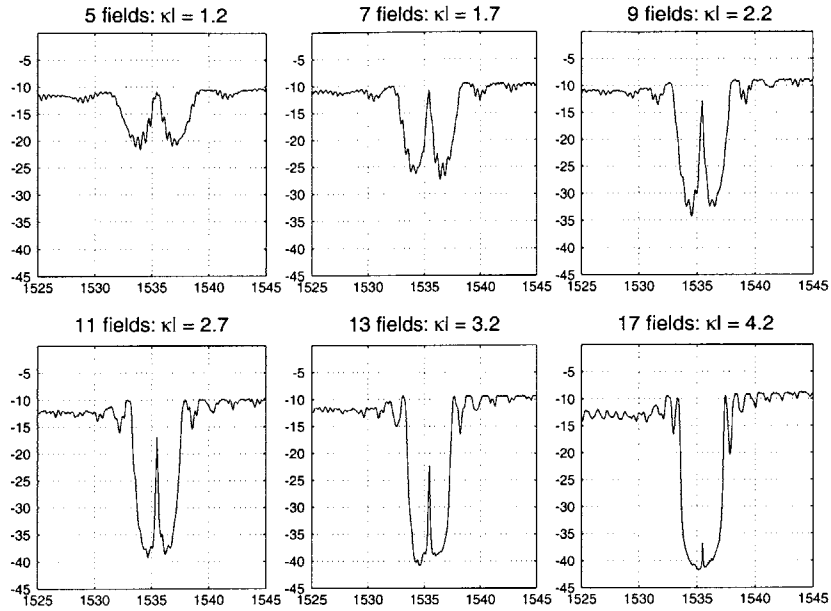


Figure 6.21: Transmission spectra of six quarter-wave shifted resonators with the same nominal period and increasing grating length. As expected, the resonance becomes finer as the Bragg-grating length increases. All resonances are well centered within the stopband indicating the coherence of the gratings.

6.8 Summary

Efforts to develop a technology to pattern Bragg gratings for the integrated resonant channel-dropping filter have been reported. The technology was designed to produce long, coherent periodic structures, while providing the flexibility to introduce abrupt phase shifts, linewidth changes, etc. This technology combines interference lithography and *e*-beam lithography, using interferometrically generated gratings as segmented references in order to correct pattern placement errors during *e*-beam writing. Using a stochastic model of pattern placement, the effect of interfield placement errors on the performance of Bragg gratings was determined, and tolerances on interfield errors were calculated, based on desired device characteristics.

The segmented-grid method was used to generate Bragg-grating patterns on an x-ray mask. These patterns were etched on single-mode waveguides to fabricate a series of Bragg reflectors and QWS resonators. A system was developed to measure

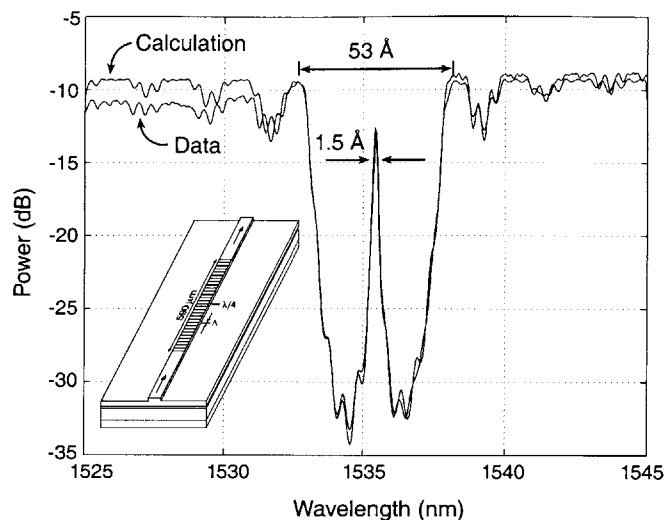


Figure 6.22: Comparison of the measured data for a QWS resonator with the theoretically-calculated spectrum. The performance of the devices agrees very well with the theoretical prediction.

interfield errors with the *e*-beam tool, using vernier-like outrigger structures and a frequency domain technique, very similar to the method used to phase-lock the *e*-beam written gratings to the interferometric fiducials. The measured interfield errors were larger than expected. This was attributed to a combination of factors: (1) precise alignment was performed in only one direction, and (2) lack of orthogonality between the fiducial gratings and the axes along which the pattern was written. Additional problems were discovered during the fabrication of these devices: the period of the fiducial gratings did not correspond to the desired period, and overlay between the optical and x-ray lithographic levels was not adequate. Nevertheless, the devices exhibited good performance.

Based on these encouraging results, a second generation of devices, including channel-dropping filters, was designed. The segmented-grid SPLEBL method was implemented on MIT's *e*-beam system, and used to generate Bragg-grating patterns for these devices. The fabrication processes were improved, in order to circumvent the difficulties found. This work is reported in the next two chapters.

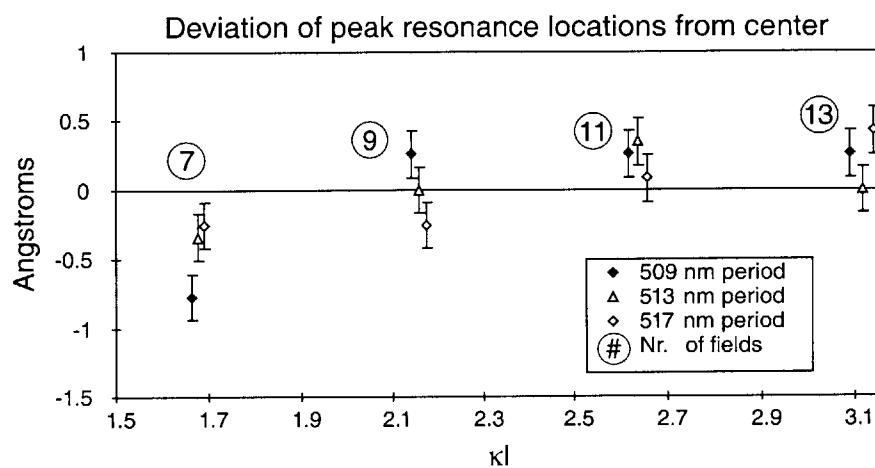


Figure 6.23: Resonance offset from the stopband center, plotted for twelve resonators. The offsets all fall within $\pm 1 \text{ \AA}$, which corresponds to 1% of the stopband width. From these data, the standard deviation of e -beam field placement was inferred to be $\sigma_x = 5 \text{ nm}$. The value estimated from outrigger-grating measurements is $\sigma_x = 8.7 \text{ nm}$.

Chapter 7

Further development of the segmented-grid method

7.1 Implementation on MIT's VS-2A system

In 1994, IBM Research donated the vector scan tool VS-2A to MIT's Nanostructures Laboratory. After the machine was installed and brought into operation, the segmented-grid spatial-phase locking algorithm was implemented on it, as had been done on VS-6. Figure 7.1 shows a system diagram of the VS-2A machine. Although the two systems are in general quite similar, some differences exist between them. VS-2A was donated without a digital pattern generator (DPG), an essential part of a lithography system which generates the sequence of signals that deflect and blank the beam, in order to expose the desired patterns within a field. The DPG is also used to raster-scan the beam to image the substrate and to perform mark registration functions. To remedy the situation, new pattern-generation hardware was implemented¹, using an Alacron AL860XP microprocessor board, which was installed in the control computer (see Fig. 7.1). The choice of a microprocessor board (as op-

¹This work was accomplished by S. Silverman, based upon a design by V. Bögli, at the Lawrence Berkeley National Laboratory

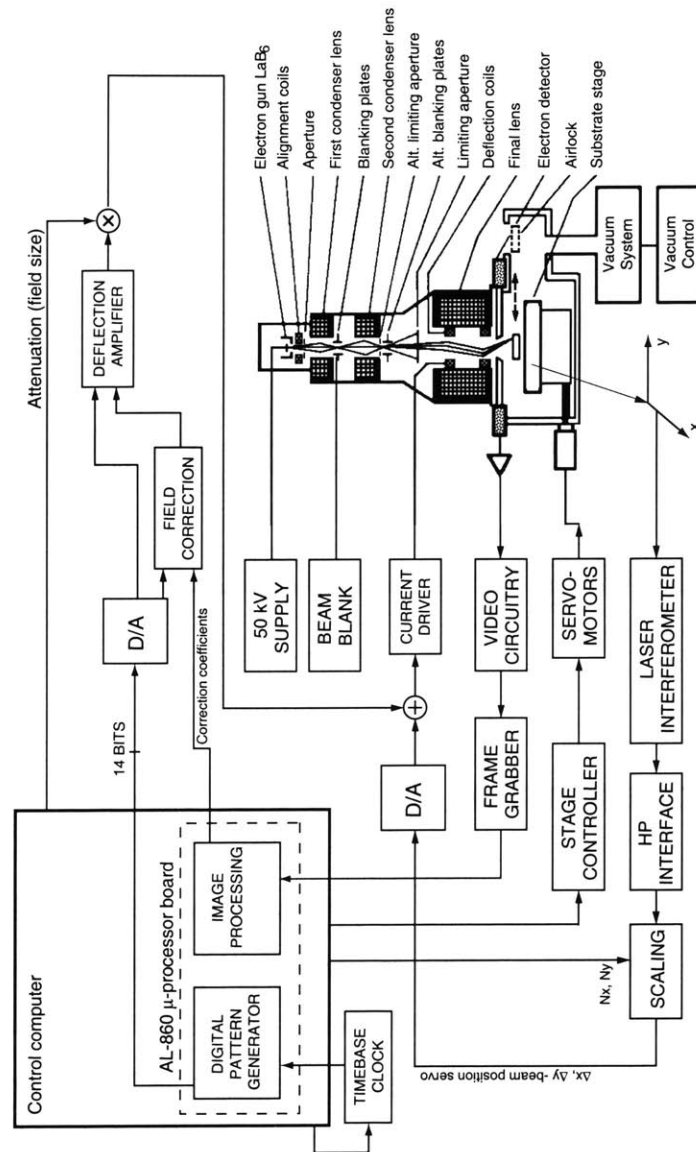


Figure 7.1: System diagram of the VS-2A *e*-beam lithography tool. The operation of the system is coordinated by a control computer. A digital pattern generator provides signals for beam deflection and blanking. To perform field registration, an electron detector collects back-scattered electrons from the substrate as the beam is raster-scanned. The detector signal is amplified by video circuitry and captured with a frame grabber, to create an image of the substrate surface. The image is transferred to an image processing module, which extracts alignment information from the image, and computes correction coefficients. These coefficients are used for fine adjustment of the field's position and orientation. The incremental corrections are fed to the beam-deflection subsystem. The DPG and image processing module were implemented in software on a microprocessor board. To compensate for mechanical stage vibrations, the stage position is measured by a laser interferometer, which generates error signals that are fed-back into the beam deflection system, so that the beam position tracks substrate movement.

posed to more specialized digital-signal-processing hardware) was fortunate, because its general-purpose processing and I/O hardware could be put to several uses. The segmented-grid phase-locking algorithm, summarized in the previous chapter, was implemented on this hardware. Significant performance improvements were obtained, compared to the previous VS-6 implementation, which used different image processing hardware [56]. The time required to extract the spatial phase from a grating image improved from ~ 20 seconds for the VS-6 hardware to less than 0.25 seconds for the new implementation. The interfield-error measurement routine was also implemented using the microprocessor board.

To measure the inherent pattern-placement capability of the *e*-beam system (without SPLEBL), gratings were patterned within several adjacent fields [148], as shown in Fig. 7.2 (a). Interfield error statistics were collected for two modes of operation. In the first mode, adjacent fields were written consecutively; for the second mode, field exposure was sequenced so that a ten-minute interval elapsed between the exposure of adjacent fields. The first mode was intended to test the smallest magnitude of interfield errors achievable with the system, where long-term drift does not have a significant influence; the second mode evaluated the long-term stability of the tool, which becomes an important factor when long gratings are exposed. During pattern exposure, one field is typically written in approximately 20 seconds, so that patterns spanning 30 or more fields will accumulate drift-induced errors comparable to those measured with a ten-minute time lapse between fields. The results for consecutive field exposure, shown in Fig. 7.2 (b), indicate that the best achievable interfield errors — with no field-placement correction — have a mean $\bar{x} = 26$ nm and an uncertainty $\sigma_x = 23$ nm. When the interval between adjacent field exposures was increased to 10 minutes, pattern placement was considerably degraded: $\bar{x} = 4.5$ nm, $\sigma_x = 127$ nm [148].

These results were obtained with the machine operating in an essentially uncontrolled environment; no effort was made to control room temperature, electromagnetic interference, acoustic noise, etc., because the system was not intended to run as an

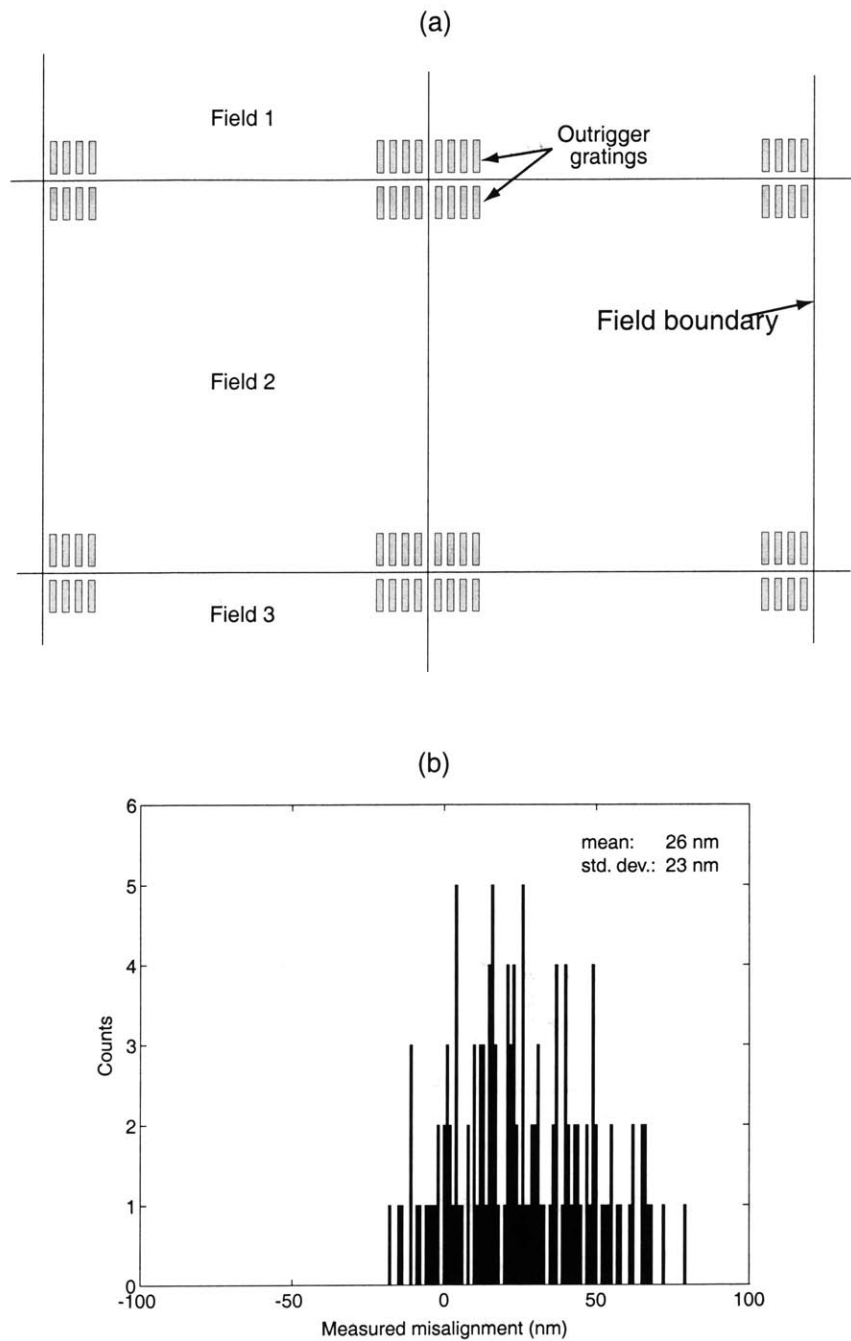


Figure 7.2: (a) Schematic representation of the method used to evaluate VS-2A's pattern-placement capability. Several fields were tiled together, and gratings were written at the corners of each field. Interfield errors were then measured, according to the method described in the previous chapter. Field exposure was sequenced in two modes: (1) adjacent fields were exposed consecutively; (2) fields were exposed with a ten-minute interval between adjacent fields. (b) Measured interfield errors for consecutive field exposure.

“open-loop” — pattern placement was to be referenced to an interferometrically generated fiducial grid. Typically, a large fraction of the cost of industrial e -beam lithography systems (several millions of dollars) is allocated to environmental control. Such costly investment is beyond the budget of a university-based research group. Moreover, research in SPLEBL is intended to obviate the need for tight environmental control, and thus decrease the cost of e -beam tools.

The performance of the segmented-grid implementation on VS-2A was compared to that obtained with VS-6, by repeating the VS-6 experiments with the newly implemented system. First, repeatability of alignment was measured. As described in the previous chapter, this was accomplished by repeatedly aligning the e -beam field to a stationary grating. The experimental conditions were very nearly the same as they had been for the VS-6 experiment, reported in ref. [56]: the grating sample was a 200-nm-thick gold grating on a silicon nitride membrane; the grating was exposed with IL, and had a period $p = 200$ nm. The field size was calibrated to $102.4 \mu\text{m}$, so that one period of the grating was equivalent to 32 pixels. Alignment statistics were collected for several beam currents (i.e., several signal-to-noise ratios), and the results are shown in Table 7.1. The results obtained previously for VS-6 are included for comparison.²

Table 7.1: Alignment repeatability as a function of beam current.

Beam current (pA)	alignment uncertainty (nm)	
	VS-2A	VS-6
100	-	0.33
75	2.18	0.39
50	1.93	0.40
25	1.89	0.46
10	1.86	0.69

From these results, it is immediately apparent that the two sets of data follow

²Appendix D contains more complete data — histograms of the collected data for both experiments are included.

different trends. Alignment precision (given by the uncertainty in locking the field position to the grating) is poorer for VS-2A than for VS-6, and it is essentially independent of the SNR. The VS-6 data, however, show a clear dependence on SNR. It is therefore reasonable to conclude from these observations that alignment precision is SNR-limited for VS-6, but is limited by a different factor for VS-2A, which is most likely the short-term stability of the machine. The design of the VS-6 tool has been optimized to provide maximum short-term stability. Rapid movement between the sample and the electron optics, due to stage vibrations, has been greatly reduced by the use of a locking stage [143]. However, direct mechanical coupling between the stage and the electron optics does not exist on VS-2A. Instead, the more traditional approach of a servo loop is used: while exposing a field, the laser interferometer measures stage movement (vibrations) with respect to the column. The measured stage positions in x and y are used to generate error signals, which are fed to the deflection amplifier to dynamically correct the beam position, so that it follows stage movement (see Fig. 7.1). Such a system is limited by the interferometer's resolution, in this case approximately 5 nm. This issue will be examined in more detail in Section 7.2.

The performance of the system was further evaluated by repeating the fabrication process for making the Bragg-grating mask, as described in the previous chapter. The same fabrication procedure was followed, with one exception: the beam-deflection axes were aligned to the k -vector of the fiducial gratings by rotating the field, as shown in Fig. 7.3. In this way, the orthogonality of the beam deflection axes was not compromised. After gold-plating the e -beam generated gratings, interfield errors were measured, using the outrigger structures. Figure 7.4 shows the results, which are clearly better than those obtained with VS-6 (see Fig 6.16). From these interfield error data, the standard deviation of field-placement errors was estimated by deconvolving the measurement uncertainty (3.8 nm) and dividing by $\sqrt{2}$, resulting in a field-placement uncertainty $\sigma_x = 4.3$ nm. According to this estimate field placement errors (with respect to the fiducial gratings) of 20.3 nm (mean + 3σ) were achieved with this system.

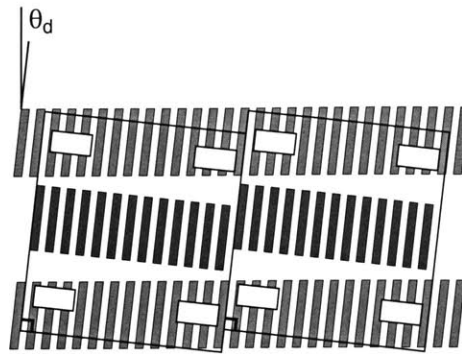


Figure 7.3: Strategy adopted to accommodate an angular error θ_d in the direction of the fiducial grating lines. The fields were rotated to match θ_d without compromising the orthogonality between beam-deflection axes (compare Fig. 6.17). The angle θ_d is greatly exaggerated in this diagram. In practice, θ_d was less than 1° .

7.2 Measurement of short-term beam stability

To characterize the electron beam's position stability with respect to the sample, the method developed by Kratschmer *et al.* for measuring the beam stability of VS-6 was used [162]. In this technique, beam movement with respect to the substrate stage is measured by placing an electron detector in the beam path, and partially blocking the beam at the focal plane with a very sharp edge [163] (see Fig. 7.5). Movement of the beam with respect to the edge results in a change in the amount of current reaching the detector.

To block high-energy electrons, the substrate must be relatively thick ($> 50 \mu\text{m}$). It is customary to use anisotropic etching to fabricate a sharp edge on a silicon substrate. However, it was found that an adequately sharp edge could be obtained by much simpler means. A 4-inch-diameter $\langle 100 \rangle$ silicon wafer was carefully cleaved along one of the $\langle 100 \rangle$ crystallographic planes. The quality of the cleave was verified with a high-resolution scanning electron microscope (LEO DSM-982). The cleaved edge was determined to be sharper than the resolution of the microscope ($\sim 4 \text{ nm}$). The cleaved facet was observed with a Linnik interferometer and determined to be flat to less than one fringe ($\sim 0.25 \mu\text{m}$). The edge was deemed adequate to perform the measurement.

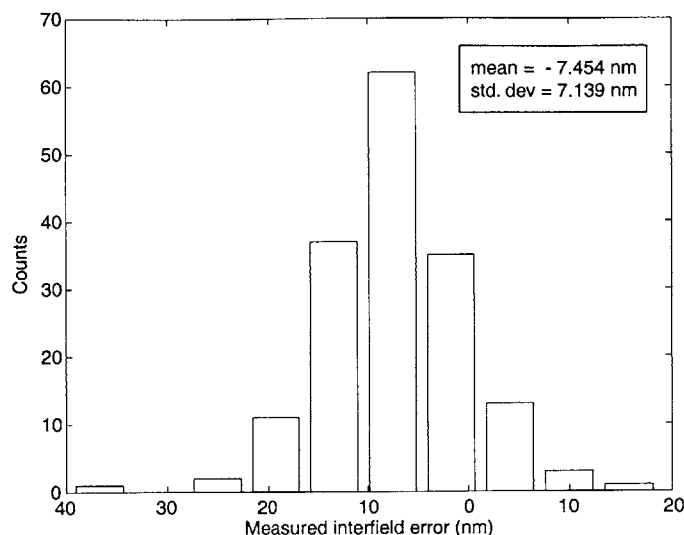


Figure 7.4: Histogram of interfield errors obtained with segmented-grid SPLEBL in VS-2A. Field placement was significantly better than that obtained with VS-6 (Fig. 6.16).

The cleaved edge was mounted on a sample holder at a slight angle, as shown in Fig. 7.5. Since the electron beam has a finite angle of convergence, the sample must be inclined to prevent partial blocking of the beam by the thick edge, which would cause a measurement artifact. The edge should be inclined to match the beam's semi-angle of convergence, which is approximately 5 mrad. The sample was mounted at a slightly larger inclination (15 mrad.) to leave some margin for error, since the angle of convergence is not known exactly. The unblocked beam passed through a hole in the sample holder, and was collected by a diode detector.

The beam was raster-scanned about the edge, and the signal from the transmission detector was used to form the image shown in Fig. 7.6. Note that the edge appears blurred in this high-magnification image, due to the finite beam diameter.

In order to characterize beam-position stability with the edge measurement technique, the beam diameter must be determined first. Beam diameter is an important characteristic of a lithography machine, since it determines its resolution, i.e., the minimum feature size that can be exposed with the system. When this experiment was carried out, the minimum diameter of the VS-2A machine had not yet been mea-

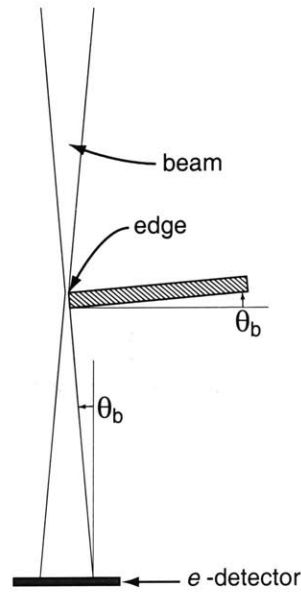


Figure 7.5: Schematic diagram of the edge-measurement technique. The beam is scanned across a sharp edge and the transmitted fraction is measured with an electron detector. The edge must be mounted at an angle θ_b , the semi-angle of convergence of the beam, to prevent measurement artifacts. The sample holder has been omitted from this diagram.

sured, so this information was a useful byproduct of this measurement. The beam diameter was measured by repeatedly scanning the beam across the edge. An oscilloscope was connected to the output of the transmission detector, and the scope trace was synchronized with the beam scanning signal. Figure 7.7 shows a trace obtained in this way. Beam diameter can be estimated from the width of the transition region between 100% transmission (left part of the trace in Fig. 7.7) and 0% transmission (right part of the trace). If the beam is scanned across a line of length l in time T , the full width at half-maximum beam diameter is given by [163]

$$d_{\text{FWHM}} \approx 1.74 \times (t_{25\%} - t_{75\%}) \times \frac{l}{T} \quad (7.1)$$

assuming the beam current-distribution is a circularly-symmetric Gaussian. The beam diameter was measured for several beam currents; the results are shown in Table 7.2.

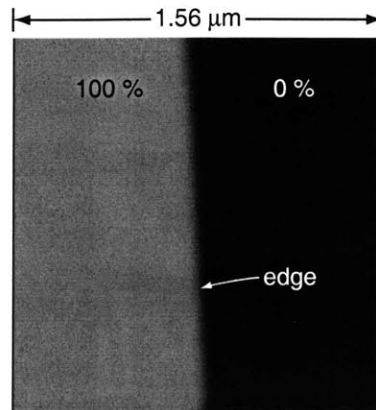


Figure 7.6: Transmitted-electron image of a cleaved silicon edge. The edge is blurred due to limited resolution, i.e., non-zero beam diameter.

Table 7.2: Beam diameter vs. beam current.

Beam current (pA)	d_{FWHM} (nm)
75	74
50	67
25	62
15	54

Near the 50% point, where half of the beam is transmitted, the relationship between the detector signal and beam displacement is approximately linear. Once the slope of the transfer function about this operating point is known (i.e., once the beam diameter has been determined), beam stability can be measured very accurately, by disabling beam scanning and using the deflection system to center the beam on the edge. Any fluctuations in the beam's position with respect to the edge will cause the detector signal to change.

All static beam measurements were carried out at a beam current of 75 pA. To set up the measurement, the beam was focused by scanning it across the edge and maximizing the slope of the oscilloscope trace at the edge transition. The slope of the transfer function was measured from the oscilloscope trace, and determined to be about 15 mV/nm. A more exact number was obtained by first centering the beam on

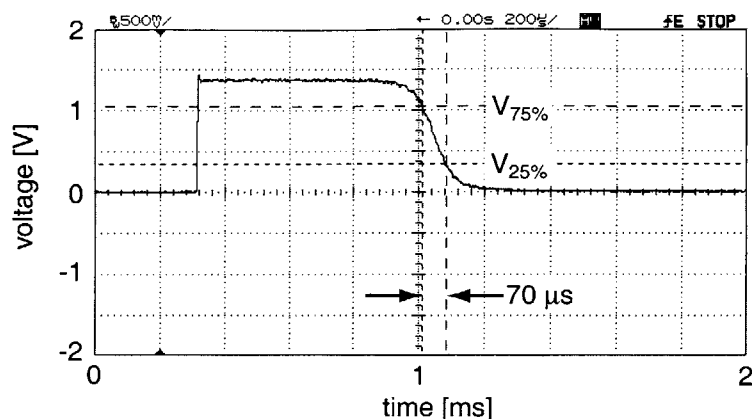


Figure 7.7: Oscilloscope trace of the transmitted-electron signal as the beam was scanned across the edge. The beam diameter was computed from the distance between the 25% and 75% transmission points. For this example, the beam current was 75 pA. The beam was scanned along a line of length $l = 1.56 \mu\text{m}$ in time $T = 2.56 \text{ ms}$. The calculated FWHM beam diameter was 74.3 nm.

the edge and then applying a shift of 4 nm with the field correction unit (the unit used to finely position the field during alignment). The unit is calibrated against the laser interferometer, so that the error in the beam's shift is guaranteed to be significantly less than 1%. The detector output voltage was observed to vary by $55 \pm 1 \text{ mV}$. Hence, the slope was determined to be $13.9 \pm 0.25 \text{ mV/nm}$. A value of 14 mV/nm was used in calculating beam displacement from the detector signal.

The detector signal was measured by means of an HP 3561A spectrum analyzer. The trace shown in Fig. 7.8 (a) was recorded with the interferometer feedback disabled. The beam oscillates with respect to the sample, with a peak-to-peak (P-P) amplitude of $\sim 20 \text{ nm}$. The power spectrum of the signal, shown in Fig. 7.8 (b), indicated that strong frequency components exist at 54, 60 Hz, with weaker contributions at 113, 120, 180 Hz, etc. Figure 7.9 shows the signal trace (a) and power spectrum (b), acquired after the interferometer feedback was activated. The beam position fluctuations have a P-P amplitude of $\sim 9 \text{ nm}$. The frequency components at 54 and 113 Hz have been effectively eliminated. These results agree very well with those obtained by Kratschmer *et al.* [143].

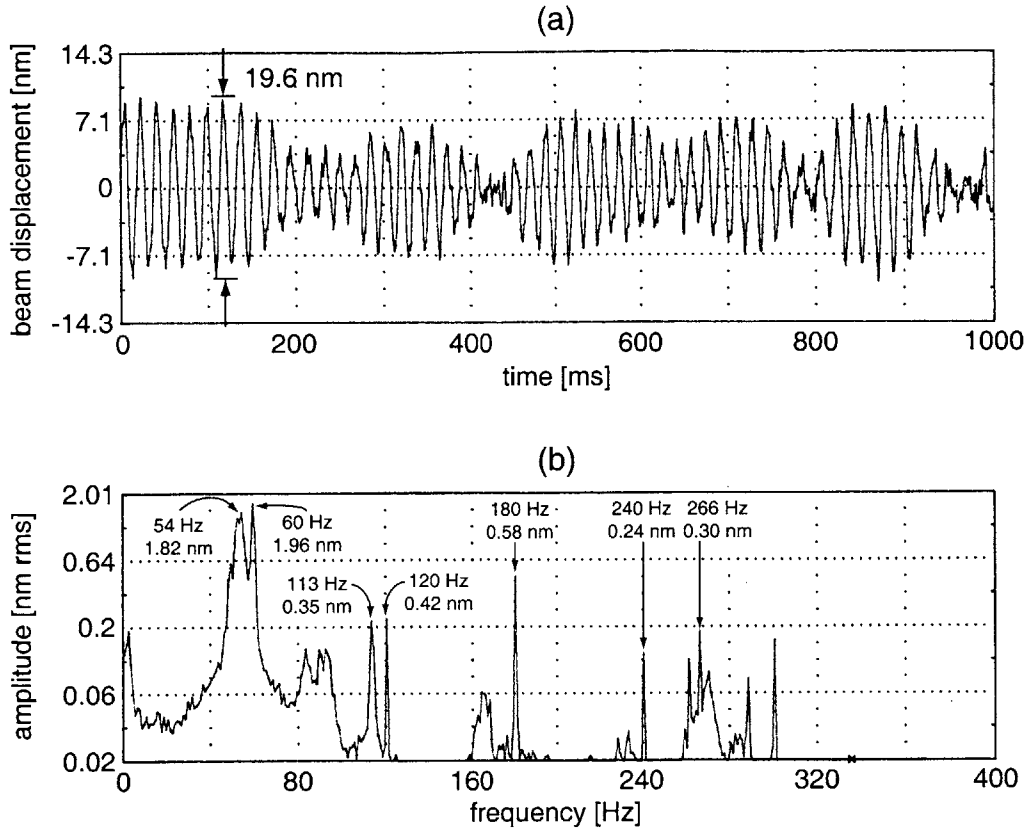


Figure 7.8: Measurement of beam-to-sample position fluctuations, with the interferometer feedback disabled. (a) Time domain trace. (b) Power spectrum computed from (a). The amplitude is plotted on a logarithmic scale (the units are dB-nm).

By comparing both power spectra, it is possible to identify noise sources. The peaks at 60 Hz and multiples thereof are due to electromagnetic interference — note that there is little change in their magnitude when the interferometer feedback is activated. Mechanical stage vibrations can be seen when the interferometer feedback is off. They appear as relatively broad peaks centered at 55, 113 and 266 Hz, which disappear when the interferometer feedback is activated.

Kratschmer *et al.* found that noise in the interferometer feedback loop restricted P-P beam-position stability to approximately two times the resolution of the interferometer, which they attributed to quantization noise introduced by the interferometer (as opposed to electromagnetic interference). They were able to verify this assertion by locking the stage to the final lens, and deactivating the interferometer feedback.

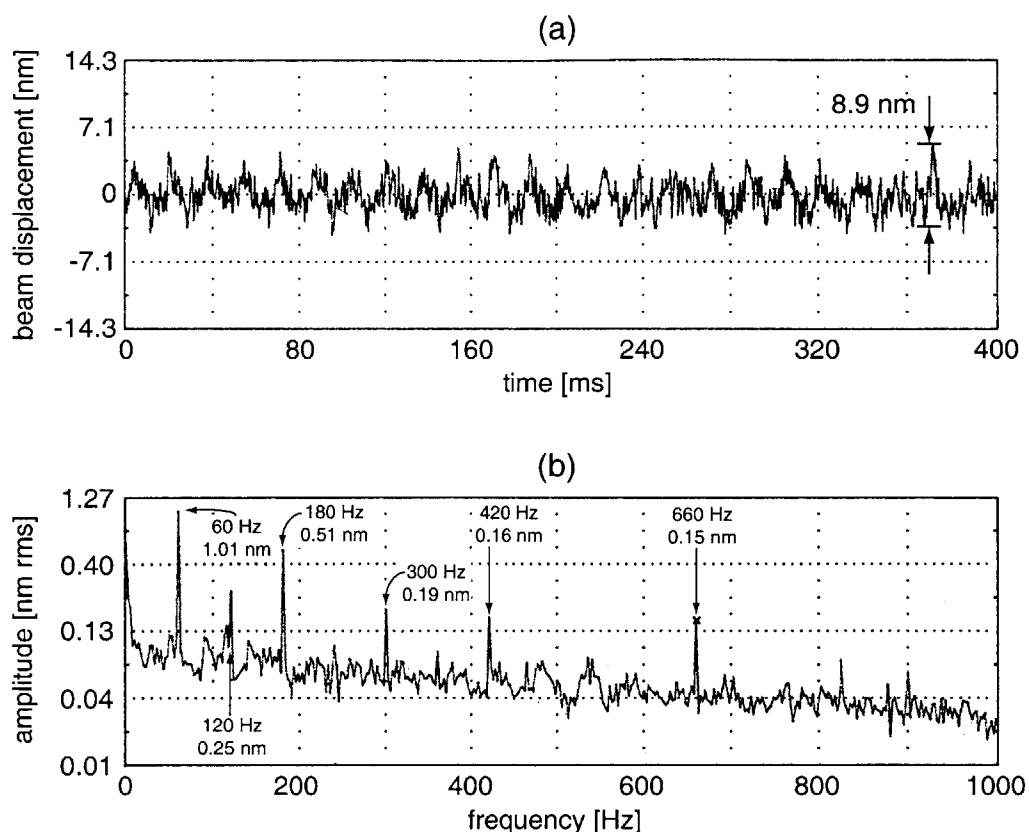


Figure 7.9: Beam-position fluctuations recorded with the interferometer feedback enabled. (a) Time domain trace. (b) Power spectrum. Note high-frequency fluctuations with an amplitude equal to the resolution of the interferometer (~ 5 nm). These are attributed to quantization noise.

The P-P amplitude of beam displacement decreased by a factor of four, to 2.5 nm. This stage locking experiment could not be repeated with VS-2A, but some evidence to support the assertion that laser interferometer quantization is limiting beam stability can be found in the measured power spectra. With the interferometer feedback deactivated, the noise floor in the power spectrum is less than 0.02 nm RMS, as shown in Fig. 7.10. When the beam-position servo is enabled, wideband noise is introduced, making the noise floor rise by approximately 12 dB. The high-frequency noise can be seen clearly in the time-domain signal trace (Fig. 7.9 (a)). This noise can only be caused by the interferometer. In this application, the relatively high bandwidth of the interferometer feedback signal (50 kHz) has a negative impact, since it allows the quantization noise of the interferometer to fully influence beam position, even for

high frequencies (where no mechanical vibrations are present).

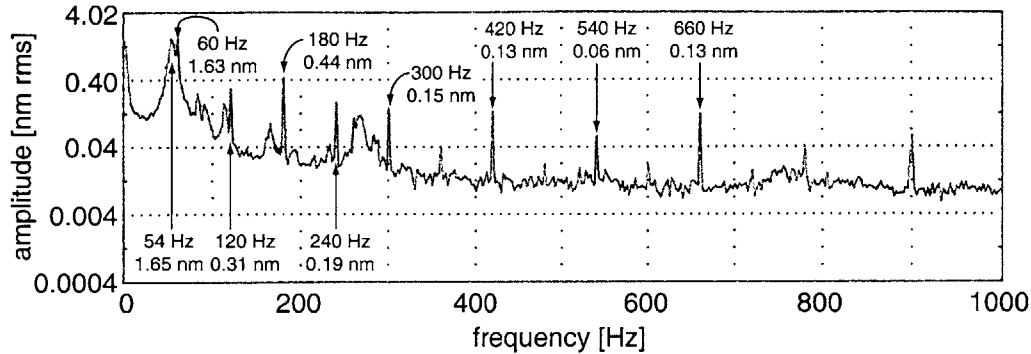


Figure 7.10: Power spectrum of beam position measured with the interferometer feedback deactivated. At high frequencies the noise floor is below 0.02 nm RMS.

The magnitude of servo noise should decrease if the interferometer resolution is increased and the feedback loop bandwidth is constrained. Laser interferometers with $\lambda/2048$ (~ 0.3 nm) resolution [164] are now available commercially, but their cost is prohibitive. However, the resolution of the *e*-beam tool's HP 5527A interferometer could be increased with a simple modification, thanks to the low-bandwidth constraint on the feedback loop. This is usually not the case in engineering: constraints tend to make matters more difficult! The method used to enhance the resolution of the interferometer is described in the next section.

The magnitude of electromagnetic interference components measured on VS-2A was found to be roughly equal to the measurements of Kratschmer *et al.* Therefore, by improving the performance of the interferometer feedback loop, it should be possible to attain short-term beam stability of ~ 2.5 nm P-P. Further improvements would require the reduction of electromagnetic interference, by shielding the beam path and eliminating all ground loops in the system.

7.3 Increasing the resolution of a heterodyne interferometer

The laser interferometer used to measure stage movement is formally known as a *heterodyne displacement-measuring interferometer* [40, 165]. Figure 7.11 illustrates its principle of operation. A dual-frequency HeNe laser source emits light at optical frequencies f_1 and f_2 . Each frequency component has a different polarization state, so that it is possible to separate both components with polarizing filters. This light source is used to illuminate a Michelson interferometer. The laser beam is separated into measurement and reference beams of orthogonal polarization (and hence different frequency) with a polarizing beam splitter. After returning to the beam splitter, the measurement and reference beams are combined onto a common polarization state by a linear polarizer and illuminate a photodiode, which produces an electrical signal V_M . In the example shown in Fig. 7.11, the frequency components f_1 and f_2 correspond to reference and measurement beams respectively. If the test reflector remains stationary, the measurement signal V_M oscillates with frequency $f_M = f_1 - f_2$. The optical configuration depicted in Fig. 7.11 measures the displacement of a retroreflector. A different, plane-mirror configuration is used to measure the displacement of $x - y$ stages, but relies on the same principle [165, 166].

Movement of the test reflector shifts the frequency of the reflected measurement beam by Δf ($f_M = f_1 - f_2 \pm \Delta f$), according to the Doppler effect. If the test mirror moves with velocity $v(t)$, then the frequency shift is given by [167]

$$\Delta f(t) = \frac{2nv(t)}{\lambda} \quad (7.2)$$

where n is the refractive index of the medium through which the measurement beam propagates, and λ is the wavelength of the measurement beam.

A reference signal V_R is generated by directing a portion of the laser source output towards a second polarizer/photodiode detector. The frequency of oscillation of this

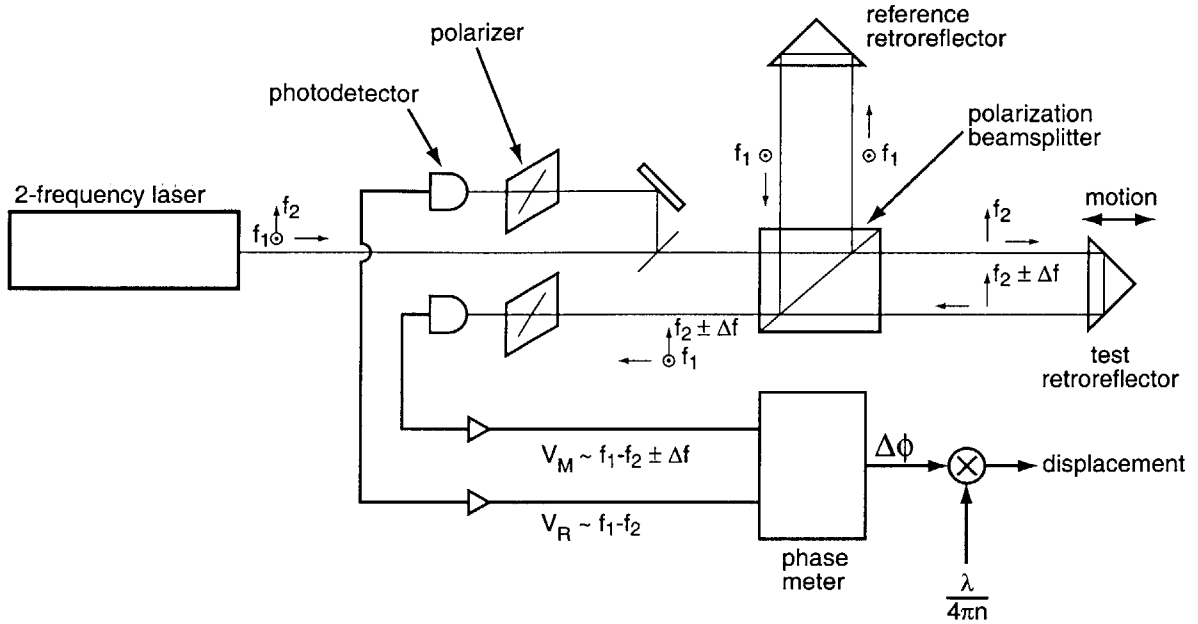


Figure 7.11: Schematic diagram of a heterodyne interferometer. f_1 and f_2 are the two frequencies emitted by the laser. A reference signal V_R is generated by splitting a fraction of the laser beam, and directing it towards a polarizer/detector. The output of the interferometer is similarly directed towards a detector, to generate the measurement signal V_M . The difference in phase between the two signals (measured electronically) is proportional to the displacement of the test reflector.

signal is $f_R = f_1 - f_2$. The displacement $L(t)$ of the test reflector along coordinate x is related to the phase of the measured signal by

$$\left. \begin{aligned} L(t) &= x(t) - x(0) = \int_0^t v(\tau) d\tau \\ \Delta\phi_M(t) &= \phi_M(t) - \phi_M(0) = 2\pi \int_0^t \Delta f(\tau) d\tau \end{aligned} \right\} \Rightarrow \Delta\phi_M(t) = \frac{4\pi n L(t)}{\lambda} \quad (7.3)$$

where $t = 0$ is defined as the instant the laser source is turned on. Note that only *displacements* can be measured with this apparatus. The position $x(0)$ must be determined by other means.

Displacements can be measured with sub-wavelength resolution by measuring the phase difference between V_M and V_R . Phase measurement is accomplished by means of specialized electronics, which are essential components of the heterodyne interferometer [167]. The HP 5527A interferometer used in VS-2A has a minimum resolution

of $\lambda/128 \approx 5$ nm. The most modern commercially available instruments boast a resolution of $\lambda/2048 \approx 0.3$ nm [164].

Heterodyne interferometers are commonly used to measure the position of rapidly-moving machinery in real time [168], which requires high-bandwidth operation of the phase measuring electronics [167]. Modern instruments operate at beat frequencies ($f_2 - f_1$) of ~ 20 MHz, in order to track displacements at velocities up to 2.1 m/s [164]. The measurement electronics used in these instruments are very sophisticated and costly.

In VS-2A, the laser interferometer performs two slightly different functions: it measures the stage position during sample translation between fields, and it compensates sub-wavelength-amplitude vibrations of the nominally static stage during pattern exposure within a single field. Based on this observation, a simple, low-cost solution was put forward: a custom-designed phase detector could be used for vibration compensation, a regime where low-amplitude, low-frequency stage displacements occur. The beam-position servo loop would then use the custom phase-measurement electronics, bypassing the interferometer's circuitry. When field-to-field stage movement occurred, the custom circuit would be deactivated. The proposed phase-measuring circuit is shown in Fig. 7.12. The concept is based on an analog circuit used by Goodberlet *et al.* in an implementation of SPLEBL that used a global grid [169, 148, 170]. It consists of a phase detector and a low-pass filter, components which are commonly used in phase-locked loop implementations [146]. The inputs are signals V_M and V_R . The output is a signal proportional to the phase difference between the inputs. A numerical simulation of such a phase-measuring circuit by Goodberlet [169] has shown that increasing the time constant τ of the filter, i.e., performing the phase comparison over several cycles of V_M and V_R , results in an increased phase-measuring precision. Therefore, a longer integration time, results in higher displacement resolution, at the expense of lower bandwidth. However, for this application, a lower bandwidth is desired in eliminating stage vibrations. Hence, this simple circuit should be quite effective for providing short-term stability to the

e-beam tool.

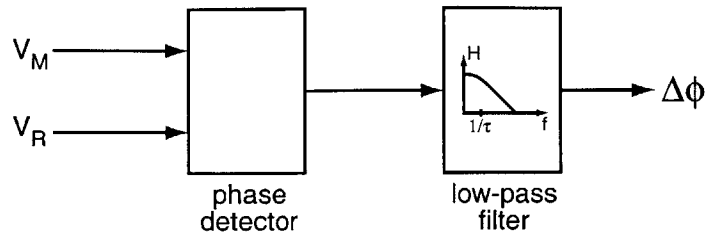


Figure 7.12: Simple band-limited phase-measuring circuit proposed to increase the interferometer's resolution. The longer the time constant τ is made, the more precise the estimate for $\Delta\phi$ is.

For the HP5527A interferometer, $f_2 - f_1 = 1.5$ MHz. From the power spectra shown in Figs. 7.8 and 7.9, it was concluded that mechanical vibrations are significant for frequencies below 200 Hz. It is then possible to integrate over ~ 7500 cycles of the reference and measurement signals, thus attaining significantly increased resolution.

The basic concept presented above was refined and implemented by M.A. Finlayson [171]. A prototype circuit was built, according to the circuit diagram shown in Fig. 7.13. The low pass filter was implemented as a simple first-order RC filter, with time constant $\tau = 1$ ms (for a bandwidth of 1 kHz, which is slightly larger than needed). The circuit was first tested with synthesized reference and measurement signals. The performance of the phase detection circuit was limited by noise in the output signal to 0.45° RMS, which would correspond to a precision of 0.4 nm RMS, if the circuit were used with the laser interferometer.

The circuit was tested on the laser interferometer by J.T. Hastings. The displacement of a stationary mirror was measured with the interferometer, over a time interval of 15 minutes. The interferometer's digital output was compared to the analog circuit's output. The measured displacement of the mirror varied as a function of time, due to drift in the mirror's position, changes in the refractive index, and air turbulence. This preliminary experiment showed that the phase-measuring circuit increased the resolution of the interferometer to less than 5 nm and eliminated high-frequency quantization noise. The data are plotted in Fig. 7.14. From these

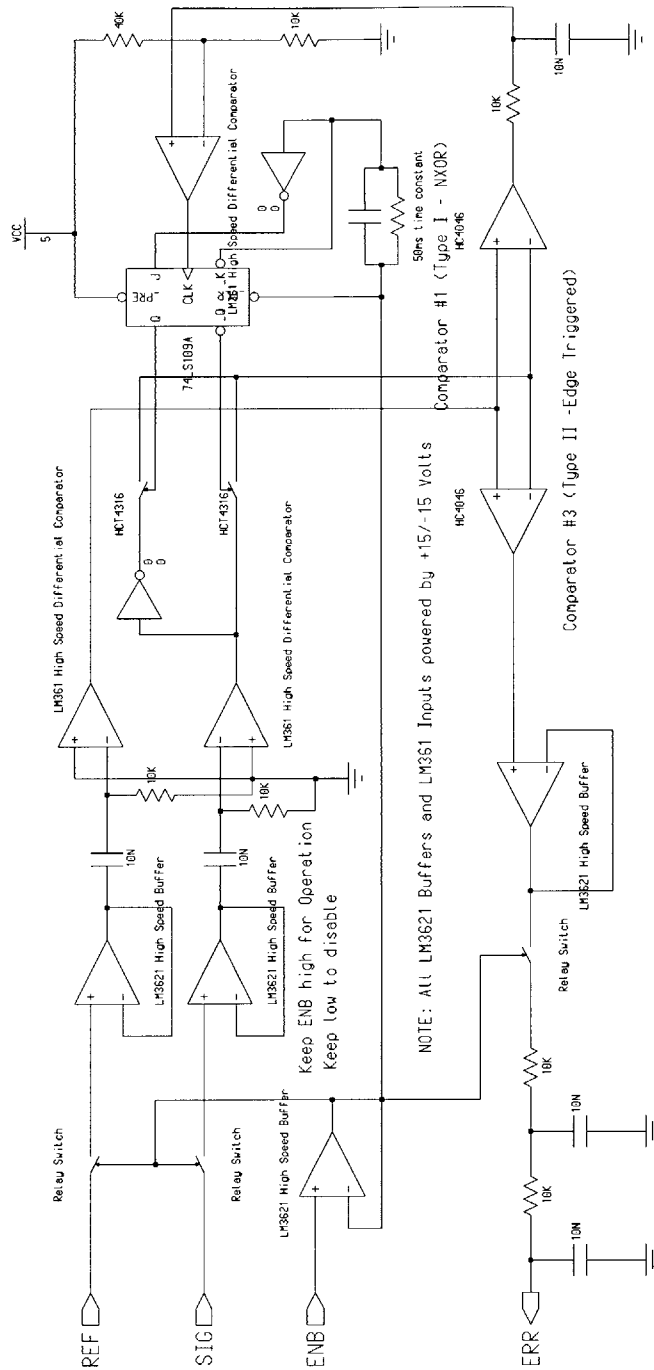


Figure 7.13: Circuit diagram of a prototype phase-measuring circuit for the heterodyne interferometer [171]. Using this circuit, it should be possible to increase the interferometer's resolution to ~ 0.4 nm. The inputs are V_R (REF in the diagram), V_M (SIG) and an enabling voltage (ENB). The output is an analog voltage (ERR) proportional to $\Delta\phi$.

measurements, the resolution of the modified interferometer was estimated to be better than 1 nm. A more controlled experiment is required to obtain a better estimate of the resolution achieved.

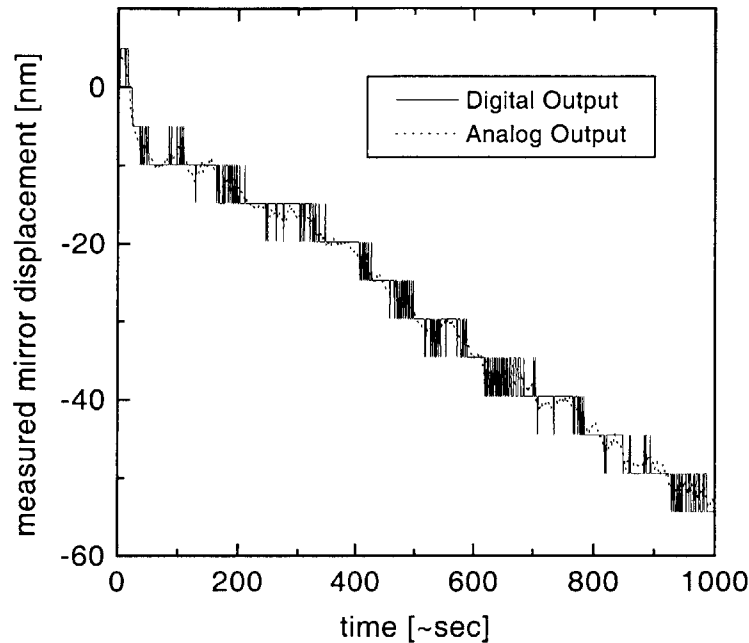


Figure 7.14: Displacement of a nominally stationary mirror, as measured by the heterodyne interferometer. The digital output is quantized to $\lambda/128 \approx 5$ nm. The displacements measured by the analog circuit coincide with the digital values, but show increased resolution. The measured displacement changed with time, because of thermal drift and refractive-index variation.

These encouraging results indicate that short-term stability of the *e*-beam tool may improve significantly if the phase-measuring hardware is incorporated to it. Further work on this project could proceed as follows:

1. Construct two phase-measurement circuits (one for each axis of stage motion), and incorporate them into the interferometer's electronic chassis.
2. Modify the system control software to activate the custom-built circuits only when the stage is stationary. The current beam-position-servo hardware would then be used to correct for the constant term in stage position error, which can be as large as several μm . Dynamic corrections would be made by the custom built hardware.

3. Measure system performance with an “edge measurement”. Adjust the filter time constant to eliminate mechanical vibrations without introducing high-frequency noise.

7.4 Summary

The segmented-grid method was implemented on the VS-2A vector-scan *e*-beam tool, which was donated to MIT by IBM. The pattern-placement performance of the machine was evaluated with and without spatial-phase locking. Pattern placement errors were reduced dramatically when spatial-phase locking was used. The repeatability of phase locking was measured, and was found to be inferior to the repeatability previously obtained with the VS-6 tool. The difference was attributed to the short-term stability of the electron beam position.

VS-2A’s beam position stability was evaluated with an “edge-measurement” experiment, and was compared to a similar measurement performed with VS-6. The conclusion was drawn from the comparison of data from the two experiments, that significant noise is contributed by the beam position servo used to compensate for mechanical stage vibrations, due to the limited resolution of the laser interferometer. A simple means to improve the resolution of the interferometer was proposed and partially implemented.

The fabrication process used to fabricate the Bragg grating mask (described in the previous chapter) was repeated with the VS-2A tool. Interfield errors were measured, by means of outrigger gratings. Residual field placement errors were found to be much smaller for VS-2A than for VS-6. The larger errors in the VS-6 exposure are most likely caused by the locking stage, which introduces random rotations to each field, as described in the previous chapter.

Although the pattern placement attainable with the segmented-grid method could be further improved by increasing the short-term stability of the *e*-beam tool, the

performance obtained was adequate to provide phase coherence in the patterning of Bragg gratings. The newly-implemented system was used in the fabrication of a new generation of Bragg-grating based devices, as reported in the next chapter.

Chapter 8

Bragg grating fabrication for channel-dropping filters

This chapter reports the use of segmented-grid SPLEBL to generate Bragg-grating patterns for a second generation of optical devices, including channel-dropping filters. The devices were implemented using a materials system and waveguide geometry different from those used for the first generation (see Chapter 6). The same grating fabrication methodology was used, where the waveguides are patterned by optical lithography and the Bragg gratings by x-ray lithography. Several innovations were introduced into the x-ray mask fabrication process, in order to address problems encountered in the previous generation. Specifically, overlay problems (due to the mix-and-match strategy), ambiguity in selecting the period of the fiducial-grating, and angular mismatch between the direction of fiducial gratings and device patterns were effectively eliminated. In order to solve these problems, the x-ray mask fabrication process necessarily became more complex.

The chapter begins with an overview of the device characteristics and fabrication process. The process used to fabricate the Bragg-grating mask is then described in detail.

8.1 Overview of device characteristics and fabrication process

The second generation of devices was designed by J.N. Damask, T.E. Murphy, and M.J. Khan for implementation in an InGaAsP/InP materials system. A channel waveguide geometry was adopted, as shown in Fig. 8.1. This geometry was chosen for low dispersion and low mode distortion [125]. The core material is $\text{In}_{0.91}\text{Ga}_{0.09}\text{As}_{0.18}\text{P}_{0.82}$ and the cladding is InP. To fabricate the devices, a uniform layer of core material is grown by molecular beam epitaxy (MBE) on an InP substrate. The waveguides and gratings are lithographically defined and etched into the core layer. The waveguides are then buried within the cladding by an overgrowth of InP. A low-temperature gas-source MBE overgrowth process has been developed by Koontz *et al.* [172], in order to grow the cladding material without affecting the waveguide and grating profiles etched into the core.

Figure 8.1 (d) indicates the dimensions of various device features. Other relevant device parameters are given in Table 8.1. The height of the waveguide core is $1.1\ \mu\text{m}$ (compared to 200 nm for the strip-loaded rib design used previously — see Fig. 6.10). Therefore, the fabrication process described in Chapter 6 — where the waveguide is etched, a new coat of resist is applied, and the Bragg gratings are patterned on the top surface of the waveguide — could no longer be used. It is not possible to spin-coat a layer of resist and perform high-resolution lithography reliably over the uneven surface topography of the structures shown in Fig. 8.1.

A novel patterning technique was developed by Lim *et al.* [173] to overcome this difficulty. The technique, known as the *dual-layer hardmask process* (DLHP), allows all lithographic patterning to be done on an essentially planar surface (see Fig. 8.2). In the DLHP the order of patterning has been reversed: the Bragg-grating patterns are defined first and the waveguides second. A thin ($\sim 50\ \text{nm}$) hardmask layer is deposited on the surface of the core material, followed by a layer of high-resolution resist (such as PMMA). The grating patterns are defined in the resist via x-ray lithography and

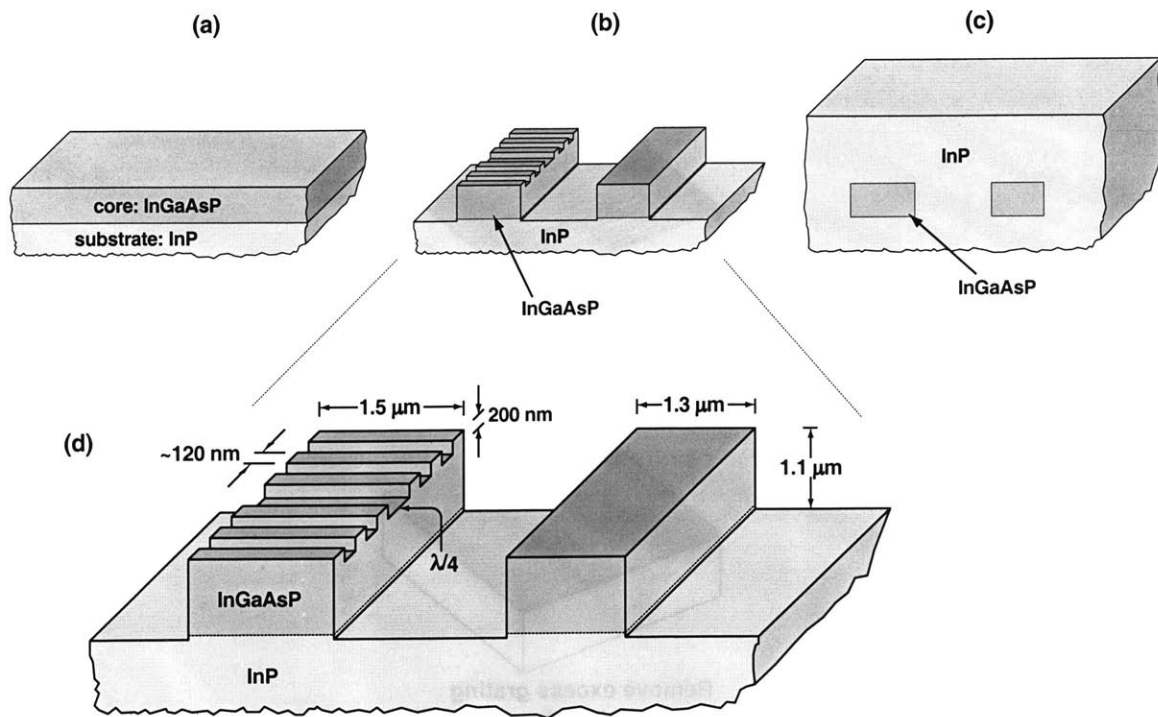


Figure 8.1: Illustration of channel-waveguide geometry adopted in the fabrication of InGaAsP/InP-based optical devices. Fabrication proceeds as follows: (a) A layer of core material is grown on an InP substrate by MBE. (b) The waveguides and gratings are etched into the core layer. (c) InP overgrowth is performed to bury the waveguides. (d) Some device dimensions.

etched into the hardmask (Fig. 8.2 (a)). The resist is then removed, and a layer of photoresist is applied. Waveguide patterns are exposed in the photoresist with optical lithography. The waveguide exposure is aligned to the existing grating pattern by means of alignment marks. After the resist is developed, a second hardmask layer of a different material is evaporated at normal incidence and lifted off (Fig. 8.2 (b)). A reactive-ion etching step follows, in which the grating hardmask is completely etched, except for those areas where it is protected by the waveguide hardmask. Note that this is a self-aligned process, so that the grating patterns can be wider than the waveguides, and lateral alignment tolerances between grating and waveguide levels are easily met. Once the grating hardmask has been etched, another RIE step takes place (with a different chemistry) to etch the waveguides into the core material (Fig. 8.2 (c)). The waveguide hardmask is then selectively removed, exposing the grating hardmask

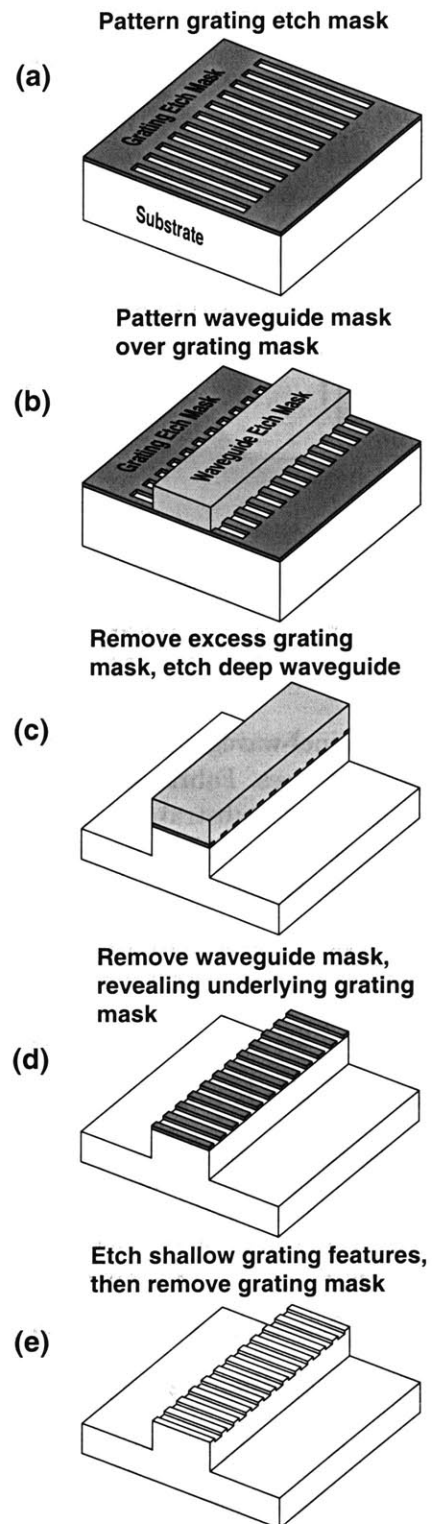


Figure 8.2: The dual-layer hardmask process.

Table 8.1: Optical and geometrical parameters of InGaAsP/InP devices.

Material parameters and feature dimensions	
Core height	1.1 μm
Overgrowth thickness	3 μm
Core index	3.229
Cladding index	3.166
Bus width	1.3 μm
Resonator width	1.5 μm
Grating depth	200 nm
Duty cycle	0.5
Waveguide parameters	
Effective index (n_{eff})	3.183
Grating parameters	
Grating strength (κ)	58 cm^{-1}
Grating period	244.39 nm
Periods per e -beam field	256

(Fig. 8.2 (d)). The Bragg gratings are reactive-ion-etched into the top surfaces of the waveguides, and the grating hardmask is stripped (Fig. 8.2 (e)). The InP-cladding overgrowth process is then carried out, to create the final buried-channel structure.

Etching is done by RIE in order to obtain vertical sidewalls. The choice of hardmask materials and thicknesses depends upon the materials being etched (DLHP is a general-purpose method, which can be applied to a variety of materials systems), subject to the following constraints:

- a) The top hardmask must provide good selectivity in etching the bottom hardmask and the substrate.
- b) The top hardmask must be removed without affecting the bottom hardmask or the substrate.
- c) The bottom hardmask must provide good selectivity in etching the substrate.
- d) The bottom hardmask must be stripped without affecting the substrate.

M.H. Lim optimized DLHP to fabricate InP-based devices: the grating hardmask consists of a 50-nm-thick layer of evaporated silicon oxide, and the waveguide mask consists of 200 nm of nickel. The oxide mask is etched in a CHF_3 plasma, with a 300 V DC bias. The InGaAsP core is etched in a plasma of $\text{O}_2:\text{H}_2:\text{CH}_4$ 2.5 sccm:19 sccm:19 sccm at a chamber pressure of 4 mTorr and 300 V DC bias [173]. The nickel layer is removed with a commercial chemical wet etch and the oxide mask is stripped with a buffered-HF solution.

It is essential to ensure that the InP/InGaAsP surfaces are free of contaminants (i.e., any hardmask or resist residues) so that epitaxial growth of the InP cladding is possible, resulting in a single crystal with a low defect density (defects in the overgrown film are expected to cause waveguide loss, due to scattering). Figure 8.3 shows a side-coupled resonator structure, etched into the core material with the DLHP. The structure has well-defined features, straight vertical sidewalls, and smooth etched surfaces — it is nearly ideal. The next section will describe the lithographic process used to define device features.

8.2 Description of mask set and lithographic process

Addressing all problems encountered previously caused the lithographic process to become fairly complex. Figure 8.4 illustrates the final process in simplified form.

The first issue addressed in the mask-set design for the CDF devices was the elimination of overlay problems, the result of using of several lithographic techniques. For the previous device generation (as described in Chapter 6), waveguide patterns were exposed with an optical-projection stepper. Bragg gratings and alignment marks were exposed on the x-ray mask using the VS-6 vector-scan tool at IBM. The phase progression of the gratings was controlled by referencing to IL fiducials, but the locations of all patterns were determined by the e-beam tool's coordinate system. Overlay

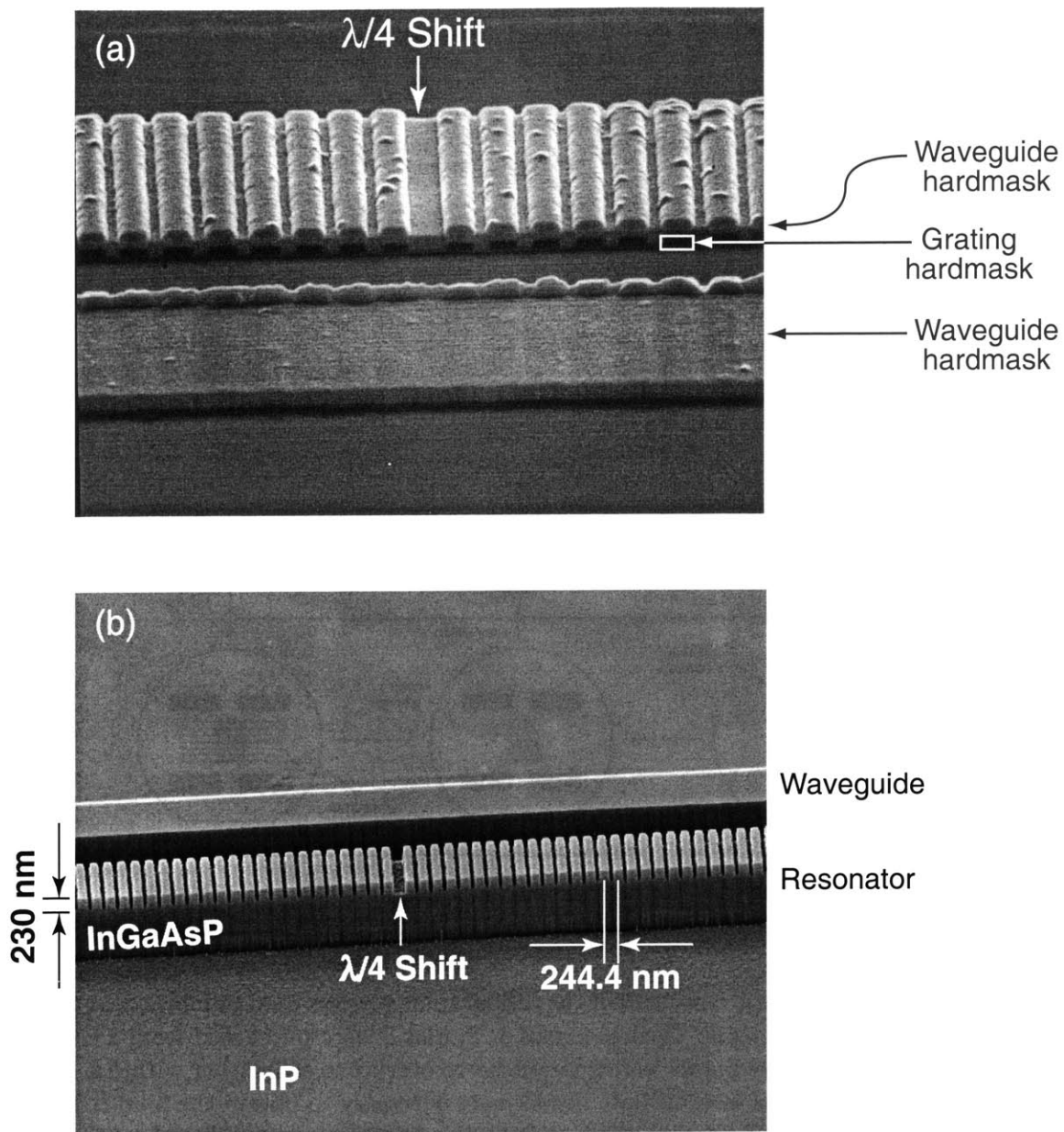


Figure 8.3: (a) SEM of patterned hardmask features that define a grating resonator, side-coupled to a bus waveguide. (b) Etched structure, after both hardmasks have been removed.

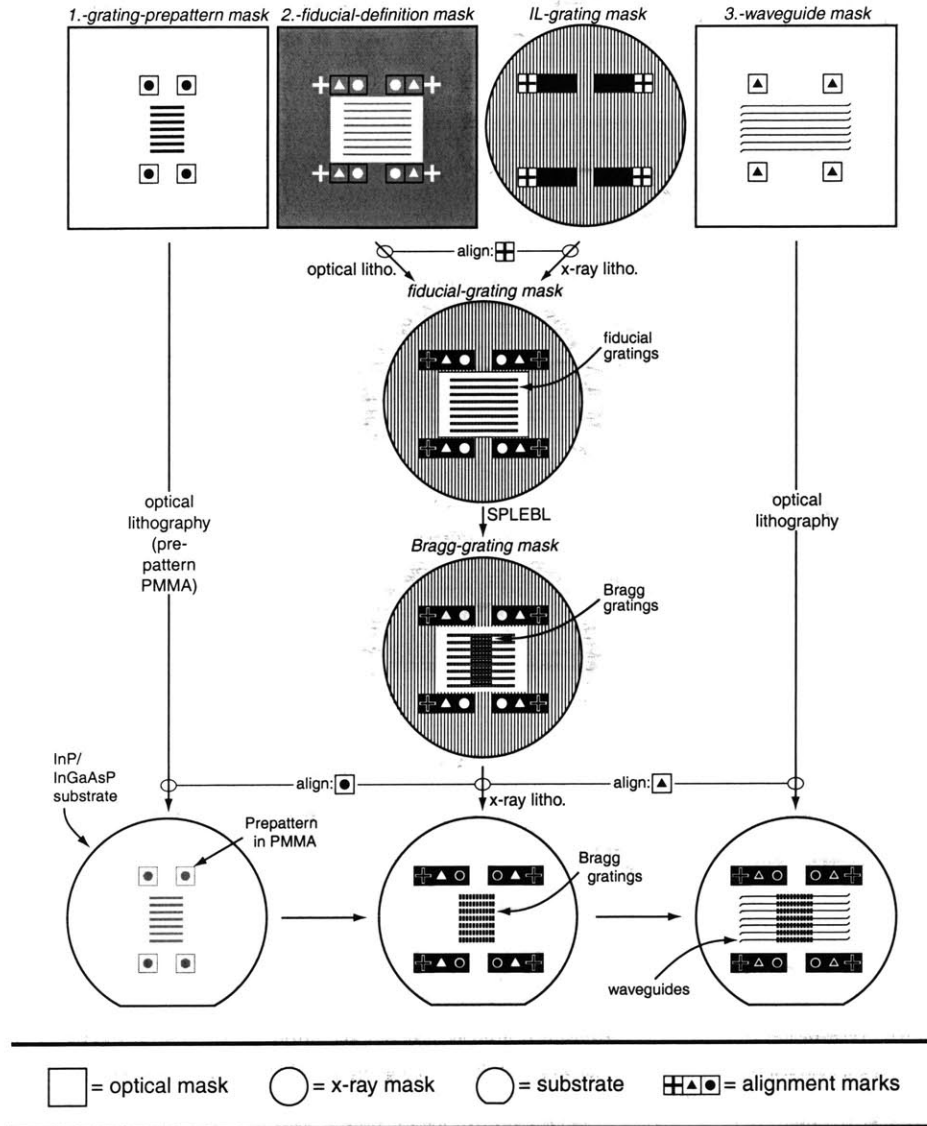


Figure 8.4: Schematic flowchart of the lithographic process used in fabricating the second generation devices. Optical masks 1, 2, and 3 were purchased from a commercial vendor. These masks were guaranteed to overlay to each other within a 100 nm tolerance. Several intermediate masks were necessary to obtain the final Bragg grating mask. The IL-grating mask defines the phase-coherent fiducial gratings, with a period of 244.4 nm. Alignment marks, which index the k -vector of the grating, are exposed on the mask by SEBL. The pattern on the fiducial definition mask is combined with the IL-grating mask, to create the fiducial-grating mask. Bragg-grating patterns are written onto this mask by SPLEBL. Note that the alignment marks on the fiducial grating mask are defined by means of the fiducial definition mask, thus ensuring proper overlay between the optical and x-ray levels. All marks are depicted in symbolic form here.

between the optical and x-ray levels was not satisfactory. To eliminate this problem, all optical exposures required by the new process of Fig. 8.4 were done in proximity, as opposed to using a projection stepper. Two optical masks were designed: one, the *waveguide mask*, defined the waveguide patterns and alignment marks to be printed on the device substrates. The second, the *fiducial definition mask*, was used to define the fiducial grating areas and alignment marks (designed to overlay with the waveguide level) on the x-ray mask; these patterns were transferred to the x-ray mask using proximity optical lithography. Phase-coherent fiducial gratings were patterned on the x-ray mask using another x-ray mask containing an interferometrically-generated grating (this mask is called the *IL-grating mask*). The transfer of patterns from one x-ray mask to another is commonly done by x-ray lithography, in the Nanostructures Laboratory.

The final *Bragg-grating mask* contains patterns such as fiducial gratings and out-rigger structures which should not print on the substrate. For this reason a third mask, the *grating pre-pattern mask*, was also designed. This mask is used to remove resist from all areas of the substrate surface except those areas corresponding to the Bragg-grating patterns. In this way, extraneous features are not transferred from the mask to the substrate.

The three optical masks described above were purchased from a commercial vendor. They were all exposed using the same tool, and were guaranteed to overlay to one other within a 100-nm tolerance. Period control and angular alignment of the fiducial gratings were issues addressed during the fabrication of the IL-grating mask, reported next.

8.3 Fabrication of the IL-grating mask

8.3.1 Period calibration

Experience has shown that the period of IL-exposed gratings can only be controlled within a few nanometers, due to uncertainty in setting the interference angle (see Chapter 2). However, the period of Bragg gratings must be controlled much more precisely. For InP-based devices, a free space wavelength of ~ 1550 nm corresponds to a Bragg-grating period of ~ 244 nm. A change in period of 0.1 nm is roughly equivalent to a change in resonant frequency of 100 GHz, which is the channel spacing in a typical WDM communications system. Therefore, the period of the Bragg grating must be controlled to within 0.1 nm for the device to operate within 100 GHz of the desired frequency. This assumes that period is the only factor which determines the Bragg wavelength. The effective index of the waveguide, given by the refractive indices of the core and cladding, as well as the waveguide geometry, must also be controlled. For the previous generation of devices, the resonant wavelength was limited by the rather coarse control of grating period. Period control was improved, so that it was no longer a limiting factor.

A method was developed for calibrating the IL system to the required precision before exposing the x-ray mask. In this method, the periodicity of the standing wave is compared to a standard of known period. Table 8.1 shows that the required period for the Bragg grating was $p = 244.39$ nm.

The optics of the IL system were aligned so that the angle of interference was $\theta = 45^\circ 55'$. This angle was measured with the goniometer, before the spatial filters were put in place. After aligning the spatial filters, the geometrical parameters of the system were determined by measuring the distances between the spatial filters and the center of the substrate holder. $a = 926.8 \pm 0.25$ mm, $c = 901.7 \pm 0.25$ mm were calculated from these measurements, which would result in a period of 244.9 nm. There was an obvious discrepancy between the angle of interference, as measured

with the goniometer, and the measured distances between the spatial filters. At this point it was not clear which measurement would more accurately predict the actual period of the grating.

Several 4-inch-diameter wafers were coated with plating base (100 nm Ti, 200 nm Au) and a tri-layer ARC/interlayer/resist stack (see Appendix B). They were then exposed with the IL apparatus. After developing the resist and etching through the interlayer and ARC, the wafers were electroplated with gold. The interlayer and ARC were then stripped. One of these wafers was used as a period standard. The actual period of the grating was measured with the *e*-beam tool (VS-2A), taking advantage of the phase measuring capability of the SPLEBL algorithm.

The period measurement was carried out as follows: the period-standard wafer was loaded into the *e*-beam machine. The field size was calibrated to $125.128 \pm 0.01 \mu\text{m}$, so that 32 pixels corresponded to a distance of $244.39 \pm 0.02 \text{ nm}$. Cosine errors in the measurement were eliminated by measuring the rotation of the grating lines with respect to the stage's axes of translation, defining a coordinate system parallel to the grating lines, and performing field calibration with respect to this coordinate system (the *e*-beam machine's control software allows one to define an alternate coordinate system quite simply). The grating was sampled at four locations within the deflection field, as is done during SPLEBL. The sampling windows were separated by 8192 pixels. The phase-locking routine was used to calculate the spatial phase of the grating at each one of the sampling windows. Period deviation from the nominal value of 244.39 nm was determined from the difference in phase between the left and right windows. The phase difference between the top and bottom windows gave the angular mismatch between the beam-deflection axes and the grating lines. The angular error was well below 1 mrad., so that cosine errors were less than 1 part in 10^6 , negligible in this case.

The measurement procedure was repeated 18 times to obtain statistically meaningful data, so as to determine the precision achieved. The results are shown in Fig. 8.5. The mean measured period (at the wafer center) was 244.84 nm, and the

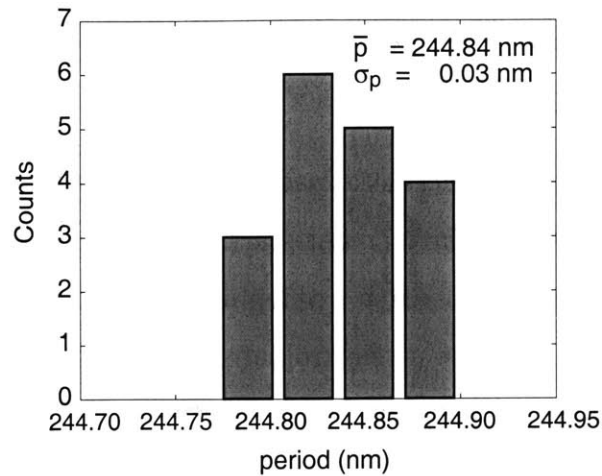


Figure 8.5: Histogram demonstrating the precision achieved in measuring the period of the standard wafer. Accuracy is determined by the wavelength of the stage-interferometer laser, known to 1 part in 10^8 , and cosine errors due to angular misalignment, which are estimated to be below 1 part in 10^6 .

standard deviation was 0.03 nm. The measurement is extremely precise, because the distance across a large number of periods is being measured. Any errors in measuring this distance (field calibration) or in measuring the spatial phase, are divided by the number of periods enclosed within (256 in this case). It is estimated that field size can be calibrated to 1 part in 10^4 , which corresponds exactly to the ratio between the standard deviation and the mean. More precise measurements should be possible without the use of field calibration, e.g., by imaging the grating at the center of the field, moving the stage by a distance corresponding to a larger number of periods, and imaging the grating again. The spatial phase of the grating at these two points will give the period. These measurements are valid only because of the spatial-phase coherence of interferometric gratings, which implies that the grating phase progression is predictable. Grating non-linearity is not significant in this case: for all practical purposes the phase of the grating is linear over the measurement distances used. If the measurement distance is increased to obtain higher precision, the hyperbolic phase progression will have to be taken into account. As expected, the actual period of the grating differed slightly from the target period. The measurement of a and c predicted the period of exposure more accurately than the angle of interference, as

measured by the goniometer.

Once calibrated, the standard grating was used to fine-tune the IL system and obtain the desired period. To calibrate the IL setup, the standard wafer was mounted on the substrate holder. The IL apparatus was configured as a holographic interferometer (see Section 5.5). Using micrometers, the position of the spatial filters was adjusted while the fringe pattern on the fluorescent screen was observed, until less than one fringe could be seen. The implication is that the phase progression of the standing wave matched the grating on the wafer to better than one period over the whole grating. The grating area was 46 mm in diameter, so that it contained ~ 188000 grating lines. Therefore, it was estimated that the standing wave's period matched the grating to within 6 parts in 10^6 . At this point, the IL system was calibrated to the standard: the period of the standing wave at the center of the wafer was 244.84 ± 0.03 nm.

This calibration is valid only when the substrate surface coincides with the plane defined by the calibration wafer's surface, referred to as the *calibration plane*. Substrate surfaces must coincide with the calibration plane if other exposures are to be matched in period to the standard, so substrate thickness variations must be accounted for: the substrate thickness must be measured, and the position of the substrate holder must be altered to compensate for thickness variations. This is particularly difficult in the case of x-ray masks, which are significantly thicker than silicon wafers; their thickness cannot be measured easily because the front surface is a delicate membrane, which may shatter if touched. To circumvent this difficulty, an accurate front-surface reference scheme was implemented using a white-light Michelson interferometer, as shown in Fig. 8.6. The interferometer was built so that the measurement arm was the space between the beam splitter and the substrate surface. The length of the reference arm could be changed by translating the reference mirror with a micrometer-driven stage. Fringes are observable on the screen only if the optical path difference between the arms is less than the coherence length of the light used to illuminate the interferometer. A collimated beam of "white" light,

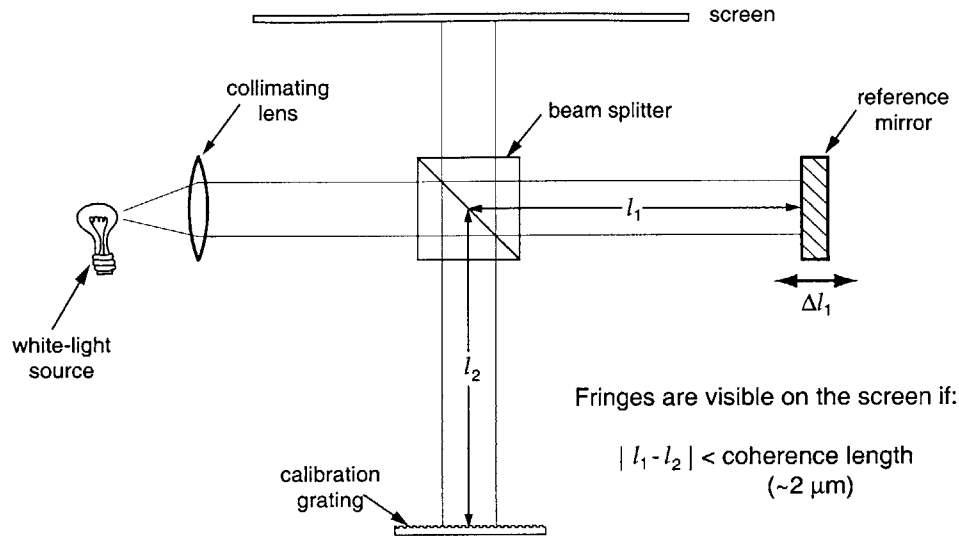


Figure 8.6: Schematic of the white-light Michelson interferometer used as a front-surface reference, to define the calibration plane.

with spectral components between 500 nm and 700 nm (approximately), was used. Wavelengths shorter than 500 nm were filtered out to prevent photoresist exposure. The coherence length is commonly estimated using [96]

$$l_c \approx \frac{\lambda_0^2}{\Delta\lambda} , \quad (8.1)$$

which gives $1.8 \mu\text{m}$ for the wavelength range used¹. Using this method ensures that the substrate surface matches the calibration plane with sufficient precision.

After calibrating the IL apparatus with the standard wafer, the Michelson interferometer's reference mirror was translated until fringes were visible on the screen, thus defining the calibration plane. Since the desired period was 244.4 nm, not 244.8 nm, a fine correction was applied: the geometrical parameter c was changed by $\Delta c = -3.40 \pm 0.01 \text{ mm}$ by moving the Michelson reference mirror towards the beam splitter by that distance.

After calibration, a blank x-ray mask (prepared with plating base and a tri-layer

¹Precision of 5 nm can be achieved with a white-light interferometer if spectral analysis techniques are employed. A resolution of a few μm is sufficient in this case.

stack) was exposed. The mask was mounted on the substrate holder and the substrate holder was moved along the \hat{z} direction until fringes were visible on the white-light interferometer's screen, indicating that the mask surface was at the calibration plane. A grating was then recorded in the resist. The resist was developed, and the interlayer and ARC were dry-etched. The mask was then gold-electroplated to a thickness of 200 nm. The remaining interlayer and ARC were stripped.

This mask, called the *precursor mask* at this point, was then put in the e-beam system, and the period of the grating was measured to be 244.42 ± 0.03 nm at the mask center. Using the procedure described above, excellent control of grating pitch was achieved.

8.3.2 Determination of grating k -vector

To index the k -vector of the IL grating, alignment marks were added to the precursor x-ray mask, which identified the direction of the grating lines unambiguously. These alignment marks were designed to overlay with complementary marks on the *fiducial-definition mask*, so that both mask patterns could be aligned under an optical microscope, producing a *fiducial-grating mask* on which the direction of the fiducial-grating lines was aligned to the fiducial rectangles.

Since the precursor x-ray mask was at this point uniformly covered with a grating, the grating had to be cleared from the areas intended for the alignment marks. The mask was coated with a 300-nm layer of PMMA and placed in the e-beam tool. Large ($300 \mu\text{m} \times 425 \mu\text{m}$) rectangular blocks were exposed in the areas allocated to the alignment marks. The areas exposed were significantly larger than the alignment marks, so that the marks could be subsequently aligned to the grating k -vector and still lie within the grating-free areas. The PMMA was developed and the mask was gold plated a second time. The rectangular areas were plated with a uniform layer of gold, thus erasing the grating image (see Fig. 8.7 (b)). The desired result was to have the rectangular areas free of gold. Because of the additive nature of the

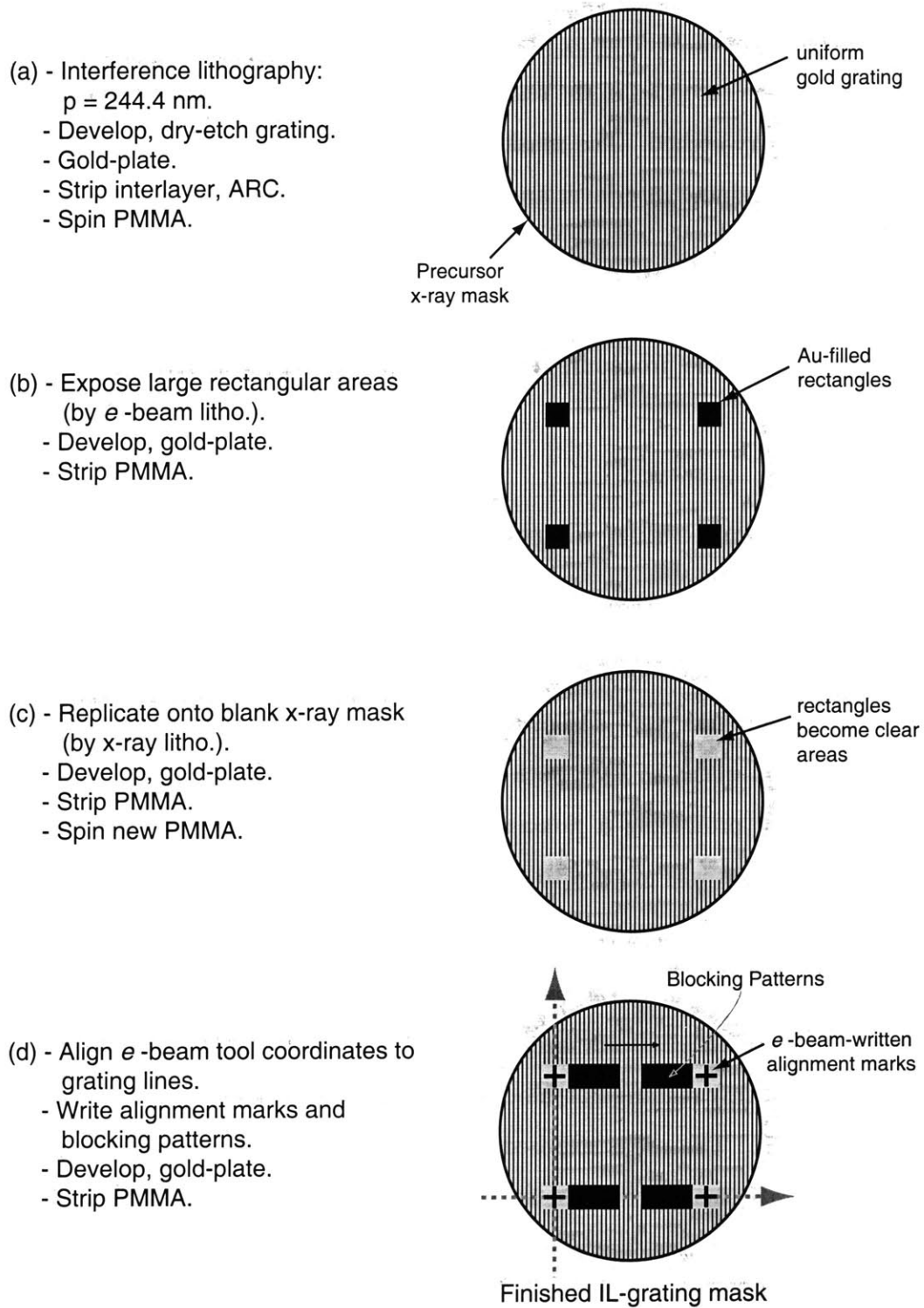


Figure 8.7: Processing sequence used in fabricating the IL-grating mask.

exposure/plating process, an extra lithographic step was needed. To reverse the tone of the image and obtain empty spaces, the mask was replicated onto a blank, PMMA coated x-ray mask by means of x-ray lithography, using the Cu_L line ($\lambda = 1.32$ nm). The two masks were brought into close proximity (approximately $4 \mu\text{m}$ apart). The gap between them was set with aluminum studs, which were evaporated onto the mesa of the grating mask². The masks were placed 25 cm away from the x-ray source, and a 12 hour exposure was carried out. The PMMA on the blank mask remained unexposed within the shadows cast by the gold absorbers in the original mask, so that upon development and plating of the replica, the phase of the grating was shifted by 180° , and the large rectangles became empty (i.e., unplated) space, as shown in Fig. 8.7 (c).

The remaining PMMA was stripped from the replica, and another PMMA layer was applied. The mask was then placed in the *e*-beam tool and rotation of the grating with respect to the stage axes was measured by recording the (x, y) locations of several points along a single grating line, over a distance of approximately 3 cm. A new, rotated coordinate system (\hat{x}_g, \hat{y}_g) was defined, which matched the measured orientation of the grating lines. Four alignment marks were then *e*-beam written within the grating-free areas. Two marks are sufficient to index the grating rotation, but two extra marks were written for redundancy. The positions of the marks were defined within the rotated coordinate system, so that they would overlay with complementary marks on the fiducial-definition (optical) mask. In addition to the alignment marks, other large areas were exposed with the *e*-beam, in order to block x-ray exposure. The function of these blocking areas will become clear in the next section. The mask was developed and plated, resulting in the pattern shown in Fig. 8.7 (d). After the PMMA was stripped, the IL-grating mask was complete.

To verify the alignment between the *e*-beam-written marks and the grating lines, the mask was again placed in the *e*-beam machine. The stage coordinates (x, y) of two alignment marks were used to define the mask's coordinate system (x_g, y_g)

²For a description of the mask/microgap-stud configuration used, see refs. [104, 174, 175].

(($x_g = 0, y_g = 0$) was defined to be the center of the mask). The grating's spatial phase was measured along several points, where x_g remained constant and y_g was assigned random values between -1.5 cm and +1.5 cm. The spatial phase of the grating remained constant within one tenth of a period over a distance of 3 cm. Consequently, the angular alignment between the e -beam-written marks and the k -vector of the grating was estimated to be $\sim 0.8 \mu\text{rad}$. ($\tan^{-1}(\frac{24 \text{ nm}}{3 \text{ cm}}) \approx 8 \times 10^{-7}$), a negligible error.

To align an x-ray mask to an underlying substrate, one observes the overlay of the alignment marks on the mask with marks on the substrate. The substrate marks are imaged through the membrane. To facilitate alignment, light transmission through the membrane is increased by removing the x-ray-mask plating base in the areas surrounding the alignment marks. A procedure developed by M. Burkhardt [176] allows the plating base to be stripped without affecting the gold absorbers. Figure 8.8 shows a scanning-electron micrograph of one set of alignment marks on the finished IL-grating mask.

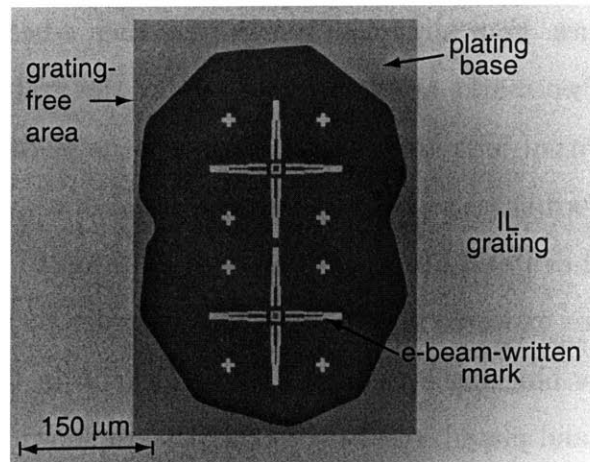


Figure 8.8: Scanning electron micrograph of the e -beam written alignment marks on the IL-grating mask. The plating base has been cleared from the irregularly-shaped area to facilitate alignment under an optical microscope.

8.4 Fabrication of fiducial-grating mask

Two lithographic exposures were combined to fabricate the fiducial-grating x-ray mask, as shown in Fig. 8.9. An optical exposure was performed on a blank, PMMA-

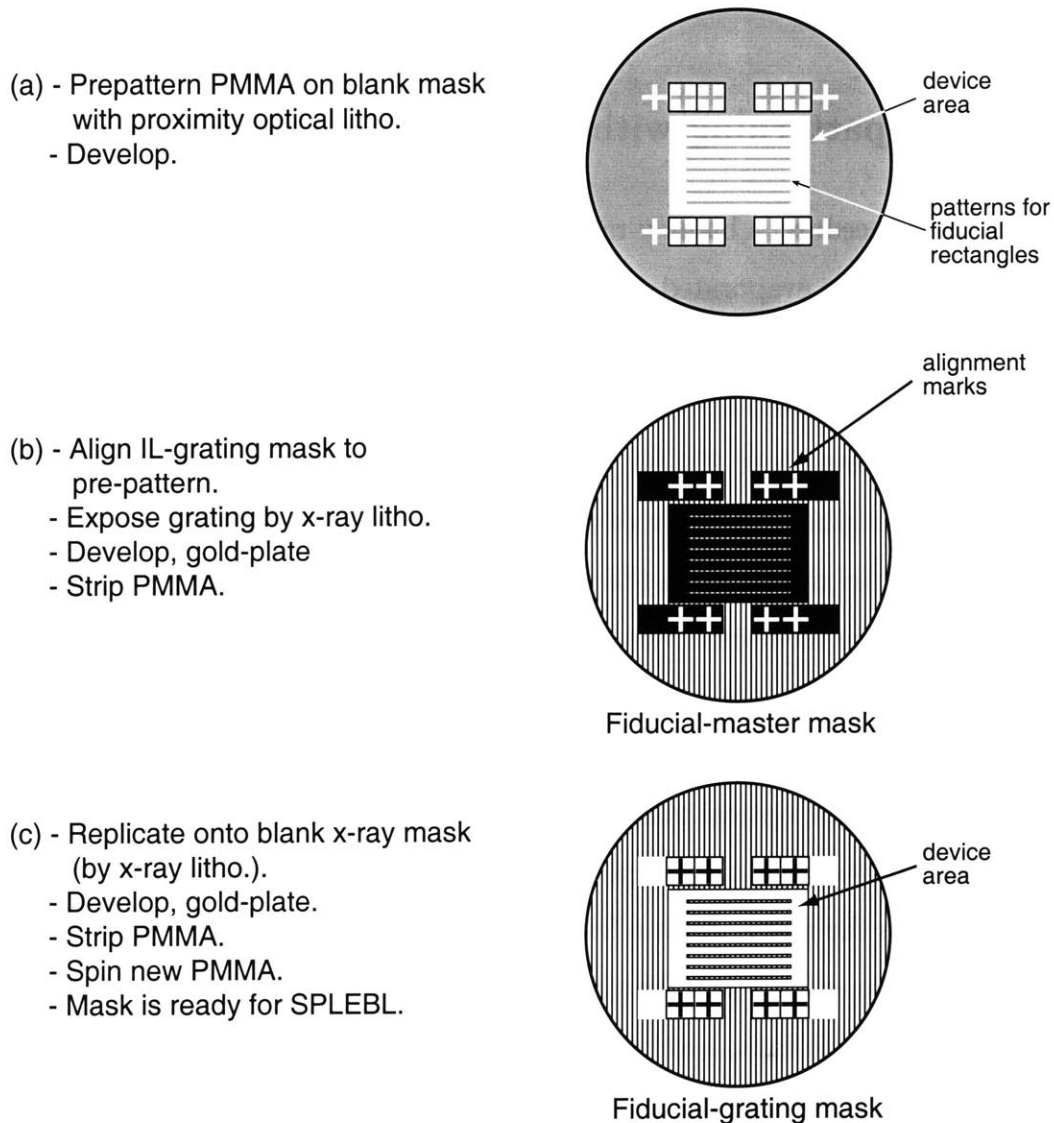


Figure 8.9: Fabrication sequence used to fabricate the fiducial-grating mask.

coated x-ray mask, using the fiducial-definition mask. After development, PMMA was left in the areas allocated to the fiducial gratings, as well as two sets of alignment marks. One set of marks was used to align the IL-grating mask to the pre-patterned PMMA. The second set of marks was designed to align the finished mask to the

waveguide level during device fabrication. Note that the location of all alignment marks was defined by the optical masks, which were a matched set. The location of the fiducial gratings (and hence of the SPLEBL-written gratings) was likewise defined by an optical mask. In this way, size mismatch between different lithographic levels in this mix-and-match process was effectively eliminated.

8.4.1 Pre-patterning with the fiducial-definition mask

To begin this procedure, a blank x-ray mask was coated with plating base. Aluminum microgap studs were evaporated on the mask's mesa, to a height of $2\ \mu\text{m}$. The mask was then spin coated with 280 nm of PMMA. The pattern on the fiducial-definition mask was transferred into the PMMA by means of proximity optical exposure, using light with a wavelength of 220 nm (PMMA is sensitive to this wavelength, but not to longer wavelengths). In order to reproduce the smallest features on the mask ($1\ \mu\text{m}$) faithfully, the gap between the optical mask and the membrane surface had to be minimized. The membrane was brought into close proximity to the optical mask by applying gentle pressure to its back side with a nitrogen stream [157], as shown in Fig. 8.10. The exposure was carried out as follows: the x-ray mask was placed on a special holder. The optical mask was carefully placed on the microgap studs. Air was trapped between the membrane and the optical mask, causing the membrane to bulge away from the mask. After a few minutes, the trapped air had escaped, and the gap had settled to $\sim 3-4\ \mu\text{m}$. The gap was estimated by illuminating the setup with quasi-monochromatic light, and looking at the fringes that resulted. These fringes are due to Fabry-Perot interference in the cavity formed by mask and membrane surfaces. The length of the cavity — the gap — can be estimated by changing the viewing angle and observing the transitions between constructive and destructive interference. A light source centered at $\lambda = 546\ \text{nm}$ ³ was used. Fringes are counted as the viewing angle is varied from 0° (normal) to 45° . For this wavelength, the number of fringes counted, minus one is roughly equal to the gap in μm [174].

³Edmund Scientific, Barrington, NJ, part no. J38-033.

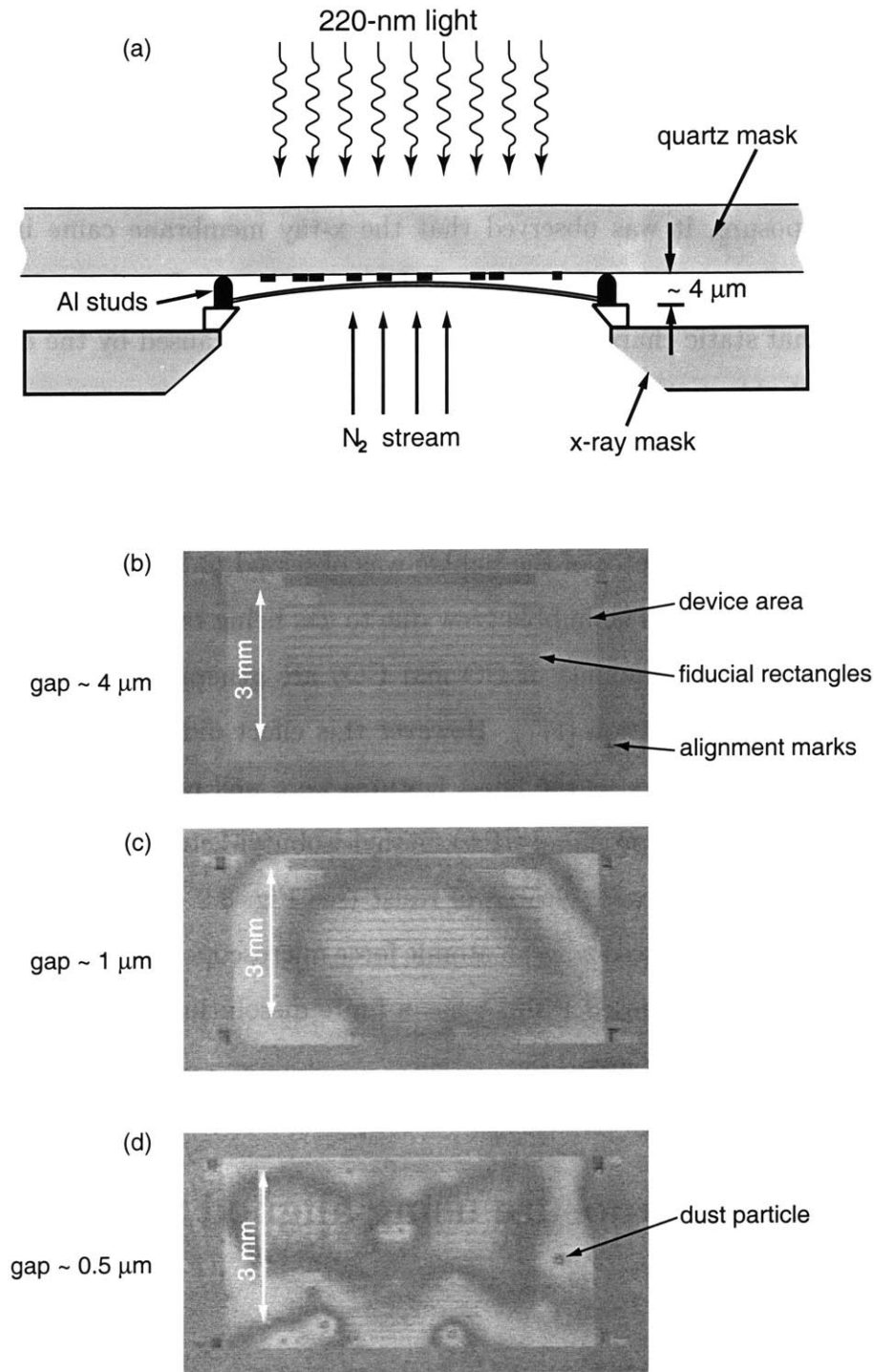


Figure 8.10: Method used to achieve a small gaps between the optical mask and the x-ray membrane, in order to minimize diffraction effects. (a) Schematic of the setup. (b), (c), and (d) Interference fringes observed as the gap decreased from $\sim 4 \mu\text{m}$ to $\sim 0.5 \mu\text{m}$. Note that dust particles can affect the quality of the exposure; extreme care should be taken to ensure that the number of particles on either surface is minimized.

Next, the nitrogen flow was turned on. N_2 pressure was regulated to 2 p.s.i. and flow rate was controlled with a needle valve. The flow was slowly increased, until the measured gap became less than $1\ \mu\text{m}$. The masks were then placed under the UV source and exposed for approximately 15 min. (the dose used was $780\ \text{mJ}/\text{cm}^2$).

During exposure, it was observed that the x-ray membrane came into contact with the chromium on the outer edges of the pattern area, forming a bubble. It is conjectured that static charge buildup on the membrane, caused by the dry-nitrogen flow on its back side, induced this condition. The bubble grew as exposure progressed, as was confirmed by halting the exposure at various times before completion and counting the number of fringes between the edges (which were in contact) and the center. The gap at the center of the bubble was observed to be as large as $2.5\ \mu\text{m}$ at the end of the exposure. The bubble grew due to gas being released during exposure: it is known that small amounts of CO and CO_2 are generated during exposure of PMMA to deep-UV radiation [177]. However this effect did not significantly affect the quality of the exposure — the finest features were well reproduced. The PMMA was developed in a 2:1 isopropanol (IPA):methyl-isobutyl-ketone (MiBK) solution for 60 s. The exposed areas were cleared of resist (see Fig. 8.9 (a)). At this point, the resist thickness was measured with an atomic force microscope (AFM) and determined to be 250 nm. The unexposed PMMA has a finite dissolution rate in the developer, resulting in film thickness loss [178].

8.5 Grating exposure using aligned x-ray lithography

X-ray lithography was used to expose the fiducial gratings on the prepatterned x-ray mask. The e -beam-written alignment marks were used to align the k -vector of the gratings to the axes of the prepattern. An x-ray exposure system with a mask aligner [160, 179, 180] was used to perform the exposure. Figure 8.11 is a photograph

of the system, which consists of an alignment microscope and an exposure station — an x-ray source placed on top of an air-tight enclosure.

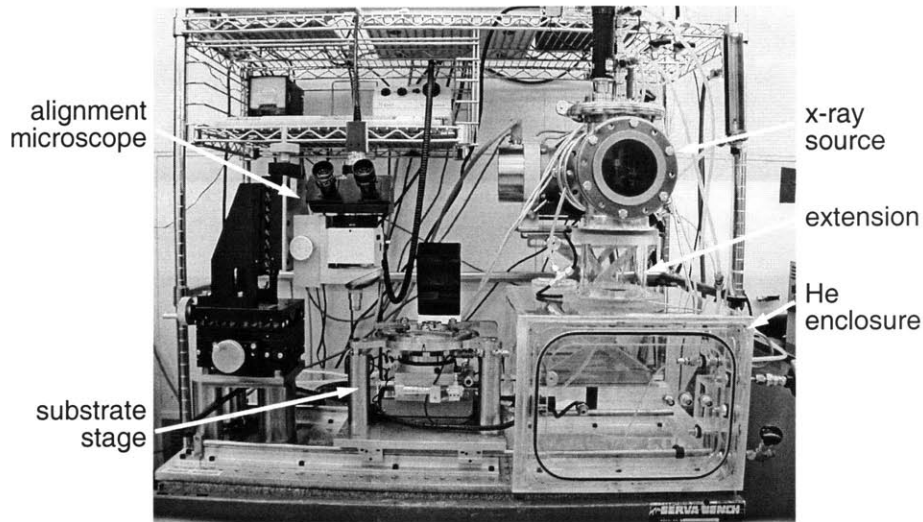


Figure 8.11: Photograph of the x-ray lithography system used to align and expose the IL-grating pattern on a pre-patterned x-ray mask. The x-ray source was moved away from the mask/substrate in order to decrease penumbral blur, by adding an extension to the helium enclosure

The alignment apparatus (which holds the mask and substrate) sits on a platform that can be translated between the alignment and exposure stations. The mask is aligned to the substrate under the microscope, and the platform is moved into the exposure station. The enclosure is sealed and filled with helium, since the Cu_L line is strongly absorbed by air. Once all air within the enclosure has been replaced by helium, exposure can proceed.

In order to test the quality of the exposure, the IL-grating mask was used to print a grating on a PMMA-coated silicon wafer before performing an aligned exposure on an x-ray mask. After developing the resist, the silicon wafer was cleaved, and the grating was observed in cross section with the SEM. The quality of the grating was found to be quite poor (see Fig. 8.12). Grating lines were ill-defined and significant resist was lost, indicative of low contrast. This result is almost certainly due to penumbral blur. The area of x-ray emission within the source is circular, and approximately 1 mm in diameter. The distance between source and mask was 13.9 cm, and the mask-

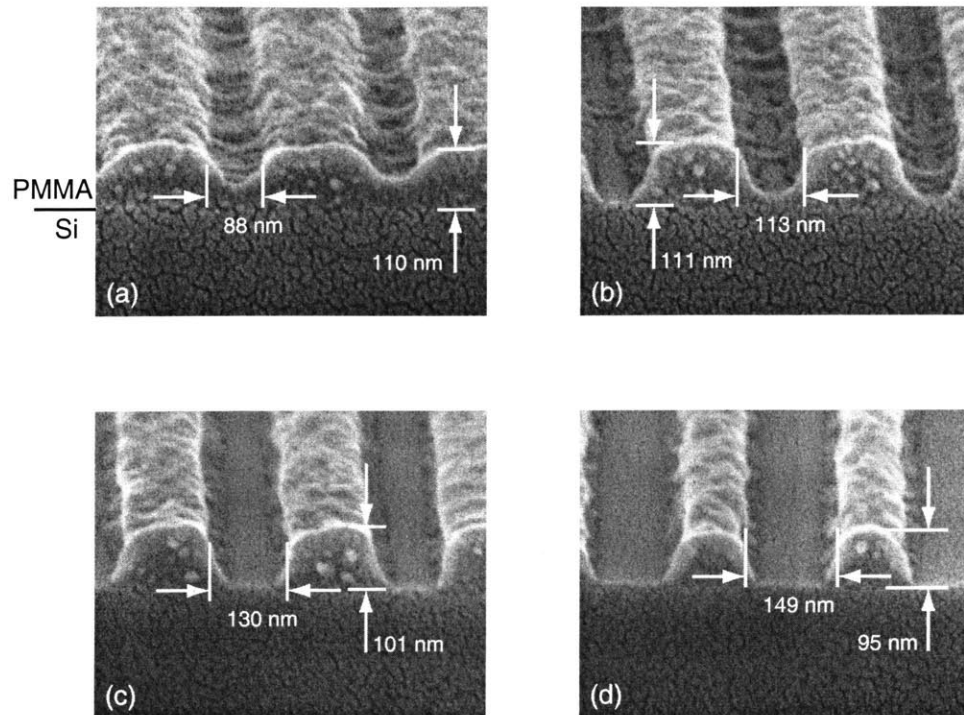


Figure 8.12: Cross-sectional scanning electron micrographs of a grating exposed in PMMA, during various stages of development. The exposure conditions were: initial resist thickness – 275 nm; source-to-mask distance – 13.9 cm; exposure time – 10 h. The spaces on the mask were 78-nm wide. (a) After 10 s of development. (b) 20 s. (c) 30 s. (d) 40 s. The poor process latitude was attributed to excessive penumbra

to-substrate gap was 4 μm . Accordingly, the extent of the penumbra was calculated to be ~ 30 nm. Edges on either side of each grating line were blurred by penumbra, i.e, 60% of each 120-nm-wide line was partially exposed, resulting in low contrast.

To minimize penumbra, one can either reduce the x-ray emission source diameter, or increase the distance between source and mask. The x-ray lithography apparatus at MIT relies on electron bombardment sources: electrons are emitted from a heated tungsten filament and are accelerated to an energy of 8 keV by an electric field. They impinge upon a copper target, which emits x-rays. The electric field focuses the electrons onto a spot at the target. Logically, the diameter of the area bombarded by electrons determines the size of the x-ray source.

A significant amount of effort was invested in trying to obtain a smaller x-ray

source by finely adjusting the electrodes that focus the electron beam on the target. Unfortunately, these efforts were unsuccessful. The only other option was to move the source away from the mask, by adding an extension to the helium enclosure (see Fig. 8.11). The source-to-mask distance was increased to 25 cm, reducing the penumbra by half. However this reduced the x-ray flux by a factor of four, thus increasing the time required to expose PMMA to more than 40 hours. The result of a test exposure with increased distance, shown in Fig. 8.13, indicates that the grating is adequately reproduced with this configuration. Longer exposure times were justified by the obvious gain in process latitude. Process latitude was further

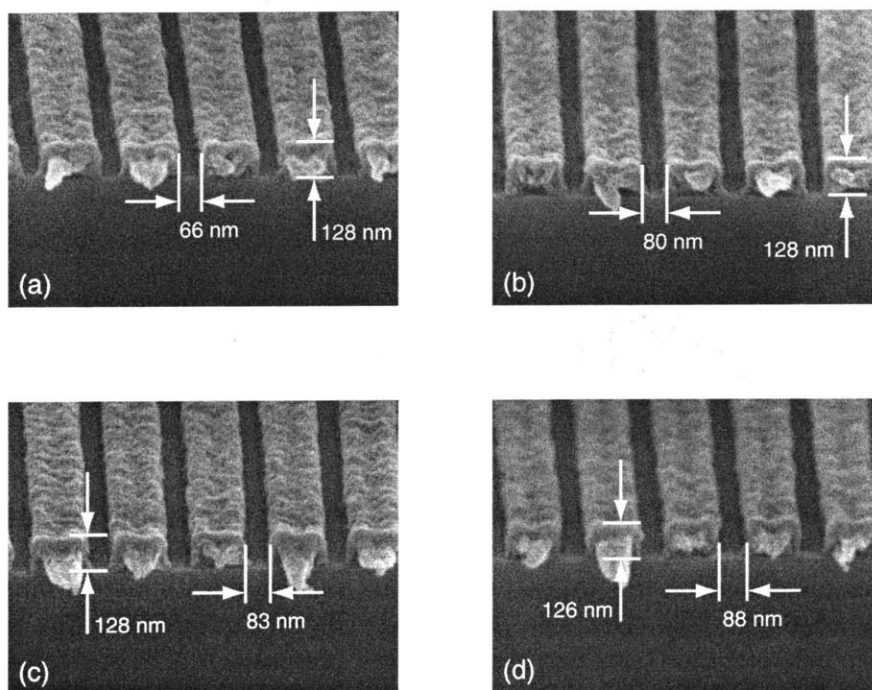


Figure 8.13: Cross-sectional SEM's of a grating exposed after increasing the source-to-mask distance to 25 cm. The initial resist thickness was 160 nm, and the exposure was 28 hours long. (a) After 45 s. of development. (b) 60 s. (c) 75 s. (d) 90 s. Exposure latitude has been greatly enhanced. Overdevelopment by 100% resulted in less than 10% decrease in linewidth.

improved by using a different developer mixture of 63:21:16 IPA:MiBK:MEK (methyl-ethyl-ketone), which was seen to provide better contrast for *e*-beam-exposed PMMA than the usual 2:1 IPA:MiBK solution [181].

During alignment of the IL-grating mask to the pre-patterned PMMA, it was observed that obtaining adequate overlay on all four marks was not possible (see Fig. 8.14), probably due to a scale mismatch between the *e*-beam-written marks and the optical mask set. However, since only angular alignment was required, the mask was positioned so that optimal alignment was attained for both left-hand-side marks only.

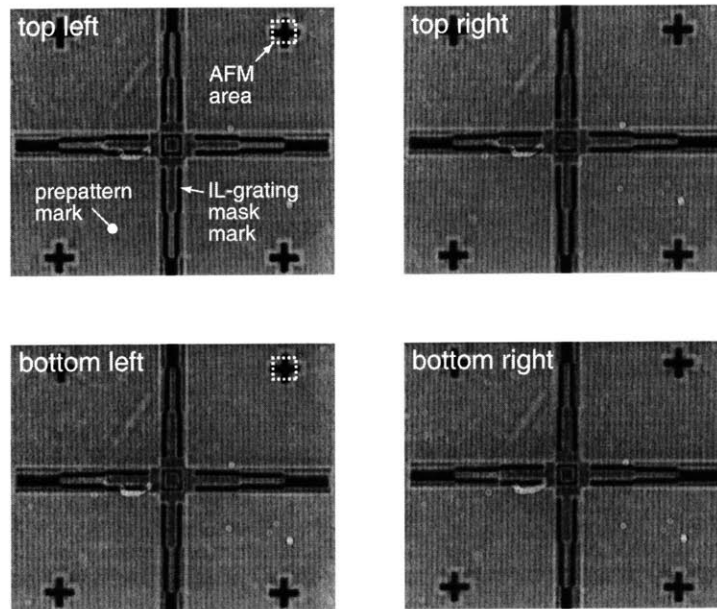


Figure 8.14: Images of alignment marks, as observed through the alignment microscope, which was equipped with a 20 \times , long-working-distance objective. The mask was positioned on the pre-pattern, so that the left side alignment marks were properly overlaid. The right side marks were slightly misaligned, due to a size mismatch between the IL-grating mask and the pre-pattern. (This effect is hardly visible in these images — it was quite challenging to obtain good alignment by observing these marks with the optical microscope.) This did not represent a problem, since only angular alignment was needed. The “AFM areas” were scanned with an atomic force microscope during development, to measure overlay errors.

After x-ray exposure, the mask was developed in the IPA:MiBK:MEK mixture at $21 \pm 0.1^\circ\text{C}$ for 70 s. There is some dose variability between x-ray exposures, so development was done in 10-second increments, followed by inspection under the optical microscope. When the resist was seen to clear in large areas, the mask was further developed by 10%, to ensure that the fine grating patterns developed out

properly.

Overlay between pre-pattern and IL-grating exposure was measured in mid-development (after 30 or 40 seconds of development) by scanning both left-hand-side alignment marks with an AFM. An example is shown in Fig. 8.15. Overlay information was lost at the completion of development, since the pre-patterned marks disappeared.

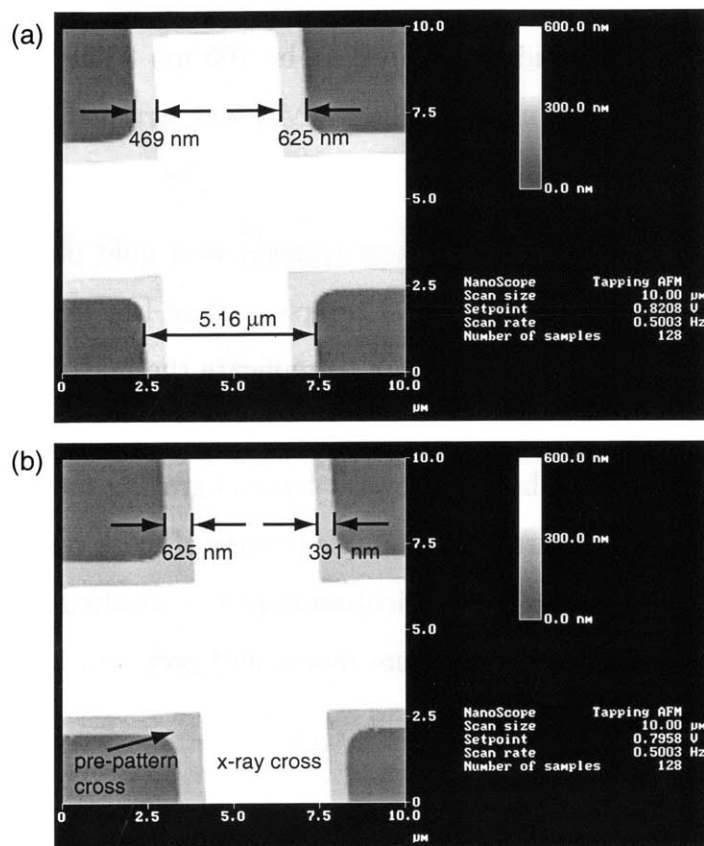


Figure 8.15: AFM images of the top-left (a) and bottom-left (b) alignment marks. The total misalignment for this exposure was -195 nm. Hence, the angular error between the IL-grating image and the pre-pattern was -35 μ rad. (i.e., the IL-grating was rotated by this angle with respect to the prepattern).

Three *fiducial-master masks* were fabricated using the prepattern/aligned x-ray exposure process. The maximum overlay error measured with the AFM was approximately 250 nm. The distance between top and bottom alignment marks is 5.6 mm. Angular misalignment between the grating and prepattern was thus estimated to be

under $50 \mu\text{rad.}$, significantly better than the 0.5° attained for the previous device generation.

Alignment marks, designed to align the x-ray mask to the waveguide optical layer, were transferred to the fiducial-master during the prepattern exposure. The large blocks exposed by *e*-beam on the IL-grating mask protected these marks from x-ray exposure (see Fig. 8.9 (b)).

After development of the x-ray exposure was complete, PMMA thickness was measured with the AFM, and determined to be 200 nm. The mask was then gold plated to a thickness of 200 nm, and the PMMA was stripped. This completed the fabrication of the fiducial-master mask.

Since the areas allocated to the Bragg gratings were gold plated, the tone of the pattern on the master mask had to be reversed. The last step in fabricating the fiducial-grating x-ray mask was therefore to replicate the master onto a blank mask using x-ray lithography, thus reversing the tone of the pattern (see Fig. 8.9 (c)). This extra step is advantageous, because several fiducial-grating masks can be obtained from the master through the relatively simple process of mask replication, as opposed to the lengthy and labor-intensive fabrication sequence required to make the master. Several replicas of the master mask were made, and prepared for SPLEBL by spin-coating a new layer of PMMA onto them.

8.6 Generation of Bragg-grating data

Fabrication of the second generation of optical devices was an ambitious undertaking. Several types of devices were included in the mask set, and the total number of devices was increased, as compared to the previous generation. Figure 8.16 shows the general device layout of one chip and identifies the different device types.

The layout of the previous chip had been simple enough that the Bragg-grating pattern data could be generated and laid out manually, field by field. The complex-

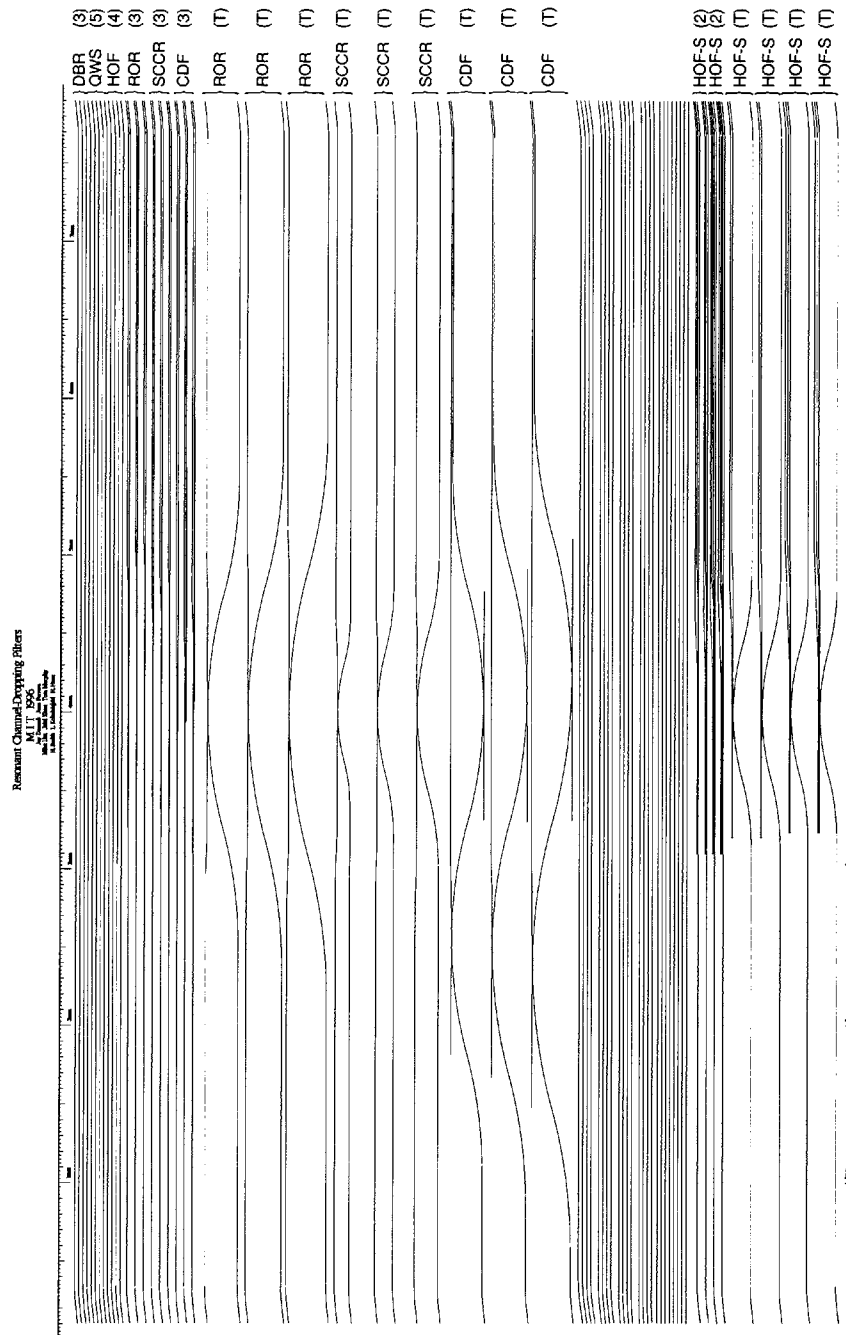


Figure 8.16: Layout of the CDF mask. Several kinds of devices have been included in the design: distributed Bragg reflectors (DBR), quarter-wave shifted transmission resonators, side-coupled resonant optical reflectors (ROR) [182, 183], single side-coupled receivers (SCCR) [183], channel-dropping filters (CDF) [119], and higher-order channel-dropping filters (HOF) [184]. In some devices (labeled “T”), the bus waveguide is curved, so that the evanescent coupling between bus and resonators changes as a function of position.

ity and size of the data set for the current device generation made manual layout impossible — automatic generation using a computer was required. Computer code was written to generate the Bragg grating patterns. The description of Bragg gratings was made as general as possible: a Bragg grating can contain as many as 5 quarter-wave shifts, used in higher-order filters [138]. Moreover, several gratings can be contained within one device. (For example, the channel-dropping filter relies on two quarter-wave-shifted gratings.)

Grating characteristics are specified as a series of commands within a plain-text script file. The code (called `bragg_layout`) reads the script file, parses the commands, and generates the appropriate pattern data. The syntax used in the script file will be described briefly. At the top of the script, a series of parameters is defined using the following commands:

```
lambda = <double>;  
fieldsize = <int>;  
virtual_fieldsize = <int>;  
pixel_period = <int>;  
line_dx = <int>;  
outrig_w = <int>;  
outrig_filename = <string>;
```

`lambda` is the smallest unit of length in the pattern, i.e., the pixel size⁴. `lambda` is specified in micrometers, as a double-precision floating-point number. All other parameters, with the exception of `outrig_filename` (which is an alphanumeric string) are given as non-negative integers, in units of `lambda`. `fieldsize` is the number of pixels in one field, 16384 for VS-2A. Since fields are overlapped so as to measure interfield errors, Bragg-grating patterns can occupy only a fraction of the field — described by `virtual_fieldsize`, which was set to 8192 pixels, or one half of the field. `pixel_period` is the number of pixels in one period of the Bragg grating; this parameter was set to 32. Consequently, $\lambda = \frac{0.2444 \mu\text{m}}{32} = 0.0076375 \mu\text{m}$. `line_dx` specifies the width of the *e*-beam-written grating lines. Although a linewidth of 16 pixels is the desired value (for 50% grating duty cycle), the non-zero beam diameter

⁴this unfortunate choice of terminology was borrowed from computer-aided design of VLSI circuits and is not to be confused with wavelength!

must be taken into account: `line_dx = 8` was used. The width of the outrigger structures was specified with `outrig_w = 576`: two 256-pixel-wide gratings on either side of a 64-pixel gap.

Positions of all the outrigger-grating centers are written to an output file named by `outrig_filename`. If a file with that name already exists, its contents can be cleared with the command

```
clear_outrig;
```

After the initial parameter definitions, the layout of Bragg gratings is specified by a sequence of commands of the form

```
device("device_name", x_c, y_c, fid_y1, fid_y2, fid_w, d);  
begin;  
grating(start_x, center_y, width, teeth_1, teeth2, teeth3, teeth4,  
        teeth5, teeth6);  
grating(start_x, center_y, width, teeth_1, teeth2, teeth3, teeth4,  
        teeth5, teeth6);  
...  
end;
```

A device is defined as a set of gratings which are written within the area enclosed between two given fiducial gratings. The pattern data are written to a file called `device_name.kic`, in a format readable by KIC [185], a popular program for circuit design. The KIC format is based on CIF [186]. The KIC pattern data was translated into a binary file readable by the *e*-beam tool, using converter software written by S. Silverman.

`x_c` and `y_c` are the coordinates (in μm) of the center of the first *e*-beam field to be written. For quarter-wave shifted gratings (or multiple-QWS gratings), `x_c` can be optimized so that field boundaries are as distant as possible from the quarter-wave shifts, where the optical mode is strongest. This minimizes the effect of interfield errors on the performance of the devices. [139, 125]. `fid_y1` and `fid_y2` are the coordinates of the fiducial grating centers along the \hat{y} direction. `fid_w` is the width of the fiducial gratings (in μm) and `d` is the distance (in μm) between the edges of the fiducial gratings and the centers of the outrigger structures.

Within each `device` environment, there can be multiple `grating` commands. The parameters that define each grating are: `start_x`, the x coordinate (in μm) of the left edge of the first grating line; `center_y` the y coordinate (in μm) of the grating's center; `width`, the Bragg-grating width (in μm); `teeth1` . . . `teeth6`, the number of periods before a QWS (for a straight grating only `teeth1` is non-zero, for a QWS grating `teeth1` and `teeth2` are non-zero, etc.)

Figure 8.17 shows a simple script and the resulting grating pattern. The size of grating features has been enlarged, to show clearly how the data in each field are generated and how the fields overlap together, producing the desired result. The script used to generate the Bragg-grating data for device fabrication is reproduced in Appendix E.

8.7 Bragg grating exposure

The same procedure used for the previous device generation was used to expose the e -beam written gratings. The mask coordinate system was defined by measuring the position of two alignment marks on the fiducial-grating mask. The direction of the grating lines was observed to be well aligned to the mask's coordinate system — no angular error could be measured. A field size of $125.13 \pm 0.01 \mu\text{m}$ was used to expose the grating segments. The beam current was set to 116.7 pA and a pixel dwell-time of $2.8 \mu\text{s}$ was used, so that the nominal exposure dose was $560 \mu\text{C}/\text{cm}^2$. Field displacement statistics during exposure were essentially the same as those reported in Section 7.1 ($\bar{x} = -3.1 \text{ nm}$, $\sigma_x = 2.5 \text{ nm}$). After exposure, the resist was developed in 63:21:16 IPA:MiBK:MEK at $21 \pm 0.1^\circ\text{C}$ for 90 seconds. The gratings were then gold plated to a thickness of 200 nm. The fabrication of the Bragg-grating mask was then complete. Figure 8.18 shows scanning-electron micrographs of some of the device gratings. The Bragg-grating x-ray mask was used in conjunction with the pre-pattern and waveguide optical masks to define and etch the structure shown in Fig. 8.3, which proved that the fabrication process worked as expected.

(a)

```

# File example.script
# generate a simple stitched QWS grating

#define parameters:
lambda = 0.005; # in um (for fieldsize 81.92 um)
fieldsize = 16384;
virtual_fieldsize = 8192;
pixel_period = 128;
line_dx = 64;
outrig_w = 256;

device("example", 0.0, 0.0, 30.0, -30.0, 10.0, 5.0);
begin;
grating(0.0, 0.0, 5.0, 64, 64, 0, 0, 0, 0);
end;

```

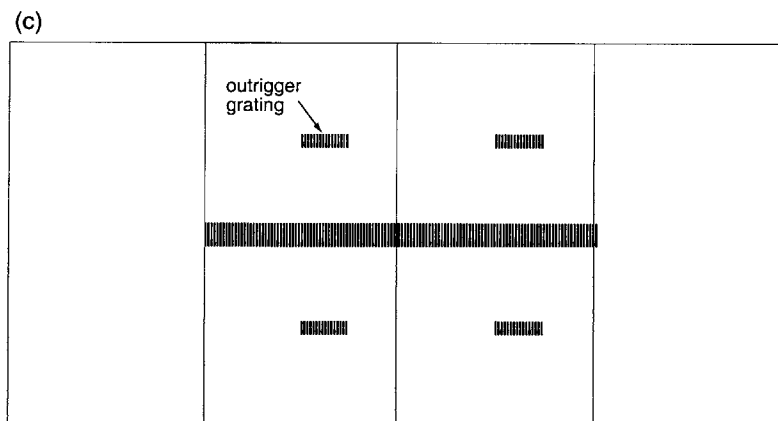
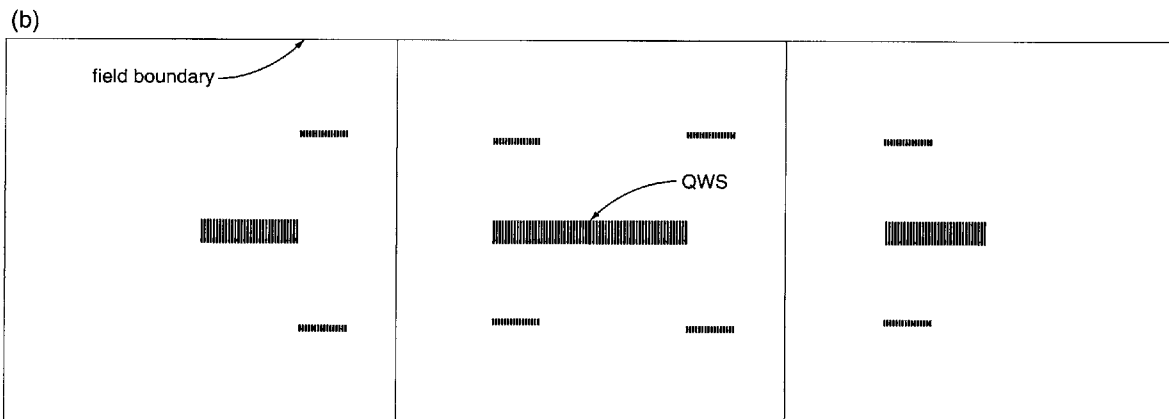


Figure 8.17: (a) Sample script, used to generate a simple QWS grating. (b) Pattern data generated for each *e*-beam field. (c) Once the fields are appropriately overlapped, the desired pattern results.

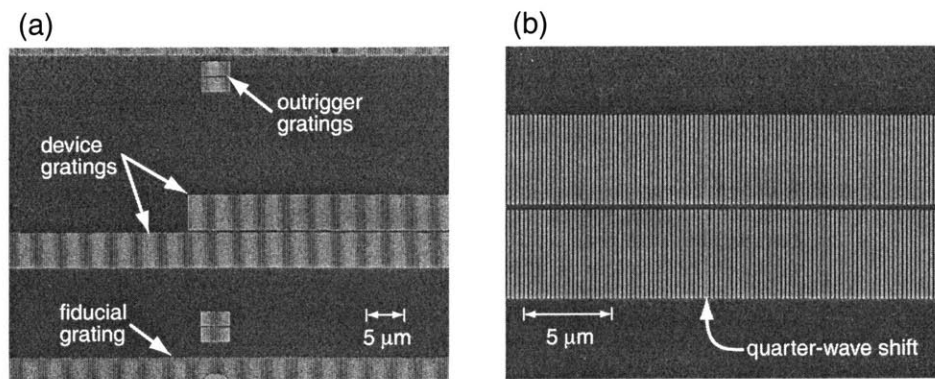


Figure 8.18: Scanning electron micrographs of *e*-beam-written Bragg gratings for a second-order filter. The bright and dark bands in (a) are a moiré pattern, due to the interaction of the SEM raster scan and the periodic grating.

The mask was used to fabricate devices as soon as it was completed, and there was no opportunity to measure the outrigger gratings to determine interfield errors. There is little reason to believe, however, that interfield error statistics will be different than those obtained for the previous device generation, as it was shown that field placement errors depend on the short-term stability of the *e*-beam tool. Once devices are fabricated and tested, and the mask is no longer used, it'll be a simple matter to automatically measure all interfield errors.

At the time of writing, the first group of devices is being fabricated. Optical measurement results should be available shortly, and will be reported in the technical literature.

Chapter 9

Conclusion

Research on two aspects of the spatial-phase-locking method has been reported in this document: the characterization of periodic structures exposed by interference lithography and the implementation of a segmented-grid spatial-phase-locking scheme, which was applied to the fabrication of grating-based optical devices.

Interference lithography is a natural candidate technology to fabricate stable metrological standards for position measurement and pattern-placement control in the nanometer domain. An investigation was undertaken to determine if structures fabricated by IL could provide placement information over large areas ($\sim 10 \text{ cm} \times 10 \text{ cm}$) with errors of only a few nanometers. A simple model was developed to describe the operation of the IL apparatus, in order to evaluate the impact of different variables on the phase progression of gratings (and hence of grids, since a grid consists of two orthogonal gratings). Using this model, the conclusion was quickly reached, that it is infeasible to fabricate gratings with such tight error tolerances repeatably. Several experimental procedures were developed to measure the phase progression of IL gratings, based on the concept of self-comparison. The data obtained from these measurements support the conclusion reached from the theoretical model. It was found that substrate mounting errors and uncertainty in setting the position of the spatial filters limited the accuracy of the measurements to 50 nm in a 30 mm \times

30 mm area. This number is a direct measure of the repeatability one can expect from the system. The measurements reported here are by no means definitive, and systematic errors can certainly be reduced, but the author would like to venture the guess that accuracies of a few nanometers over large areas will not be achieved by such a brute-force approach.

The measurements showed, however, that the phase progression of IL gratings is a smooth monotonic function; high-frequency variations in the spatial phase were not detected. While the phase progression of a grid might not be predictable *a priori*, an alternative might be to fabricate a “master grid”, whose phase progression would be characterized by means of a high-end coordinate measuring tool. A means to replicate this master grid repeatably would then be needed. If the idea has merit, further research efforts could be directed towards this objective. A more detailed proposal can be found within the body of this dissertation, in Chapter 4.

A variant of the spatial-phase locking technique, using a segmented reference, was applied to the fabrication of Bragg gratings by electron-beam lithography, where spatial-phase coherence is important, but not absolute position. The segmented-grid method was first implemented on the vector-scan tool VS-6 at IBM Research. Interfield errors were measured from the overlap of specially designed outrigger structures. The actual interfield errors obtained with the VS-6 system were found to be significantly larger than the detectivity of the spatial-phase-locking algorithm. From the measured interfield errors, field placement errors were estimated to have a magnitude (mean + 3σ) of 58 nm. The additional errors were attributed to random sample rotations introduced by the locking stage in the VS-6 tool. This hypothesis was not verified, however, as no further experiments were carried out with this system. The segmented-grid method was then implemented on the VS-2A system at MIT. The field placement attained with this tool (estimated from outrigger measurements to be 20 nm mean + 3σ) was significantly better. Experimental evidence indicated that field placement was limited by the short-term stability of the VS-2A tool, which is restricted by the resolution of the laser interferometer. A simple, low-cost solution

was proposed to increase the resolution of the interferometer. This scheme was partially implemented and very encouraging preliminary results were obtained. Specific proposals for further work on this area are given in Chapter 7.

The fabrication procedures developed for this application achieved considerable success. A first generation of devices was fabricated and tested. The devices demonstrated satisfactory performance. Several refinements were introduced into the segmented-grid method, to ensure that the period and orientation of the Bragg gratings could be adequately controlled. These refinements resulted in a robust lithographic technology, which is specifically designed to fabricate Bragg-grating-based integrated-optical devices. The Bragg-grating patterns generated with this technology satisfied strict design specifications. This technology was used in fabricating a second generation of devices, which includes channel-dropping filters. At the time of writing, the devices are in the last stages of fabrication. The author has been involved in a collaborative effort to fabricate channel-dropping filters for several years, and eagerly awaits the measurement results.

Appendix A

Substrate preparation for IL exposure

The following procedure was used to prepare the wafers used in the moiré pattern experiment. The antireflection-coating (ARC) layer thickness is optimized to minimize substrate reflections.

1. Clean wafer surface by immersing in RCA organic clean solution (5:1:1 DI water:hydrogen peroxide:ammonium hydroxide, at 80°C).
2. Spin-coat a 350-nm-thick layer of Brewer ARC-XL compound.
3. Bake in an oven at 180°C for 30 min.
4. Spin-coat a 170-nm-thick layer of thinned Shipley 1813 photoresist.
5. Bake in oven at 90°C for for 30 min.
6. Store in a light-tight container to prevent unwanted exposure.

Appendix B

Substrate preparation for tri-level resist process

The gratings described in section 5.3 were recorded on a tri-layer ARC/oxide interlayer/resist stack. The interlayer was used as a hard mask, to transfer the resist image through the ARC layer to the wafer surface via reactive-ion etching. The wafers were prepared according to the following procedure.

1. Clean wafer surface by immersing in RCA organic clean solution (5:1:1 DI water:hydrogen peroxide:ammonium hydroxide, at 80°C).
2. Spin-coat a 350-nm-thick layer of Brewer ARC-XL compound.
3. Bake in an oven at 180°C for 30 min.
4. Evaporate a 40-nm-thick layer of silicon oxide (SiO_x). An *e*-beam evaporator was used.
5. Immediately after evaporation, apply hexamethyl-disilazane (HMDS) as an adhesion promoter for the resist:
 - (a) Place the wafer in the resist spinner.

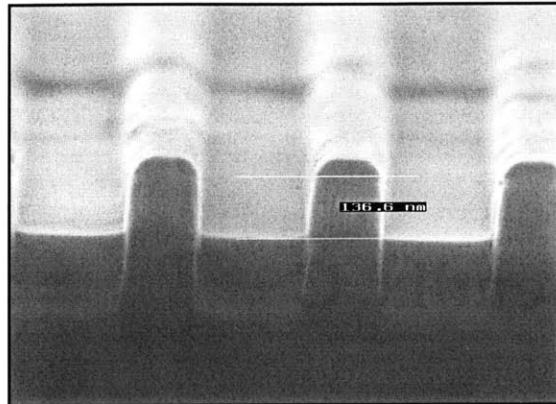
- (b) Cover the oxide surface with a puddle of HMDS.
 - (c) Let stand for 1 minute.
 - (d) Remove excess HMDS by spinning wafer for approx. 15 seconds.
6. Spin-coat a 200-nm-thick layer of Sumitomo PFI-34 (a high-contrast i-line resist).
 7. Bake in oven at 90°C for for 30 min.
 8. Store in a light-tight container to prevent unwanted exposure.

Appendix C

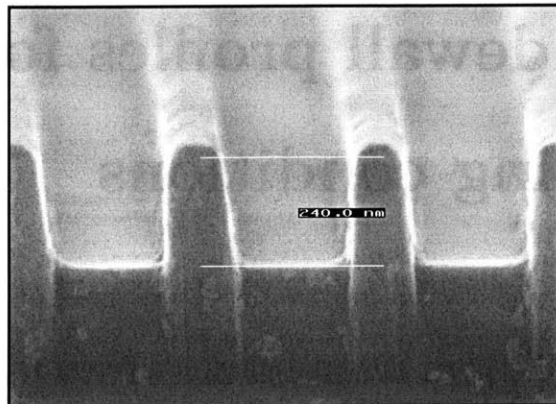
Si sidewall profiles for different etching conditions

The following pages show the effect of different DC biases during reactive-ion etching into a silicon substrate. The etch mask was a 40-nm-thick chromium grating. The gas flow rates used in all processes are $\text{CF}_4:\text{O}_2$ 13.5 sccm:1.5 sccm. The chamber pressure was varied to keep the etch rate approximately constant.

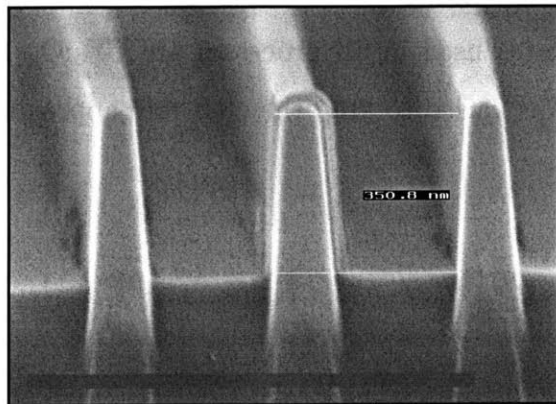
Pressure: 10 mTorr
DC bias: 500 V
Etch rate: 18 nm/min.



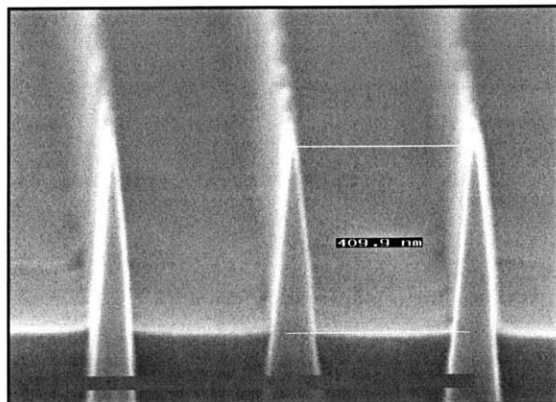
5 min



10 min

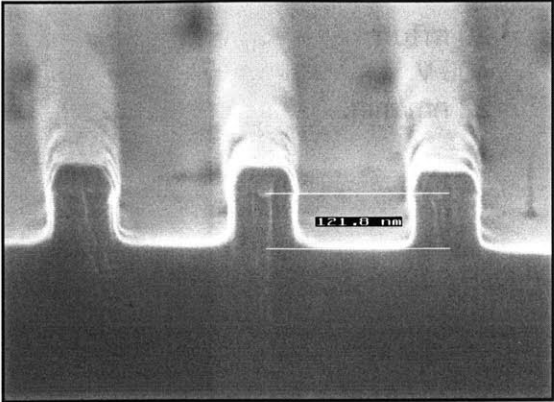


15 min

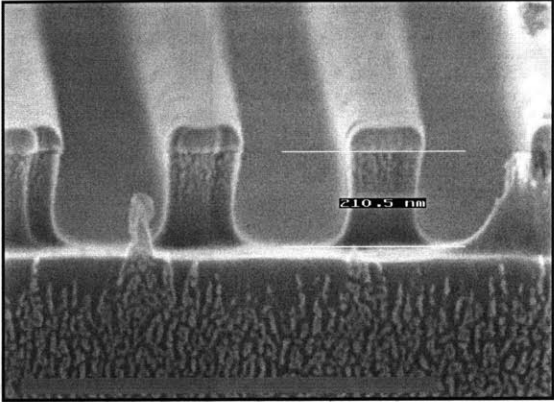


20 min

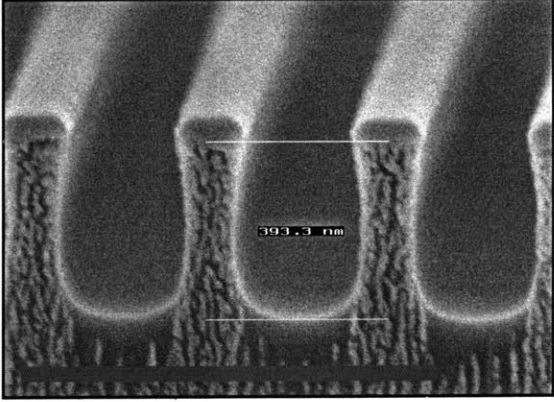
Pressure: 30 mTorr
DC bias: 300 V
Etch rate: 20 nm/min.



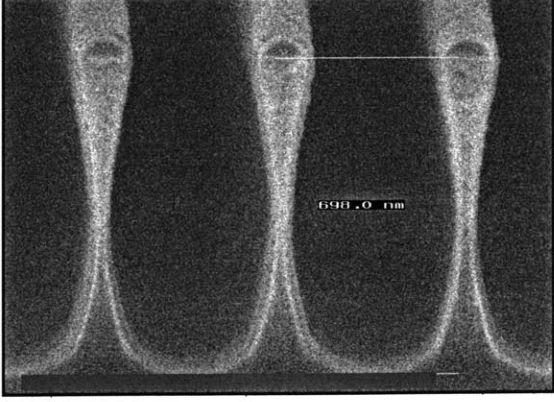
5 min



10 min

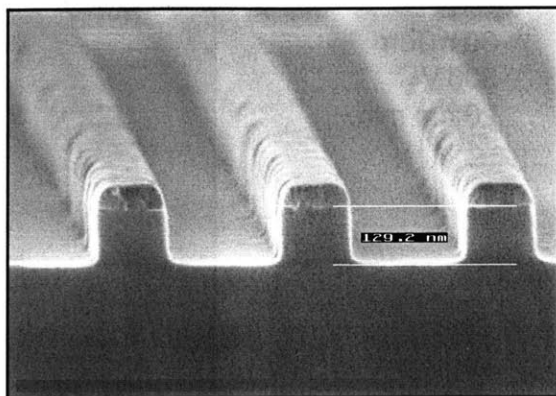


15 min

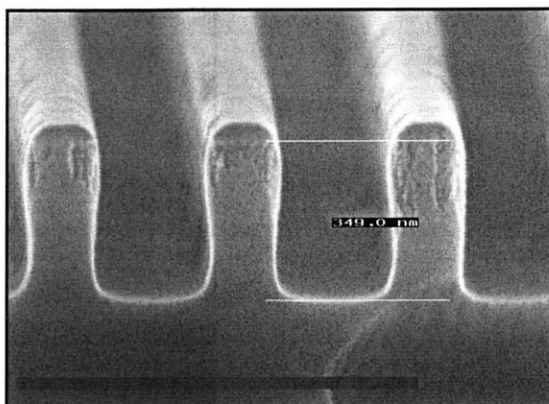


30 min

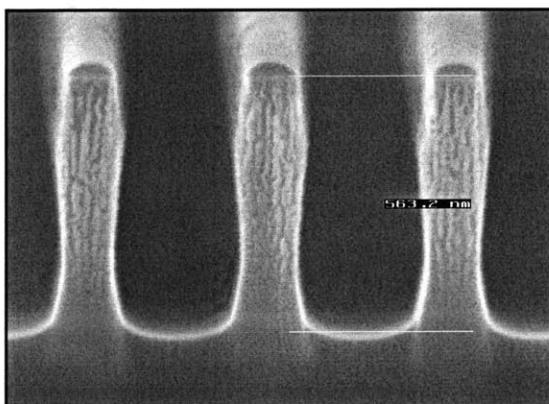
Pressure: 20 mTorr
DC bias: 400 V
Etch rate: 22 nm/min.



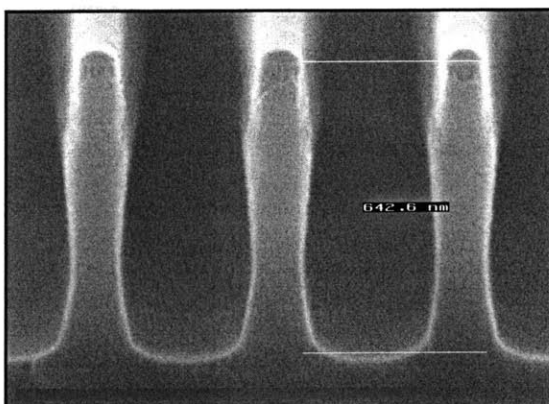
5 min



10 min



15 min



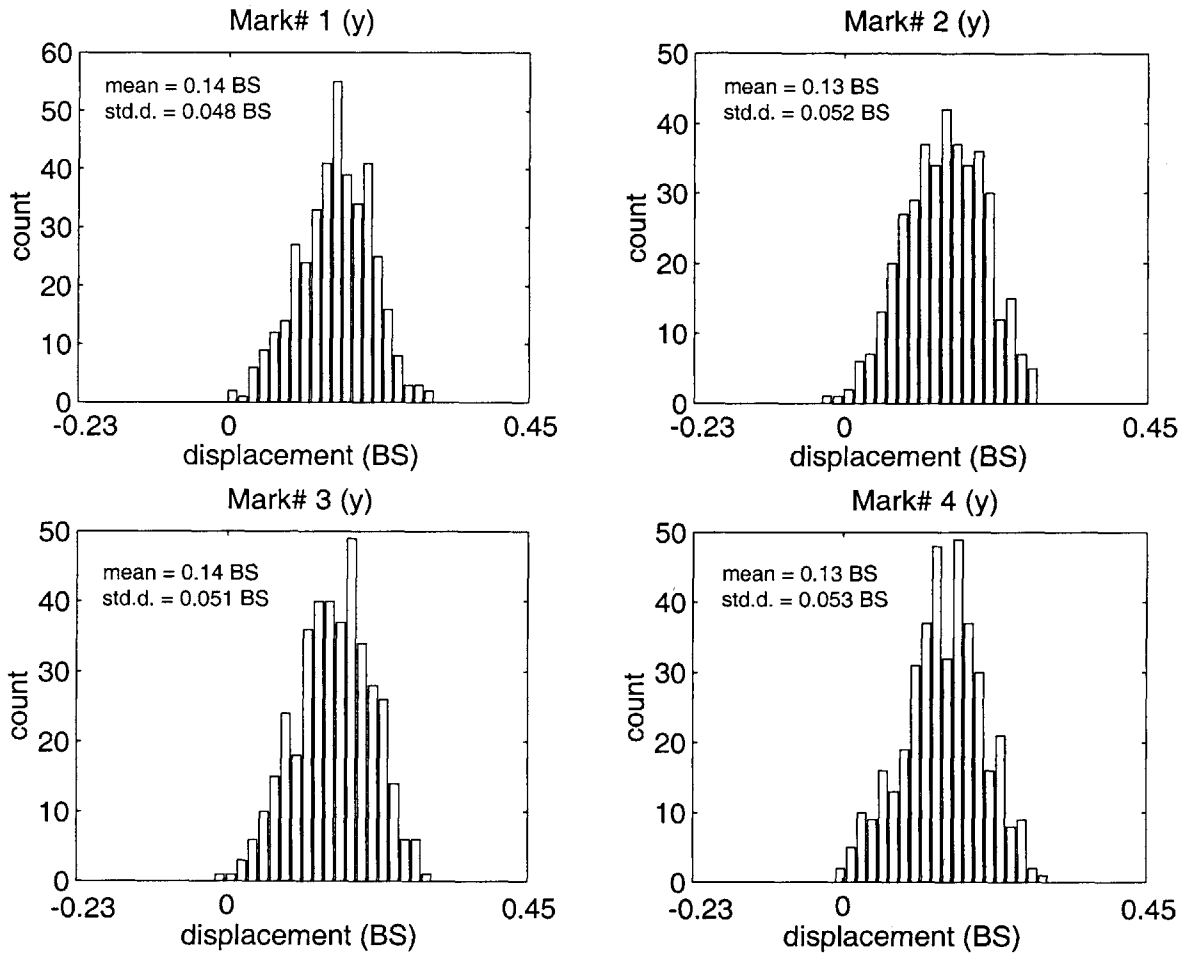
20 min

Appendix D

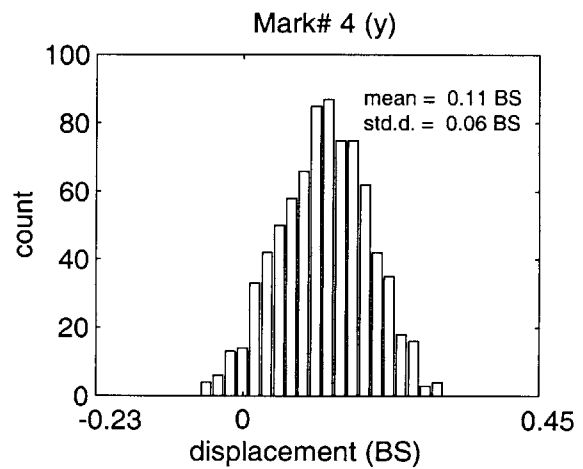
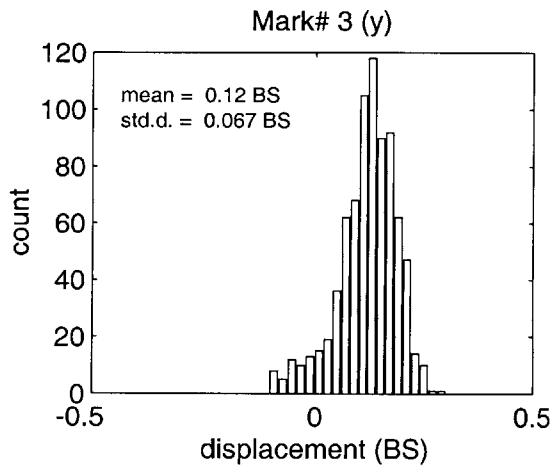
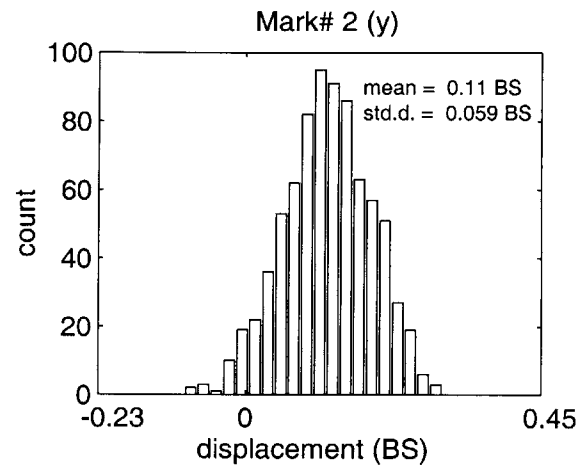
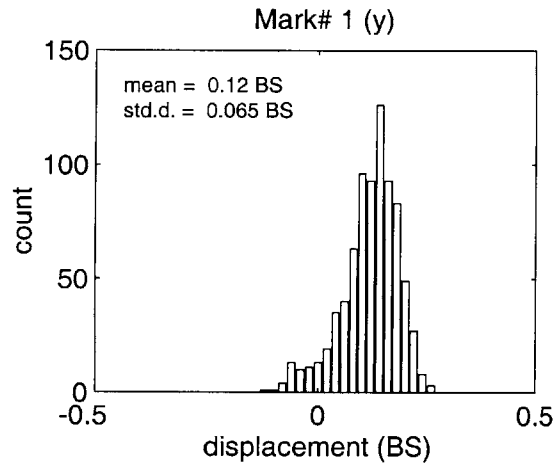
Repeatability of alignment with two vector-scan *e*-beam tools

To estimate the repeatability of alignment using segmented-grid SPLEBL, alignment statistics were collected by repeating the alignment algorithm on a stationary grating. The experiment was performed on two different systems: VS-6 at IBM, Yorktown Heights, NY and VS-2A, at MIT. Histograms of alignment statistics obtained for different beam currents on both systems are shown in the following pages.

VS-6 : dataset "od100pa"
Beam current = 100 pA
Field size = 102.4 mm
1 beam step = 6.25 nm



VS-6 : dataset "od75pa"
Beam current = 75 pA
Field size = 102.4 mm
1 beam step = 6.25 nm

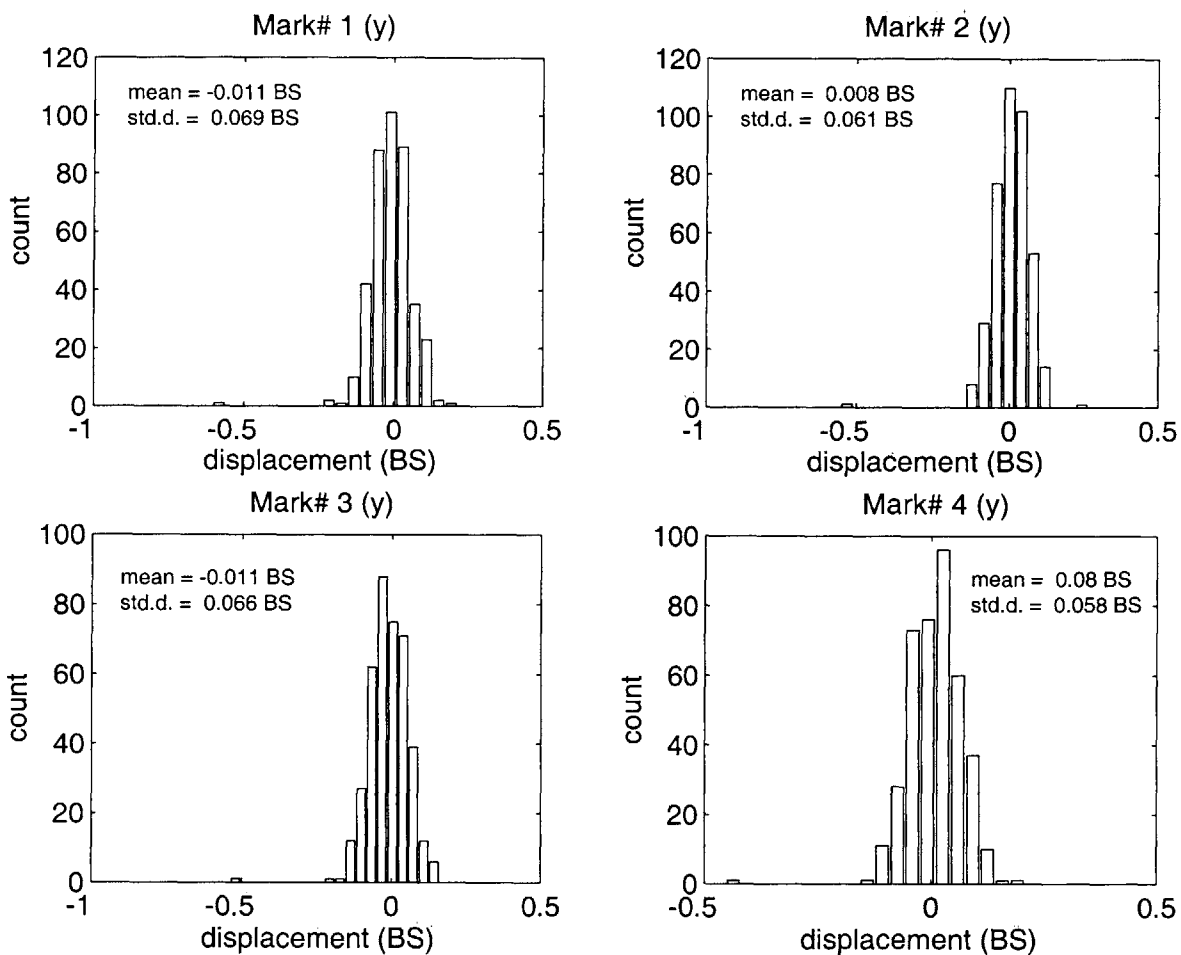


VS-6 : dataset "od50pa"

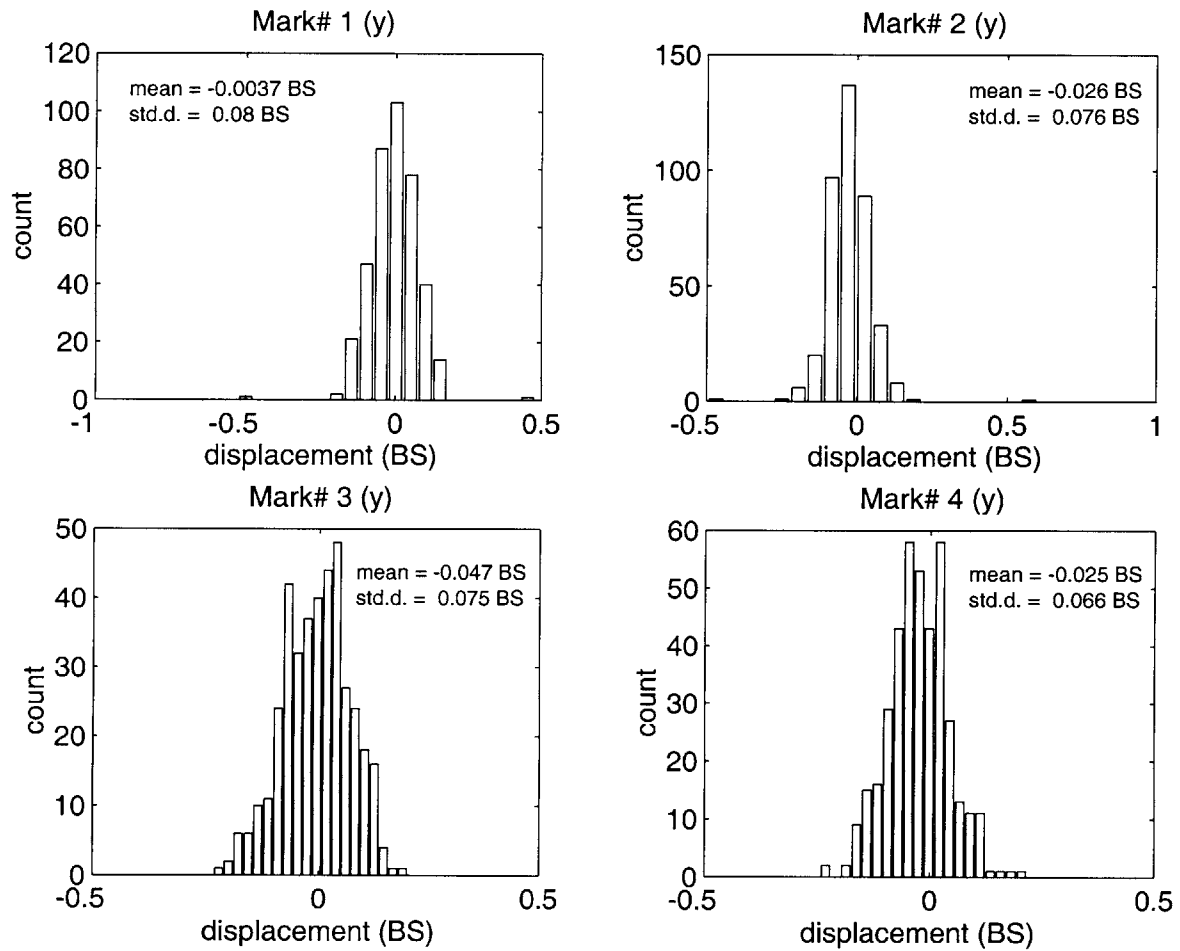
Beam current = 50 pA

Field size = 102.4 mm

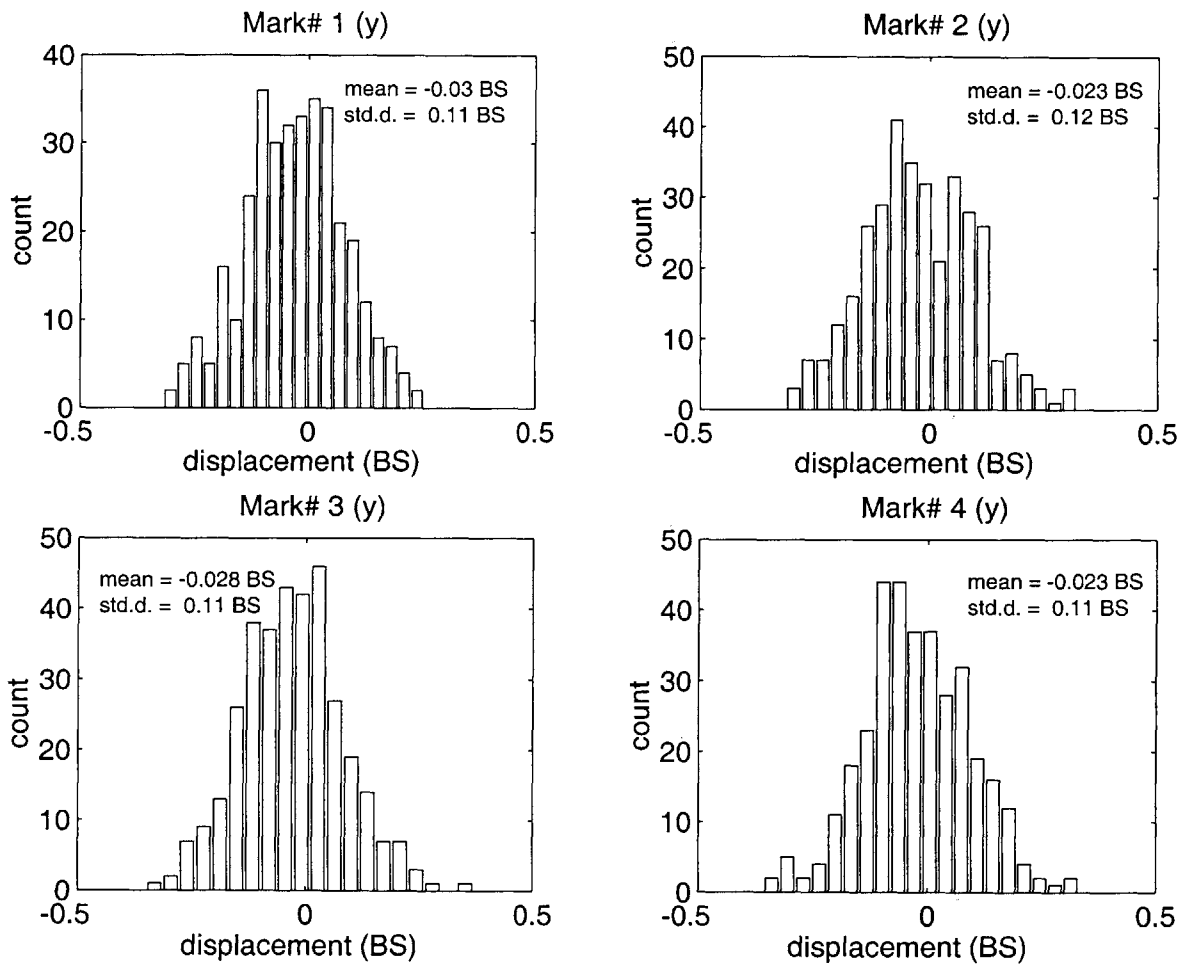
1 beam step = 6.25 nm



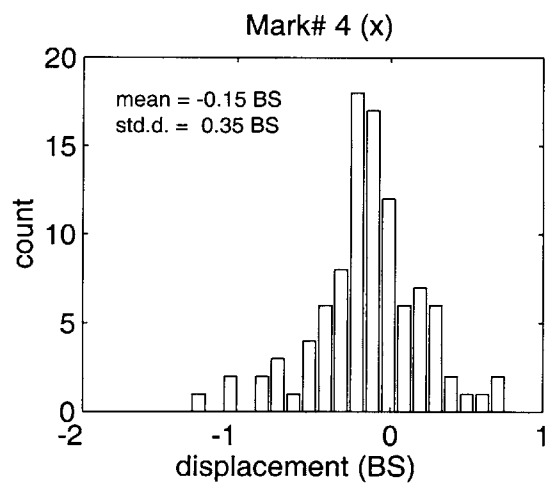
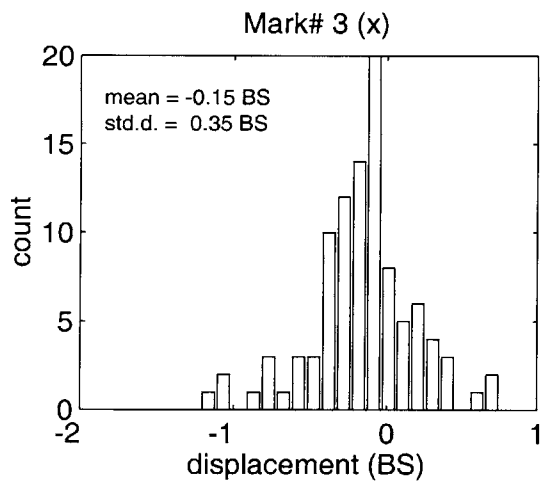
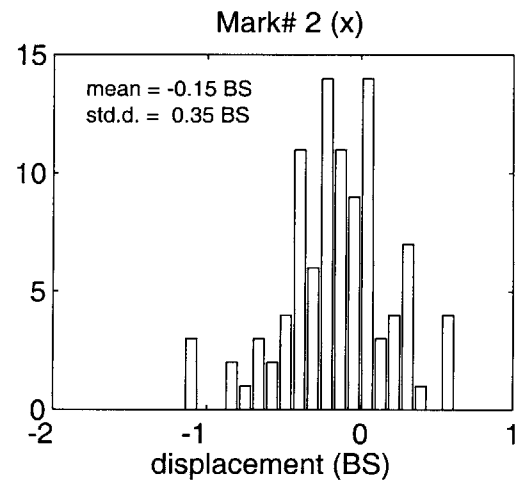
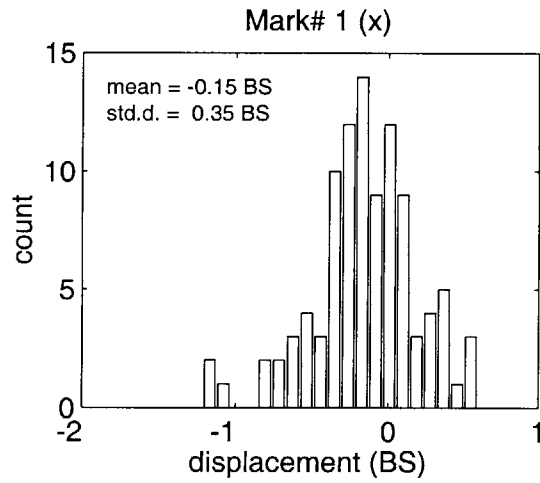
VS-6 : dataset "od25pa"
Beam current = 25 pA
Field size = 102.4 mm
1 beam step = 6.25 nm



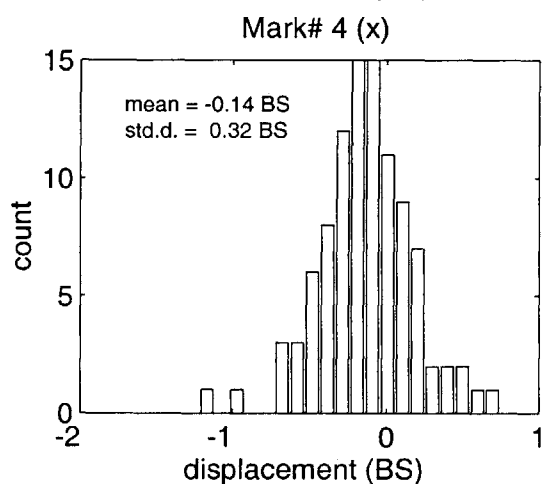
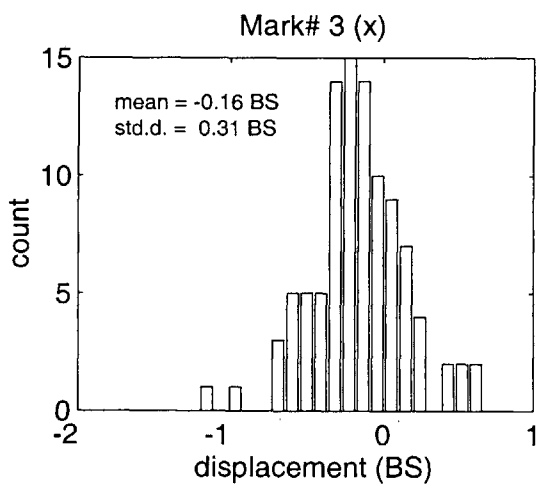
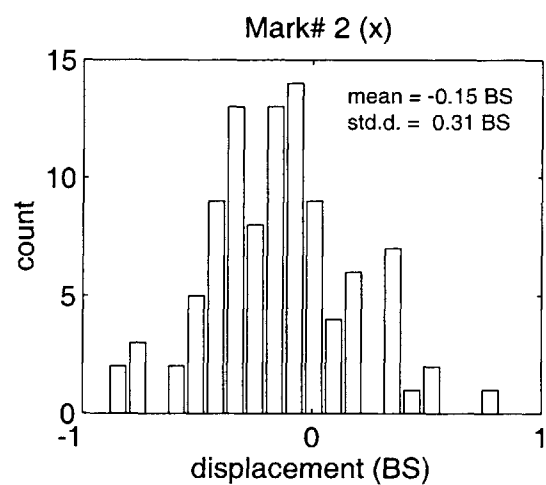
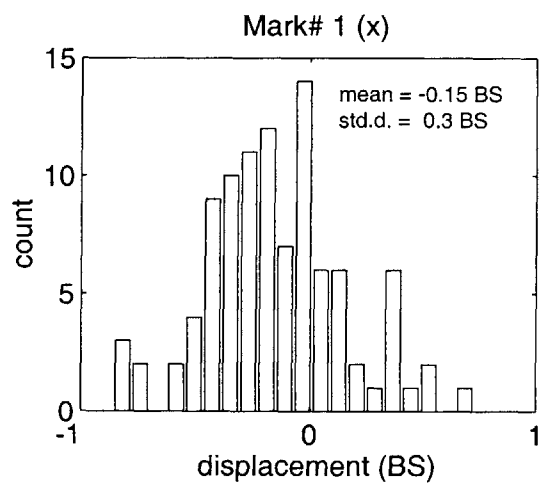
VS-6 : dataset "od10pa"
Beam current = 10 pA
Field size = 102.4 mm
1 beam step = 6.25 nm



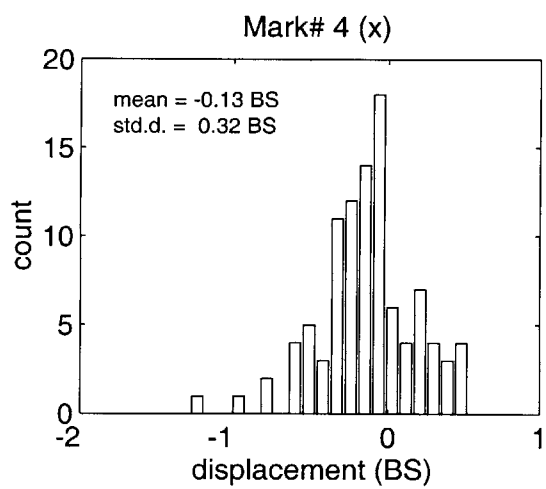
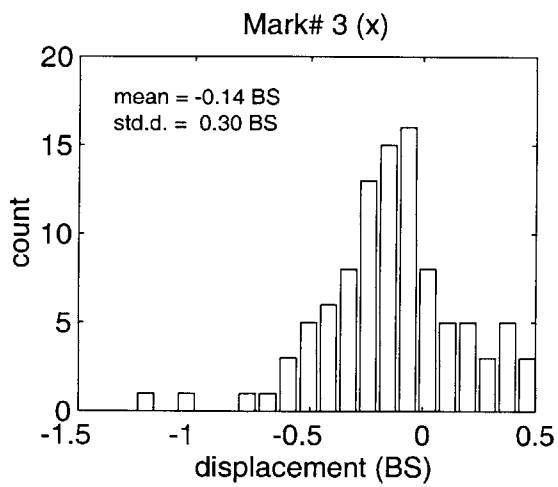
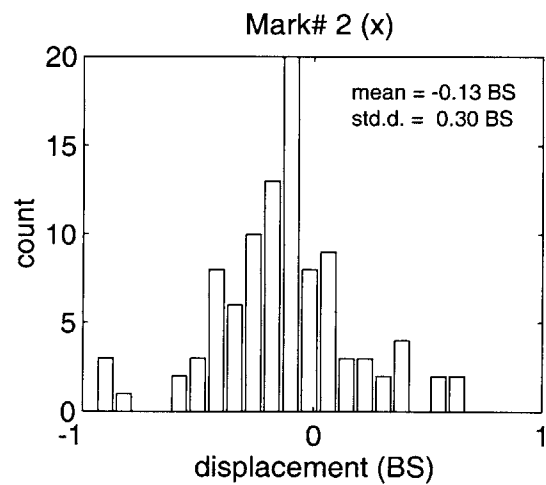
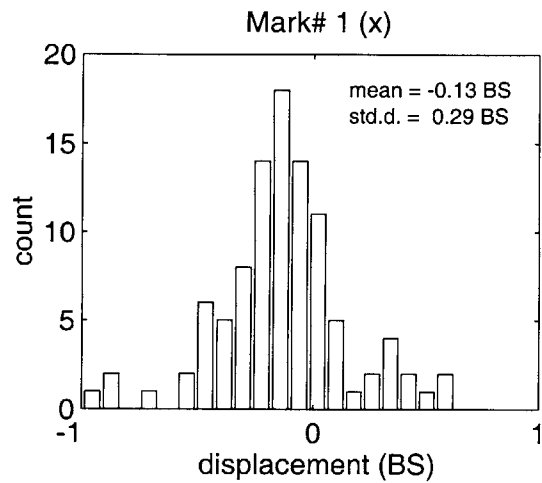
VS-2A : dataset "x1"
Beam current = 75 pA
Field size = 102.4 mm
1 beam step = 6.25 nm



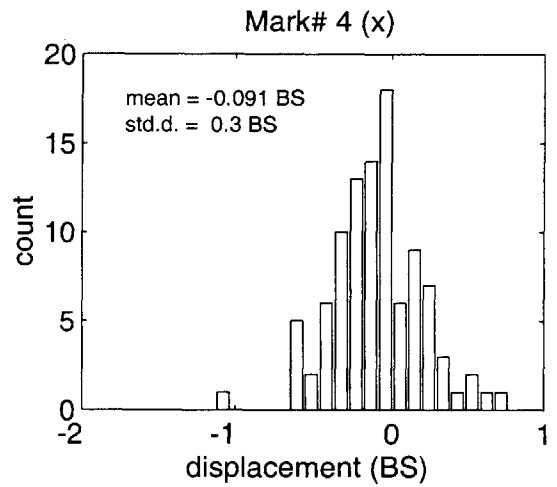
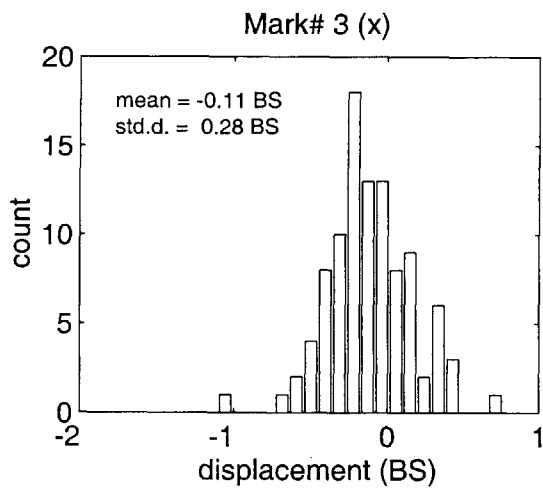
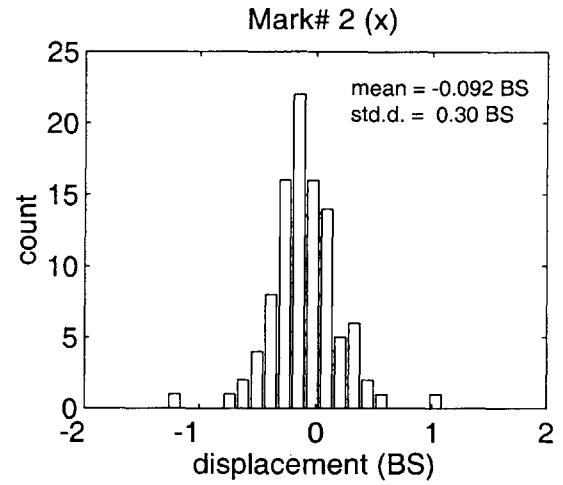
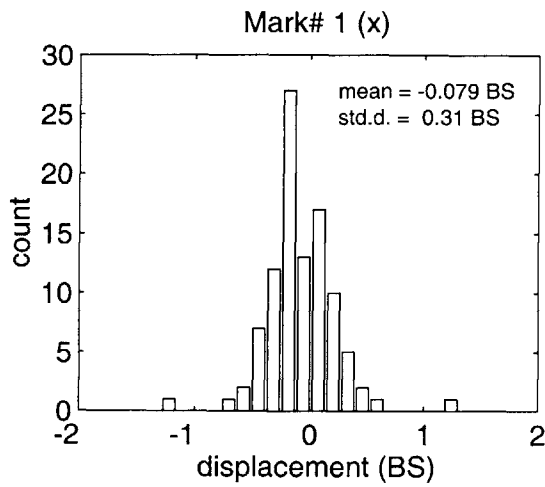
VS-2A : dataset "x4"
Beam current = 50 pA
Field size = 102.4 mm
1 beam step = 6.25 nm



VS-2A : dataset "x6"
Beam current = 25 pA
Field size = 102.4 mm
1 beam step = 6.25 nm



VS-2A : dataset "x8"
Beam current = 10 pA
Field size = 102.4 mm
1 beam step = 6.25 nm



Appendix E

Bragg-grating definition script

The Bragg-grating patterns described in Chapter 8 were generated by means of the following script.

```
# File cdf6.script
# layout uses input from this file to generate cdf 6.0 gratings

#define parameters:
lambda = 0.0076375; # in um (for fieldsize 125.1328 um)
fieldsize = 16384;
virtual_fieldsize = 8192;
pixel_period = 32;
line_dx = 8;          # determined from dose matrix to give 55:45 L:S
outrig_w = 256;
#outrig_filename = outrig.dat;

clear_outrig;          # erase outrigger file

device("dbr-1", -824.8500, 2397.8, 2410.6, 2385.0, 10.0, 0.0);
begin;
grating(-856.1332,2400.0000,4.8880,7006,0,0,0,0,0);
end;

device("dbr-2", -1680.8610, 2372.0, 2385.0, 2359.4, 10.0, 0.0);
begin;
grating(-1712.1442,2374.4000,4.8880,14011,0,0,0,0,0);
end;
```

```
device("dbr-3", -2536.9942, 2346.2, 2359.4, 2333.8, 10.0, 0.0);
begin;
grating(-2568.2774,2348.8000,4.8880,21017,0,0,0,0,0);
end;

device("qws-1", -250.2656, 2320.6, 2333.8, 2308.2, 10.0, 0.0);
begin;
grating(-256.4978,2323.2000,4.8880,1049,1049,0,0,0,0);
end;

device("qws-2", -312.8320, 2295.4, 2308.2, 2282.6, 10.0, 0.0);
begin;
grating(-315.8870,2297.6000,4.8880,1292,1292,0,0,0,0);
end;

device("qws-3", -375.3984, 2269.8, 2282.6, 2257.0, 10.0, 0.0);
begin;
grating(-394.3394,2272.0000,4.8880,1613,1613,0,0,0,0);
end;

device("qws-4", -437.9648, 2244.2, 2257.0, 2231.4, 10.0, 0.0);
begin;
grating(-453.7286,2246.4000,4.8880,1856,1856,0,0,0,0);
end;

device("qws-5", -563.0976, 2218.6, 2231.4, 2205.8, 10.0, 0.0);
begin;
grating(-591.5702,2220.8000,4.8880,2420,2420,0,0,0,0);
end;

device("hof-1", -1188.2728, 2193.0, 2205.8, 2180.2, 10.0, 0.0);
begin;
grating(-1182.8960,2195.2000,4.8880,1523,3315,3315,1523,0,0);
end;

device("hof-2", -1083.6696, 2167.4, 2180.2, 2154.6, 10.0, 0.0);
begin;
grating(-1064.3620,2169.6000,4.8880,1370,2983,2983,1370,0,0);
end;

device("hof-3", -981.9992, 2141.8, 2154.6, 2129.0, 10.0, 0.0);
begin;
grating(-967.8240,2144.0000,4.8880,1246,2712,2712,1246,0,0);
end;
```

```
device("hof-4", -1751.1260, 2118.2, 2129.0, 2107.4, 10.0, 0.0);  
begin;  
grating(-1734.8734,2118.4000,4.8880,1202,2741,3152,3152,2741,1202);  
end;
```

```
device("ror-1", -750.7968, 2079.8, 2103.4, 2056.2, 10.0, 3.2);  
begin;  
grating(-733.0778,2079.9000,3.9104,2999,2999,0,0,0,0);  
end;
```

```
device("ror-2", -813.3632, 2030.6, 2056.2, 2005.0, 10.0, 3.2);  
begin;  
grating(-811.2858,2029.0000,3.9104,3319,3319,0,0,0,0);  
end;
```

```
device("ror-3", -875.9296, 1979.4, 2005.0, 1953.8, 10.0, 3.2);  
begin;  
grating(-902.4470,1978.1500,3.9104,3692,3692,0,0,0,0);  
end;
```

```
device("sccr-1", -539.6352, 1928.2, 1953.8, 1902.6, 10.0, 3.2);  
begin;  
grating(-539.2686,1926.5000,3.9104,1278,3134,0,0,0,0);  
end;
```

```
device("sccr-2", -602.2016, 1877.0, 1902.6, 1851.4, 10.0, 3.2);  
begin;  
grating(-617.4766,1875.6000,3.9104,1598,3454,0,0,0,0);  
end;
```

```
device("sccr-3", -727.3344, 1825.8, 1851.4, 1800.2, 10.0, 3.2);  
begin;  
grating(-721.5910,1824.8000,3.9104,2024,3880,0,0,0,0);  
end;
```

```
device("cdf-1", -1360.3304, 1774.6, 1800.2, 1749.0, 10.0, 3.2);  
begin;  
grating(-137.9638,1773.0500,3.9104,1195,3051,0,0,0,0);  
grating(-1339.8008,1765.3000,3.9104,2987,2987,0,0,0,0);  
end;
```

```
device("cdf-2", -1563.4268, 1723.4, 1749.0, 1697.8, 10.0, 3.2);  
begin;  
grating(-294.3798,1722.1500,3.9104,1515,3371,0,0,0,0);
```

```
grating(-1558.5388,1713.8000,3.9104,3307,3307,0,0,0,0);
end;

device("cdf-3", -1842.0428, 1672.2, 1697.8, 1646.6, 10.0, 3.2);
begin;
grating(-476.7022,1671.3000,3.9104,1888,3744,0,0,0,0);
grating(-1865.7496,1662.2500,3.9104,3680,3680,0,0,0,0);
end;

device("ror-t1", -750.7968, 1581.2, 1606.2, 1556.2, 10.0, 3.2);
begin;
grating(-733.0778,1579.0500,3.9104,2999,2999,0,0,0,0);
end;

device("ror-t2", -813.3632, 1325.2, 1350.2, 1300.2, 10.0, 3.2);
begin;
grating(-811.2858,1323.4000,3.9104,3319,3319,0,0,0,0);
end;

device("ror-t3", -875.9296, 1069.2, 1094.2, 1044.2, 10.0, 3.2);
begin;
grating(-902.4470,1067.7500,3.9104,3692,3692,0,0,0,0);
end;

device("sccr-t1", -312.8320, 762.0, 787.0, 737.0, 10.0, 3.2);
begin;
grating(-312.4654,760.1000,3.9104,1278,3134,0,0,0,0);
end;

device("sccr-t2", -375.3984, 506.0, 531.0, 481.0, 10.0, 3.2);
begin;
grating(-390.6734,504.6000,3.9104,1598,3454,0,0,0,0);
end;

device("sccr-t3", -500.5312, 250.0, 275.0, 225.0, 10.0, 3.2);
begin;
grating(-494.7878,249.2000,3.9104,2024,3880,0,0,0,0);
end;

device("cdf-t1a", 1128.1504, 32.4, 57.4, 7.4, 10.0, 3.2);
begin;
grating(1148.8251125,30.6000,3.9104,1195,3051,0,0,0,0);
end;

device("cdf-t1b", -791.8560, -162.7, -137.7, -187.7, 10.0, 3.2);
```

```
begin;
grating(-771.1201875,-170.5500,3.9104,2987,2987,0,0,0,0);
end;

device("cdf-t2a", 1133.0384, -223.6, -198.6, -248.6, 10.0, 3.2);
begin;
grating(1138.14025,-225.0500,3.9104,1515,3371,0,0,0,0);
end;

device("cdf-t2b", -921.8768, -433.05, -411.5, -454.6, 10.0, 0.0);
begin;
grating(-916.912425,-444.6500,3.9104,3307,3307,0,0,0,0);
end;

device("cdf-t3a", 1171.6536, -483.05, -461.5, -504.6, 10.0, 3.2);
begin;
grating(1147.962075,-480.7000,3.9104,1888,3744,0,0,0,0);
end;

device("cdf-t3b", -1085.3804, -719.05, -694.05, -744.05, 10.0, 3.2);
begin;
grating(-1109.0337375,-727.6000,3.9104,3680,3680,0,0,0,0);
end;

device("hofs2-1", -711.4484, -1500.4, -1474.8, -1526.0, 10.0, 3.2);
begin;
grating(-244.0334,-1501.7000,4.8880,1415,3271,0,0,0,0);
grating(-697.6398,-1506.9500,4.8880,3271,3271,0,0,0,0);
end;

device("hofs2-2", -711.4484, -1551.5, -1526.0, -1577.2, 10.0, 3.2);
begin;
grating(-244.0334,-1552.9000,4.8880,1415,3271,0,0,0,0);
grating(-697.6398,-1558.1500,4.8880,3271,3271,0,0,0,0);
end;

device("hofs3-1", -615.3992, -1602.8, -1577.2, -1628.4, 10.0, 3.2);
begin;
grating(-177.0678,-1599.0000,4.8880,1278,3134,0,0,0,0);
grating(-630.6742,-1604.2500,4.8880,3134,3134,0,0,0,0);
grating(-630.6742,-1609.5000,4.8880,3134,3134,0,0,0,0);
end;

device("hofs3-2", -615.3992, -1654.0, -1628.4, -1679.6, 10.0, 3.2);
begin;
```

```
grating(-177.0678,-1650.2000,4.8880,1278,3134,0,0,0,0);
grating(-630.6742,-1655.4500,4.8880,3134,3134,0,0,0,0);
grating(-630.6742,-1660.7000,4.8880,3134,3134,0,0,0,0);
end;

device("hoft2-1", -813.3632, -1715.8, -1690.8, -1740.8, 10.0, 3.2);
begin;
grating(-345.9482,-1717.4500,4.8880,1415,3271,0,0,0,0);
grating(-799.5546,-1722.7000,4.8880,3271,3271,0,0,0,0);
end;

device("hoft2-2", -813.3632, -1895.0, -1870.0, -1920.0, 10.0, 3.2);
begin;
grating(-345.9482,-1896.6500,4.8880,1415,3271,0,0,0,0);
grating(-799.5546,-1901.9000,4.8880,3271,3271,0,0,0,0);
end;

device("hoft3-1", -750.7968, -2074.2, -2049.2, -2099.2, 10.0, 3.2);
begin;
grating(-312.4654,-2070.8000,4.8880,1278,3134,0,0,0,0);
grating(-766.0718,-2076.0500,4.8880,3134,3134,0,0,0,0);
grating(-766.0718,-2081.3000,4.8880,3134,3134,0,0,0,0);
end;

device("hoft3-2", -750.7968, -2253.4, -2228.4, -2278.4, 10.0, 3.2);
begin;
grating(-312.4654,-2250.0000,4.8880,1278,3134,0,0,0,0);
grating(-766.0718,-2255.2500,4.8880,3134,3134,0,0,0,0);
grating(-766.0718,-2260.5000,4.8880,3134,3134,0,0,0,0);
end;
```

References

- [1] J. S. Kilby, IEEE Trans. Electron Devices **ED-23**, 648 (1976).
- [2] H. I. Smith, Proceedings of the IEEE **62**, 1361 (1974).
- [3] D. L. Spears and H. I. Smith, Electron. Lett. **8**, 102 (1972).
- [4] M. Komuro, N. Atoda, and H. Kawakatsu, J. Electrochem. Soc. **126**, 283 (1979).
- [5] R. L. Seliger, J. W. Ward, V. Wang, and R. L. Kubena, Appl. Phys. Lett. **34**, 310 (1979).
- [6] Taiwan Semiconductor Manufacturing Company Ltd., press release, may 17, 1999.
- [7] D. M. Tennant et al., J. Vac Sci. Technol. **11**, 2509 (1993).
- [8] D. A. Buck and K. R. Shoulders, Proceedings of the Eastern Joint Computer Conference (1958).
- [9] G. Möllenstedt and R. Speidel, Physikalische Blätter **16**, 192 (1960).
- [10] M. von Ardenne, Zeitschrift für Technische Physik **19**, 407 (1938).
- [11] C. W. Oatley, New Scientist **12**, 153 (1958).
- [12] C. W. Oatley, W. C. Nixon, and R. F. W. Pease, Advances in Electronics and Electron Physics **21**, 181 (1965).
- [13] R. F. W. Pease, Contemp. Phys. **22**, 265 (1981).
- [14] M. Hatzakis, IBM J. Res. Develop. **32**, 441 (1988).
- [15] I. Haller, M. Hatzakis, and R. Srinivasan, IBM J. Res. Develop. **12**, 251 (1968).
- [16] A. N. Broers, W. W. Molzen, J. J. Cuomo, and N. D. Wittles, Appl. Phys. Lett. **29**, 596 (1976).
- [17] A. N. Broers and M. Hatzakis, Scientific American **227**, 34 (1972).

- [18] M. G. R. Thomson, *J. Vac. Sci. Technol.* **12**, 1156 (1975).
- [19] P. Rissman, E.-D. Liu, and G. Owen, *J. Vac. Sci. Technol. B* **1**, 1014 (1983).
- [20] Z. W. Chen, G. A. C. Jones, and H. Ahmed, *J. Vac. Sci. Technol. B* **6**, 2009 (1988).
- [21] E. Munro, *J. Vac. Sci. Technol.* **12**, 1146 (1976).
- [22] H. C. Chu and E. Munro, *J. Vac. Sci. Technol.* **19**, 1053 (1981).
- [23] G. Owen, *J. Vac. Sci. Technol.* **19**, 1064 (1981).
- [24] P. W. Hawkes, *Principles of electron optics*, Academic Press, 1989.
- [25] O. Cahen and J. Tritel, High performance step and repeat machine using an electron beam and laser interferometers, in *Electron and ion beam science and technology 4th international conference*, edited by R. Bakish, pages 581–587, Electrochem. Soc., 1970.
- [26] O. Cahen, R. Sigelle, and J. Tritel, Automatic control of an electron beam pattern generator, in *Electron and ion beam science and technology 5th international conference*, edited by R. Bakish, pages 92–101, Electrochem. Soc., 1972.
- [27] G. L. Varnell, D. F. Spicer, A. C. Rodger, and R. D. Holland, *J. Electrochem. Soc.* **121**, 109C (1974).
- [28] D. S. Alles, F. R. Ashley, A. M. Johnson, and R. L. Townsend, *J. Vac. Sci. Technol.* **12**, 1252 (1976).
- [29] J. Pasiecznik and J. W. Reeds, *J. Vac. Sci. Technol.* **15**, 909 (1978).
- [30] A. D. Wilson and T. Studwell, *J. Vac. Sci. Technol.* **16**, 1819 (1979).
- [31] J. Nishizawa, *J. Vac. Sci. Technol.* **16**, 1934 (1979).
- [32] T. R. Groves, J. G. Hartley, H. C. Pfeiffer, D. Puisto, and D. K. Bailey, *IBM J. Res. Develop.* **37**, 411 (1993).
- [33] W. B. Glendinning and W. M. Goodreau, *Proc. of SPIE* **480**, 141 (1984).
- [34] B. Hubner, R. Jede, I. Specht, and R. Zengerle, *Microelectronic Engineering* **30**, 41 (1996).
- [35] D. R. S. Cumming, S. Thomas, S. P. Beaumont, and J. M. R. Weaver, *J. Vac. Sci. Technol. B* **14**, 4115 (1996).
- [36] M. R. Raugh, *Proc. of SPIE* **480**, 145 (1984).

- [37] G. Matsuoka, M. Ichihashi, H. Murakoshi, and K. Yamamoto, *J. Vac. Sci. Technol. B* **5**, 79 (1986).
- [38] T. Hatsuzawa, K. Toyoda, and Y. Tanimura, *Review of Scientific Instruments* **61**, 975 (1990).
- [39] H. Bosse and W. Hassler-Grohne, *Proc. of SPIE* **3236**, 160 (1997).
- [40] J. N. Dukes and G. B. Gordon, *Hewlett-Packard J.* **21**, 2 (1970).
- [41] H. I. Smith, *Submicron- and Nanometer Structures Technology*, Lecture Notes, NanoStructures Press, Sudbury, MA (1994).
- [42] "paleography", *Encyclopaedia Britannica*.
- [43] D. R. Herriott, R. J. Collier, D. S. Alles, and J. W. Stafford, *IEEE Trans. Electron Devices* **ED-22**, 385 (1985).
- [44] R. A. Geshner, *Solid State Technology* **22**, 69 (1979).
- [45] J. C. Wiesner and N. C. Yew, *Perkin-Elmer Technical News* **10**, 31 (1982).
- [46] J. L. Freyer and K. P. Standiford, *Solid State Technology* **26**, 165 (1983).
- [47] F. Abboud and J. Smith, *Proc. of SPIE* **1671**, 111 (1992).
- [48] H. Pearce-Percy et al., *J. Vac. Sci. Technol. B* **12**, 3393 (1994).
- [49] F. Abboud et al., *Proc. of SPIE* **3096**, 116 (1997).
- [50] Semiconductor Industry Association, National technology roadmap for semiconductors, p. 83 (1997), available at <http://notes.sematech.org/ntrs/Rdmpmem.nsf>
- [51] *Ibid.*, p. 94.
- [52] H. I. Smith, S. R. Chinn, and P. D. DeGraff, *J. Vac. Sci. Technol.* **12**, 1262 (1975).
- [53] E. H. Anderson, V. Boegli, M. L. Schattenburg, D. P. Kern, and H. I. Smith, *J. Vac. Sci. Technol. B* **9**, 3606 (1991).
- [54] H. I. Smith, S. D. Hector, M. L. Schattenburg, and E. H. Anderson, *J. Vac. Sci. Technol. B* **9**, 2992 (1991).
- [55] J. Ferrera et al., *J. Vac. Sci. Technol. B* **11**, 2342 (1993).
- [56] J. Ferrera, *Highly Coherent Gratings for Optoelectronics: An Application of Spatial-Phase-Locked Electron Beam Lithography*, Master's thesis, Massachusetts Institute of Technology, 1994.

- [57] T. Young, A course of lectures on natural philosophy and the mechanical arts, 1807.
- [58] A. A. Michelson, *Studies in optics*, University of Chicago Press, 1927.
- [59] D. Rudolph and G. Schmahl, *Umschau in Wissenschaft und Technik* **67**, 225 (1967).
- [60] G. Schmahl and D. Rudolph, *Holographic diffraction gratings*, volume XIV of *Progress in optics*, E. Wolf, ed., pages 197–244, North-Holland, 1976.
- [61] D. C. Flanders, D. C. Shaver, and H. I. Smith, *Appl. Phys. Lett.* **32**, 597 (1978).
- [62] N. N. Efremow, N. P. Economou, K. Bezjian, S. S. Dana, and H. I. Smith, *J. Vac. Sci. Technol.* **19**, 1234 (1981).
- [63] A. M. Hawryluk, H. I. Smith, and D. J. Ehrlich, *J. Vac. Sci. Technol. B* **1**, 1200 (1983).
- [64] E. H. Anderson, C. M. Horwitz, and H. I. Smith, *Appl. Phys. Lett.* **43**, 874 (1983).
- [65] H. J. Lezec, E. H. Anderson, , and H. I. Smith, *J. Vac. Sci. Technol. B* **1**, 1204 (1983).
- [66] E. H. Anderson, K. Komatsu, and H. I. Smith, *J. Vac. Sci. Technol. B* **6**, 216 (1988).
- [67] A. Yen, R. A. Ghanbari, E. H. Anderson, and H. I. Smith, *Microelectronic Engineering* **11**, 201 (1990).
- [68] A. Yen, H. I. Smith, M. L. Schattenburg, and G. N. Taylor, *J. Electrochem. Soc.* **139**, 616 (1992).
- [69] A. Yen, E. H. Anderson, R. A. Ghanbari, M. L. Schattenburg, and H. I. Smith, *Applied Optics* **31**, 4540 (1992).
- [70] A. Yen, M. L. Schattenburg, and H. I. Smith, *Applied Optics* **31**, 2972 (1992).
- [71] A. M. Hawryluk, N. M. Ceglio, R. H. Price, J. Melngailis, and H. I. Smith, *A. I. P. Conference Proceedings* , 286 (1981).
- [72] A. M. Hawryluk, N. M. Ceglio, R. H. Price, J. Melngailis, and H. I. Smith, *J. Vac. Sci. Technol.* **19**, 897 (1981).
- [73] M. L. Schattenburg, E. H. Anderson, and H. I. Smith, *Physica Scripta* **41**, 13 (1990).
- [74] K. Ismail, F. Legoues, N. H. Karam, J. Carter, and H. I. Smith, *Appl. Phys. Lett.* **59**, 2418 (1991).

- [75] D. Keith, M. Schattenburg, H. Smith, and D. Pritchard, *Phys. Rev. Lett.* **61**, 1580 (1988).
- [76] J. M. Carter, D. B. Olster, M. L. Schattenburg, A. Yen, and H. I. Smith, *J. Vac. Sci. Technol. B* **10**, 2909 (1992).
- [77] R. E. Grisenti et al., *He atom diffraction from nanostructured transmission gratings: the role of imperfections*, Submitted to *Phys. Rev. A*, 1999.
- [78] J. T. M. V. Beek, R. C. Fleming, P. S. Hindle, J. D. Prentiss, and M. L. Schattenburg, *J. Vac. Sci. Technol. B* **16**, 3911 (1998).
- [79] Y. C. Ku et al., *J. Vac. Sci. Technol. B* **10**, 3169 (1992).
- [80] M. H. Lim, J. Ferrera, K. P. Pipe, and H. I. Smith, *A holographic phase-shifting interferometer technique to measure in-plane distortion*, submitted to the 1999 International Conference on Electron, Ion and Photon Beam Technology and Nanofabrication, 1999.
- [81] M. McGehee, M. Diaz-Garcia, R. Gupta, F. Hide, and A. J. Heeger, *Semiconducting polymer distributed feedback lasers*, in *LEOS '97 Conference Proceedings*, pages 172–174, IEEE, 1997.
- [82] S.-K. Han and B.-H. Choi, *J. Electrochem. Soc.* **144**, 1760 (1997).
- [83] A. Talneau, N. Bouadma, S. Slempek, A. Ougazzaden, and S. Hansmann, *IEEE Photonics Technology Letters* **9**, 1316 (1997).
- [84] L. Hofmann, A. Klehr, A. Knauer, V. B. Smirnitski, and W. Stolz, *Electronics Letters* **35**, 902 (1999).
- [85] M. L. Schattenburg et al., *Opt. Eng.* **30**, 1590 (1991).
- [86] R. J. Aucoin and M. L. Schattenburg, *J. Vac. Sci. Technol. B* **13**, 3007 (1995).
- [87] S. Miller, Coherent, Inc., private communication.
- [88] H. A. Haus, *Waves and Fields in Optoelectronics*, Prentice-Hall, 1984.
- [89] J. W. Goodman, *Introduction to Fourier Optics*, McGraw-Hill, 1998.
- [90] E. H. Anderson, *Fabrication and Electromagnetic Applications of Periodic Nanostructures*, PhD thesis, Massachusetts Institute of Technology, 1988.
- [91] H. I. Smith, E. H. Anderson, and M. L. Schattenburg, U. S. patent 5,142,385, 1992.
- [92] K. P. Pipe, *Distortion analysis on an improved mask technology for x-ray lithography*, Master's thesis, Massachusetts Institute of Technology, 1999.
- [93] A. E. Siegman, *Lasers*, University Science Books, 1986.

- [94] Coherent INNOVA Sabre laser, users' manual.
- [95] J. B. Marion and M. A. Heald, *Classical electromagnetic radiation*, Harcourt Brace Jovanovich, San Diego, 2nd edition, 1980.
- [96] M. Born and E. Wolf, *Principles of optics*, Pergamon Press, Oxford, 6th edition, 1993.
- [97] D. H. Staelin, A. W. Morgenthaler, and J. A. Kong, *Electromagnetic waves*, Prentice-Hall, 1994.
- [98] J. S. Lim, *Two-dimensional signal and image processing*, Prentice-Hall, 1990.
- [99] P. Jaquinot and R. Roizen, *Apodisation*, volume III of *Progress in optics*, E. Wolf, ed., pages 31–188, North-Holland, 1964.
- [100] A. K. Wong and A. R. Neureuther, IEEE Transactions on Semiconductor Manufacturing **8**, 419 (1995).
- [101] C. Cerjan, Scalar wave diffraction from a circular aperture, in *OSA Proceedings on Extreme Ultraviolet Lithography*, Optical Society of America, 1995.
- [102] J. Ferrera, M. L. Schattenburg, and H. I. Smith, J. Vac Sci. Technol. B **14**, 4009 (1996).
- [103] D. Dewey, D. N. Humphries, G. Y. McLean, and D. A. Moschella, Proc. of SPIE **2280**, 257 (1994).
- [104] A. Moel, M. L. Schattenburg, J. M. Carter, and H. I. Smith, J. Vac Sci. Technol. B **7**, 1692 (1989).
- [105] H. Goldstein, *Classical Mechanics*, Addison-Wesley, 1980.
- [106] D. C. Flanders, A. M. Hawryluk, and H. I. Smith, J. Vac Sci. Technol. **16**, 1949 (1979).
- [107] A. M. Hawryluk, H. I. Smith, R. M. Osgood, and D. J. Ehrlich, Opt. Lett. **7**, 402 (1982).
- [108] D. M. Tennant et al., J. Vac Sci. Technol. B **10**, 2530 (1992).
- [109] D. M. Tennant et al., Microelectronic Engineering **27**, 427 (1995).
- [110] T. A. Savas, M. L. Schattenburg, J. M. Carter, and H. I. Smith, J. Vac Sci. Technol. B **14**, 4167 (1996).
- [111] T. A. Savas, *Achromatic Interference Lithography*, PhD thesis, Massachusetts Institute of Technology, 1999, (in preparation).
- [112] M. T. Takac et al., J. Vac Sci. Technol. B **15**, 2173 (1997).

- [113] J. E. Greivenkamp and J. H. Bruning, in *Optical Shop Testing*, edited by D. Malacara, page 501, Wiley, 1992.
- [114] D. W. Robinson, Phase unwrapping methods, in *Interferogram analysis*, chapter 6, Institute of Physics Publishing, 1993.
- [115] R. J. Collier, E. T. Doherty, and K. S. Pennington, *Appl. Opt. Lett.* **7**, 223 (1965), and references therein.
- [116] S. Yokozeki and T. Suzuki, *Appl. Opt.* **9**, 2805 (1970).
- [117] C. M. Vest, *Holographic interferometry*, Wiley, 1979.
- [118] J. C. Wyant, Holographic and moiré techniques, in *Optical Shop Testing*, edited by D. Malacara, Wiley, 1978.
- [119] H. A. Haus and Y. Lai, *J. Lightwave Technol.* **10**, 57 (1991).
- [120] Y. Yano et al., 2.6 Tb/s WDM transmission experiment using optical duobinary coding, in *22nd European Independent Conference on Optical Communications*, volume 5, pages 3–6, IEEE, 1996.
- [121] M. Murakami, T. Matsuda, and T. Imai, Quarter terabit (25*10 Gb/s) over 9288 km WDM transmission experiment using nonlinear supported RZ pulse in higher order fiber dispersion managed line, in *24th European Independent Conference on Optical Communications*, volume 3, pages 77–81, IEEE, 1998.
- [122] A. E. Willner and S.-M. Hwang, *Photon. Tech. Lett.* **6**, 760 (1996).
- [123] R. Ramaswami, *Optical networks: a practical perspective*, Morgan Kaufmann Publishers, 1998.
- [124] H. A. Haus and C. V. Shank, *IEEE J. of Quantum Electron.* **QE-12**, 532 (1976).
- [125] J. N. Damask, *Integrated-optic grating-based filters for optical communications systems*, PhD thesis, Massachusetts Institute of Technology, 1996.
- [126] W. Walecki et al., *Appl. Phys. Lett.* **57**, 2641 (1990).
- [127] T. Ishihara et al., *Appl. Phys. Lett.* **60**, 2460 (1992).
- [128] A. Talneau, J. P. Chandouineau, J. Charil, and A. Ougazzaden, *IEEE Photon. Technol. Lett.* **7**, 721 (1995).
- [129] A. Talneau, S. Slempek, and A. Ougazzaden, *IEEE J. of Selected Topics in Quantum Electronics* **3**, 628 (1997).
- [130] T. Numai, *Jap. J. of Appl. Phys.* **30**, 2519 (1991).

- [131] K. Utaka, S. Akiba, K. Sakai, and Y. Matsushima, *IEEE J. of Quantum Electron.* **QE-22**, 1042 (1986).
- [132] M. Okai, S. Tsuji, M. Hirao, and H. Matsumura, *Electron. Lett.* **23**, 370 (1987).
- [133] Y. Twu et al., *Electron. Lett.* **25**, 1045 (1989).
- [134] C. H. Henry, R. F. Kazarinov, H. J. Lee, N. A. Olsson, and K. J. Orlowsky, *IEEE J. of Quantum Electron.* **QE-23**, 1426 (1987).
- [135] M. Levy et al., *IEEE Photon. Technol. Lett.* **4**, 1378 (1992).
- [136] J.-M. Verdiell et al., *IEEE Photon. Technol. Lett.* **5**, 619 (1993).
- [137] M. G. Young et al., *Electron. Lett.* **31**, 1750 (1995).
- [138] H. A. Haus and Y. Lai, *IEEE J. of Quantum Electron.* **28**, 205 (1992).
- [139] V. V. Wong et al., *J. Vac Sci. Technol. B* **13**, 2859 (1995).
- [140] B. E. Little, C. Wu, and W.-P. Huang, Synthesis of optical wavelength filter responses, in *LEOS '95. IEEE Lasers and Electro-Optics Society 1995 Annual Meeting*, pages 235–236, IEEE, 1995.
- [141] B. E. Little and C. Wu, *IEEE Photon. Technol. Lett.* **9**, 76 (1997).
- [142] T. H. P. Chang et al., *IBM Journal of Research and Development* **32**, 462 (1988).
- [143] E. Kratschmer, S. Rishton, H. E. Luhn, D. P. Kern, and T. H. P. Chang, *J. Vac Sci. Technol. B* **7**, 1418 (1989).
- [144] A. Chitayat, *J. Vac Sci. Technol. B* **7**, 1412 (1989).
- [145] V. Bögli and D. P. Kern, *J. Vac Sci. Technol. B* **8**, 1994 (1990).
- [146] P. Horowitz and W. Hill, *The Art of Electronics*, Cambridge University Press, 1980.
- [147] W. H. Press, S. A. Teukolsky, W. T. Vetterling, and B. P. Flannery, *Numerical recipes in C : the art of scientific computing*, pages 197–244, Cambridge University Press, 2nd edition, 1995.
- [148] J. Goodberlet, J. Ferrera, and H. I. Smith, *J. Vac. Sci. Technol. B* **15**, 2293 (1997).
- [149] J. N. Damask, V. V. Wong, J. Ferrera, H. I. Smith, and H. A. Haus, High-coherence qws gratings for optoelectronic devices: Why spatial-phase-locked e-beam lithography is necessary, in *Fiber Communications Conference*, 1994.

- [150] J. N. Damask, J. Ferrera, V. V. Wong, H. I. Smith, and H. A. Haus, Limitations and solutions for the use of integrated lambda /4-shifted distributed bragg resonators in wavelength-division multiplexing applications, in *Proc. of SPIE*, volume 2213, pages 137–151, 1994.
- [151] J. N. Damask, *A deterministic analysis of the coherence-degradation effects of stitching errors along a DBR grating*, Internal memorandum, 1993.
- [152] V. V. Wong, *Fabrication of distributed feedback devices using X-ray lithography*, PhD thesis, Massachusetts Institute of Technology, 1995.
- [153] W. Chu, M. L. Schattenburg, and H. I. Smith, *Microelectronic Engineering* **17**, 223 (1992).
- [154] W. T. Tsang, R. M. Kapre, R. A. Logan, and T. Tanbun-Ek, *IEEE Photon. Technol. Lett.* **5**, 978 (1993).
- [155] J. N. Damask, *A new photonic device: the integrated resonant channel-dropping filter*, Master's thesis, Massachusetts Institute of Technology, 1993.
- [156] A. Yanof et al., *Proc. of SPIE* **2194**, 36 (1994).
- [157] I. Y. Yang et al., *J. Vac Sci. Technol. B* **13**, 2741 (1995).
- [158] A. W. Yanof, *J. Vac Sci. Technol. B* **9**, 3310 (1991).
- [159] M. Mondol, H. Li, G. Owen, and H. I. Smith, *J. Vac Sci. Technol. B* **12**, 4024 (1994).
- [160] A. Moel, E. E. Moon, R. Frankel, and H. I. Smith, *J. Vac Sci. Technol. B* **11**, 2191 (1993).
- [161] V. V. Wong et al., *J. Vac. Sci. Technol. B* **12**, 3741 (1994).
- [162] E. Kratschmer, S. A. Rishton, D. P. Kern, and T. H. P. Chang, *J. Vac Sci. Technol. B* **6**, 2074 (1988).
- [163] S. A. Rishton, S. P. Beaumont, and C. D. W. Wilkinson, *J. Phys. E* **17**, 296 (1984).
- [164] F. C. Demarest, *Meas. Sci. Technol.* **9**, 1024 (1998).
- [165] P. Hariharan, *Interferometry with lasers*, volume XXIV of *Progress in optics*, *E. Wolf, ed.*, pages 108–164, North-Holland, 1987.
- [166] N. Bobroff, *Meas. Sci. Technol.* **4**, 907 (1993).
- [167] N. M. Oldham, J. A. Kramar, P. S. Hetrick, and E. C. Teague, *Precision Eng.* **15**, 173 (1993).
- [168] A. H. Slocum, *Precision machine design*, Prentice Hall, 1992.

- [169] J. Goodberlet, J. Ferrera, and H. I. Smith, *Electronics Letters* **33**, 1269 (1997).
- [170] J. Goodberlet, J. Carter, and H. I. Smith, *J. Vac Sci. Technol. B* **16**, 3672 (1998).
- [171] M. A. Finalyson, *Improvement of the resolution of a digital heterodyne interferometer using an analog circuit*, Summer research report, 1998.
- [172] E. M. Koontz et al., *Appl. Phys. Lett.* **71**, 1400 (1997).
- [173] M. H. Lim, T. E. Murphy, J. Ferrera, J. N. Damask, and H. I. Smith, *Fabrication techniques for grating-based optical devices*, submitted to the 1999 International Conference on Electron, Ion and Photon Beam Technology and Nanofabrication, 1999.
- [174] M. L. Schattenburg, I. Tanaka, and H. I. Smith, *Microelectronic Engineering* **6**, 273 (1987).
- [175] A. Moel et al., *J. Vac Sci. Technol. B* **9**, 3287 (1991).
- [176] M. Burkhardt, *Fabrication technology and measurement of coupled quantum dot devices*, PhD thesis, Massachusetts Institute of Technology, 1995.
- [177] J. O. Choi, J. A. Moore, J. C. Corelli, J. P. Silverman, and H. Bakhru, *J. Vac Sci. Technol. B* **6**, 2286 (1988).
- [178] R. J. Hawryluk, H. I. Smith, A. Soares, and A. M. Hawryluk, *J. Appl. Phys.* **46**, 2528 (1975).
- [179] A. Moel, M. L. Schattenburg, J. M. Carter, and H. I. Smith, *J. Vac Sci. Technol. B* **8**, 1648 (1990).
- [180] A. Moel, *An aligner for X-ray nanolithography*, PhD thesis, Massachusetts Institute of Technology, 1993.
- [181] J. Ferrera and S. A. Rishton, 1991, unpublished results.
- [182] H. A. Haus and Y. Lai, *J. Lightwave Technol.* **9**, 754 (1991).
- [183] J. N. Damask, *J. Lightwave Tech.* **14**, 812 (1996).
- [184] M. J. Khan, *Gain-distributed feedback filters*, Master's thesis, Massachusetts Institute of Technology, 1996.
- [185] G. Billingsley and K. Keller, *KIC: a graphics editor for integrated circuits*, Internal memorandum, University of California at Berkeley.
- [186] C. A. Mead and L. A. Conway, *Introduction to VLSI Systems*, Addison-Wesley, 1980.